Examining the tectonic context of sedimentary copper deposits using geological and passive seismic methods

Tobermory Cameron Mackay-Champion

University of Oxford

A thesis submitted for the degree of
Doctor of Philosophy

University College

April 2025

I would like to dedicate this thesis to my wonderful family. Dad, Mum, Appin, Durness, Nanny - you are all awesome!

Acknowledgements

I am grateful to BHP for funding this research, and to First Quantum Minerals Ltd. and the Geological Survey of Zambia for partnering with me during our research in Zambia.

I would like to thank my supervisors, Professor Michael Daly, Professor John-Michael Kendall, and Associate Professor Richard Palin. Thank you for sharing your expertise and time with me throughout this project, and for giving me the opportunity to work with you and study such a fascinating field of geoscience. I am hugely grateful. I have so enjoyed working with you all, and you have taught me a great deal.

I would like to thank Dr Nicholas Harmon, from Woods Hole Oceanographic Institute, for being such a generous support and for hosting me across the pond. Thanks also to Dr Thomas Hudson for providing crucial insights during the early stages of this project. I would also like to acknowledge the support of Professor Mike Searle, who has been a constant source of geological knowledge and inspiration during my time at the University of Oxford.

Finally, I would like to thank my family and friends. I could not have done this without you. Thank you for all your love and support, and for putting up with all my geologically-themed monologues.

Declaration

I confirm the work submitted here is my own and has not been submitted in whole or in part for consideration for any other degree or qualification in this, or any other university. Whilst this thesis is my own work, parts were completed in collaboration with others, the specifics of which are outlined below.

Chapter 2: *The Application of MEMS Accelerometers to Regional-scale Passive Seismology: A Case Study of the Sercel WiNG Nodes.* **Mackay-Champion, T.C**., Hudson, T., Harmon, N., Ogden, C., Wilcox, S., Finch, L., Lane, V., Kendall, J-M., and Daly, M.C.

- This manuscript is under review at *Seismica*.
- *Conceptualization and project design*: M.C. Daly., T. Mackay-Champion, T. Hudson, J-M. Kendall. *Data collection*: T. Mackay-Champion, S. Wilcox, L. Finch, V. Lane, J-M. Kendall. M.C. Daly. *Data analysis*: T. Mackay-Champion, C. Ogden (receiver function analysis). *Project advisor*: T. Hudson, N. Harmon. *Writing*: T. Mackay-Champion.

Chapter 3: *Towards Optimal P-T Estimates: An Inverse Method for Quantifying P-T Conditions and Uncertainty in Phase Equilibrium Modelling.* **Mackay-Champion, T.C.,** Cawood, I.P.

- This manuscript is under review at the *Journal of Metamorphic Geology*.
- *Conceptualization and project design*: T. Mackay-Champion, I. Cawood. *Data collection*: T. Mackay-Champion, I. Cawood. *Data analysis*: T. Mackay-Champion. *Method development and software creation*: T. Mackay-Champion. *Writing*: T. Mackay-Champion, I. Cawood.

Chapter 4: *The Metamorphic and Structural History of the Kansanshi Cu-Au Mine, and Its Implications for the Tectonics of the Zambian Copperbelt.* **Mackay-Champion, T.C.,** Purkiss, M., Chanda, M., Palin, R., Zimba, M., Daly, M.C.

- *Conceptualization and project design*: T. Mackay-Champion, M. C. Daly. *Data collection*: T. Mackay-Champion, M. Chanda, M. Zimba, M. Purkiss. *Data analysis*: T. Mackay-Champion, M. Purkiss (sedimentary log of KRX082). *Project advisor*: M. Daly, R. Palin. *Writing*: T. Mackay-Champion.

Chapter 5: *Ambient Noise Tomography for Local to Regional Mineral Exploration Using Nodal MEMS Accelerometers: A Case Study from the Kansanshi Cu-Au Mine, Zambia.* **Mackay-Champion, T. C.,** Harmon, N., Mutelekesha, S., Chanda, M., Hudson, T., Kendall, J-M., Daly, M.C.

- This manuscript is under review at *GEOPHYSICS*.
- *Conceptualization and project design*: T. Mackay-Champion, M.C. Daly., T. Hudson, J-M. Kendall. *Data collection*: T. Mackay-Champion, S. Mutelekesha, M. Chanda. *Data analysis*: T. Mackay-Champion. *Project advisor*: N. Harmon. *Writing*: T. Mackay-Champion.

Tobermory Cameron Mackay-Champion
April 2025

Abstract

The fundamental importance of metals such as copper (Cu), nickel, lithium, and cobalt to electricity transmission and battery technology has seen them become critical components of the energy transition to a Net Zero future. However, the declining effectiveness of mineral exploration programs has led many to predict a global deficit of metals such as Cu in the coming decade. Sedimentary-Cu deposits currently account for a significant amount of the world's copper production, yet the exploration for new deposits is severely hampered by our limited understanding of the first-order geological processes controlling deposit formation. The purpose of this thesis is to test new technologies and workflows to better understand the formation of sedimentary copper deposits and improve the exploration performance for these deposits. The thesis uses the Kansanshi Copper (Cu) – Gold (Au) mine of the Central African Copperbelt as a natural laboratory for this work. Kansanshi is the third largest copper producer in Africa, with a resource estimate of 982.3 Mt of copper as of December 2023. Herein, I show that novel nodal seismometers (Sercel WiNG nodes) are appropriate for passive seismology at a subregional to regional scale. I found that an experimental network comprised of 30 WiNG nodes was able to reliably image a significant body of source sediments beneath the Kansanshi mine. This supports the importance of local sediment accommodation space to the formation of sediment-Cu deposits, and the suitability of ambient noise tomography as a tool in mineral exploration. I have broadened this perspective through the development of a new workflow for analysing the Pressure (P) – Temperature (T) history of metamorphic rocks. This was integrated with detailed field mapping and structural analysis to provide a new model for the geodynamic and structural evolution of the Kansanshi mine. I conclude that Kansanshi comprises an allochthonous, kyanite-grade (550–620 °C, 7.5–9.5 kbar) metamorphic sheet that was thrust over a Lower Roan depocentre during the later stages of the Lufilian Orogeny, both during and prior to Cu-Au mineralisation. Integrating these diverse geophysical and geological approaches in terms of technology and process has resulted in new insights into the formation of one of the world's premier sediment-hosted Cu mines. In addition, it has added a new tool to the sedimentary Cu exploration tool kit and insight into the formation of the Central African Copperbelt regionally.

Table of contents

List of figures **xv**

List of tables **xvii**

1 Introduction **1**
1.1 Sediment-hosted copper and its importance for a net-zero future 1
1.2 Deposit models 2
1.3 Research overview 3
1.4 The Central African Copperbelt 4
1.4.1 Kansanshi copper-gold deposit 7
1.5 The role of passive seismology in mineral exploration 8
1.6 The importance of metamorphic petrology and uncertainty analysis . . . 10
1.7 Thesis structure 11

2 The Application of MEMS Accelerometers to Regional-scale Passive Seismology. **13**
2.1 Introduction 13
2.2 Methods 14
2.2.1 Array details 14
2.2.2 Instrument specifications and response 16
2.2.3 Ambient noise analysis 18
2.2.4 Earthquake analysis 19
2.2.4.1 Arrival time analysis 19
2.2.4.2 Receiver function calculation 19
2.3 Results 21
2.3.1 Ambient noise analysis 21
2.3.2 Ambient noise analysis 24
2.3.3 Earthquake analysis 25
2.3.3.1 Arrival time analysis 26
2.3.3.2 Crustal thickness estimate 29
2.4 Discussion 31
2.5 Conclusions 32

3 Towards Optimal Estimates of P-T Conditions and Uncertainty. **33**

3.1 Introduction . . . 34
3.2 Uncertainties . . . 35
3.2.1 Geological uncertainty . . . 35
3.2.2 Analytical uncertainty . . . 36
3.2.3 Parameter uncertainty . . . 37
3.2.4 Model uncertainty . . . 38
3.2.5 Combined uncertainties and correlations . . . 40
3.3 Inversion method . . . 41
3.3.1 Best-fit *P-T* conditions: the grid-search inversion . . . 42
3.3.2 Uncertainty analysis: bootstrap resampling . . . 45
3.3.3 Diagnostics . . . 45
3.3.3.1 Quality of data fit (X_i, X_{total}) . . . 45
3.3.3.2 Sensitivity (ΔP, ΔT) . . . 46
3.3.3.3 Standard error (SE) . . . 48
3.3.4 Applying the workflow . . . 48
3.3.4.1 Observations setup . . . 48
3.3.4.2 Predictions setup . . . 49
3.3.4.3 Result interrogation . . . 49
3.3.4.4 Result reporting . . . 50
3.4 Natural examples . . . 51
3.4.1 Sample descriptions . . . 51
3.4.2 ICSV13 . . . 52
3.4.2.1 Conventional methods of analysis . . . 52
3.4.2.2 Grid-search inversion and uncertainty analysis . . . 54
3.4.3 ICSV117 . . . 55
3.4.3.1 Conventional methods of analysis . . . 55
3.4.3.2 Grid-search inversion and uncertainty analysis . . . 56
3.5 Synthetics . . . 57
3.5.1 The impact of mineral measurement uncertainty, *MMU* . . . 58
3.5.2 The impact of bulk composition uncertainty, *BCU* . . . 60
3.5.3 The impact of observational uncertainty, *OU* . . . 62
3.5.4 The impact of uncertainty source and variable type across *P-T* space . . . 62
3.5.5 A comparison between uncertainty sources along a geotherm . . . 67
3.6 Discussion . . . 68
3.6.1 Uncertainty estimates in pelitic systems . . . 69
3.6.1.1 The impact of uncertainty source . . . 69
3.6.1.2 The impact of variable type . . . 70
3.6.1.3 The impact of metamorphic grade . . . 71
3.6.1.4 Tectonometamorphic controls on uncertainty in natural systems . . . 72

3.6.1.5 Comparison with prior uncertainty estimates 72
3.6.2 Quantitative petrological modelling 73
3.6.2.1 Comparison to other quantitative workflows 73
3.6.2.2 Advantages and limitations of the new workflow 74
3.7 Conclusions 76
3.8 Software Availability 77

4 The Metamorphic and Structural Evolution of the Kansanshi Cu-Au Mine and NW Zambia 79
4.1 Introduction 79
4.2 Geological Setting and previous tectonic models 80
4.3 Field relationships and structural analysis 82
4.3.1 The Paleoproterozoic - Mesoproterozoic basement 84
4.3.2 The Neoproterozoic Katangan Supergroup sediments 85
4.3.2.1 KRX082 drill core 87
4.3.3 The metamorphic sheet 89
4.3.4 Felsic and mafic intrusions 90
4.3.5 Structural analysis 90
4.4 Pressure-temperature evolution of metamorphism 93
4.4.1 Methods 93
4.4.1.1 Approach 93
4.4.1.2 Data collection 94
4.4.2 Results 95
4.4.2.1 Z03b: garnet-kyanite schist 95
4.4.2.2 Z10: biotite-epidote-kyanite schist 97
4.4.2.3 Z36: garnet-biotite schist 100
4.4.2.4 Z29: biotite-muscovite schist 103
4.4.2.5 Z34: garnet-biotite schist with felsic intrusions 105
4.4.3 Metamorphic Synthesis 107
4.5 Tectonic Synthesis 109
4.6 Discussion 112
4.6.1 Comparison to previous tectonic models 112
4.6.2 Sediment thickness beneath Kansanshi 112
4.7 Conclusions 113

5 The Use of MEMS Accelerometers and Ambient Noise Tomography for Regional Mineral Exploration. 115
5.1 Introduction 115
5.1.1 Instrumentation 117
5.1.2 Geological Setting of the Kansanshi deposit 118
5.2 Ambient Noise Tomography Method 119
5.2.1 Deployment, cross-correlations, and phase velocity measurements 119

5.2.2 Phase Velocity Inversion . . . 121
5.2.3 S-wave Velocity Inversion . . . 123
5.3 Results . . . 124
5.3.1 Cross-correlations and phase velocity . . . 124
5.3.2 2-D Phase Velocity Maps . . . 124
5.3.3 2-D S-wave Cross-section . . . 126
5.4 Discussion . . . 128
5.4.1 The Geological Structure of the Kansanshi Cu-Au Mine . . . 128
5.4.1.1 A comparison with the results from Chapter 4 . . . 129
5.4.2 The Mineral System at Kansanshi . . . 130
5.4.3 Limitations of the approach . . . 131
5.5 Conclusions . . . 131

6 Conclusions 133
6.1 Thesis conclusions . . . 133
6.1.1 The application of MEMS accelerometers to regional-scale passive seismology . . . 133
6.1.2 Towards Optimal Estimates of *P-T* Conditions and Uncertainty . 134
6.1.3 The tectonic evolution of the Kansanshi Cu-Au mine and the use of MEMS accelerometers in mineral exploration . . . 135
6.1.4 The Kansanshi Cu-Au mineral system . . . 136
6.2 Summary . . . 138
6.3 Future work . . . 138
6.3.1 Ambient noise tomography . . . 138
6.3.2 Metamorphic methodology . . . 139
6.3.3 Kansanshi Cu-Au mine . . . 139
6.4 Finding the next Copperbelt . . . 140

References 141

Appendix A The Application of MEMS Accelerometers to Regional-scale Passive Seismology. 159

Appendix B Towards Optimal Estimates of *P-T* Conditions and Uncertainty. 165
B.1 Methods: Natural Sample . . . 165
B.1.1 Analytical setup and mineral recalculation . . . 165
B.1.2 Thermobarometry . . . 166
B.1.2.1 Conventional thermometry . . . 166
B.1.2.2 Multi-equilibrium barometry . . . 166
B.1.2.3 Phase equilibrium modelling . . . 167
B.1.2.4 Constraining $a\mathrm{H_2O}$ . . . 168
B.2 Comparison between LinaForma and Bingo-Antidote . . . 168

B.2.1 Integration with other software 168
B.2.2 The objective functions and diagnostics 169
B.2.3 The inversion technique 169

Appendix C The Metamorphic and Structural Evolution of the Kansanshi Cu-Au Mine and NW Zambia 173
C.1 Outcrop locations 173
C.2 Structural measurements 178
C.3 Sample locations and compositions 180
C.4 Data from Electron Probe Microanalysis of samples 180
C.5 Garnet profiles 217

Appendix D The Use of MEMS Accelerometers and Ambient Noise Tomography for Regional Mineral Exploration. 221
D.1 Error analysis 224
D.2 Resolution estimates 224
D.3 Phase velocity tomography trade-off 225
D.4 Phase velocity maps with accompanying resolution and error estimates . 226
D.5 S-wave inversion trade-off 231

List of figures

1.1 Simplified geological map of Zambia 4
1.2 Field photos of Kansanshi Mine 7
1.3 Poor level of outcrop exposure in NW Zambia 8
1.4 Seismometer deployment methods 10

2.1 Deployment map of the Oxford seismometer network 15
2.2 Deployment techniques for the WiNG nodes. 15
2.3 Instrument response of the WiNG node, ESPCD and geophone 17
2.4 Probabilistic Power Spectral Density analysis for 5th November 2020 . . . 22
2.5 Ambient noise analysis 24
2.6 Instrument response to a Mw 7.6 Alaskan earthquake 25
2.7 Response of the seismometer network to a Mw 7.0 Greece Earthquake . . 27
2.8 Response of the ON012 WiNG node to a selection of earthquakes 28
2.9 STA/LTA plots for a selection of earthquakes 29
2.10 Receiver functions calculated for the MW 7.6 Alaska earthquake 30
2.11 H-k stacking results 30

3.1 Schematic summary of the primary sources of uncertainty in thermobarometry 39
3.2 Schematic summary of common problems associated with the application of intersecting mineral composition variables 42
3.3 Schematic summary of the presented workflow and methods 44
3.4 Workflow example using natural sample ICSV13 47
3.5 Example of compiled final result of ICSV13 and ICSV117 53
3.6 Uncertainty in P-T estimate as a result of mineral measurement uncertainty 59
3.7 Uncertainty in P-T estimate as a result of bulk composition uncertainty . 61
3.8 Uncertainty in P-T estimate as a result of observational uncertainty . . . 63
3.9 The distribution of uncertainty in T and P 64
3.10 The uncertainty in T and P for each variable 66
3.11 The change of uncertainty in T and P along a geotherm 68

4.1 Simplified geological map of Zambia 81
4.2 Geological map of Solwezi and Kansanshi 83
4.3 Tectonostratigraphic column for Solwezi and Kansanshi. 84
4.4 Sedimentary log of Core KRX082 88

4.5 Geological cross-section of Solwezi area . . . 91
4.6 P-T result for Sample Z03b . . . 96
4.7 P-T result for Sample Z10 . . . 98
4.8 P-T result for Sample Z36 . . . 101
4.9 Garnet pressure paths for Sample Z36 . . . 102
4.10 P-T result for Sample Z29 . . . 104
4.11 P-T result for Sample Z34 . . . 105
4.12 P-T estimates from this study and from the literature. . . . 107
4.13 Tectonic model for Kansanshi and the NW Zambian Copperbelt. . . . 110

5.1 Tectonic map of the Central African Copperbelt . . . 118
5.2 Deployment map for the Solwezi seismometer network . . . 120
5.3 Station-pair cross-correlation moveout. . . . 124
5.4 Average surface-wave phase velocities . . . 125
5.5 Depth sensitivity of the surface waves . . . 126
5.6 2-D phase velocity models . . . 126
5.7 2-D S-wave model . . . 127
5.8 Tectonic interpretation . . . 128

A.1 H-k stacking results for Guralp CMP-ESPCD . . . 161
A.2 H-k stacking results for WiNG node . . . 162

B.1 Number of bootstrap resamples relative to best-fit median and IQR . . . 170
B.2 Petrographic images of ICSV13 and ICSV117 . . . 170
B.3 Binned temperature and pressure domains used in this study . . . 171
B.4 Geotherm from Copley & Weller (2022) . . . 171

C.1 Garnet profiles for sample Z03b. . . . 217
C.2 Garnet profiles for sample Z36. . . . 218
C.3 Garnet profiles for sample Z34. . . . 219

D.1 Model damping trade-off for phase velocity tomography . . . 225
D.2 Characteristic length trade-off for phase velocity tomography . . . 225
D.3 Phase velocity tomography outputs for 2.5s Rayleigh wave. . . . 226
D.4 Phase velocity tomography outputs for 3.5s Rayleigh wave. . . . 227
D.5 Phase velocity tomography outputs for 4.5s Rayleigh wave. . . . 228
D.6 Phase velocity tomography outputs for 5.5s Rayleigh wave. . . . 229
D.7 Phase velocity tomography outputs for 6.5s Rayleigh wave. . . . 230
D.8 Phase velocity tomography outputs for 7.0s Rayleigh wave. . . . 231
D.9 S-wave damping trade-off. . . . 232

List of tables

3.1 Mineral composition variable definitions for common pelitic and metabasic minerals at sub-solidus conditions. . . . 43
3.2 Definitions of parameters used in the inversion analysis . . . 46
3.3 Bulk composition of ICSV13 and ICSV117 . . . 51
3.4 Variables used for parametric bootstrap resampling of samples . . . 54
3.5 Inversion output and diagnostics for ICSV13. . . . 55
3.6 Inversion output and diagnostics for ICSV117. . . . 56
3.7 Standard deviation of each oxide mol% applied to the worldwide median pelite bulk composition used in the Monte-Carlo simulation. . . . 60
3.8 Median temperature and pressure uncertainty across different metamorphic zones and facies series . . . 71

4.1 Inversion fit values for sample lithologies. . . . 95

A.1 Oxford Seismograph Network Details . . . 160
A.2 Values used for the STA/LTA analysis. . . . 163

B.1 EPMA peak and background measurement parameters . . . 165

C.1 Solwezi outcrop locations . . . 173
C.2 Solwezi structural measurements . . . 178
C.3 Sample locations . . . 180
C.4 Water-saturated mole % composition of each sample. . . . 180
C.5 Sample Z03b EPMA analysis . . . 181
C.6 Sample Z10 EPMA analysis . . . 193
C.7 Sample Z29 EPMA analysis . . . 196
C.8 Sample Z34 EPMA analysis . . . 201
C.9 Sample Z36 EPMA analysis . . . 209

D.1 Solwezi Seismograph Network Details . . . 222

Chapter 1

Introduction

1.1 Sediment-hosted copper and its importance for a net-zero future

The fundamental importance of metals such as copper (Cu), nickel, lithium, and cobalt to electricity transmission and battery technology has seen them become critical components of the energy transition to a Net Zero future. However, S&P Global Market Intelligence have estimated a 20 million tonne deficit in Cu by 2035 as global electrification increases demand. This problem is exacerbated by the declining effectiveness of mineral exploration programs. The discovery rate of deposits has been in decline over the past thirty years (*Okada*, 2021), and the recent growth of exploration budgets has not led to a meaningful increase in the number of major discoveries (*White and Hook*, 2023; *McKeith et al.*, 2010). In order to reverse these fortunes, we must develop new methods for metal exploration (*Watzel*, 2023) and new tools and techniques for exploring for and defining subsurface deposits (*Wood and Hedenquist*, 2019).

Sediment-hosted Cu deposits currently account for ∼23 % of the world's Cu production (*Hitzman et al.*, 2005), and largely comprise relatively thin (< 30 m) zones of disseminated and veinlet Cu-sulphides that occur concordant with lithological layering within sedimentary basins (*Hitzman et al.*, 2010). The deposits occur within a variety of sedimentary rock types, but are typically found at or near the contact between red-bed sequences and overlying shales, siltones or carbonates (*Hitzman et al.*, 2010). The majority of sediment-hosted deposits are small and sub-economic. However, there are currently three known basins which contain supergiant deposits (> 24 Mt contained Cu): the Neoproterozoic Katanga Basin (the Central African Copperbelt) (*Selley et al.*, 2005), the Permian Zechstein basin of Europe (*Vaughan et al.*, 1989), and the Paleoproterozoic Kodaro-Udokan basin of Siberia (*Bakun et al.*, 1966). Economic deposits within these basins are highly desirable due to their high grades of ore and high quantity of ore relative to porphyry Cu and volcanogenic massive sulphide deposits, respectively (*Dominish et al.*, 2019). Despite this, exploration for sediment-hosted metal deposits has been less successful than that for magmatic deposits because the first-order geological controls on the location of sediment-hosted deposits are poorly understood, which severely limits predictive capabilities for identifying new target areas (*Hoggard et al.*, 2020).

1.2 Deposit models

Traditionally, mineral exploration relies heavily on the use of "type" deposit models for locating and exploiting mineral deposits (*Bidgood and Hitzman*, 2023). Examples of these models include the Carlin-type gold deposits (*Cline et al.*, 2005) and Bushveld-type Platinum Group Element (PGE) deposits (*Maier*, 2005). Exploration campaigns have sought to find areas with analogous geological conditions to that of the type deposit of interest. This approach has a number of significant drawbacks. Firstly, a strict focus on the type deposit means potential deposits may be missed if they lack certain characteristics which are thought to be important. An example of this false negative can be found in the Eastern Goldfields of the Austrailian Yilgarn craton, where it was previously believed that gold was predominantly hosted in mafic rocks. However, major discoveries have now occurred in other rock types (e.g., conglomeratic sequences, Kanowna Belle, 8.5 Moz) which were previously believed to be barren (*McCuaig and Hronsky*, 2014). Another clear drawback of the type deposit approach is the false positive, where promising geological analogs are discovered to be barren due to a critical missing factor that is unidentified in the deposit model. In the Central African Copperbelt (CACB) the overt focus on locating the oft-mineralised "ore shale" has resulted in many sub-economic discoveries as other critical factors such as heat flow gradients and petrophysical properties are ignored (*Purkiss*, 2024). These problems can largely be attributed to the contrast in spatial scales between deposit models, which focus on deposit-scale observations, and exploration campaigns which begin at continental to regional scales. For example, the size of a geochemical footprint above a deposit may be on the order of tens of square kilometres (*Sillitoe*, 2010) and are often not indicative of well-endowed versus sub-economic deposits. To put this into context, Ivanhoe Mines recently acquired 22,195 km^2 of greenfield prospecting rights in Angola for sedimentary-copper exploration. This is a significant difference in spatial scale, which helps to explain why the success of greenfield exploration campaigns is estimated to be ∼0.5 % (*González-Barros and Espí*, 2019) and why a new method and framework for mineral exploration is so required.

As a result of this problem, the exploration industry has increasingly worked towards developing a framework for understanding mineral deposits at a larger range of scales. This is known as the Mineral Systems Concept (*Wyborn et al.*, 1994) and is heavily inspired by the petroleum systems approach widely used in the oil and gas exploration industry (e.g., *Demaison and Huizinga*, 1991). The Mineral Systems Concept focuses on identifying the sources of metals, the mechanisms and pathways for their mobilization and transport, and then the structures and conditions required for trapping and depositing the metals in a specific location. Within this framework, (*Hitzman et al.*, 2010) described four important controls on the formation of significant sediment-hosted metal deposits: 1) the presence of metal source sediments, 2) the presence of reduced sediments to serve

as chemical traps, 3) saline brines for leaching and transporting metals, and 4) the expulsion of mineralizing fluids through focused zones.

These four controls have provided much-needed clarity to the exploration workflow and provoke a number of important questions. Firstly, at what geographical and temporal scale are these factors important? Clearly the formation of a deposit relies upon chemical local traps and focusing zones, but it is not clear whether the source sediments need to be located near to the deposit in space or time. Secondly, what controls the variability in size and deposit-style seen among sediment-hosted deposits? For example, deposits can range from cross-cutting vein-hosted deposits (e.g., Kansanshi Cu-Au deposit of Zambia) to flat-lying, stratiform deposits (e.g., Kamoa-Kakula Cu deposit of the Democratic Republic of the Congo). Finally, how might we explore for the presence of these four controls?

1.3 Research overview

In this thesis, I propose that ambient noise seismic tomography using MEMS accelerometers can be used to help answer these questions and to locate areas of interest for metal exploration. To test this, I examine the suitability of MEMS accelerometers for low-frequency (< 1 Hz) passive seismic studies. I then use these accelerometers to examine the structural setting of the Kansanshi Cu-Au mine in the CACB (Zambia). This research provides insight into whether local sediment sources play a critical role in forming large deposits and demonstrates the effectiveness of ambient noise tomography using MEMS accelerometers for identifying exploration targets. Understanding the variability in size and deposit style among sediment-hosted mineral deposits requires insight into their geodynamic evolution — specifically, their structural, temperature, and pressure histories. To address this, I develop a novel metamorphic method for quantifying the pressure-temperature history of key rock formations. By integrating this new method with detailed field mapping and the ambient noise tomography results, I reconstruct the geodynamic evolution of the Kansanshi Cu-Au mine during the formation of the CACB. Ths work allows me to postulate why the Kansanshi Cu-Au mine displays a significantly different style of mineralisation to the standard stratiform deposits within the CACB.

The Central African Copperbelt, and specifically the Kansanshi Cu-Au mine, was chosen as a natural laboratory for this thesis because it displays a range of mineralisation types and there remain significant unknowns surrounding the tectonostratigraphic evolution of the basin and the structural controls on the development of its mineral deposits (*Alessio et al.*, 2019). This problem is exemplified by Kansanshi, a major operation of First Quantum Minerals Ltd., which for many years was Africa's largest copper producer (Fig. 1.2). An overview of the tectonics of the CACB and the Kansanshi deposit is given below.

1.4 The Central African Copperbelt

The Central African Copperbelt of Zambia and the Democratic Republic of the Congo is the world's largest sediment-hosted copper and cobalt province (*Selley et al.*, 2005) and contributes about 14 % and 60 % of the world's supply of these two metals respectively. The CACB is hosted in the Neoproterozoic Katangan Basin, which crops out between the Congo, Kalahari and Bangweulu cratons of Central Africa (light grey, Fig. 1.1). The CACB and surrounding areas have been traditionally divided into several terranes,

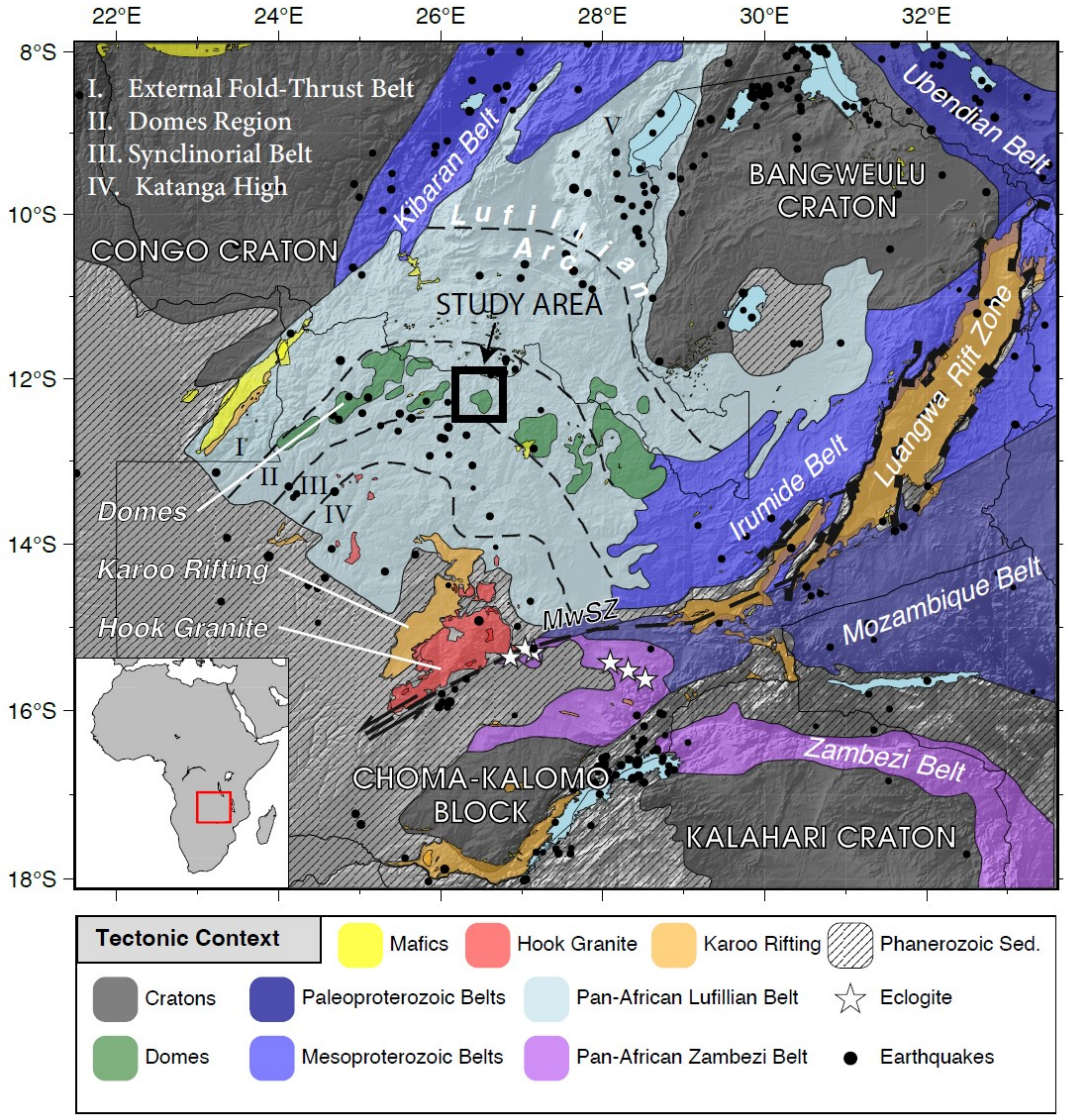

Fig. 1.1 Simplified geological map of Zambia, after *Kounoudis et al.* (2024) and *Porada and Berhorst* (2000). The location of the Kansanshi Cu-mine and Solwezi Dome is demarcated by a black polygon.

spanning three separate time periods. The oldest rocks in the region are Archaean to Palaeoproterozoic and belong to the Congo, Bangweuelu and Kalahari cratons which crop out to the northwest, northest and south of the CACB respectively. These cratons

exhibit lithospheric thicknesses in excess of 200 km (*Schaeffer and Lebedev*, 2013). The Bangweulu craton is surrounded by two Mesoproterozoic belts called the Irumide and the Kabaran belts, which crop out to the east and west of the craton margin respectively. In relation to the Neoproterozoic CACB, the third preserved time period, all the aforementioned terranes can be considered basement lithologies and define the boundaries of the basin (*Daly et al.*, 2024).

The CACB itself can be divided into four domains: (1) the foreland succession, (2) the external fold-thrust belt, (2) the Domes Region, (3) the Synclinorial Belt, and (4) the Katangan High, including the Hook Batholith (*Porada and Berhorst*, 2000). To the south of the CACB, historically defined by the Mwembeshi Shear Zone, lies the Neoproterozoic Zambezi Belt.

The foreland succession The northern margin of the CACB comprises the Archaen-Palaeoproterozoic Congo and Bangweulu cratons and the Mesoproterozoic Kilbaran and Irumide belts. These form the basement to the CACB. The foreland is characterized by relatively undeformed, autochthonous sub-horizontal to gently dipping Katangan Supergroup sediments onlapping these basement rocks (*Unrug*, 1988). Historically this region as been referred to as the Shaba, Katangan or Kundulungu aulacogen or Golfe du Katanga (*De Swardt et al.*, 1964; *Unrug*, 1988; *Porada*, 1989).

External fold-thrust belt Structurally above the foreland succession lies the external fold-thrust belt, which crops out in the Zambian Copperbelt and the southern Democratic Republic of the Congo. This belt is characterized by northward thin-skinned thrusting and imbrication of the Katangan Supergroup stratigraphy above evaporite-rich detachments (*Coward and Daly*, 1984; *Daly*, 1986; *Kampunzu and Cailteux*, 1999). These lubricated detachments accommodated significant lateral transport up to 65 km (*Jackson et al.*, 2003) and 150 km northwards (*Porada and Berhorst*, 2000). The evaporites also facilitated fluid overpressuring and diapirism, as well as the extrusion of salt glaciers (*François*, 1973; *Jackson et al.*, 2003). The metamorphic grade of the external belt decreases from greenschist to prehnite-pumpellyite down structural section towards the north (*Selley et al.*, 2005).

Domes Region Structurally above the fold-thrust belt lies the Domes Region of the CACB, named after five large antiformal domes of Mesoproterozoic basement rock that crop out along strike from one another in northwest (NW) Zambia. The Domes Region is an arcuate zone ∼50 km across strike and features the highest levels of deformation and metamorphism of the entire CACB. The metasediments in the Domes Region range from biotite to garnet-kyanite + melt grade (*Cosi et al.*, 1992; *John et al.*, 2004; *Eglinger et al.*, 2016) – *Eglinger et al.* (2016) postulated it to be the site of the suture zone between the Congo and Kalahari cratons, in contrast *Daly et al.* (2024) argue it

represents a completely closed and inverted, hyper-extended local basin, of the order of 100 km wide within a broad inter-cratonic zone separating the two cratons. The Kansanshi Cu-Au mine, to be discussed below, crops out in the Domes Region.

Synclinorial Belt To the south of the Domes Region lies the Synclinorial belt. Few studies have focused on this region, likely due to the relatively poor exposure and the absence of current mining operations. However, it is known to comprise intensely deformed rocks ranging from argillaceous sediments up to biotite-grade metapelites (*Porada and Berhorst*, 2000; *Goscombe et al.*, 2020), with steep north-vergent folds in the south (*Unrug*, 1988; *Daly et al.*, 1984). It is unclear how similar the lithologies are between the Synclinorial Belt and the northern Domes region and external fold-thrust belt. However, the synclinorial belt certainly displays less evidence for salt tectonics (*Daly et al.*, 2024).

Katanga High and Hook batholith Structurally above the Synclinorial Belt lies the Katanga High and the Hook Batholith, separated by the Mwembeshi Shear Zone from the Zambezi Belt to the southeast. The Katanga High is characterized by extensive outcrops of carbonate rocks and low- to high-grade metapelites (**?**). The Katanga High contains the Matala Dome basement inlier, which is surrounded by kyanite-bearing metasediments of Lufilian age (*Naydenov et al.*, 2016). The southeast part of the Katanga High is intruded by the Lufilian-age Hook Batholith, a bimodal magmatic body of felsic units and minor mafic units (*Hanson et al.*, 1988; *Milani et al.*, 2015; *Naydenov et al.*, 2014). The felsic units consist of an alkali-calcic suite of monzogranite, granodiorite and granite and an alkali suite of syenite and alkali-granite (*Lobo-Guerrero Sanz*, 2005; *Naydenov et al.*, 2014). The mafic units are predominantly small outcrops of syn-tectonic gabbro and demonstrate the involvement of mantle components in the generation of the Hook Batholith (*Milani et al.*, 2015).

Mwembeshi Shear Zone and the Zambezi Belt The south-eastern margin of the CACB has historically been defined by the Mwembeshi Shear Zone (MSZ) (e.g., *De Swardt et al.*, 1964; *Daly*, 1986). The MSZ is commonly described as a major strike-slip fault, although the fault kinematics and tectonic significance are debated. Some studies have defined the MSZ as a suture zone between the Congo and Kalahari cratons with several phases of deformation, including reverse and dextral motion followed by a later sinistral phase (e.g., *Coward and Daly*, 1984; *Daly et al.*, 2024). *Porada and Berhorst* (2000) concluded that the MSZ represented the reactivation of a pre-existing lithospheric zone of Paleoproterozoic weakness, supporting sinistral movement of the CACB relative to the south-lying Zambezi Belt during the Lufilian orogeny. However, recent studies informed by geophysical analysis such as SKS-splitting have called into question the significance of the MSZ. For example, *Kounoudis et al.* (2024) documented

no change in shear-wave anisotropy across the MSZ, which would be highly unusual for a lithospheric-scale structure.

To the southeast of the MSZ lies the Zambezi Belt, a E-W trending, Pan-African belt which crops out in southern Zambia and northern Zimbabwe. The relationship between the CACB and the Zambezi Belt has been debated. Some studies argue that the Zambezi belt comprises rocks whose protoliths are the same as the lithologies seen in the Katangan basin (e.g., *Drysdall et al.*, 1972), while other studies suggest the CACB and the Zambezi Belt are distinct basins juxtaposed during the Lufilian orogeny (*De Swardt et al.*, 1964; *Daly et al.*, 2024). *Burke* (1977) and *John et al.* (2003) suggested that the belt represents a Lufilian-age oceanic suture zone separating the Congo and Kalahari cratons.

1.4.1 Kansanshi copper-gold deposit

As discussed above, the Kansanshi Cu-Au mine is hosted in the Domes Region of the CACB (Fig. 1.1). Despite the history of Kansanshi, being originally exploited

Fig. 1.2 Kansanshi Cu-Au Mine. A) High-grade Cu-bearing veins. B) Northwest pit.

by indigenous peoples and then targeted by various mining companies from 1906 onwards, the metamorphic and deformational complexity have thus-far prevented the formulation of a coherent geodynamic and structural model for the deposit (*MacIntyre*, 2019). Without properly understanding these first-order constraints, it is difficult to understand the underlying mineral system (*McCuaig and Hronsky*, 2014) and therefore difficult to explore for analogous deposits. Kansanshi does not appear to wholly conform to the sediment-hosted stratiform copper deposit model of the traditional Copperbelt (*Hitzman et al.*, 2012), which only goes up to greenschist facies metamorphism (*Rainaud et al.*, 2005), and does not contain the metre-wide, cross-cutting, high-grade veins for which Kansanshi is famous (Fig. 1.2A). Kansanshi is also unique because of its significant endowment of Au, with 982 Mt of ore at 0.11g/t of Au.

1.5 The role of passive seismology in mineral exploration

Understanding the tectonic evolution of Kansanshi and the questions surrounding its mineralisation is complicated by the poor level of outcrop in the area. This is not unique to Kansanshi – the search for new mineral districts is increasing focused on areas below cover (*McCuaig and Hronsky*, 2014) (Fig. 1.3). For example, the project area

Fig. 1.3 Poor level of exposure ∼20 km south of Solwezi, NW Zambia.

surrounding a significant nickel deposit known as Enterprise in NW Zambia is largely under cover with only 0.75 % of the area expressed as outcrop (*Kuhn et al.*, 2019).

In the absence of quality geological constraints, the application of geophysical tools becomes essential to the understanding of the geological structure of an area and to the success of mineral exploration campaigns. The industry currently relies on a plethora of different methods, using both passive and active sources, such seismic imaging, gravity surveys, magnetic surveys, and electrical resistivity. Each of these methods has its own strengths and weaknesses. Active seismic imaging provides excellent recovery of structure in the sub-surface but is often prohibitively expensive with costs amounting to multiple £10,000s per square kilometre (*Davies et al.*, 2004).

Passive seismology is the use of natural seismic wavefields to gain information about the interior of the Earth. Many different analytical techniques are employed in passive seismology, each capable of examining specific Earth features by utilising different components of the seismic wavefield. For example, local earthquake tomography has been successfully used to image the architecture beneath porphyry deposits (*Comte et al.*, 2023). In recent years, a number of studies have started to promote the use of a passive technique known as Ambient Noise Tomography (ANT) for examining the structure around mineral deposits. The advantage of passive seismic data is the low-cost

relative to active seismic studies. ANT uses the difference in phase between ambient surface waves travelling through an array of seismometers to examine the 3-D seismic velocity structure within an area of interest (*Shapiro et al.*, 2005). These ambient surface waves can be generated by distant earthquakes, by the oceans, or by more local sources such as mine blasts. This represents a significant advantage of ANT: it can be performed in areas lacking local seismicity. The phase difference of these surface waves is calculated using cross-correlations of the ambient recordings of pairs of stations within the array. The studies which have promoted ANT within the mineral exploration industry have focused on small-scale surveys with a limited depth of penetration to 100s metres or a couple of kilometres at most (e.g., *Stork et al.*, 2018; *Hollis et al.*, 2018; *Colombero et al.*, 2022; *Jones et al.*, 2024). This limited depth of penetration, coupled with the often-restricted lateral extent provides only a small window into the structural context governing the formation of a metal deposit. However, ANT has also been widely used to examine crustal and mantle structures on regional to continental scales (e.g., *Ward et al.*, 2013). This would be useful for identifying the first-order structures governing the location of mineral deposits, but the resolution of these models is too low for exploration at a mining license or exploration-license scale. This thesis evaluates the effectiveness of ANT for local to regional-scale exploration in sedimentary Cu environments.

The choice of instrumentation is an important consideration here. When designing a passive seismic experiment, selecting the appropriate instrument for recording ground motions is essential. The instrument's performance at various frequencies determines which frequency components of the seismic wavefield can be analysed. Along with the spacing of the stations, the choice of instrument controls the range of seismic techniques that can be applied in a given experiment. Ambient Noise Tomography is an example of this: stations need to be spaced at least two wavelengths apart to accurately measure a given surface wave (*Bensen et al.*, 2007), and the depth of peak sensitivity of a surface wave increases with period such that regional-scale surface wave analysis requires the measurement of surface waves with periods well in excess of 1 s. However, higher frequencies (1 – 50 Hz) are needed for the analysis of microseismic activity which has proven critical to fields such as geothermal exploration (e.g., *Hudson et al.*, 2023).

A wide range of instruments have been developed to accommodate the varying needs of passive seismic techniques, including geophones, broadband seismometers and nodal seismometers (Fig. 1.4). Geophones are compact devices that measure ground velocity using a mass-spring system with a coil and magnet. They are widely used in seismic surveys for oil and gas exploration due to their ruggedness and low cost. However, the low frequency response of a geophone is capped by the resonant frequency which is often around 4.5 Hz. Broadband seismometers, such as Güralp CMG-ESPCDs (Fig 1.4B), are highly sensitive instruments designed to measure a wide range of frequencies. For example, the aforementioned instrument reliably measures waveforms with periods

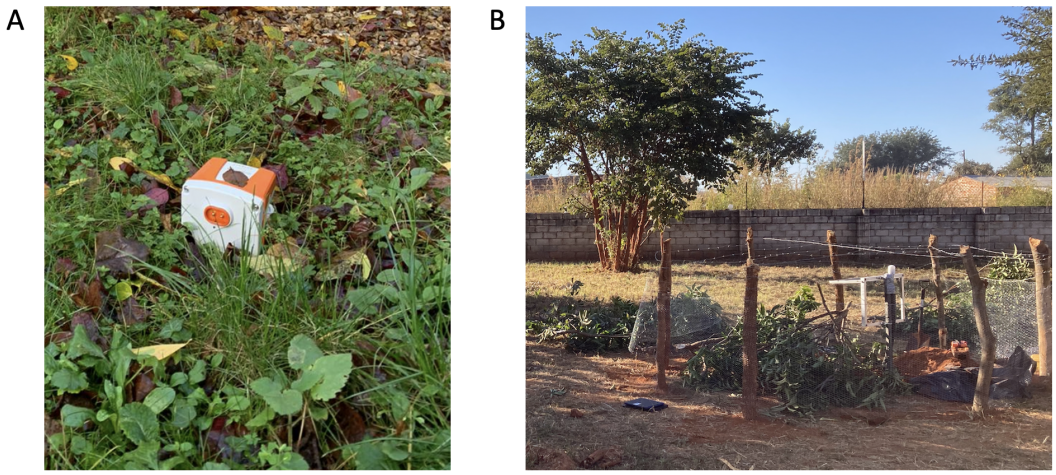

Fig. 1.4 A) Deployment of a Sercel WiNG node (MEMS-accelerometer). The WiNG node is ∼20 cm wide. B) Deployment of a Güralp CMG-ESPCD.

from 0.02–100 Hz. These seismometers offer superior sensitivity but are typically more expensive (£10,000s), less portable, and take several hours to deploy. These disadvantages make passive seismology unattractive for mineral exploration purposes. In recent years, Micro ElectroMechanical Systems (MEMS) accelerometers have become increasingly common in geophysical studies. MEMS sensors have a number of advantages over conventional instruments: their lightweight and compact design makes deploying large arrays easier, the instrument sensitivity to external factors such as temperature are an order of magnitude less than standard geophones (*Laine and Mougenot*, 2014), the sensors lack the data jitter seen in geophones (*Herrmann et al.*, 2021), and the instrument response in acceleration is constant across the frequency domain (*Tellier et al.*, 2020). Given these advantages, MEMS accelerometers should be highly suitable for exploration programs. While several studies have proven the suitability of seismic nodes for regional (10s–100s km) scale geophysical studies (e.g., *Ward et al.*, 2018), no work has been done to assess the applicability of a network of MEMS sensors to regional- and sub-regional/local scale passive seismic studies.

1.6 The importance of metamorphic petrology and uncertainty analysis

The quantification of the pressure and temperature (P-T) history of metamorphic rocks holds implications for constraining geothermal gradients in the subsurface, interpreting sources of economic raw material (e.g., critical metals), and solving geodynamic problems more generally. Phase equilibrium modelling is a widely used approach to decipher the evolution of natural metamorphic assemblages. This modelling relies on datasets including thermodynamic end-member properties and activity–composition (a–X) relations of

minerals, fluid and melt (e.g., *Holland and Powell*, 1998). Such datasets are inherently quantitative, and when integrated with appropriate software, can be used to produce sophisticated forward models predicting equilibrium phase assemblages, phase compositions, and other such variables for different points in pressure-temperature-composition (P-T-X) space (e.g., *Spear et al.*, 2016). Despite the quantitative foundation of these techniques, metamorphic studies predominantly determine the P-T evolution of a rock using qualitative to semi-quantitative comparisons between the forward modeled predicted outputs and the measured values from the rock (*Powell and Holland*, 2008). Additionally, few studies account for any form of uncertainty. Accurately understanding and quantifying these uncertainties is essential for extracting reliable insights from petrological studies and interpreting the data with a clear appreciation of the potential range of values. This thesis introduces a novel workflow to quantitatively determine the best-fit P-T conditions and associated uncertainties for a rock system. This allows me to provide confidence intervals on the metamorphic evolution of rocks within the Kansanshi deposit and to examine the conditions leading to the formation of this world-class deposit.

1.7 Thesis structure

In summary, this thesis explores two key methodological developments and their application to understanding the tectonic evolution and structural configuration of the Kansanshi Cu-Au deposit, with implications for the broader Central African Copperbelt mineral system. First, I assess the suitability of MEMS accelerometers for low-frequency (< 1 Hz) passive seismic studies (Chapter 2). Second, I present a novel workflow for quantitatively determining the best-fit pressure-temperature (P–T) conditions and their associated uncertainties in metamorphic rocks (Chapter 3). These methods are then applied in two complementary studies. In Chapter 4, the metamorphic workflow is integrated with new field mapping and structural analysis to examine the tectonic evolution of the Kansanshi Cu-Au deposit. This is followed by a passive seismic study (Chapter 5), in which I use a network of MEMS accelerometers and ambient noise tomography to investigate the subsurface structural configuration of the deposit. The geophysical approach provides constraints on the Kansanshi mineral system that cannot be obtained through geological investigation alone. The thesis concludes with a synthesis of findings in Chapter 6.

Chapter 2: *The Application of MEMS Accelerometers to Regional-scale Passive Seismology: A Case Study of the Sercel WiNG Nodes.* **Mackay-Champion, T.C.**, Hudson, T., Harmon, N., Ogden, C., Wilcox, S., Finch, L., Lane, V., Kendall, J-M., and Daly, M.C.

Chapter 3: *Towards Optimal P-T Estimates: An Inverse Method for Quantifying P-T Conditions and Uncertainty in Phase Equilibrium Modelling.* **Mackay-Champion, T.C.,** Cawood, I.P.

Chapter 4: *The Metamorphic and Structural History of the Kansanshi Cu-Au Mine, and Its Implications for the Tectonics of the Zambian Copperbelt.* **Mackay-Champion, T.C.,** Purkiss, M., Chanda, M., Palin, R., Zimba, M., Daly, M.C.

Chapter 5: *Ambient Noise Tomography for Local to Regional Mineral Exploration Using Nodal MEMS Accelerometers: A Case Study from the Kansanshi Cu-Au Mine, Zambia.* **Mackay-Champion, T. C.,** Harmon, N., Mutelekesha, S., Chanda, M., Hudson, T., Kendall, J-M., Daly, M.C.

Chapter 2

The Application of MEMS Accelerometers to Regional-scale Passive Seismology: A Case Study of the Sercel WiNG Nodes.

Abstract

Micro ElectroMechanical Systems (MEMS) accelerometers have become increasingly common in geophysical studies. Despite this, no work has been done to assess the suitability of an array of MEMS sensors to low-frequency, regional-scale passive seismic studies. Consequently, a month's-long deployment of twenty MEMS-based Sercel WING nodes, two Güralp CMG-ESPCDS and one 4.5 Hz geophone-Reftek system was undertaken to assess the performance of MEMS accelerometers in comparison to conventional seismometers. We show that the WiNG nodes reliably record over 100 Hz to 0.03 Hz, with a -136 dB broadband noise-floor between 100–1 Hz, and a $1/f$ noise-floor at frequencies below 1 Hz. The nodes accurately recorded earthquakes with epicentral distances ranging from 72°to 40 km. In particular, the low-period (c. 10–30s) surface waves of two teleseismic earthquakes were clearly resolved above the WiNG node's noise floor. A set of three WiNG nodes deployed in a 3-component configuration provided an estimate of the crustal thickness beneath Oxford of 39.0 ± 2.0 km using the H-k stacking technique. This compares favourably with the estimate provided by the conventional 3-component ESPCD (37.9 ± 1.3 km) and aligns well with previous results in the literature. The MEMS-based systems have a number of clear advantages over conventional systems, including the speed of deployment, the low cost, the compact design, and the use of an internal battery and GPS. The strong performance of the WiNG nodes during this study shows that these MEMS-based accelerometers are well-suited for passive seismology at a local, regional, and potentially larger scale.

2.1 Introduction

Since the early 2000s, Micro ElectroMechanical Systems (MEMS) accelerometers have become increasingly common in geophysical studies, particularly within the field of seismic exploration for hydrocarbons (e.g., *Laine and Mougenot*, 2007). Closed-loop MEMS sensors, as opposed to open-loop which demonstrate poorer bandwidth, rely on force-balance systems which work by recording the voltage required to keep a positive electrode stationary between a pair of negative electrodes (*Herrmann et al.*, 2021).

These sensors record in units of acceleration, which can be readily equated to force. MEMS sensors have a number of advantages over conventional instruments: their lightweight and compact design makes deploying large arrays easier, the instrument sensitivity to external factors such as temperature are an order of magnitude less than standard geophones (*Laine and Mougenot*, 2014), the sensors lack the data jitter seen in geophones (*Herrmann et al.*, 2021), and the instrument response in acceleration is constant across the frequency domain (*Tellier et al.*, 2020). MEMS sensors have been widely used in a number of different fields, from regional-local earthquake detection (e.g., *d'Alessandro et al.*, 2014) and the monitoring of local seismic risk using dense arrays (e.g., *Fuławka et al.*, 2022), to Martian seismology on the NASA InSight Mission (*Pike et al.*, 2014; *Lognonné et al.*, 2020) and ocean-bottom deployments (*Tellier and Herrmann*, 2020). Despite this burgeoning utilisation and the proven ability of MEMS sensors to record well below 1 Hz (*Fougerat et al.*, 2018), no work has yet assessed the suitability of an array of MEMS sensors for regional-scale passive seismic studies relying on frequencies below 10 Hz. Given the advantages listed above, MEMS sensors could pose a significant benefit to passive seismic studies if shown to have the appropriate bandwidth, noise floor and sensitivity. Consequently, we test the suitability of MEMS-based nodal seismometers to regional passive seismology by comparing the results of an array of vertical-component Sercel WiNG nodes deployed in Oxfordshire, UK, to the results for two Güralp CMG-ESPCDs and a 4.5 Hz geophone (connected to a Reftek-RT130 datalogger) which were deployed coincident to the nodes. We focus on the noise characteristics of the MEMS sensors and the suitability of the array for ambient noise analysis, as well as the recovery of earthquakes and their application to crustal thickness estimates using H-k stacking of receiver functions. The Sercel WiNG nodes, deployed in partnership with Sercel and equipped with the latest Sercel MEMS technology called *Quietseis*, demonstrate all the requirements of a MEMS seismometer outlined by *d'Alessandro et al.* (2019). We therefore view them as a representative case study for the performance of MEMS-based sensors.

2.2 Methods

2.2.1 Array details

An array of 20 Sercel WiNG nodes were deployed throughout Oxfordshire between 19th October - 16th November 2020. The array was approximately 50 km long, and trended NW-SE (Fig. 2.1). At two sites, the WiNG nodes were deployed alongside more conventional seismometers. The first site, in central Oxford, hosted a 60s–100 Hz Güralp CMG-ESPCD and a GS-11D 4.5Hz geophone with a RefTek DAS130-01 broadband data logger, and three WiNG nodes deployed in a 3-component configuration. The second site in north Oxfordshire hosted a 60s–50 Hz Güralp CMG-ESPCD and a single, vertical-component WiNG node. Both ESPCDs were directly buried, in vaults

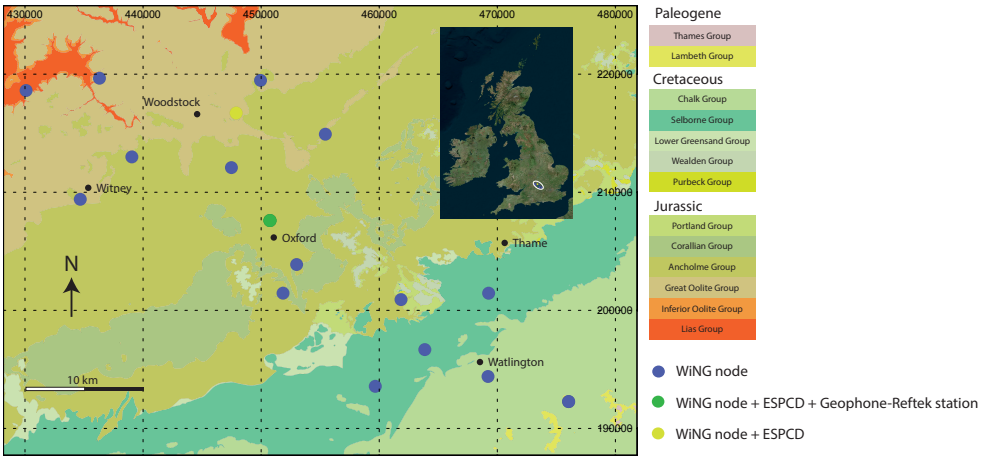

Fig. 2.1 Deployment map. The BGS 1:50K EW236 Whitney Bedrock map is reproduced with the permission of the British Geological Survey © UKRI 2023. All Rights Reserved.

~1 m deep. The pits were backfilled with soil and sand. The geophone was also buried to a depth of ~30 cm. The WiNG nodes were lightly buried such that the top of the casing was a maximum of 5 cm below the surface. Unlike the geophone and the ESPCD, the WiNG nodes have an internal GPS system. Consequently, the nodes need a shallow burial to prevent loss of the GPS signal. Alternatively, the nodes can be spiked into the ground (Fig. 2.2).

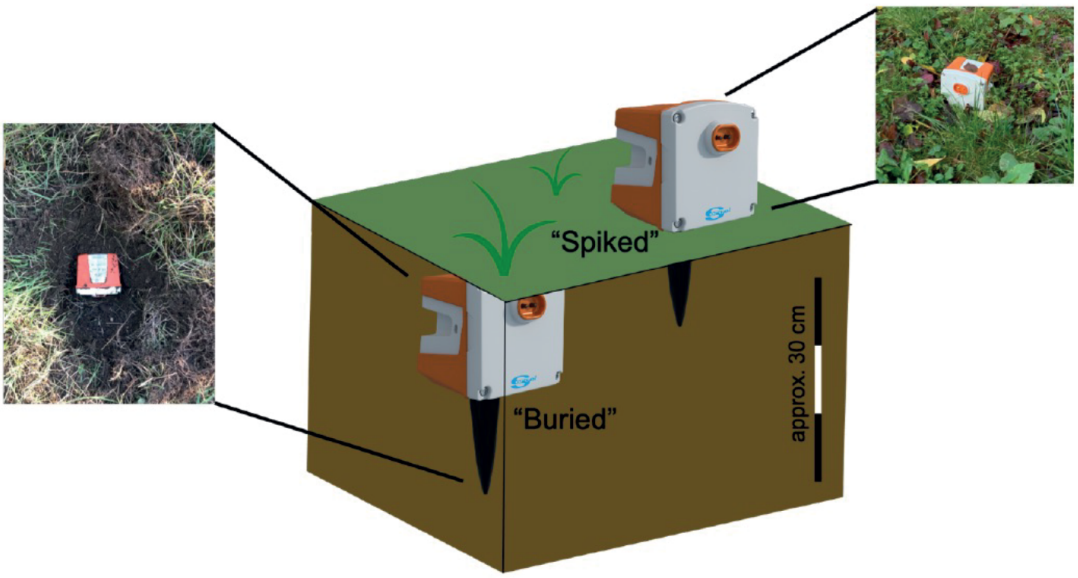

Fig. 2.2 Deployment techniques for the WiNG nodes.

2.2.2 Instrument specifications and response

The Sercel WiNG nodes are vertical-component only and use a closed-loop MEMS accelerometer to record ground motion with an adjustable sampling frequency from 250 to 1000 Hz. They are approximately 750g and are fully self-contained with their own internal GPS and lithium-ion battery. The battery lasts between 30–50 days, depending on the instrument set-up. According to the manufacturers, the MEMS sensor has a constant amplitude response across the frequency domain, with a bandwidth of 0 (DC) to 400 Hz. The noise floor is purported to be 15 $\mu \mathrm{ms}^{-2}/\sqrt{\mathrm{Hz}}$ with a constant clip level of 5 ms^{-2}, resulting in a frequency-independent dynamic range of 128 dB. The incoming acceleration signal is recorded as a 24bit output, ranging from -2^{23} to 2^{23}. To be converted back into acceleration, this bit-value must first be converted into voltage using a scalar value unique to the array (in this case, 67 $\mu V/count$). The voltage can then be converted into acceleration using the instrument's sensitivity value of 0.425 V/ms^{-2}. This sensitivity correction is independent of frequency. The manufacturer states a phase accuracy of < 20 μs, which is equivalent to a frequency of 50 kHz. As such, no phase correction is required for the frequency range of interest (Fig. 2.3A).

Two different broadband seismometers were used in the deployment: a 60s–50 Hz Güralp CMG-ESPCD and a 60s–100 Hz Güralp CMG-ESPCD. These instruments are conventional broadband seismometers, measuring ground velocity, which have been extensively used for passive seismology. They rely on a system of internal masses coupled with an external battery and GPS unit. The masses comprise a transducer coil attached to a boom that is suspended by a leaf spring and swings on a frictionless hinge. A triangular spring supports the mass's weight. The mass will tend to remain stationary in response to external vibrations while the body of the seismometer moves. The differential motion between the mass and the seismometer is measured using a capacitive position sensor. These instruments have a flat response in velocity relative to frequency and a noise-floor below the New Low Noise Model (NLNM) of *Peterson* (1993) over the given bandwidths. The ESPCD has a sensitivity of 6000 $\mathrm{V/ms}^{-1}$ within the bandwidth, a clip level of 20 V (equivalent to 3.3 mms^{-1}), and a dynamic range of 165 dB at 1 Hz. Although the clip-level is lower than the WiNG node, the ESPCDs have a lower noise-floor and are therefore able to attain a larger dynamic range. Like the WiNG node, the ESPCD uses a 24-bit digitizer. This digitizer has a nominal sensitivity of 1 µV/count, meaning that the total amplitude correction from counts to velocity is 3 x 109 over the instrument's bandwidth. A phase correction is also required (Fig 2.3C) across the frequency range.

Finally, one GS-11D 4.5Hz geophone was deployed with a RefTek DAS130-01 broadband data logger. This is a force-feedback system, with a constant frequency response above 4.5 ± 0.75 Hz. A geophone comprises a spring-mounted wire coil moving within the magnetic field of a fixed, case-mounted permanent magnet. When the ground

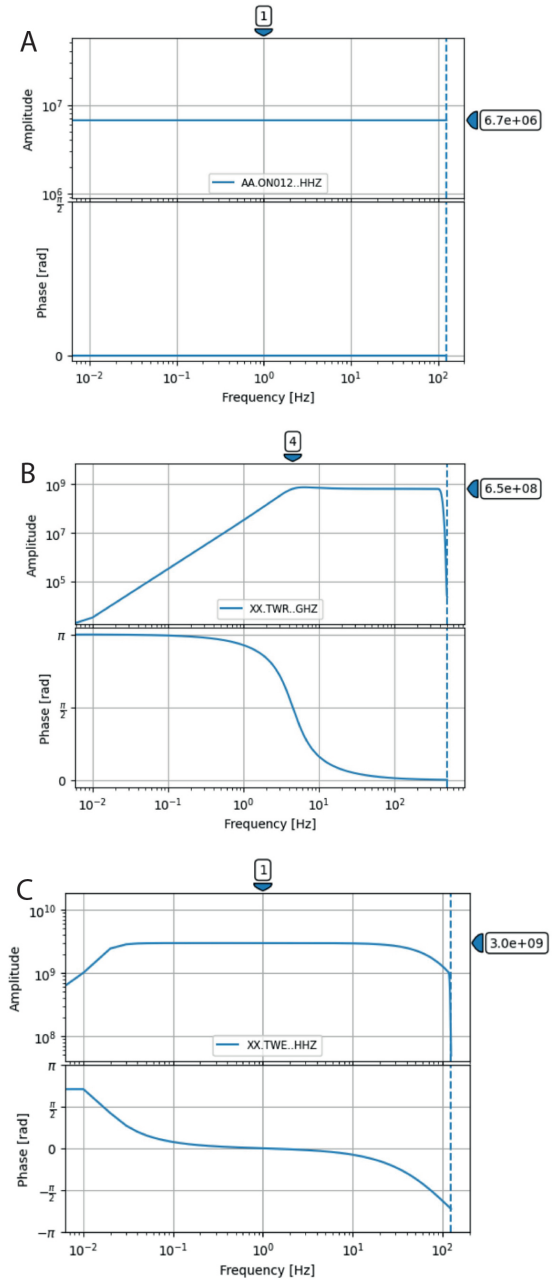

Fig. 2.3 Instrument response Bode plot showing the frequency response of three seismometers from 10^{-2} to 10^{2} Hz . A) Sercel WiNG node. B) GS-11D 4.5Hz geophone and RefTek DAS130-01 broadBand data logger. C) 60s–100 Hz Güralp CMG-ESPCD.

vibrates, the relative motion between the coil and magnet induces an electrical signal that is directly proportional to the velocity of the ground movement. Geophones are conventionally used for monitoring frequencies above their resonant frequency and below a specific spurious frequency (*Faber and Maxwell*, 1997), however methods such as the cross-correlation of ambient noise data has been successfully applied on geophone data to yield lower frequency information (e.g., *Wang et al.*, 2019). Below the resonant frequency, the sensitivity decays proportional to a damping factor (*Havskov and Alguacil*, 2016).

Above its resonant frequency, the GS-11D geophone has an open-circuit sensitivity of 32 V/ms^{-1} and an open-circuit damping of 34 %. The clip-level and noise floor data are not specified by the manufacturer. Like the ESPCDs, a frequency-dependent phase correction is required for the velocity data (Fig 2.3B).

2.2.3 Ambient noise analysis

To ascertain the potential applications of an instrument, it is crucial to understand the performance of said instrument over the frequency range of interest. For microseismic detection, frequencies between 1–50 Hz would be standard whereas regional to sub-regional scale surface wave analysis would require frequencies below 1 Hz. As such, the MEMS sensors need to demonstrate a wide bandwidth if they are to be of use in passive seismology. To examine this, probabilistic power spectral densities were constructed for the co-located WiNG node, ESPCD and geophone following the methodology of *McNamara and Buland* (2004). First, the instrument response was removed and the ESPCD and geophone data were differentiated into acceleration. The data were then downsampled to 250 Hz, representing a factor of four for the geophone, a factor of two for the MEMS sensor and no downsampling for the ESPCD. Then the time window of interest (in this case, 1 day) was split into sliding windows of 60mins, with a 50 % overlap between windows. The Power Spectral Density, PSD, ($(ms^2)^2/Hz$) was calculated using the Welch Method for each window, and then converted into decibels relative to $1(ms^2)^2/Hz$ (*Welch*, 1967). These are the units used by the noise models of *Peterson* (1993). The PSDs were then downsampled into 1/8th octave bins, and the probability at each frequency point was calculated following Equation 4 of *McNamara and Buland* (2004).

Array beamforming on ambient noise cross-correlations calculated for the network of WiNG nodes were used to assess the instrument's suitability for ambient noise tomography. Prior to the calculation of the cross-correlations, a 1-bit amplitude normalization, downsampling to 4 Hz and a moving-average frequency normalization ("spectral whitening") was performed to the raw seismograms, following *Bensen et al.* (2007). The seismograms for each instrument were binned into 4hr-long sections, and the cross-correlation for each station-pair was calculated for each bin. A linear stack was then taken of every bin for each individual cross-correlation to create a final cross-correlation for each station pair (420 total). Only the WiNG nodes were included in the analysis, as it was important to determine their performance alone. Following stacking, array-scale beamforming was performed to determine the average phase velocity of waves traveling through the entire network. The beamforming was calculated following *Gerstoft et al.* (2006), in which a series of plane waves are simulated for the array over a range of periods and velocities (Equation 2.1).

$$p(f, v) = e^{\frac{-2\pi i f d}{v}} \tag{2.1}$$

Where p is the phase of the plane wave, f is the frequency of interest, d is the separation distances for each station-pair, and v is the phase velocity. The beam power is calculated by computing the similarity between the phase of the plane waves and the cross-spectral density matrix of the ambient noise cross-correlations, C (Equation 2.2).

$$B(f, v) = \left| p(f, v)^T \cdot C \cdot p(f, v) \right|^2 \tag{2.2}$$

2.2.4 Earthquake analysis

The analysis of earthquakes, on a regional and local scale, is fundamental to many techniques in seismology. MEMS sensors must reliably detect and record these earthquakes if they are to be of wide use. Teleseismic earthquakes are of particular interest, because the sensor would need to have a low enough noise floor to suitably detect highly attenuated, low frequency waves. As such, the performance of the MEMS sensors was examined for two teleseismic earthquakes and several local to regional earthquakes.

2.2.4.1 Arrival time analysis

Arrival time analysis, using the conventional short-term average – long-term average (STA/LTA) technique of *Withers et al.* (1998), was performed on a MW 7.0 earthquake from Greece (epicentral distance of 24 °), a MW 7.6 earthquake from Alaska (epicentral distance of 72 °), and a MW 0.9 earthquake from Stoke-on-Trent, UK (epicentral distance of 1.26 °). This was done to assess the signal-to-noise ratio achieved by the MEMS sensor (proxied by the STA/LTA value), and the reliability of the MEMS sensor detection when compared to the arrival times estimated from the ESPCDs and geophone. The conventional STA/LTA technique computes the ratio of the average absolute amplitude in the "short time" window against the average absolute amplitude in the "long time" window. A threshold ratio value is used as a "trigger"; an earthquake arrival is "triggered" once the ratio value exceeds that of the pre-set threshold. The analysis was performed on acceleration data, and a suitable bandpass filter was applied prior to analysis. The frequency values used for each analysis can be found in Appendix A.

2.2.4.2 Receiver function calculation

Upcoming P-waves beneath a seismometer will generate P-to-S conversions at any sharp velocity interfaces such as the Moho (e.g., *Langston*, 1979). The time delay between the arrival of the direct P phase and the converted S-waves increases with the depth to the interface. Usually these phases are obscured by the coda of the P-wave. However, the converted phases should have the same shape as the direct P-wave and can therefore be revealed by deconvolving the vertical-component P-wave pulse from the radial component, which most strongly records the converted phases. This deconvolved

waveform is known as a Receiver Function (RF). Following Equation 2.3, the receiver function can be thought of as the Earth's response (r) to the input P-wave (s). This is convolved with the instrument response (i) and the addition of random noise (n).

$$d(t) = s(t) * r(t) * i(t) + n(t) \tag{2.3}$$

Deconvolution recovers the RF from the data by removing the effects of the input wave, the instrument response, and the noise. We calculate RFs using the time-domain iterative deconvolution method of *Ligorría and Ammon* (1999). This method iteratively minimizes the difference between the observed radial component seismogram and a predicted signal generated by the convolution of an iteratively updated (one spike at a time) spike train with the vertical component of the seismogram. The RF can be viewed as a finite sequence of spikes convolved with a finite-bandwidth wavelet (w_e), which accounts for attenuation effects and finite sampling constraints (Equation 2.4).

$$r(t) = \sum_{k=1}^{N} a_k \delta(t - \tau_k) * w_e(t) \tag{2.4}$$

A common choice for w_e is a Gaussian wavelet with a defined width (e.g., *Crotwell and Owens*, 2005), which obscures the inherent sparseness by distributing each spike over a finite duration (*Ligorría and Ammon*, 1999). We perform the iterative deconvolution with Gaussian width factors of between 0.8–4.0.

H-k stacking The traveltimes of the P-to-S conversions at the Moho (Ps) and intracrustal reverberations ($PpPs$,$PpSs$ and $PsPs$), revealed by the calculation of receiver functions, are routinely used to estimate the crustal thickness (H) and the V_p/V_s ratio (k) using the H-k stacking routine of *Zhu and Kanamori* (2000). This approach uses a grid-search over possible values of H and k, with a stacking function evaluated at each point (Equation 2.5).

$$s(H,k) = \sum_{j=1}^{N} = w_1 r_j(t^{Ps}) + w_2 r_j(t^{PsPs}) - w_3 r_j(t^{PsPs+PpSs}) \tag{2.5}$$

Where $r_j(t_1)$ are the receiver function amplitudes at the predicted arrival times of the Ps conversion and subsequent reverberations for the jth receiver function, w_1, w_2 and w_3 are the stacking weights for the different phases ($\sum_{i=1}^{3} w_i = 1$)), and N is the total number of receiver functons for a given station. The predicted traveltimes for the respective phases are given by Equations 2.6-2.8.

$$t^{Ps} = H \left[\sqrt{\frac{1}{V_s^2} - p^2} - \sqrt{\frac{1}{V_p^2} - p^2} \right] \tag{2.6}$$

$$t^{PpPs} = H\left[\sqrt{\frac{1}{V_s^2} - p^2} + \sqrt{\frac{1}{V_p^2} - p^2}\right] \tag{2.7}$$

$$t^{PsPs+PpSs} = 2H\left[\sqrt{\frac{1}{V_s^2} - p^2}\right] \tag{2.8}$$

The best-fit values for H and k are taken where $s(H, k)$ is a maximum, with the 95 % contour of s values defining the respective uncertainties (*Ogden et al.*, 2019). However, the result is strongly influenced by the input parameters such as the phase weights (w), the choice of receiver function stacking strategy (linear versus phase weighted), the subset of stacked RFs, and the frequency content of the receiver functions. To overcome this parameter sensitivity, *Ogden et al.* (2019) proposed an adapted H-k method in which the standard H-k method is repeated 1,000 times with the input parameters and data parameters (e.g., receiver function frequency content) randomly selected between plausible limits. The relability of each result is assessed using 10 criterion (see *Ogden et al.* (2019) for further details), and cluster analysis is used to select the final solution from the distribution of individidual estimates. All station H-k results are inspected manually, and any results passing ≤ 5 criteria are removed. This study uses the adapted H-k method of *Ogden et al.* (2019) to estimate crustal thickness in Oxfordshire.

Cluster analysis and the meaning of different results *Ogden et al.* (2019) employ a hierarchical cluster analysis approach to identify the best H-k solution and its uncertainty. The *Caliński and Harabasz* (1974) and *Duda and Hart* (1973) methods are used to identify the number of clusters in the H-k results. The optimum cluster is selected as the cluster with the minimum overall variance, including within-cluster and error variance. From this optimum cluster, the final H-k solution is the measurement with the lowest combined rescaled (0-1) errors in H-k. As such, the final cluster solution can be considered the best individual result from all 1000 analyses. The mean solution is the mean of H and k from the 1000 analyses. This mean result is more representative of the solution uncertainty than the final cluster result.

2.3 Results

2.3.1 Ambient noise analysis

The Probabilistic Power Spectral Densities (PPSD) illuminate several key differences between the co-deployed 60s–100 Hz ESPCD, 4.5 Hz geophone, and the WiNG node (MEMS sensor) (Fig. 2.4). This site was located in central Oxford, and consequently has a high level of anthropogenic noise between 100–10 Hz. All of the three instruments show a similar topology between 100–10 Hz, with amplitudes of between -130 to -85 dB and clear peaks at approximately 90 Hz and 10 Hz. The geophone and ESPCD

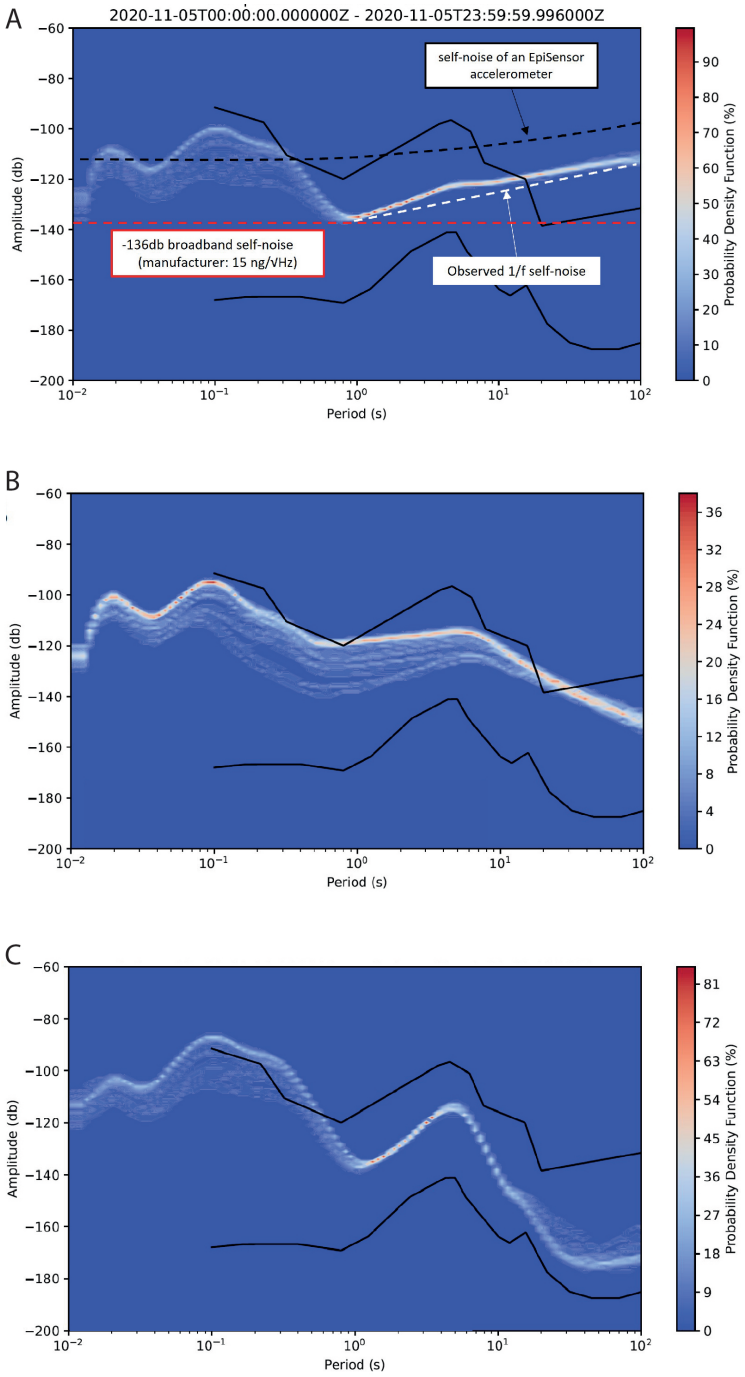

Fig. 2.4 Probabilistic Power Spectral Density analysis for 5th November 2020. A) Sercel WiNG node. B) 4.5 Hz Geophone. C) 60s– 100 Hz ESPCD. Each instrument has a sampling frequency of 250 Hz in units of acceleration for this analysis. The solid black lines are the New High Noise Model (top) and New Low Noise Model (bottom) of *Peterson* (1993).

both show higher amplitudes throughout this frequency range compared to the WiNG node, which may be due to being closer to the source of the noise or more likely to do with a higher degree of coupling with the ground. The WiNG node was buried in topsoil, which may have contributed a degree of damping of the high frequency signals,

while the geophone was buried more deeply (∼30 cm), and the ESPCD was buried even more deeply (∼1 m). All three instruments see a reduction in amplitude for signals between 10 to 1 Hz. The ESPCD shows an amplitude reduction of ∼70 dB and the WiNG node shows a reduction of ∼60 dB. The geophone displays a smaller change of only ∼25 dB, likely due to the geophone's resonance at 4.5 Hz. Nevertheless, the reduction in amplitude seen by each instrument corresponds well with the reduction seen in the New High Noise Model (NHNM) of *Peterson* (1993). The MEMS sensor and the ESPCD both show a tightly clustered amplitude of approximately -135 to -140 dB, with an amplitude trough at 1 Hz. On the other hand, the geophone displays a trough at ∼4 Hz, and exhibits a significant spread in amplitude from -140 dB up to -120 dB. This larger spread in amplitude no doubt corresponds to the change in behaviour of the geophone at its resonant frequency.

At periods larger than 1 s, the behaviour of the three instruments diverges. Below 1 s, the WiNG node displays a broadband noise floor of 15 $\mu\text{ms}^{-2}/\sqrt{\text{Hz}}$, equivalent to a constant noise of -136 dB. Signals with amplitudes below this noise floor would not be distinguishable from the background random noise of the sensor. This is some way above the New Low Noise Model (NLNM) of *Peterson* (1993), suggesting that the sensors would not perform well in seismically quiet areas. Above 1 s, the WiNG node shows a tightly clustered amplitude with a slope of $1/f$. This is a well-known feature of electrical circuits known as "flicker noise" or "pink noise" and decreases the dynamic range of the sensor at the affected periods (*Sleeman et al.*, 2006). As with the broadband noise floor, any signal of interest would need to have an amplitude above the $1/f$ noise if it were to be adequately detected. The primary microseism at 5–8 s is an example of such a signal, which can be clearly seen above the noise floor. The noise floor of a widely used force-balance accelerometer known as the *EpiSensor* is plotted for comparison, after *Koymans et al.* (2021). The WiNG node displays a lower noise floor, making it more suitable for passive seismology. The geophone also records the primary microseism, although the variation in amplitude of -125 to -115 dB is likely caused by the resonance of the geophone and does not present variations in the primary microseism itself. This is surmised because the ESPCD displays a tight clustering of amplitude at -115 dB for the primary microseism. Beyond the primary microseism, the geophone displays a linear drop in amplitude. This is indicative of a drop in sensitivity and suggests that the low-frequency corner of the bandwidth has been exceeded. As already mentioned, the ESPCD displays a clear primary microseism, and a secondary microseism can also be detected at around 12–15 s. The strength of this secondary microseism clearly varies with the time window. Above 30 s, the ESPCD exhibits a plateau in amplitude indicative of "the hum" (*Kobayashi and Nishida*, 1998). The amplitudes observed by the ESPCD fall well within the NHNM to NLNM window at periods above 1 s and are consequently above the stated noise floor of the instrument.

2.3.2 Ambient noise analysis

The flicker noise displayed by the WiNG nodes below 1Hz is random (*Halford*, 1968). Consequently, cross-correlations between pairs of stations will be independent of flicker noise when stacked over a sufficient period of time. The cross-correlation of the ambient noise between the 20 station pairs creates a clear moveout of approximately 3 km/s, which is indicative of Rayleigh waves travelling through the network of WiNG nodes (Fig. 2.5A).

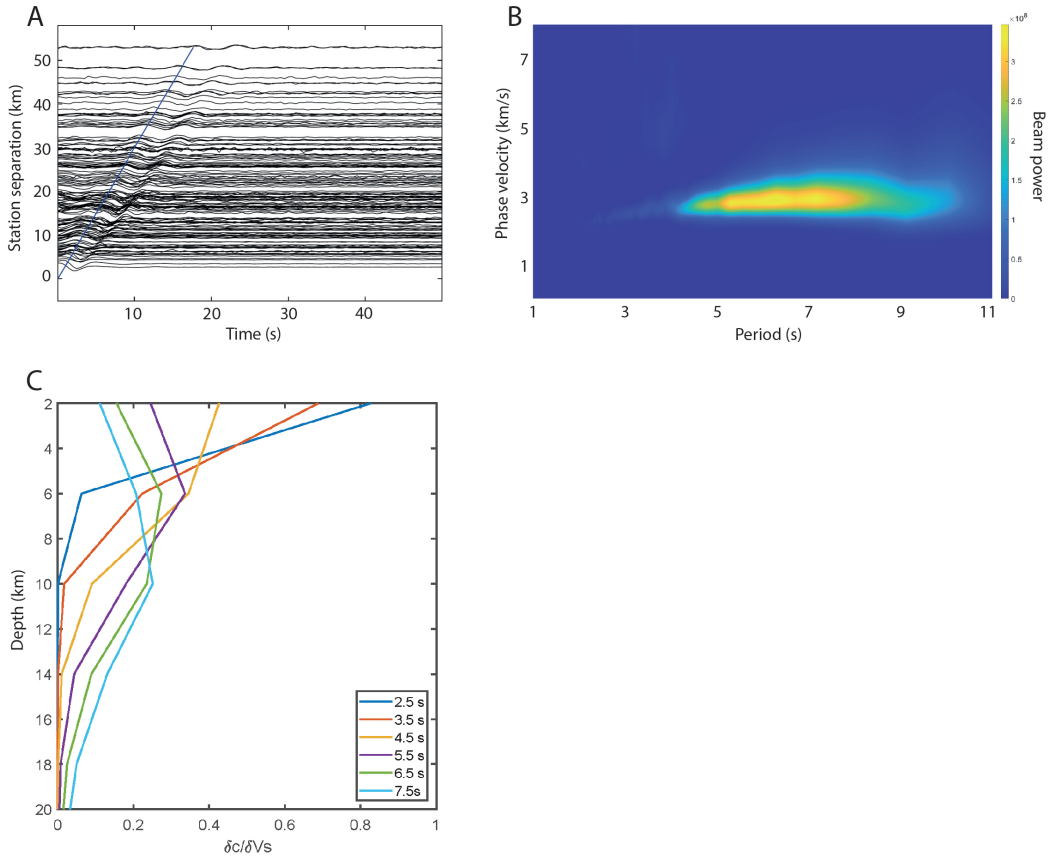

Fig. 2.5 A) One-side cross-correlation moveout. The blue line corresponds to a velocity of 3 km/s. B) Ambient noise surface wave phase velocity derived from array beamforming. C) Sensitivity kernels for surface waves of given periods.

The array beamforming of these cross-correlations demonstrates that the array can detect surface waves with periods of at least 7.5 s (Fig. 2.5B). The phase velocities are all within an appropriate range of 2.8–3.5 km/s, indicative of crustal Rayleigh Waves (e.g., *Harmon and Rychert*, 2016). Surface waves of this period can be used to constraint crustal structure to $>$ 15 km (Fig. 2.5. The maximum station separation in the array is approximately 50 km. Given that the phase velocity of a given surface wave can only be accurately determined if the station separation is equal to at least 2 wavelengths (*Harmon et al.*, 2008), the 7.5 s upper period limit was imposed on the array by the

station separation and not the performance of the sensors themselves. As will be shown in Section 2.3.3, the WiNG nodes can reliably record signals below 20 seconds.

2.3.3 Earthquake analysis

For the MEMS accelerometer to prove useful to the field of passive seismology, it must be able to detect local to teleseismic earthquakes. This provides several tests for the sensor. In particular, the low frequency arrivals associated with teleseismic earthquakes, such as the $<$ 1Hz surface waves, must be above the $1/f$ noise floor if they are to be adequately resolved at individual stations. For more local earthquakes, the high frequency arrivals need to be resolved from the background anthropogenic noise.

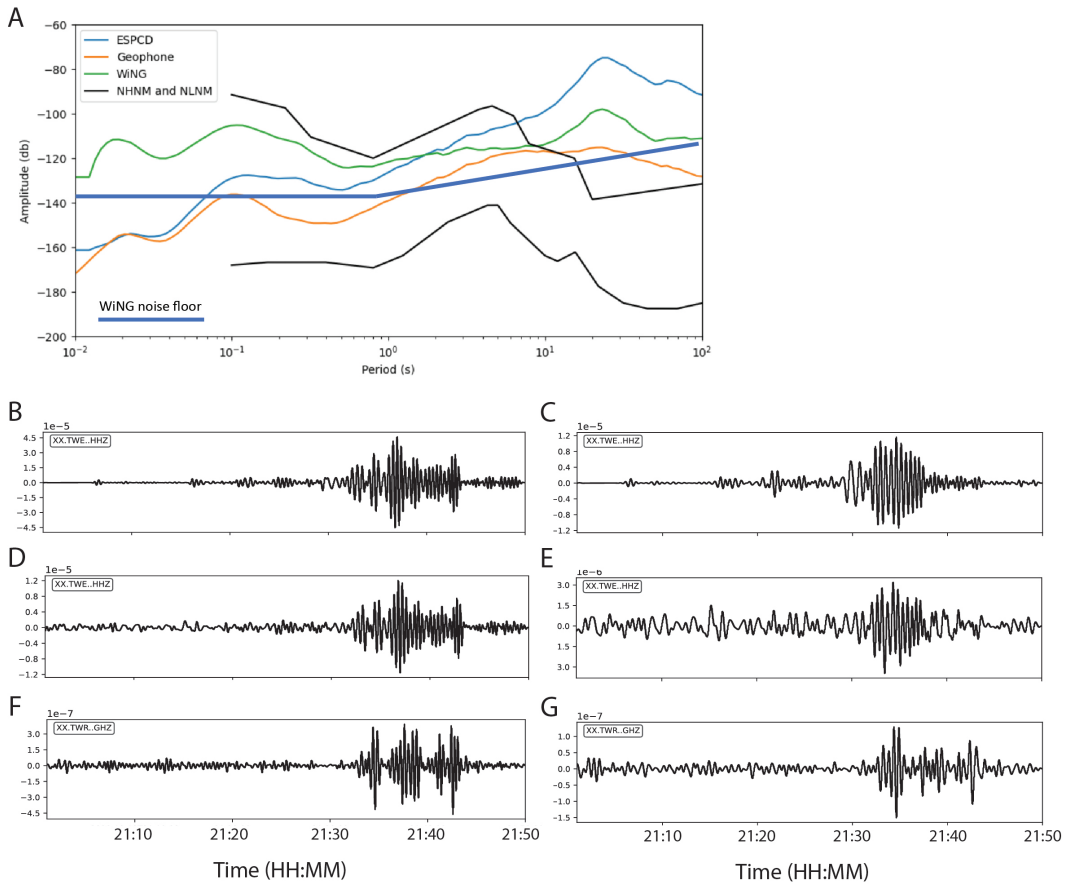

Fig. 2.6 Instrument response to a MW 7.6 Alaska earthquake on 19th Oct. 2020. A) Instrument Power Spectral Density, in units of acceleration decibels relative to 1. (B, C) ESPCD acceleration data with 20 s and 30 s and low-pass filter, respectively. (D, E) WiNG node acceleration data with a 20 s and 30 s low-pass filter, respectively. (F, G) 4.5 Hz geophone acceleration data with a 20 s and 30 s low-pass filter, respectively.

A MW 7.6 earthquake from Alaska was recorded by the array on 19th October 2020, from an epicentral distance of 72 °(*British Geological Survey*, 2020) (Fig. 2.6). The Power Spectral Density plot shows that both the WiNG node and the ESPCD measure a peak in amplitude at periods 20–30 s, corresponding to the arrival of the

low period surface wave (Fig. 2.6A). This arrival is well above the $1/f$ noise floor of the MEMS sensor so can be clearly resolved. In contrast, the geophone shows a far broader area of increased amplitude. The lower amplitude of the WiNG node peak (-95 dB) in comparison to the peak of the ESPCD (-75 dB) is likely caused by the higher quality of coupling between the ESPCD and the ground provided by the deep burial of the seismometer. The surface wave train is clear in the ESPCD and WiNG record, but heavily distorted in the geophone data (e.g., compare Fig. 2.6D and F). The WiNG node reliably records signals down to 20 Hz (Fig. 2.6C). At 30 Hz, a surface wave arrival can still be seen (Fig. 2.6E), although the noise floor is high and some of the signal is clearly lost. No signal is observed below 40 Hz. Although this performance is clearly worse than the broadband ESPCD, it is significantly better than the geophone and show that MEMS accelerometers are capable of reliably recording low-frequency arrivals.

The strong performance of the WiNG node at low frequencies is repeated for the MW 7.0 earthquake from Greece, which occurred at an epicentral distance of 24°(*USGS*, 2020). The earthquake can be clearly seen arriving at all of the deployed node stations (Fig. 2.7). Akin to the Alaska earthquake, a clear P and surface wave arrival can be observed, and the amplitude of the arrivals is demonstrably higher than the sensor noise floor (Fig. 2.8C). The WiNG nodes also perform well in regional and local earthquakes. The MW 2.7 North Sea earthquake (epicentral distance of 6.45 (*British Geological Survey*, 2020)) shows clear arrivals between 3–6 Hz (Fig. 2.8A), and the low MW 0.9 Worcester earthquake (epicentral distance of 0.64°(*British Geological Survey*, 2020) can also be distinguished from the background noise (Fig. 2.8B).

2.3.3.1 Arrival time analysis

Arrival-time analysis was performed on a selection of regional and teleseismic earthquakes (Fig. 2.9). For this analysis, the geophone and ESPCD data were differentiated into units of acceleration to provide a fair comparison to the WiNG node. This is particularly important because acceleration data features a -90° phase shift relative to velocity. The first earthquake analysed was a MW 1.3 from Stoke-on-Trent, with an epicentral distance of 1.27°(*British Geological Survey*, 2020) (Fig. 2.9A). The high noise levels of Oxford made this earthquake undetectable at many stations (Fig. 2.9A[ii]). This manifests in a poor-quality pick at several of the stations. However, there is a clear trend of picks at approximately 50 seconds, which aligns with the ESPCD seismogram and demonstrates that an array of nodes can be utilised to detect earthquakes with relatively low amplitudes. The further two arrival plots are for the aforementioned teleseismic Alaska (Fig. 2.9B) and Greece (Fig. 2.9C) earthquakes. The strong alignment of picks at 125 s and 110 s respectively demonstrate the quality of picking achieved by the WiNG nodes. The WiNG nodes also have comparable, and in some cases, higher STA/LTA values than the ESPCDs, suggesting a comparable signal-to-noise ratio. The performance of the nodes, and the abundance of nodes readily deployed within an array

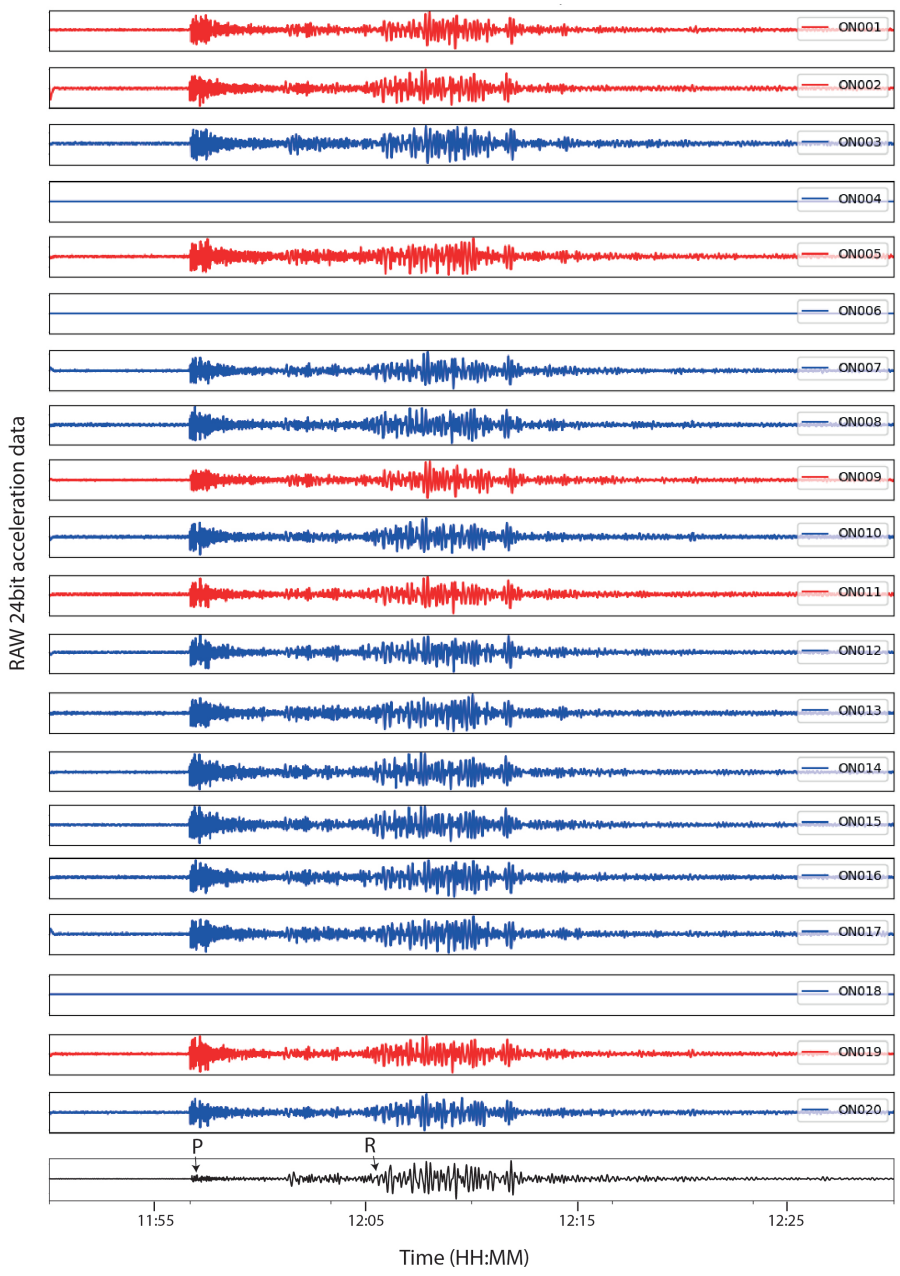

Fig. 2.7 The response of the WiNG node network to the Greece Earthquake (MW 7.0), 30th Oct. 2020. A bandpass filter of 0.05–1 Hz has been applied. The blue plots correspond to nodes that were buried underground. The red plots correspond to nodes that were spiked into the ground (see Fig.2.2). The black plot corresponds to the 60s–100 Hz ESPCD. P = P-wave, R = Rayleigh-wave.

would clearly lend itself well to earthquake detection and location algorithms such as QuakeMigrate (*Winder et al.*, 2019).

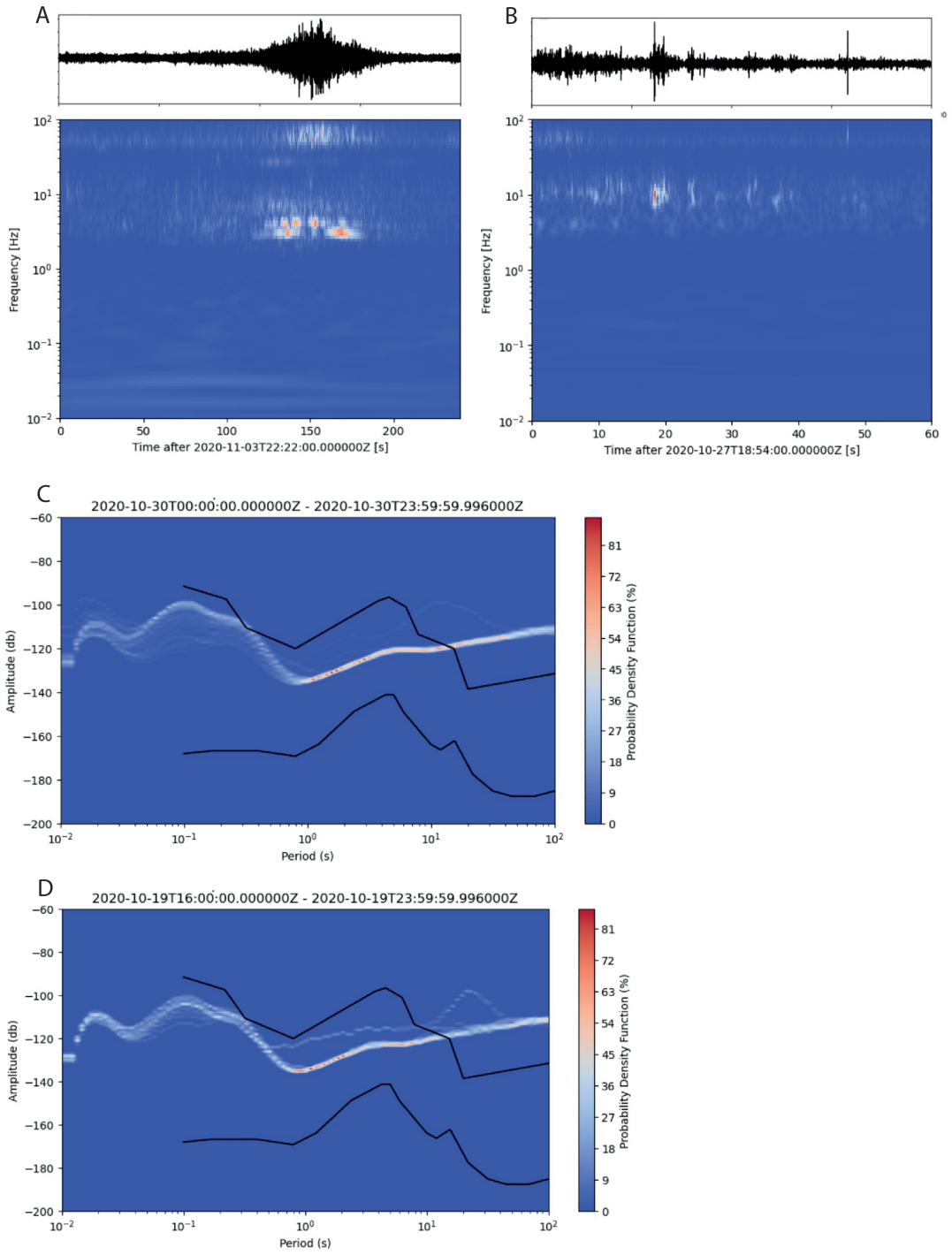

Fig. 2.8 Response of the ON012 WiNG node to a selection of earthquakes. A) ON012 WiNG node response to the MW 2.7 North Sea earthquake (time-series and accompanying frequency-time plot). B) ON012 WiNG node response to the MW 0.9 Worcester earthquake (time-series and frequency-time plot); C) ON012 WiNG node PPSD analysis of 30th Oct. 2020, featuring the MW 7.0 Greece earthquake; D) ON012 WiNG node PPSD analysis of 19th Oct. 2020, featuring the MW 7.6 Alaska earthquake.

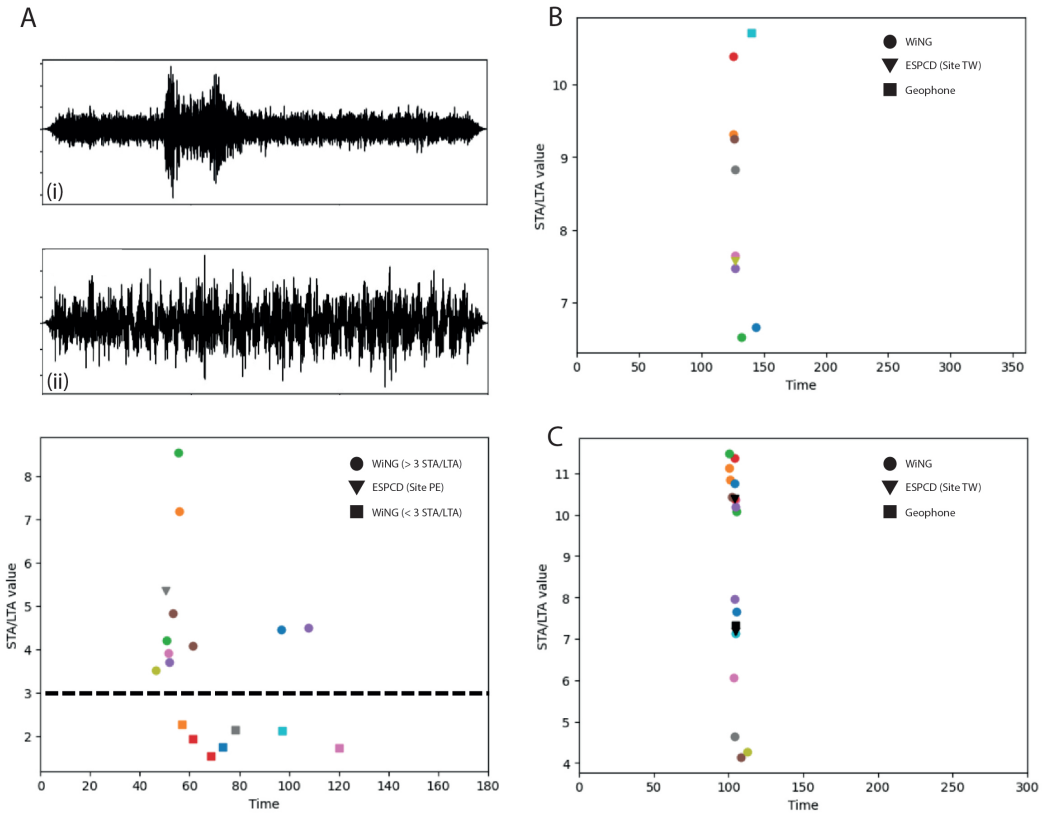

Fig. 2.9 STA/LTA plots for a selection of earthquakes. Ai) MW 1.3 Stoke-on-Trent STA/LTA with accompanying time-series from WiNG node ON012. Aii) Response of the 60s - 100 Hz ESPCD to the Stoke-on-Trent earthquake. B) MW 7.6 Alaksa STA/LTA. C) MW 7.0 Greece STA/LTA;

2.3.3.2 Crustal thickness estimate

Due to the short deployment time of only 28 days, there were only four earthquakes recorded with an epicentral distance between 30°-90° from which to calculate receiver functions, and only one of these earthquakes produced an adequate receiver function (the Alaska earthquake of Fig. 2.6). Nevertheless, both the ESPCD and the 3C-WiNG system recorded this earthquake and therefore a comparison between the ESPCD-derived RF and the WiNG-derived RF is possible (Fig. 2.10).

The RFs are shown for both 1.0 Hz and 2.0 Hz, corresponding to a Gaussian width factor of 2.0 and 4.0 respectively. The WiNG-derived RF shows a strong similarity with the ESPCD-derived RF at each frequency, particularly within the 0–10 s range. The ESPCD system provided a crustal thickness estimate of 37.9 ± 1.3 km and a Vp/Vs ratio of 1.78 ± 0.02 (Fig. 2.11A), while the 3C-WiNG system provided a crustal thickness estimate of 39.0 ± 2.0 km and a Vp/Vs ratio of 1.77 ± 0.04 (Fig. 2.11B). These two estimates of crustal thickness both agree within error. Although these results are only based on a single earthquake, the values align well with the crustal thicknesses

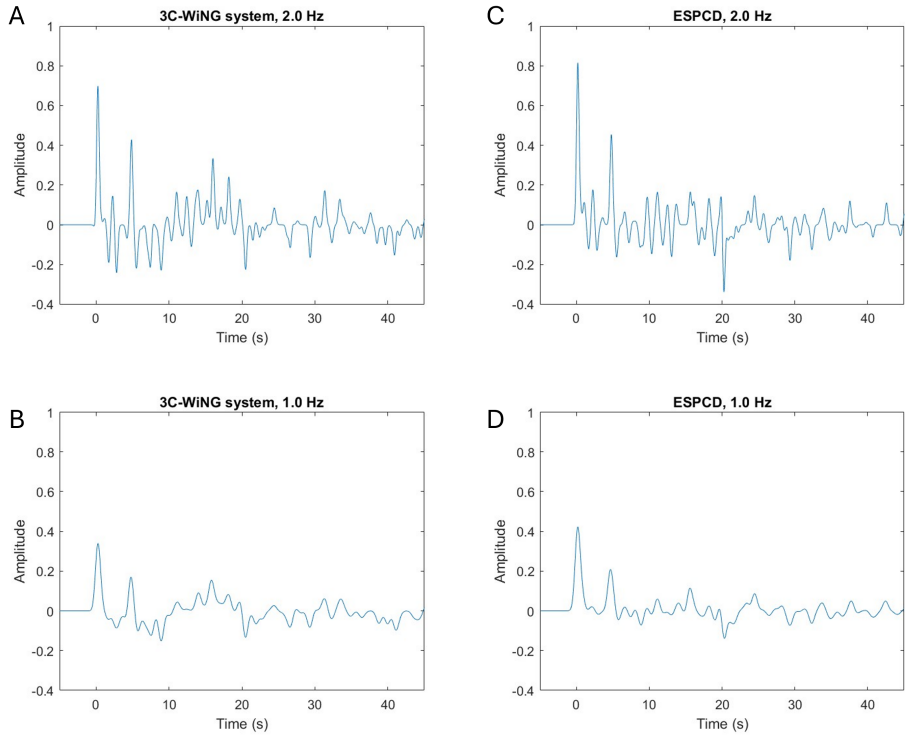

Fig. 2.10 Receiver functions calculated for the MW 7.6 Alaska earthquake on 19th Oct. 2020. A) 2.0 Hz RF for the 3C-WiNG system. B) 1.0 Hz RF for the 3C-WiNG system. C) 2.0 Hz RF for the 60s–100 Hz Güralp ESPCD. D) 1.0 Hz RF for the 60s–100 Hz ESPCD.

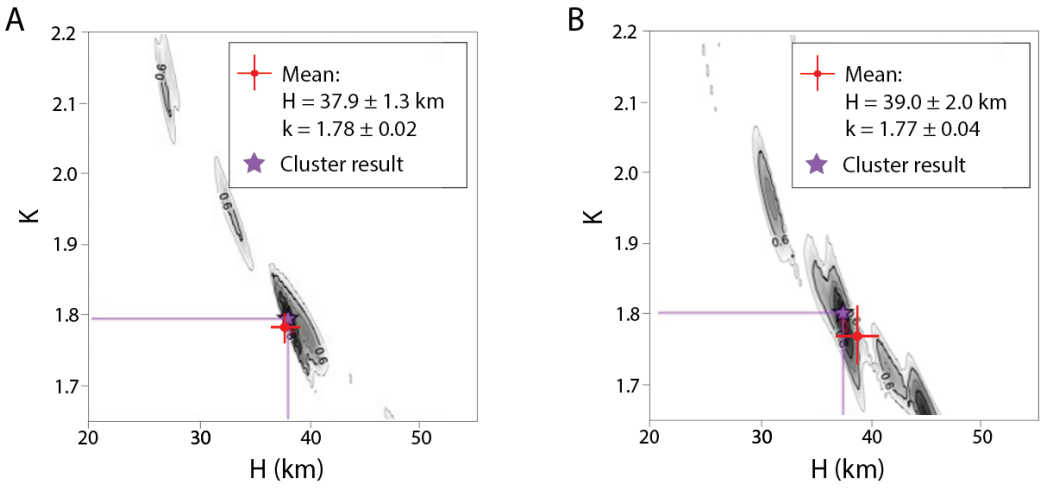

Fig. 2.11 H-k stacking results. A) 60s–100 Hz Güralp ESPCD. B) 3C-WiNG system.

(36–39 km) and Vp/Vs ratios (1.72–1.77) calculated by *Tomlinson et al.* (2006) for the Midland Microcraton, on which Oxford lies.

2.4 Discussion

The MEMS sensor has been shown to record accurate information over a wide range of frequencies suitable for passive seismology. The self-noise of an instrument is a fundamental limit on its ability to record events. The WiNG nodes are characterised by a broadband noisefloor of -136dB for periods between 1s to 0.01 s. This is significantly below the NHNM, so signals within this frequency range will likely be recorded reliably. At periods above 1 s, "flicker" noise with a slope of $1/f$ exceeds the broadband noise-floor and surpasses the NHNM at around 15–20 s period. Consequently, it is possible that arrivals in this frequency range may be masked by the "flicker" noise. However, this study has shown that low-frequency surface waves from teleseismic earthquakes can be well resolved in both the time and frequency domain, with reliable measurement down to 30 s. At periods less than 30 s, the WiNG data compares well with that of the ESPCD (Fig. 2.6). It should be noted that the WiNG nodes were all deployed in relatively water-rich topsoil, with only centimetre-scale burial, whereas the ESPCDs were directly buried in vaults $\sim$1 m deep. As such, the 30 s limit may represent a coupling or damping issue and the low-frequency limit might improve at drier, firmer sites.

The random nature of the flicker noise also meant that cross-correlation techniques proved able to extract meaningful phase information from ambient surface waves travelling across the array, up to a period of at least 7.5 s. Given the low-frequency performance of the WiNG nodes, the 7.5 s limit of the array beamforming is more than likely imposed by the relatively small instrument spacing within the array. It seems probable that the WiNG nodes could be used for regional and country-scale ambient noise and earthquake surface-wave tomography studies if an appropriate instrument spacing is used. The pseudo-3C WiNG system performed well for the receiver function analysis, providing a crustal thickness estimate within error of that achieved by the conventional ESCPD. The WiNG system had a larger error to its estimate, but that can largely be accounted for by the lack of rigid orthogonality and potential tilting of the 3 separate WiNG nodes (doubling as the three separate components) during the deployment. The manufacturer of the WiNG nodes has developed a metal stage to ensure orthogonality and reduce the effects of tilting. Given this, the WiNG nodes are certainly suitable for receiver function analysis.

The WiNG nodes, and other such nodal systems which rely on a MEMS accelerometer, have many clear advantages over the conventional seismometer systems. The nodes are significantly cheaper, costing £100s in comparison to the average ESPCD set-up costing £10,000s. The nodes can be deployed within a matter of minutes, versus a number of hours for the average ESPCD deployment. The nodes leave a far smaller surface footprint once deployed, which greatly helps with site security. The nodes are fully integrated with an internal GPS and lithium-ion battery, so require no supporting

equipment, and therefore provide a smaller logistical challenge when deploying a large array. The low cost, smaller size, and high speed of deployment means a large array of instruments can be deployed more easily and in a smaller time frame. However, the integrated nature of the nodal systems presents several disadvantages when compared with conventional seismometers. The internal GPS means that the node cannot be buried to a great depth because this would obscure the signal of the GPS. Geophones and ESPCDs rely on external GPS systems, meaning the seismometers can be buried at any depth and connected to a GPS on the surface. This increased depth of burial improves coupling with the ground, as can be seen by the higher amplitudes of the teleseismic arrivals in the ESPCD data when compared to the WiNG node data. The burial also shields the seismometer from signals of no interest, such as shallow anthropogenic noise. Finally, deep burial does make the seismometer more difficult to recover which can deter would-be thieves. The WiNG nodes also rely on an internal battery, which means that they can only record for a maximum of 50 days. For longer deployments, this means multiple trips into the field for re-charging. A final disadvantage of the MEMS sensor is the flicker noise below 1 Hz, which is an attribute of all electronic circuits. This means that low amplitude signals could be obscured by the noise-floor of the sensor, particularly at low-noise sites and especially at periods greater than 15–20 s where the noise surpasses the NHNM.

2.5 Conclusions

This study has shown that the WiNG nodes reliably record over 100 Hz to 0.03 Hz, with a -136 dB broadband noise-floor between 100–1 Hz, and a $1/f$ noise-floor at frequencies below 1 Hz. The nodes reliably recorded earthquakes with epicentral distances from 72° to 40 km. The cross-correlation of ambient noise recorded by pairs of nodes revealed the phase velocity of surface waves with periods of up to 7.5s, which are sensitive to seismic velocities at depths well in excess of 10 km. Three nodes in a 3-component configuration estimated the crustal thickness beneath Oxford at 39.0 ± 2.0 km, consistent with previous results and within error of the conventional 3-component ESPCD estimate of 37.9 ± 1.3 km. Further discussion of the MEMS accelerometers' performance and suitability for mineral exploration is provided in Chapter 6.

Chapter 3

Towards Optimal P-T Estimates: An Inverse Method for Quantifying P-T Conditions and Uncertainty in Phase Equilibrium Modelling

Abstract

Phase equilibrium modelling is reliant on quantitative solution models and thermodynamic databases. However, metamorphic studies often employ qualitative to semi-quantitative methods when comparing forward modeled data to the natural datasets that these forward models aim to replicate. These studies frequently overlook, or are unable to quantify, fundamental sources of uncertainty associated with the input data or the technique itself. Accurately constraining these uncertainties is essential for extracting reliable insights from petrological studies and interpreting the data within a well-defined range of confidence. This study introduces an inverse method to quantitatively determine the best-fit P-T conditions and associated uncertainties for a given rock system. The technique computes the difference (misfit) between observed data, such as mineral compositions and/or modal volumes, and forward models across a user-defined P-T grid. The grid point with the lowest misfit value is identified as the best-fit solution. Bootstrap resampling (repeated sampling of the dataset with replacement) enables the user to quantify the uncertainty of the inverse solution. Additionally, three diagnostic metrics—quality of data fit, variable sensitivity, and standard error—are implemented to validate and refine the best-fit solution.

The outlined workflow, LinaForma, is applied on a kyanite-zone pelite (ICSV13) and a garnet+plagioclase-zone metabasite (ICSV117) from the Greater Himalayan Sequence in the Zanskar Himalaya, NW India. The estimated peak P-T conditions and uncertainties for each rock align with results from classical thermobarometric methods, including conventional thermometry, multi-equilibrium barometry, and the pseudosection peak assemblage field. Discrepancies in ICSV117 highlight scenarios where model limitations and/or natural variability may result in different solutions. To assess broader trends in P-T uncertainty in sub-solidus metamorphic conditions, the workflow is then applied to the worldwide median pelite composition of *Forshaw and Pattison* (2023). The results show that P-T uncertainty varies significantly across metamorphic grade. Lower grades exhibit nearly double the P-T uncertainty of higher grades, with uncertainties ranging from 25–30 °C and 1.2–1.8 kbar at lower-temperature conditions (1 σ, biotite zone and garnet zone) to 16 °C and 0.8 kbar at higher-temperature conditions

(1 σ, cordierite/andalusite/staurolite/kyanite zone and sillimanite zone). This pattern is partially mirrored across the facies series, with the highest temperature uncertainty occurring in the lowest-pressure cordierite-andalusite-sillimanite series (1 σ = 29 °C) and the lowest temperature uncertainty in the highest-pressure staurolite-kyanite-sillimanite series (1 σ = 16 °C), whereas the pressure uncertainty remains relatively constant across all facies series (1 σ = 0.9–1.1 kbar).

3.1 Introduction

Phase equilibrium modelling is the cornerstone of modern metamorphic petrology, providing a powerful means to decipher the evolution of metamorphic sequences and, in turn, offering critical insights into the processes that shape Earth's crust and mantle. This modelling relies on large quantitative datasets including thermodynamic end-member properties and activity–composition (a–X) relations of minerals, fluid and melt (e.g., *Holland and Powell*, 1998). When integrated with appropriate software, these datasets can be used to produce sophisticated forward models that predict equilibrium phase assemblages, compositions, modal volumes, and other such variables across pressure-temperature-composition (P-T-X) space (e.g., *Spear et al.*, 2016).

Despite the quantitative foundation of these techniques, metamorphic studies predominantly determine the P-T evolution of a rock using qualitative to semi-quantitative comparisons between the forward modeled predicted outputs and the measured values from the rock (*Powell and Holland*, 2008). The quality of these comparisons depends on understanding the uncertainties associated with both the modelling process and the input data. As is standard in most scientific fields, any calculation must include a quantifiable estimate of propagated uncertainties, along with a recognition of uncertainties that cannot be quantified (*Powell and Holland*, 1994, 2008). However, in petrological studies, such uncertainties are often overlooked, such that derived P-T estimates can not be interpreted within a defined confidence range.

Although several programs employ quantitative approaches for determining optimal P-T conditions (e.g., *Berman*, 1991; *Gordon*, 1992; *Powell and Holland*, 1994; *Duesterhoeft and Lanari*, 2020), many of these tools lack direct integration with phase equilibrium modelling, or do not place a strong emphasis on uncertainty quantification. Therefore, our ability to assess the impact of uncertainties on P-T estimates derived using the latest thermobarometric techniques, remains limited. The aim of this study is to 1) outline the main sources of uncertainty in metamorphic systems, 2) present a new workflow for quantitatively determining the "best-fit" P-T conditions and associated uncertainty for a given rock system, and 3) quantify the uncertainty across P-T space in a typical pelite (the worldwide median pelite composition; *Forshaw and Pattison*, 2023) at subsolidus conditions.

3.2 Uncertainties

In order to account for and quantify uncertainties associated with thermobarometric information, it is essential to first consider the individual sources of uncertainty. This study recognises four fundamental sources: geological, analytical, parameter, and model, summarised in Fig. 3.1. For previous discussions of uncertainties in thermobarometry, see *Powell* (1985); *Hodges and McKenna* (1987); *Powell and Holland* (1988, 1994); *Kohn and Spear* (1991a,b); *Worley and Powell* (2000) and *Powell and Holland* (2008).

3.2.1 Geological uncertainty

Geological uncertainty is the non-analytical uncertainty involved in accurately representing the inherent variability of natural systems. These uncertainties may change the accuracy, but not precision, of the result. Specifically, this stems from sampling bias, the interpreted scale of equilibrium, disequilibrium processes, and selection of the equilibrium assemblage (Fig. 3.1).

Sampling bias and natural inhomogeneity contribute to uncertainties in the measured (or calculated) bulk composition due to petrological differences between samples, such as variations in mineral abundances or compositions. Additionally, the method used to determine bulk composition can vary depending on the interpretation of the scale and degree to which equilibrium has been achieved within the mineral assemblage. For instance, XRF analysis assumes that chemical equilibrium is achieved at the scale of the entire 'rock', producing a 'total' bulk composition. However, many metamorphic rocks preserve chemical zoning in porphyroblasts, meaning that an 'effective' bulk composition derived from a smaller-scale analysis, such as from point counting and compositional analysis of a thin section, may be more appropriate. Uncertainty in the bulk composition can have a profound effect on the topology of a pseudosection (e.g., *Stüwe and Powell*, 1995; *Stuwe*, 1997; *Guevara and Caddick*, 2016; *Palin et al.*, 2016; *Lanari and Engi*, 2017). On a sample-specific basis, this uncertainty can be estimated using replicate blocks (*Palin et al.*, 2016) or variable domains within the selected volume (*Duesterhoeft and Lanari*, 2020).

The equilibrium-based framework of thermodynamics is inherent to forward modelling the consequences of metamorphic transformation at fixed P-T-X conditions. However, kinetic factors—such as reaction affinity and diffusion rates—may influence whether a sample achieves equilibrium over the length scale of interest (e.g., *Thompson*, 1986; *Waters and Lovegrove*, 2002; *Pattison and Tinkham*, 2009; *Pattison and Spear*, 2018; *Starr and Pattison*, 2019). Consequently, many rocks preserve multiple equilibria, herein disequilibrium, which often provides more detailed information about the P-T evolution of a sample than a rock that has achieved perfect chemical and textural equilibrium (e.g., *Carlson et al.*, 2015). Although an assessment of equilibrium can be

made through careful observational criteria in thin sections and compositional phase analyses, it is impossible to definitively prove. By necessity, studies must account for varying scales of disequilibrium and carefully define the spatial or volumetric extent over which equilibrium assumptions are valid.

The phases chosen to inform the interpreted equilibrium assemblage and bulk composition are critical: including ambiguous minerals may distort the interpretation, whilst omitting key phases can yield an incomplete representation. Additional uncertainties arise when attempting to match the interpreted equilibrium assemblage and mineral measurements with those of the predicted model result. The predicted result may be reliant on assumptions in the formulation of the model which are not always consistent with natural data (e.g., *Forshaw et al.*, 2019; *Waters*, 2019). Therefore, the phases chosen to prioritise when comparing the natural obserations and model predictions will inevitably bias the solution. For example, the presence or absence of small modal volume or accessory phases (e.g., Fe-Ti-oxides) should be treated with particular caution in defining the peak assemblage of the forward model, as they contribute very little to the overall Gibbs free energy of the assemblage and require implausible precision from the a-X models (*Weller et al.*, 2024).

Although geological uncertainties are largely non-systematic, statistical approaches have been proposed to evaluate the impact of quantifiable geological uncertainties (Fig. 3.1) on estimated P-T conditions or corresponding mineral properties (*Steltenpohl and Bartley*, 1987; *Hodges and McKenna*, 1987; *Palin et al.*, 2016; *Forshaw et al.*, 2019). For example, even moderate uncertainties in modal mineral proportions due to natural petrographic variation can result in displacements of phase boundaries by approximately $\pm$ 1 kbar(*Palin et al.*, 2016).

3.2.2 Analytical uncertainty

Analytical uncertainty is the uncertainty in the measurements derived from data acquisition, processing, and calibration. This may affect the accuracy and precision of the result. Analytical uncertainty affects measured mineral compositions, modal abundances, whole-rock composition, and other non-standard rock or mineral properties such as XFe^{3+} (Fig. 3.1). The first two are explored here. This data is influenced by the geological uncertainty.

Analysis of mineral compositions via techniques such as electron probe microanalysis (EPMA) involves uncertainties on the measured weight percent oxide values derived from counting statistics, standardisation, and correction procedures. Uncertainties of these kind are treated routinely and may be negligible if undertaken at a single analytical facility (*Worley and Powell*, 2000). The measured weight % oxides are subsequently recalculated as cations per formula unit, then the mole fractions of end-members are determined by normalising groups of recalculated cations to the expected number

of cations on the specific crystallographic site. However, the direct propagation of relative uncertainties on weight % oxides into resulting uncertainties on mole fractions produces substantial correlation among the mineral components (*Kohn and Spear*, 1991b). Therefore Monte Carlo procedures are preferred to estimate uncertainties on the calculated mole fractions (e.g., *Hodges and McKenna*, 1987; *Steltenpohl and Bartley*, 1987; *Kohn and Spear*, 1991b).

Determining the modal abundance of minerals also includes uncertainties. Routinely used approaches to determine modal abundance include point counting and automated mineralogical analysis (via EPMA or scanning electron microscope). Factors that contribute to uncertainty include features such as the point size/image resolution, amount of each mineral, the grain size and shape, the spacing between points, and the number of points calculated. Automated mineralogical analysis are also subject to their own analytical uncertainties which may include classification algorithms, and thresholds used to distinguish mineral phases. Approaches to estimate these uncertainties include statistical methods assuming a binomial distribution based on the amount of each mineral and the number of points calculated (*Van der Plas and Tobi*, 1965) and bootstrap resampling (*Evans and Napier-Munn*, 2013; *Blannin et al.*, 2021).

3.2.3 Parameter uncertainty

Parameter uncertainty is the uncertainty in the forward model predictions as a result of user-selected input parameters. These choices may affect the accuracy of the result. This includes the choice of thermodynamic databases, *a-X* models, model system, and input parameters like $X_{\mathrm{Fe^{3+}}}$, fluid composition, and water content (Fig. 3.1). These choices are often influenced by both analytical and geological uncertainty.

Although ds6.2 (*Holland and Powell*, 2011) represents a significantly expanded and refined dataset, disagreements remain regarding which thermodynamic database and *a-X* models best reproduce natural observations (e.g., *Pattison and DeBuhr*, 2015; *Waters*, 2019; *Gervais and Trapy*, 2021; *Pattison and Goldsmith*, 2022). The choice of a model system is also critical. A system too small to fully capture the controlling equilibria may fail to reproduce observed mineral assemblages, mineral compositions, or modal abundances (*White et al.*, 2007). Simplified model systems often omit minor elements present in natural rocks (e.g., Zn in staurolite), which can significantly affect the stability of certain minerals. Conversely, including minor elements can introduce other problems, such as inadequate partitioning of added components across multiple solution models, which may artificially over-stabilize select phases, thereby impacting the composition and abundance of other assemblage phases. It is often not possible to compare the impact of these omissions or additions. However, the addition of Mn to the model system is shown to strongly impact the stability of garnet with changing *P-T* conditions, with minimal changes to other common pelitic minerals or the overall

topology (*Tinkham et al.*, 2001; *White et al.*, 2007). The precision and boundary range of the model system can also impact whether the desired phase information is calculated.

Several other key input parameters introduce additional uncertainties, including the ferric-to-ferrous iron ratio ($X_{Fe^{3+}}$), total H_2O in the system (MH_2O), and fluid composition (aH_2O). The oxidation state of a rock, expressed as the ratio of ferrous (FeO, Fe^{2+}) to ferric (Fe_2O_3, Fe^{3+}) iron, strongly affects phase equilibria and has been a key parameter in thermobarometric studies (*Schumacher*, 1991; *Diener and Powell*, 2010; *Forshaw et al.*, 2019). Despite its significance, routine bulk composition analyses (e.g., XRF, EPMA) cannot distinguish between Fe^{3+} and Fe^{2+}. Methods such as charge balancing, the "flank method", and empirical estimates can infer Fe^{3+} and Fe^{2+} for some minerals (e.g., garnet, pyroxene, amphibole; *Droop*, 1987; *Hofer et al.*, 1994; *Holland and Blundy*, 1994; *Hawthorne et al.*, 2012), but are ineffective for minerals with structural vacancies (e.g., biotite, white mica, chlorite, staurolite; *Schumacher*, 1991). Without costly techniques like wet chemical titration, Mössbauer spectroscopy, or XANES, $X Fe^{3+}$ is often estimated using literature values or by exploring P-X and T-X pseudosections (e.g., *Doukkari et al.*, 2018; *Schorn and Diener*, 2019).

For sub-solidus conditions, fluid-present systems are typically assumed to contain excess H_2O during prograde metamorphism (*Guiraud et al.*, 2001). In supra-solidus conditions, water content must often be estimated, with approaches varying based on the portion of metamorphic history being modeled. These different approaches substantially impact pseudosection topology and predicted melt content (see discussion in *Waters*, 2019). Under fluid-present sub-solidus conditions, devolatilisation reactions using pure H_2O are assumed to dominate. However, where fluid composition-dependent conditions are implicated, a lower aH_2O may be necessary (e.g., *Ohmoto and Kerrick*, 1977), which shifts the temperature of mineral assemblage boundaries and the solidus (e.g., *Weller et al.*, 2013).

3.2.4 Model uncertainty

Model uncertainty is the uncertainty inherent in forward model predictions stemming from the data, algorithms, and choices used to formulate the model. This may impact both the accuracy and precision of the predicted results. This should be understood separately from parameter uncertainty, which is related to user-choices. Uncertainties derived from the underlying thermodynamic dataset and a-X relations play a particularly important role in model uncertainty (Fig. 3.1).

For single-reaction thermometers and barometers, these uncertainties are dominantly expressed by the precision of the experimentally or empirically determined end-member reactions and thermodynamic parameters used in calibration (**?***Hodges and McKenna*, 1987; *Kohn and Spear*, 1991a). However, for multi-equilibrium thermobarometry and phase equilibrium modelling, the uncertainties are associated with the thermodynamic

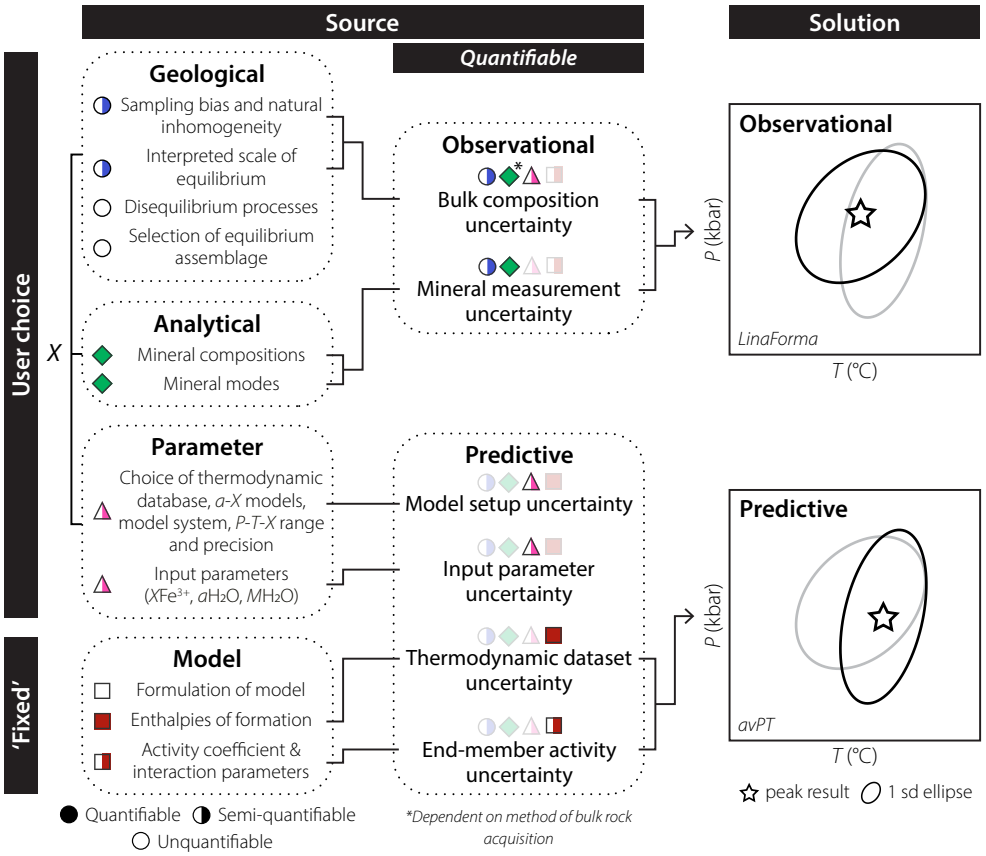

Fig. 3.1 Schematic summary of the primary sources of uncertainty in thermobarometry, detailing their propagation (where quantifiable) into P-T solution uncertainties. Observational uncertainties can be calculated using the new workflow presented in this study, LinaForma, or predictive uncertainties (specifically those stemming from model uncertainty) can be calculated using avPT mode in THERMOCALC (*Powell and Holland*, 1994).

properties of the individual mineral end-members (*Worley and Powell*, 2000) and the calibrations used will adjust within error brackets to ensure values are internally consistent (*Holland and Powell*, 1998, 2011). For these thermodynamic datasets, the uncertainties on, and correlations between, the enthalpies of formation are determined by least-squares derivation from the experimental data (*Powell and Holland*, 1993a). Such uncertainties and correlations can be propagated through the dataset onto calculated values of P and T (avPT; *Powell and Holland*, 1988, 1994). The other thermodynamic properties (e.g., entropy and molar volume) are treated as relatively well-constrained in the derivation, as they can be measured or estimated with greater confidence. However, uncertainties in activity-composition relationships and analytical measurements may introduce additional uncertainties of comparable or greater magnitude than those stemming from enthalpy uncertainties (*Powell and Holland*, 1988).

The complexity of minerals, in terms of crystal structure and the differences of site preferences for atoms during mixing, means solution (a-X) models are necessarily simplifications from natural systems (*Powell and Holland*, 1993b). The formulation of

a-X relations (see *Powell and Holland*, 1993b; *Holland and Powell*, 1996a,b, 2003) treats mineral phases as solid solutions composed of independent end-members, allowing for a range of possible ordering states (*Holland and Powell*, 1996a). Despite the nonideality characteristic of many minerals, the complexity of accounting for such features may be impracticable and therefore, where required, ideality is assumed (*Powell and Holland*, 1993b). Normalisation is applied to ensure that both the ideal mixing activity and the activity coefficient for each pure end-member are set to unity, allowing solution models to be created even for minerals such as hornblende containing complex multi-site phases (*Powell and Holland*, 1993b). However, the difficulty in constraining the activity coefficients and interaction parameter terms carries large uncertainties into a-X relationships, and the lack of a-X data for minerals makes it challenging to constrain these associated uncertainties (*Powell and Holland*, 1988). An attempt to include realistic uncertainties is detailed in *Powell and Holland* (1988), where the uncertainty on the endmember activity is dominated by the cation site with the largest normalised uncertainty, even in a complex formula unit. The decisions taken formulating these models for certain minerals (e.g., distortion of Al/Si charge balance, or not incorporating vacancies in octahedral and interlayer sites) inevitably impact how they reproduce natural compositions for the whole assemblage, and the scale of this impact will vary across P-T space (*Forshaw et al.*, 2019; *Waters*, 2019; *Dubacq and Forshaw*, 2024).

3.2.5 Combined uncertainties and correlations

A total uncertainty, derived from the summation and propagation of the outlined uncertainty sources, remains hypothetical due to the incomplete nature of propagation (*Powell and Holland*, 1988; *Kohn and Spear*, 1991b), and the inability to fully quantify all uncertainties (Fig. 3.1). As a result, any solution uncertainties represent only the partial propagation of select quantifiable sources, offering a minimum estimate (*Powell and Holland*, 2008). Furthermore, the inherent interdependence of these uncertainties means that quantitative uncertainty estimates are not entirely independent; instead, they encapsulate contributions from multiple, mutually dependent sources. This interdependence within the modeled system means changes to the system are multifaceted in effect. For example, displacements of key field boundaries are correlated such that the a-X relations used in thermodynamic modeling should consistently reproduce the correct sequence of up-temperature or up-pressure assemblages (*Green et al.*, 2016).

Despite the complex relationship between uncertainties, quantitative assessments remain essential for understanding the relative scale and impact of these uncertainties. A comprehensive assessment of the scale of all the quantifiable uncertainties (Fig. 3.1) is beyond the scope of this study. However, it is understood that imprecisely known activity-composition relationships and geological or analytical uncertainties contribute a greater uncertainty than those stemming from dataset enthalpies, which is the primary source of uncertainty considered within the thermodynamic models (*Powell*, 1985;

Powell and Holland, 2008). For "predictive" uncertainties (e.g., thermodynamic dataset and end-member activities, Fig. 3.1), the user can employ the avPT methods outlined by (*Powell and Holland*, 1988, 1994). This study focuses on quantifying "observational" uncertainties (those stemming from uncertainty in the mineral measurements and/or bulk rock composition, Fig. 3.1), though the outlined method will inherently account for some degree of these systematic uncertainties derived from the predictions.

3.3 Inversion method

Forward modelling is the process of predicting the data one would observe for a given set of model input parameters. A pseudosection is an example of a forward model, in which the equilibrium phase assemblage, phase compositions, and abundances are predicted for a rock of a given composition across *P-T* space. This is contrasted with inverse modelling in which observed data is used to estimate the underlying model parameters. Conventional thermobarometry (e.g., Ti-in-biotite geothermometer; *Henry et al.*, 2005) and multi-equilibrium thermobarometry (*Powell and Holland*, 1994) are examples of inverse methods, where *P–T* conditions are estimated from the observed mineral measurements.

Constraining the conditions of equilibration and evolution of a rock from a forward model is typically achieved using intersecting isopleths of phase compositions or modal volumes, calculated using phase equilibrium modelling. This method has been effectively applied to semi-quantitatively analyze the tectonothermal evolution of geological terranes (e.g., *Vance and Mahar*, 1998; *Hoschek*, 2004; *Štípská and Powell*, 2005). In its simplest form, this can involve using a mean or representative analysis from two variables to determine a singular point of cross over in *P-T* space (Fig. 3.2A).

Alternatively, the observed data distribution of two or more variables may define varying zones of overlap (Fig. 3.2B, C, D). In all cases the accuracy and precision of the resulting *P-T* estimates, and thereby the conclusions drawn from the sample, are significantly influenced by the variables selected (Fig. 3.2A, B, C, D). The selected variables will have differing population distributions and differing sensitivity to *P-T* changes. Even a narrow observed population distribution can correspond to a broad calculated *P–T* interval if the variable is highly responsive to *P–T* changes (Fig. 3.2B). Including, additional variables may make for a more "representative" result, but can also result in multiple zones of overlap (Fig. 3.2C), or poor to no agreement (Fig. 3.2D). Such approaches are often ultimately influenced by selection bias, choosing the variables that show best agreement for the expected conditions of equilibration.

The workflow presented in this study, LinaForma, aims to address these challenges by applying a new inverse method that allows for the simultaneous inversion of a large set of variables (Fig. 3.2E). By using a grid-search inversion coupled with bootstrap

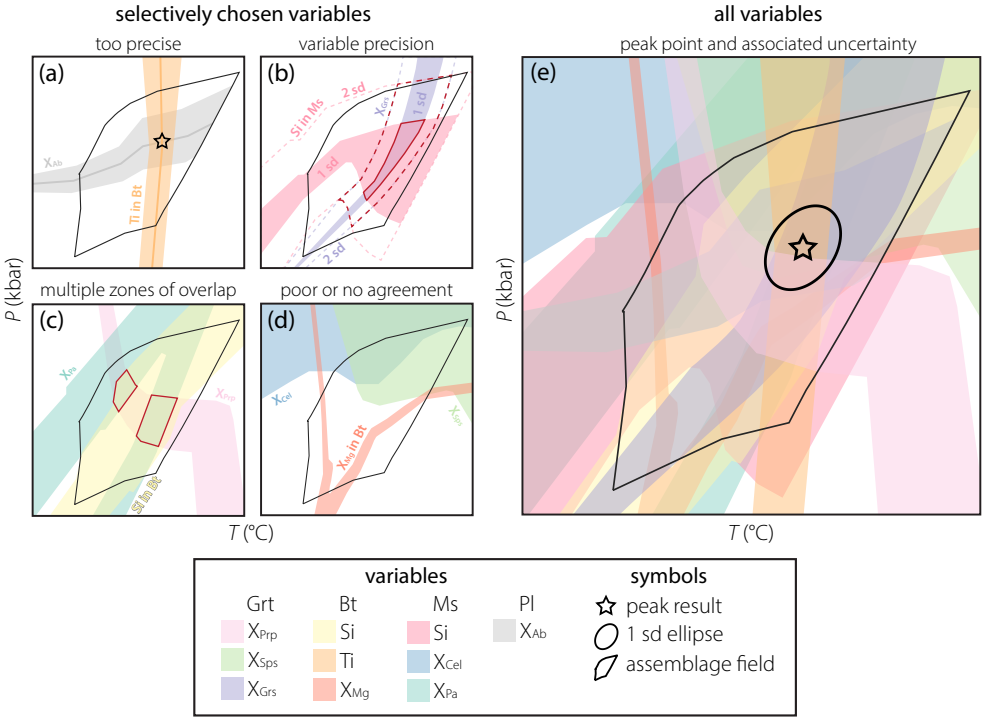

Fig. 3.2 Schematic summary of (a–d) common problems associated with application of intersecting mineral composition variables commonly applied in constraining the P-T conditions from forward models. (e) Using a large and diverse range of robust mineral composition variables to provide a more representative P-T constraint. Definitions of mineral composition variables are included in Table 3.1 for reference.

resampling of the mineral measurements, the workflow calculates the "best-fit" P-T conditions and associated uncertainties for a given bulk rock composition. A schematic of the workflow is shown in Fig. 3.3. This workflow is then applied to a kyanite-zone pelite (ICSV13) and a garnet+plagioclase-zone metabasite (ICSV117) from the Greater Himalayan Sequence in the Zanskar Himalaya, NW India (Fig. 3.5). As a large number of mineral composition variables are used in this study, their definitions are included in Table 3.1 for reference.

3.3.1 Best-fit P-T conditions: the grid-search inversion

This workflow uses a grid-search inversion to determine the optimal or "best-fit" P-T conditions for a given rock system. The grid-search involves drawing a large number of trial solutions from a regular grid in model (P-T) space. For each point on the grid (i.e., a trial solution), the difference between the forward model's predicted data and the observed data is computed using an objective, or misfit, function (Fig. 3.3A).

The best-fit solution is the point on the grid with the lowest value of the misfit function. In this case, the observed data may include mineral composition, mineral modes, and bulk properties such as the interpreted equilibrium phase assemblage and

Table 3.1 Mineral composition variable definitions for common pelitic and metabasic minerals at sub-solidus conditions.

Mineral	Variable	Definition
Garnet (Grt)	X_{Alm}	$\frac{\mathrm{Fe}^{2+}}{\mathrm{Fe}^{2+}+\mathrm{Mg}+\mathrm{Ca}+\mathrm{Mn}}$
	X_{Grs}	$\frac{\mathrm{Ca}}{\mathrm{Fe}^{2+}+\mathrm{Mg}+\mathrm{Ca}+\mathrm{Mn}}$
	X_{Sps}	$\frac{\mathrm{Mn}}{\mathrm{Fe}^{2+}+\mathrm{Mg}+\mathrm{Ca}+\mathrm{Mn}}$
	X_{Prp}	$\frac{\mathrm{Mg}}{\mathrm{Fe}^{2+}+\mathrm{Mg}+\mathrm{Ca}+\mathrm{Mn}}$
	X_{Mg}	$\frac{\mathrm{Mg}}{\mathrm{Mg}+\mathrm{Fe}^{2+}}$
Grt (without Mn)	X_{Alm}	$\frac{\mathrm{Fe}^{2+}}{\mathrm{Fe}^{2+}+\mathrm{Mg}+\mathrm{Ca}}$
	X_{Grs}	$\frac{\mathrm{Ca}}{\mathrm{Fe}^{2+}+\mathrm{Mg}+\mathrm{Ca}}$
	X_{Prp}	$\frac{\mathrm{Mg}}{\mathrm{Fe}^{2+}+\mathrm{Mg}+\mathrm{Ca}}$
	X_{Mg}	$\frac{\mathrm{Mg}}{\mathrm{Mg}+\mathrm{Fe}^{2+}}$
Staurolite (St)	X_{Mg}	$\frac{\mathrm{Mg}}{\mathrm{Mg}+\mathrm{Fe}^{2+}}$
Cordierite (Crd)	X_{Mg}	$\frac{\mathrm{Mg}}{\mathrm{Mg}+\mathrm{Fe}^{2+}}$
Chlorite (Chl)	X_{Mg}	$\frac{\mathrm{Mg}}{\mathrm{Mg}+\mathrm{Fe}^{2+}}$
Biotite (Bt)	Si	apfu
	Ti	apfu
	X_{Mg}	$\frac{\mathrm{Mg}}{\mathrm{Mg}+\mathrm{Fe}^{2+}}$
Muscovite (Ms)	Si	apfu
	X_{Cel}	Mg apfu
	X_{Pa}	$\frac{\mathrm{Na}}{\mathrm{Na}+\mathrm{Ca}+\mathrm{K}}$
Plagioclase feldspar (Pl)	X_{Ab}	$\frac{\mathrm{Na}}{\mathrm{Na}+\mathrm{Ca}+\mathrm{K}}$
Alkali feldspar (Kfs)	X_{San}	$\frac{\mathrm{K}}{\mathrm{Na}+\mathrm{Ca}+\mathrm{K}}$
Epidote (Ep)	X_{Fe}	$\frac{\mathrm{Fe}^{3+}}{\mathrm{Al}+\mathrm{Fe}^{3+}}$
Amphibole (Amph)	Ts vector	$\mathrm{Al(T)} - \mathrm{Na(A)} - \mathrm{K(A)}$
	Ed vector	$\mathrm{Na(A)} + \mathrm{K(A)}$
	Gln vector	Na(M4)
	Ti	apfu
Clinopyroxene (Cpx)	Al	apfu
	X_{Mg}	$\frac{\mathrm{Mg}}{\mathrm{Mg}+\mathrm{Fe}^{2+}}$
	Ca	apfu
	X_{Jd}	$\frac{\mathrm{Al}^{VI}}{\mathrm{Na}+\mathrm{Ca}}$

whole-rock density. The forward models for each point on the grid can be calculated using programs such as THERIAK-DOMINO (*de Capitani and Brown*, 1987; *de Capitani and Petrakakis*, 2010), Perple_X (*Connolly*, 1990, 2005), and MAGEMin (*Riel et al.*,

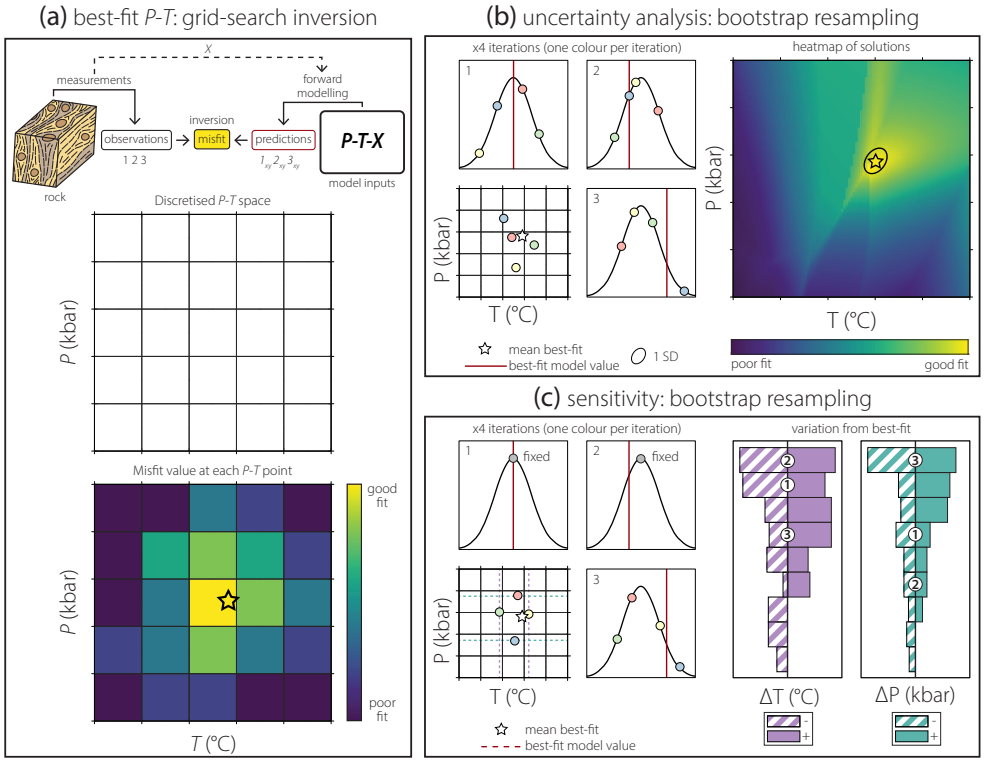

Fig. 3.3 Schematic summary of the presented workflow and methods. From observations and forward modelling of a given rock system to (a) grid-search non-linear inversion to determine the best-fit P-T conditions, to (b) bootstrap-resampling to assess the uncertainty of the P-T solution, and (c) result diagnostic using bootstrap resampling of the employed variables to assess sensitivity of the best-fit result to uncertainty in the individual variables. Thin-section schematic from *Palin et al.* (2016).

2022), which rely on Gibb's free energy minimisation to determine the most stable equilibrium assemblage as a function of P, T, and X.

This workflow uses the L1-norm misfit function (f), equivalent to the sum of absolute residuals (Equation 3.1).

$$f = \sum_{i=1}^{N} \frac{|x_i^{\text{obs}} - x_i^{\text{mod}}|}{x_i^{\text{obs}}} \tag{3.1}$$

Where N is the total number of variables, x_i^{mod} is the value of variable i predicted at the trial solution, and x_i^{obs} is the observed value of variable i. The residuals are scaled relative to the observed value of each variable to ensure that variables with large magnitudes do not have an overwhelming influence on the result. Large values of f suggest the model predictions poorly fit the observed data, whilst low values of f show the observed data and the model predictions are similar (i.e., the data "residuals" are small). The trial solution with the lowest value of f is the best-fit solution.

3.3.2 Uncertainty analysis: bootstrap resampling

Bootstrap resampling is used to estimate of the uncertainty associated with the best-fit *P-T* solution. This involves resampling the observational data with replacement, and then computing the required statistics for each resampled dataset, in this case the best-fit solution of the grid-search inversion (Fig. 3.3B). When repeated multiple times (e.g., N $\geq$ 1000), the distribution of inversion solutions obtained from the resampled datasets provides an estimate of the true mean or median solution and the population distribution (*Menke*, 1984). Bootstrap resampling can be either non-parametric or parametric. Non-parametric bootstrapping involves resampling with replacement from the original observational dataset. Parametric bootstrapping generates samples according to an assumed distribution of the observational data (*Efron*, 1979), in this case a normal distribution (Fig. 3.3B). Given the non-Gaussian nature of the probability density function in non-linear problems (*Menke*, 1984), percentile-based confidence intervals such as the interquartile range are often more informative than the standard deviation. Bootstrap-resampling is also used to assess the sensitivity of the inversion results to uncertainty in each variable (Section 3.3.3.2, Fig. 3.3C).

3.3.3 Diagnostics

The workflow includes three diagnostics with which to validate and refine the best-fit solution: (1) Quality of data fit (X_{total}) between the best-fit solution and the observations; (2) the sensitivity of the best-fit solution to each of the chosen variables; and (3) the standard error (SE). The values of these diagnostic metrics are automatically output in table format at the end of the inversion calculations. The definitions for each value in the diagnostics table are included in Table 3.2.

3.3.3.1 Quality of data fit (X_i, X_{total})

The data fit metric assesses the level of agreement between the median best-fit solution and the observations. This is quantified by assessing whether the model's predictions at the median best-fit conditions (e.g., the modeled value of X_{Alm} garnet at PT_{best}) fall within two standard deviations of the observed values. This assessment is provided in the workflow by a score for each variable (X_i) and a total score (X_{total}). These are calculated following Equations 3.2 and 3.3 respectively.

$$X_i = \frac{|x_i^{\text{obs}} - x_i^{\text{mod}}|}{2\sigma_i^{\text{obs}}} \tag{3.2}$$

$$X_{\text{total}} = \frac{1}{N}\sum_{i=1}^{N} X_i \tag{3.3}$$

Table 3.2 Definitions of parameters used in the inversion analysis and presented in the result output and diagnostics table.

Parameter	Definition
X_i	Quality of fit score for each variable. Higher values indicate a poorer fit.
ΔT	Maximum absolute temperature variation due to uncertainty in a variable, relative to the mean best-fit solution.
ΔP	Maximum absolute pressure variation due to uncertainty in a variable, relative to the mean best-fit solution.
$\mu_{\text{obs}} \pm 2\sigma$	Mean observed variable value, with two standard deviations (uncertainty).
Pred	Predicted value of variable for the median best-fit solution.
Mean	Average temperature and pressure of the solution distribution (1σ).
Median	50th percentile of the temperature and pressure distribution.
IQR	Interquartile range (25th–75th percentile) of the temperature and pressure distribution.
X_{total}	Overall quality of fit score for the inversion; values above 1 suggest poor fit.
SE	Standard error, expressed as a percentage relative to the mean solution.
# of fitted variables	Total number of data successfully fitted by the inversion (out of total).
Grid resolution	Precision/spacing of the grid in °C and kbar
Bootstrap resamples	Number of bootstrap resamples

N is equal to the total number of variables, X_i^{mod} represents the value of variable i predicted at the best-fit solution, X_i^{obs} represents the observed value of variable i, and σ_i^{obs} represents the observed standard deviation for variable i. A value of > 1 for both the total score and the individual variable scores indicates a poor fit. A total score of ≤ 1 demonstrates that the inversion fits the data acceptably well, and an individual variable score of ≤ 1 indicates that the modeled prediction fits the observations within 2 standard deviations. The workflow provides options to visualize this relationship (e.g., Fig. 3.4D). The scoring strategy above provides a metric similar to the σ_{fit} metric (square-root of the Mean Square Weighted Deviation) in *Powell and Holland* (1994).

3.3.3.2 Sensitivity (ΔP, ΔT)

Sensitivity analysis evaluates how uncertainty in input variables affect the inversion result. This is performed using bootstrap resampling, in which each variable is resampled in turn while the remaining variables are fixed at the appropriate mean value (Fig. 3.3C). The resultant spread in the best-fit solutions can then be linked directly to variation in the resampled variable. The sensitivity values are given as the maximum absolute temperature (ΔT_i) and pressure (ΔP_i) difference between the mean solution of the inversion when all the variables are re-sampled ($T^{\text{median}}, P^{\text{median}}$) and the range of solutions when only a single variable (i) is re-sampled n times ($T_i^{min} - T_i^{max}, P_i^{min} - P_i^{max}$).

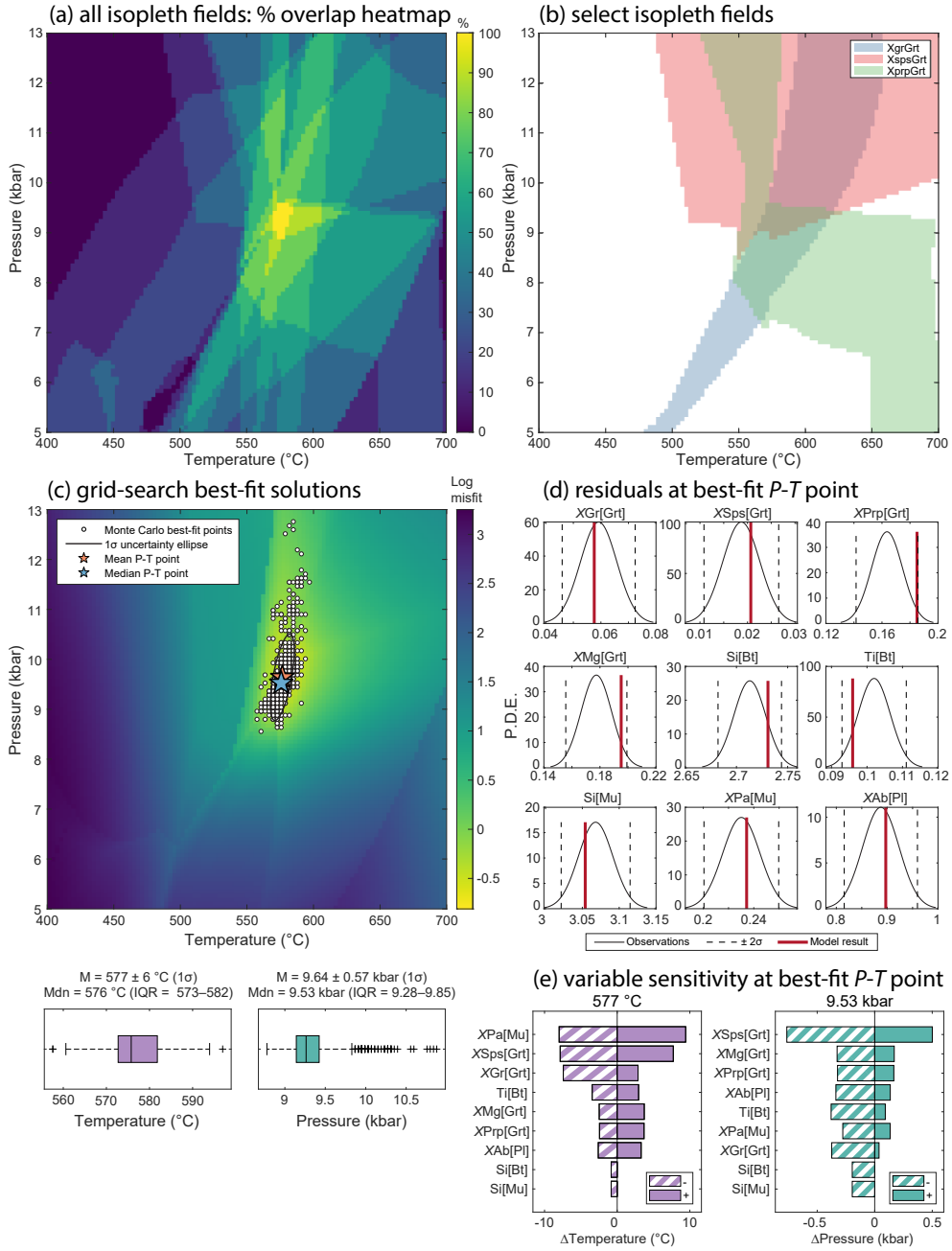

Fig. 3.4 Workflow example using natural sample ICSV13. (a) Overlapping isopleth "fields" defined by 2 σ range of mineral measurements. (b) Intersection of X_{Gr}, X_{Prp}, and X_{Sps} isopleth fields defined by 2 σ range of mineral measurements. (c) Grid-search best-fit solutions and heatmap (error-surface) for bootstrapped mineral measurement data (n = 1000), overlain with the bootstrapped mean and median best-fit result. (d) Data residuals at the median P-T point of 576 °C and 9.53 kbar, showing the fit between the model and the observations. (e) Sensitivity analysis for T and P of mineral composition variables presented as tornado plots at the mean P-T point of 577 °C and 9.64 kbar.

$$T_i^{\max} = \mathrm{mean}(T_i^n) + 2 \times \mathrm{std}(T_i^n) \tag{3.4}$$

$$T_i^{\min} = \text{mean}(T_i^n) - 2 \times \text{std}(T_i^n) \tag{3.5}$$

$$\Delta T_i = \max \left| (T^{\text{mean}} - T_i^{min}), (T_i^{max} - T^{mean}) \right| \tag{3.6}$$

Where T_i^n is the distribution of best-fit temperatures from the re-sampling of variable i. The same equations apply for pressure. The comparison is made with the mean solution rather than the median solution because the mean is less sensitive to the discretization of the model grid. A high sensitivity may be caused by a large spread in the value of observed data variables, or a large percentage change in the model values over small areas of P-T space (meaning that small differences in input value results in a large change in pressure or temperature estimate). This analysis is often displayed using tornado plots (e.g., Fig. 3.4E). The sensitivity analysis provides a similar function to the dimensionless hat value (also called the leverage value) used to quantify the influence of individual end-members on the final result in avPT (*Belsley et al.*, 1980; *Powell and Holland*, 1994). However, the values calculated by this workflow are in units of temperature and pressure.

3.3.3.3 Standard error (SE)

The standard error (SE) metric quantifies the extent to which the mean result of the inversion is expected to deviate from the true population mean (i.e., how close the estimated best-fit solution is to the "true" solution; Equation 3.7).

$$SE = \frac{\sigma}{\sqrt{N}} \tag{3.7}$$

Where N is the number of variables, and σ is the standard deviation of the bootstrap solutions for both pressure and temperature, respectively. A smaller SE value indicates that the sample mean is a more precise estimate of the population mean. Increasing the number of data variables (i.e., N) used within the inversion will typically reduce the SE.

3.3.4 Applying the workflow

3.3.4.1 Observations setup

Any variable can be used in the inversion provided an appropriate forward model can be calculated, and the data can be tabulated into grid format. The type of variables (e.g., mineral compositions and/or modal volumes) employed during the inversion should reflect the interpreted scale of chemical and textural equilibrium and the method of bulk composition acquisition. Table 3.1 lists recommended compositional variables for pelitic and metabasic lithologies in sub-solidus systems. For any major phase with a relevant solution model, and variables that can provide robust P-T constraints, at

least one variable should be included to ensure the misfit function accommodates its presence. A degree of freedom should always be preserved (e.g., for plagioclase, X_{An} and X_{Ab} should not both be included—one is sufficient to fully describe the system). Modal volume variables may be used for major volume phases but should be treated with caution or avoided for minor volume or accessory phases (*Weller et al.*, 2024). A minimum of three variables, ideally from more than one phase, should be used for any inversion. An exception to this guideline may apply to garnet, where core compositions can be interrogated independently. The inferred peak assemblage field is not inherently enforced as a constraint unless used directly as a variable or stable phases are explicitly assigned a non-zero volume (or vice-versa). The advantages and limitations of this decision are further discussed in Section 3.6.2.2.

If the bulk rock composition varies significantly across the analysed rock volume, this uncertainty can be assessed by computing a range of forward models calculated for Monte-Carlo variations in the input composition (Section 3.5.2). This range can be defined using various approaches, including replicate blocks or an uncertainty level characteristic of a type assemblage(*Palin et al.*, 2016), resampling from discrete bulk composition domains within a thin section (e.g., *Duesterhoeft and Lanari*, 2020), or an uncertainty level characteristic of the scale of variation (e.g., 5%; *Forshaw et al.*, 2019).

3.3.4.2 Predictions setup

The *P-T* grid must be sufficiently broad to avoid boundary effects influencing the best-fit solutions whilst maintaining precision to capture the true solution between grid points. If results converge on the boundary of the *P-T* range, a different range should be chosen. The spacing should align with the precision of both input data and the forward model. As a general guideline, the grid spacing should not exceed 10 °C and 100 bar.

The method of bootstrap resampling should be chosen based on the data distribution or availability. Parametric bootstrapping, using a mean and standard deviation, is suitable for normally distributed data, while non-parametric bootstrapping, using the original data, is more appropriate for non-normal data. A minimum of 1000 bootstrap resamples is recommended, though the exact number should be verified by observing the distribution of the P and T solutions against the number of bootstrap re-samples (Fig. B.1). The distribution of solutions should have stabilized prior to the selected number of bootstraps.

3.3.4.3 Result interrogation

Prior to inversion, the relationships of different variables in *P-T* space should be interrogated to assess whether mutual equilibrium is likely for the selected variables and whether appropriate modelling parameters (*P-T* range, XFe^{3+}, etc.) have been

used. This can be visualized for all variables (e.g., Fig. 3.4A) or for individual variables (e.g., Fig. 3.4B). A preliminary assessment of mutual equilibrium can be made, and variables may be filtered to exclude any that may stem from clear geological or model uncertainty. However, in most cases it is preferable to let the variables be removed through the diagnostics.

Fit diagnostics provide critical insight into the reliability of inversion results (Table 3.2). If the total score of the quality of data fit (X_{total}) is above 1, variables with fit scores (X_i) exceeding 1 should be removed sequentially, starting with the most severe, until X_{total} falls below or is equal to 1. Further variables need not be removed to reduce the score. High sensitivity values (ΔP, ΔT) are not inherently problematic unless coupled with poor fit scores. For example, X_{total} may be at or below 1 whilst several individual variables show X_{i} scores well above 1. In these instances, if the sensitivity values of the individual variables are greater than approximately 2 % of the best-fit result (Table 3.5), consider removing the poorly fitting variables. This occurs infrequently, as the L1-norm function is robust to outliers (*Claerbout and Muir*, 1973; *Li et al.*, 2015; *Ibraheem et al.*, 2021). Persistent scatter among variables, rather than isolated outliers, may indicate disequilibrium or retrogression (*Powell and Holland*, 1994), and in such cases sequential removal might not resolve the issue. Finally, the standard error (SE) of the solution should be minimized as much as possible by incorporating the maximum possible number of robust variables in the inversion.

The best-fit solution and associated uncertainty should ideally overlap the interpreted peak assemblage field. Discrepancies may indicate inconsistencies in the analyzed rock volume across different techniques, the scale of equilibrium, or the definition of the equilibrium assemblage. In some instances, the bootstrap re-sampling may highlight the possibility of multi-modal results. The distribution of the solution uncertainty can be assessed using histograms or the heatmap of solutions (Fig. 3.4C). In this case, the user could either add additional observations to help further constrain the solution or assess the merits of the various solutions based on independent constraints such as conventional thermobarometers. Significant local minima will also result in an increase in estimated uncertainty, as indicated by a higher interquartile range.

3.3.4.4 Result reporting

Results should generally be reported using the median and inter quartile range (IQR), as these metrics are suitable for non-normal distributions. The heatmap of solutions (e.g., Fig. 3.4C) should be accompanied by a pseudosection. A diagnostic table (e.g., Tables 3.2, 3.5) summarizing the best-fit solutions, uncertainty (IQR, standard error), and quality of fit for each individual variable as well as the inversion as a whole must also be provided. Given that the results depend on key parameters such as bootstrap type, number of bootstraps, grid range, and grid precision, this information should be

clearly documented. Additionally, visual aids like overlap percentage plots or sensitivity tornado plots may be valuable for various applications.

3.4 Natural examples

3.4.1 Sample descriptions

To demonstrate the applicability of the workflow, mineral compositions (collected via EPMA) of a kyanite-zone pelite (ICSV13) and a garnet+plagioclase-zone metabasite (ICSV117) from the Greater Himalayan Sequence in the Zanskar Himalaya, NW India, were inverted to determine best-fit *P-T* conditions and compared with classical thermobarometric methods. The analytical setup, mineral recalculation procedure, formulation of bulk composition, and forward modelling procedure are included in Appendix B. The bulk rock composition was collected using XRF, assuming chemical equilibrium was achieved at the 'rock-scale', the measured composition for both samples is included in Table 3.3. The input and forward model for each sample are included in Appendix B.

Table 3.3 Measured bulk composition via XRF of ICSV13 and ICSV117 in wt%.

Sample	**SiO_2**	**Al_2O_3**	**Fe_2O_3**	**MnO**	**MgO**	**CaO**	**Na_2O**	**K_2O**	**TiO_2**	**P_2O_5**	**LOI**	**Total**
ICSV13	61.23	19.13	7.10	0.09	2.65	0.47	1.52	4.12	0.98	0.09	1.96	99.31
ICSV117	47.80	14.42	14.92	0.19	6.39	9.99	2.41	0.75	2.12	0.18	0.34	99.51

ICSV13 contains the assemblage muscovite, biotite, quartz, kyanite, garnet, staurolite, and plagioclase. Accessory phases include apatite, chlorite, rutile, ilmenite, graphite, tourmaline, and monazite. A characteristic photomicrograph of the relevant minerals and textures is located in Fig. B.2A. Kyanite occurs as prismatic subhedral poikiloblasts throughout the section, whereas, staurolite appears as a singular large prismatic poikiloblast (X_{Mg} = 0.19–0.20). Both minerals overgrow the matrix fabric, display impinged grain boundaries variably defined by each other, and share a concordant inclusion trail with the same inclusion assemblage (Fig. B.2A). Garnet occurs as rounded to flattened subhedral poikiloblasts with strong compositional zoning (X_{Alm} = 0.60–0.76, X_{Prp} = 0.05–0.16, X_{Sps} = 0.19–0.02, X_{Grs} = 0.16–0.06). Biotite and muscovite define the dominant matrix fabric. Analysed biotite grains are compositionally homogenous (X_{Mg} = 0.49, Ti apfu = 0.09–0.11), whereas muscovite shows some compositional variation (Si apfu = 3.04–3.09, X_{Cel} = 0.07–0.09, X_{Pa} = 0.21–0.25). Locally weakly oriented to unoriented chlorite overgrows biotite. Plagioclase occurs as oval subhedral to anhedral grains and shows some variation across the albite–oligoclase compositional boundary (X_{Ab} 0.84–0.92). Ilmenite, forms coarser grains along kyanite and garnet boundaries. Both rutile and ilmenite occur as inclusions in peak porphyroblasts. The inferred equilibrium assemblage at peak conditions for ICSV13 is kyanite-staurolite-garnet-biotite-muscovite-plagioclase-quartz-rutile-ilmenite-H_2O.

ICSV117 contains the assemblage hornblende, plagioclase, biotite, and quartz. Accessory phases include titanite, chlorite, apatite, and ilmenite. A characteristic photomicrograph of the relevant minerals and textures is located in Fig. B.2B. Amphibole occurs as coarse acicular prismatic grains and classified as magnesiohornblende–pargasite (*Hawthorne et al.*, 2012). Vectors vary as follows: tschermakite from 0.97–1.19, edenite from 0.25–0.55, and glaucophane from 0.12–0.21. Biotite is present as coarse subhedral poikiloblasts to fine tabular grains with a homogenous composition (X_{Mg} of 0.48–0.52, Ti of 0.14–0.16 apfu). Minor chlorite occurs in replacement of biotite. Plagioclase occurs as oval to angular prismatic euhedral–subhedral grains. Strong concentric compositional zoning is locally observed. Plagioclase is defined as oligoclase (X_{Na} of 0.77–0.81). Ilmenite and titanite are the main Ti-oxide phases. Ilmenite form individual crystals, whereas titanite form polycrystalline string-of-beads textures, ilmenite occur as cores to titanite rims, though both are in contact with the matrix. Ilmenite grain boundaries is defined by shape habit of amphibole, whereas titanite, commonly forming along amphibole crystals, locally impinge amphibole grain boundaries. The inferred equilibrium assemblage at peak conditions for ICSV117 is: hornblende-biotite-plagioclase-quartz-ilmenite-titanite-H_2O.

3.4.2 ICSV13

3.4.2.1 Conventional methods of analysis

Given the inferred peak assemblage, an approximation of the peak field could be represented by either 1) the staurolite-stable field, 2) the temperature-restricted kyanite- and staurolite-stable field, or 3) the kyanite-stable field (Fig. 3.5A).

Although the kyanite+staurolite stable field directly represents the peak assemblage of the major phases, the narrow temperature range in *P-T* space is at odds with the widespread occurrence of this assemblage in metamorphic terrains (*Pattison and Spear*, 2018). This discrepancy likely arises from the influence of sluggish reaction kinetics that yield the metastable persistence staurolite, or the minimal free energy difference between staurolite and kyanite nucleation. This latter option means kyanite may form earlier (*Pattison and Spear*, 2018), or staurolite may form later than that predicted by the thermodynamic models. In ICSV13, the consistency of microstructure, inclusion suite, and inclusion trail between kyanite and staurolite is suggestive of similar timing and conditions of growth. Given that nearby assemblages are predominantly kyanite-bearing rather than kyanite+staurolite-bearing (*Cawood et al.*, 2024), the staurolite-bearing fields are disregarded for this case. Therefore, the kyanite-bearing field on Fig. 3.5A is chosen as the best representation of the peak field.

The peak assemblage field shows a wide *P-T* range over which the given rock composition may have equilibrated. Temperature ranges between ~575–700 °C and

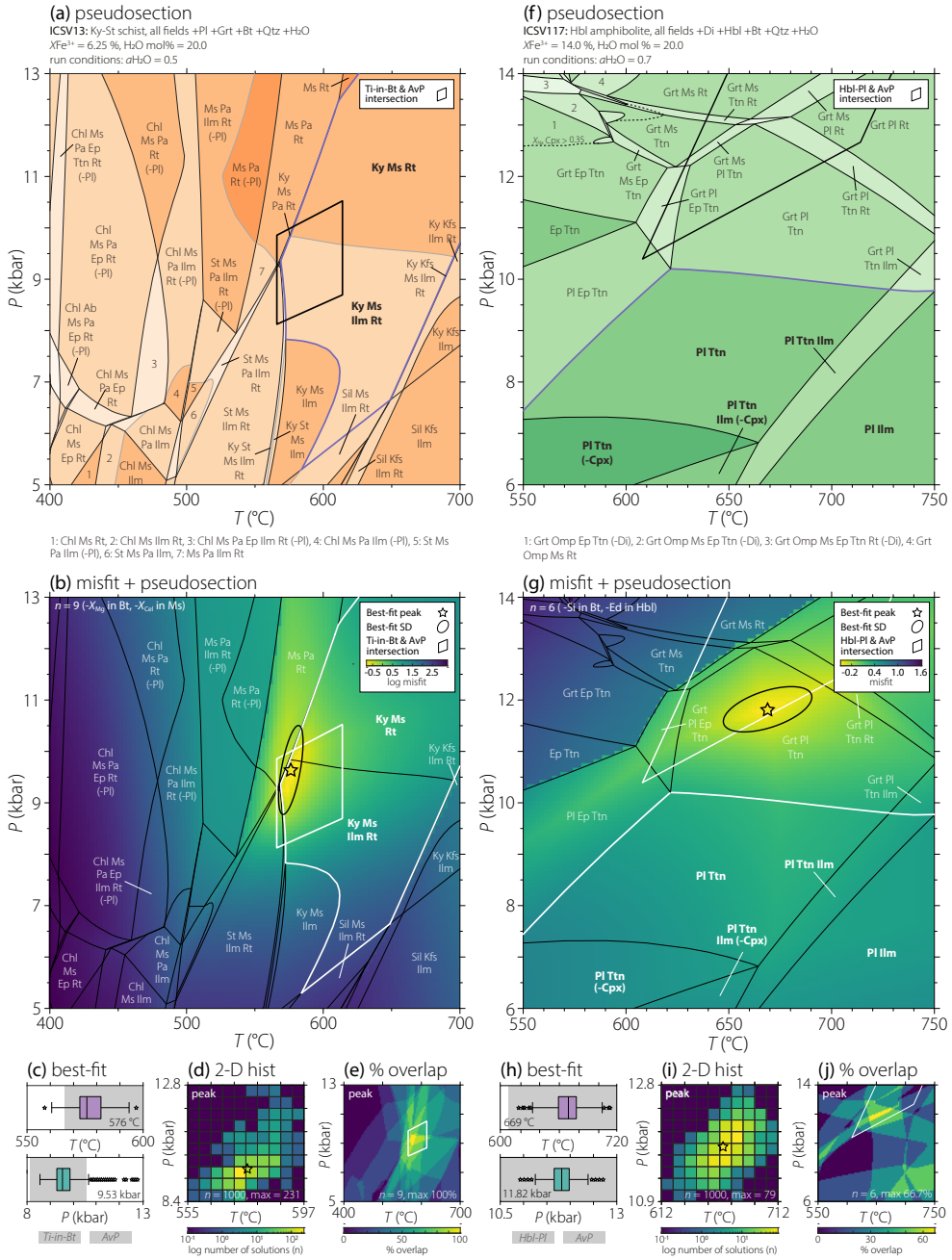

Fig. 3.5 Example of compiled final result of ICSV13 (a–e) and ICSV117 (f–j). (a, f) Pseudosection. (b, g) Heatmap (error-surface) of best-fit solutions showing the misfit of mineral composition variables, overlain with the corresponding pseudosection and the bootstrapped mean best-fit result and 1 σ uncertainty. (c, h) Boxplots of bootstrapped T and P estimates with the grey bar indicating the range of the selected thermometer and avP results. (d, i) Log-scaled 2D-histogram bin-plot of the bootstrapped data with mean best-fit result marked by the star. (e, j) % overlap of peak compositional isopleth fields.

pressure is poorly constrained owing to the dependence on the Ti-oxide phases to define the phase boundaries, which are avoided here as a primary P-T constraint (e.g., *Starr et al.*, 2020). Consequently, the broad range provided by the peak field in this

sample is well suited to applying the workflow to further constrain the conditions of metamorphism. Using the Ti-in-biotite geothermometer calibration of *Henry et al.* (2005), the temperature of metamorphism is estimated at 590 ± 24 °C, whereas pressure, determined using the avP function of THERMOCALC (*Powell and Holland*, 1994) at the matching temperature, is constrained to 9.3 ± 0.8 kbar (1 σ), in agreement with the peak assemblage field (Fig. 3.5A).

3.4.2.2 Grid-search inversion and uncertainty analysis

The inversion workflow was performed on a 100 x 100 grid in P-T space from 400–700 °C and 5–13 kbar with 1000 random sets of samples drawn from the mineral measurement data using bootstrap re-sampling assuming a normal distribution. The salient standard deviations and mean values for each mineral measurement variable are provided in Table 3.4.

Table 3.4 Variables used for parametric bootstrap resampling in ICSV13 and ICSV117 (rounded to 3 decimal places).

Mineral	**Garnet**				**Biotite**			**Muscovite**			**Plagioclase**	**Amphibole**			
Variable	X_{Grs}	X_{Sps}	X_{Prp}	X_{Mg}	Si	Ti	X_{Mg}	Si	X_{Cel}	X_{Pa}	X_{Ab}	Ts	Ed	Gln	Ti
ICSV13															
Mean	0.059	0.019	0.164	0.177	2.713	0.102	0.490	3.068	0.079	0.230	0.888				
SD	0.007	0.004	0.011	0.011	0.016	0.005	0.003	0.023	0.011	0.015	0.036				
ICSV117															
Mean					2.764	0.147	0.490				0.792	1.189	0.487	0.150	0.085
SD					0.005	0.009	0.015				0.012	0.034	0.028	0.010	0.012

Based on the interpreted peak mineral assemblage, the variables used for this analysis are X_{Gr}, X_{Sps}, X_{Prp}, X_{Mg} of garnet, Si, Ti, and X_{Mg} of biotite, Si, X_{Pa}, and X_{Cel} of muscovite, and X_{Ab} of plagioclase (see Table 3.1 for definitions). The P-T results are reported as median and IQR.

For the selected variables, the isopleth fields defined by the 2 σ population show broad agreement between the variables (Fig. 3.4A). The inversion found a best-fit solution of 576 °C (IQR 573–582 °C) and 9.53 kbar (IQR 9.28–9.85 kbar; Fig. 3.5C). This result and associated uncertainty show excellent agreement with the independent avP and Ti-in-biotite results (thermobarometer intersection) and the peak assemblage field (Fig. 3.5B). The residuals for each variable, showing the relationship between the normalised distribution of the observed data and the best-fit model prediction, are shown in Fig. 3.4D. Each of the mineral measurement variables shows strong agreement with the best-fit model, except X_{Mg} in biotite that was removed due to poor fit (X_{total} > 1), in addition X_{Cel} was also removed due to poor fit coupled with a sensitivity in excess of 2% of the mean. Both the temperature and pressure best-fit solution are particularly sensitive to the garnet composition. For example, the system has a ΔP of 0.76 kbar and 0.38 kbar for X_{Sps} and X_{Gr}, respectively (Table 3.5).

Table 3.5 Inversion output and diagnostics for ICSV13.

Variable	X_i	ΔT (°C)	ΔP (kbar)	$\mu_{obs} + 2\sigma$	$\mu_{obs} - 2\sigma$	Pred
X_{Grs}	0.08957	7.418	0.3735	0.0724	0.0459	0.0580
X_{Sps}	0.1844	7.849	0.7638	0.0266	0.0108	0.0202
X_{Prp}	0.9927	3.697	0.323	0.1857	0.1415	0.1855
X_{Mg} Grt	0.9063	3.726	0.3268	0.1992	0.1556	0.1972
Si Bt	0.5486	0.8295	0.1951	2.744	2.682	2.730
Ti Bt	0.6898	3.44	0.3789	0.1111	0.0929	0.0958
Si Ms	0.304	0.8295	0.1951	3.115	3.021	3.054
X_{Pa}	0.142	9.43	0.2775	0.2597	0.2006	0.2343
X_{Ab}	0.1607	3.301	3.301	0.9596	0.8155	0.8991
Mean = 577 ± 6 °C, 9.64 ± 0.57 kbar (1σ)						
Median = 576 °C (IQR = 573–582 °C), 9.53 kbar (IQR = 9.28–9.85 kbar)						
X_{total} (median) = 0.446						
SE (mean)= 2 °C (0.347 %), 0.19 kbar (1.99 %)						
# of fitted variables = 9/9						
Model resolution = 3.03 °C, 0.0808 kbar						
Bootstrap resamples = 1000						

3.4.3 ICSV117

3.4.3.1 Conventional methods of analysis

For the inferred equilibrium assemblage of hornblende-biotite-plagioclase-quartz-ilmenite-H_2O, a broad *P-T* zone of modeled peak assemblages show partial matches. Petrographic observations show that titanite growth dominantly post-dates ilmenite growth, however it is unclear whether titanite represents peak conditions or growth during decompression from peak conditions. In either scenario, the relationship of Ti-oxide phases is not reproduced in a clockwise *P-T* path on the modeled diagram, therefore as applied for ICSV13, the Ti-stability fields are not prioritised. Furthermore, the presence or absence of clinopyroxene is not deemed relevant to phase boundaries in clinopyroxene-absent assemblages owing to its predicted overstability in modeled metabasic systems (*Forshaw et al.*, 2019). Therefore, the high-pressure boundary of the matching peak assemblage fields is delimited by garnet and at lower temperatures by epidote stability. This zone extends for a greater range of temperatures than modeled (550–750 °C) and to lower pressures than modeled, but extends up to ~10.0 kbar (Fig. 3.5F). Using the Hornblende-Plagioclase exchange geothermometer calibration of *Holland and Blundy* (1994), the temperature of metamorphism is constrained to 644 ± 40 °C, and the pressure, using the avP function of THERMOCALC at the matching temperature, to a value of 13.6 ± 2.4 kbar (1 σ). The thermobarometer intersection shows no overlap with the peak assemblage field, temperatures are in agreement but pressures are in excess of ~10.0 kbar for avP results (Fig. 3.5F).

3.4.3.2 Grid-search inversion and uncertainty analysis

The inversion workflow was performed on a 100 x 100 grid in P-T space from 550–750 °C and 6–14 kbar with 1000 random sets of samples drawn from the mineral measurement data using bootstrap re-sampling assuming a normal distribution. The salient standard deviations and mean values for each observational variable are provided in Table 3.4. Based on the interpreted peak mineral assemblage, the variables used for this analysis include those found in pelitic compositions (Ti, Si and X_{Mg} of biotite and X_{Ab}) in addition to Ts (tschermakite, Al(T)-Na(A)-K(A)), Ed (edenite, Na(A)+K(A)), Gln (glaucophane, Na(M4)) vectors and Ti in amphibole (see Table 3.1 for full metabasic variables). The use of vectors in amphibole was deemed essential to reduce dependency of the result on overestimated (Al and A-site Na) or underestimated (Si, Ca and A-site K) cations (*Forshaw et al.*, 2019).

The mineral compositional variables produce a median best-fit solution at 669 °C (IQR = 659–677 °C) and 11.82 kbar (IQR = 11.66–11.98 kbar; Fig. 3.5G, H; Table 3.6), in agreement with the thermobarometer intersection but not the peak assemblage field. Si in biotite and the Ed vector were sequentially removed to produce an X_{total} below 1

Table 3.6 Inversion output and diagnostics for ICSV117.

Variable	$\mathbf{X_i}$	**ΔT (°C)**	**ΔP (kbar)**	$\mu_{\mathrm{obs}} + 2\sigma$	$\mu_{\mathrm{obs}} - 2\sigma$	**Pred**
Ti Bt	0.1017	29.22	0.4183	0.1650	0.1298	0.1492
X_{Mg} Bt	0.3689	9.136	0.1529	0.5210	0.4596	0.5016
X_{Ab}	1.481	1.689	0.001453	0.8162	0.7686	0.7572
Ts	1.727	1.689	0.001453	1.257	1.121	1.307
Gln	0.02863	6.099	0.4547	0.1697	0.1311	0.1499
Ti Amph	1.485	4.16	0.03779	0.1097	0.0597	0.0476
Mean = 669 ± 14 °C, 11.82 ± 0.29 kbar (1σ)						
Median = 669 °C (IQR = 659–677 °C), 11.82 kbar (IQR = 11.66–11.98 kbar)						
X_{total} (median) = 0.865						
SE (mean) = 6 °C (0.897 %), 0.12 kbar (1.02 %)						
# of fitted variables = 3/6						
Model resolution = 2.02 °C, 0.0808 kbar						
Bootstrap resamples = 1000						

(Table 3.6). The pressure of the result is largely defined by the shallow slope of X_{Mg}, X_{Ab}, Gln vector, (Fig. 3.5J), and was particularly sensitive to the values of the Gln vector and Ti in biotite, with ΔP values of 0.45 and 0.42 kbar, respectively. Although the Ti in biotite variable is relatively pressure insensitive, the value determines the intersection point with variables which are more pressure sensitive (i.e., sloping P-T gradients), and therefore has an important role to play in determining pressure (Fig. 3.5J).

The calculated *P-T* result lies within a garnet-bearing field, despite the absence of garnet in the observed assemblage (Fig. 3.5G). As previously outlined, the domain in which the misfit function is likely to find a best-fit solution reflects the phases presence or absence of phases used in the selected variables for the inversion. In this case, there is no penalty for garnet being predicted despite its absence in the interpreted equilibrium assemblage. Fixing the peak field would likely lead to little or no agreement between the selected variables within that domain (Fig. 3.5J). Three possible explanations for this discrepancy are considered. (1) The analyzed rock volume may include modally minor garnet. The lack of garnet observed within three-different observational scales (outcrop, hand sample, and thin-section scale), means this scenario is disregarded. (2) Disequilibrium processes: petrographic evidence shows that for the major assemblage chemical and textural equilibrium is dominant over the thin section-scale. Furthermore, the narrow uncertainty range of the best-fit solution and the lack of a multi-modal solution distribution (Fig. 3.5H, I) suggest the effect of disequilibrium is not significant across the analysed volumes. (3) Inaccuracies in the *a-X* solution models: for metabasic compositions there is negligible reported difference in predicted and observed modal abundances for garnet (*Forshaw et al.*, 2019), thereby making it unlikely that garnet is simply overstabilised for the modeled composition. Instead, the more significant issue likely arises from the errors in element partitioning between phases and the incorrect prediction of substitution vectors in the formulation of the *a-X* models. These decisions lead to to mismatches between predicted and observed values for amphibole and clinopyroxene. This inevitably impacts the whole assemblage, and the effect becomes more pronounced with higher modal abundances of these minerals. Given that amphibole is the modally dominant mineral in ICSV117, these mismatches create a cascading effect, impacting the predicted amphibole substitution vectors and other phase variables, such as Na content in plagioclase, both of which provide key constraints on the *P* of the best-fit solution. This also explains the overlap of the best-fit result with the independent thermobarometer intersection, as well as the deviation of the calculated *P-T* result from the peak assemblage field. In this case, the latter scenario is favoured.

3.5 Synthetics

The grid-search inversion and bootstrap resampling is now employed on the worldwide median pelite composition of *Forshaw and Pattison* (2023) to provide a generalized estimate of uncertainty across sub-solidus *P-T* space. In an inversion method such as this—assuming the method itself is inerrant and there is no model uncertainty—uncertainties in the inverse solution arise from the uncertainties in input data and/or the forward model predictions. To explore these uncertainties, we follow the framework outlined in Fig. 3.1 and consider three different sources of observational uncertainty, each influencing the inverse solution in a distinct way. (1) Mineral Measurement

Uncertainty (MMU)—uncertainty in the input data used to constrain the inverse solution (phase compositions and/or phase modal volumes). Here, the data is varied while the forward model remains fixed. (2) Bulk Composition Uncertainty (BCU)—uncertainty in the forward model predictions, propagated from uncertainty in the modeled bulk composition. In this case, the forward model is varied while the input data remains fixed. (3) Observational Uncertainty (OU)—the combined effects of both MMU and BCU, where both the input data and forward model predictions are varied simultaneously. To evaluate these uncertainties, the inverse solution is constrained using three different types of input data (a) mineral compositions only, (b) mineral modal volumes only, and (c) a combination of mineral compositions and modal volumes. This framework, allows us to assess how the impact of each uncertainty source varies across P-T space and in relationship to the different types of input data.

The variables of interest include X_{Gr}, X_{Prp} and X_{Sps} of garnet, Ti, Si and X_{Mg} of biotite, X_{Cel}, X_{Pa} and Si of muscovite, X_{Ab} of plagioclase, X_{San} of K-feldspar, X_{Mg} of chlorite, X_{Mg} of staurolite, X_{Mg} of cordierite, and X_{Fe} of epidote (see Table 3.1 for definitions). The modal volume of each of the aforementioned phases is also used for this analysis, as well as the modal volume of the three Al_2SiO_5 polymorphs, quartz, and titanite. All uncertainty measurements are calculated as one standard deviation. Where uncertainties are given for a range of pressure or temperature conditions, these are median values of the distribution of standard deviation measurements.

For each setup, forward models were created between 350–750 °C and 0.001–13 kbar for the worldwide median pelite composition in THERIAK-DOMINO (*de Capitani and Brown*, 1987; *de Capitani and Petrakakis*, 2010). This analysis does not consider the impact of varying model uncertainty. Instead, the analysis is performed using a fixed set of models, the details of which are outlined in Appendix B. In each case the system was saturated with 30 mol % of pure H_2O. To ensure the uncertainty of P-T points around the boundary of the model was not artificially decreased, the results were only considered between 1–12 kbar and 400–700 °C. The solution uncertainties for each uncertainty sources are displayed in Fig.s 3.6,3.7, and 3.8, respectively, with the biotite-, garnet-, and porphyroblast(cordierite/andalusite/staurolite/kyanite)-in lines overlaid on each plot.

3.5.1 The impact of mineral measurement uncertainty, *MMU*

For this analysis, the bulk-rock $X_{\mathrm{Fe^{3+}}}$ was fixed at 0.1, and the forward model was created over a 100 x 100 grid. Two-hundred synthetic mineral measurement datasets for each point on the P-T grid were constructed by bootstrap resampling. The value of each variable in these datasets was selected by repeated sampling of a normal distribution using the mean of the predicted data and a standard deviation equivalent to 10 % of the mean. The value of 10 % (for 1 σ) was chosen following the highest uncertainty value

estimated by *Palin et al.* (2016). The best-fit *P-T* solution was found for each of the 200 synthetic datasets generated at each *P-T* point. The spread in these 200 best-fit solutions, measured using the standard deviation, quantifies the uncertainty at each *P-T* point in the grid. The solution uncertainty for each variable type is shown in Fig. 3.6A–F. The median uncertainty over the modeled *P-T* space is shown in Fig. 3.6G, H.

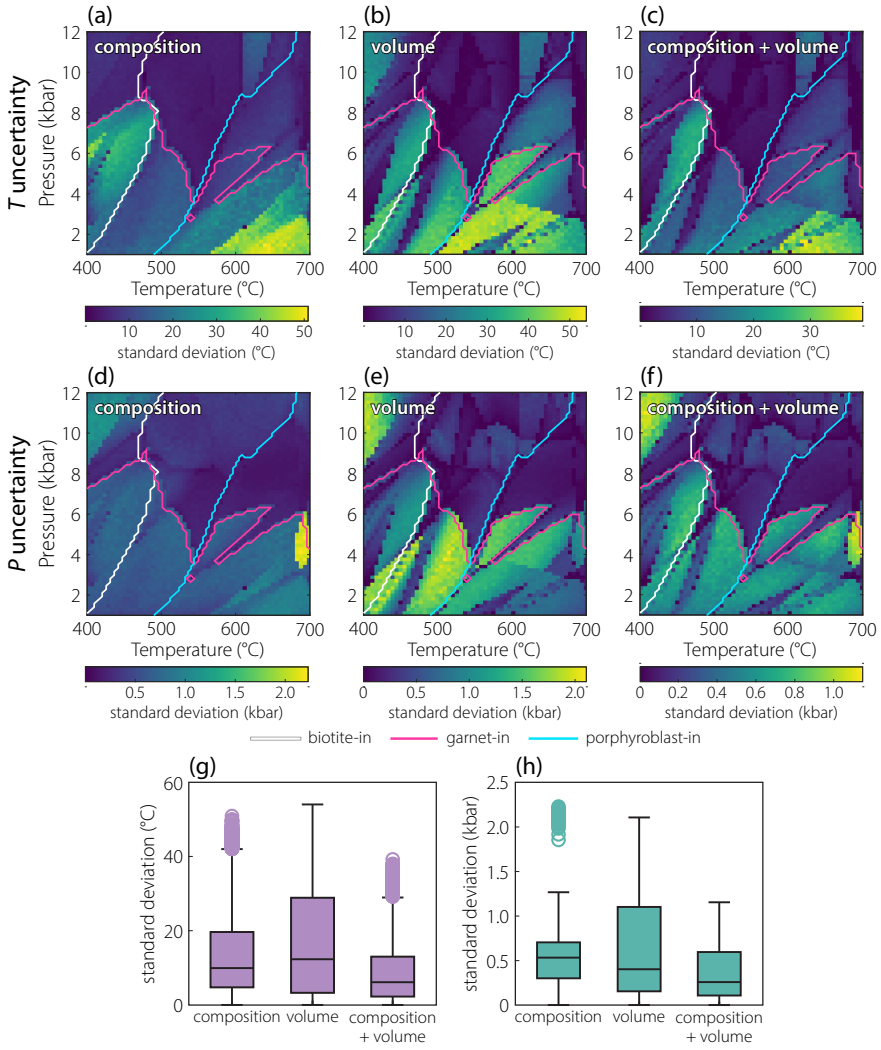

Fig. 3.6 Uncertainty (1 σ) in *P-T* estimate as a result of mineral measurement uncertainty (*MMU*). (a) Uncertainty in T using composition variables. (b) Uncertainty in P using composition variables. (c) Uncertainty in T using modal volume variables. (d) Uncertainty in P using modal volume variables. (e) Uncertainty in T using both composition and modal volume variables. (f) Uncertainty in P using both composition and modal volume variables. (g) The distribution of T uncertainty over modeled *P-T* space. (h) The distribution of P uncertainty over modeled *P-T* space. Composition relates to composition variables only. Volume relates to modal volume variables only. Combined relates to composition and modal volume variables together. Bt = biotite, Grt = garnet, and Porph = porphyroblast (cordierite/andalusite/staurolite/kyanite).

Using composition variables only, the temperature uncertainty is 9 °C, compared to 12 °C for modal volume variables only (Fig. 3.6G). When these two variable types are

combined, the uncertainty drops to 6 °C (Fig. 3.6G). This demonstrates the importance of determinacy: a greater number of variables often leads to a lower solution uncertainty. The same is true for pressure uncertainty: 0.7 kbar and 0.4 kbar using the composition and modal volume datasets, respectively, which decreases to a 0.2 kbar uncertainty when the composition and modal volume datasets are combined (Fig. 3.6H). The uncertainty is significantly controlled by the phase assemblage. For example, the temperature uncertainty, using composition and modal volume variables together, decreases from 13 °C to 3 °C where garnet is present in the assemblage.

3.5.2 The impact of bulk composition uncertainty, *BCU*

To assess the impact of *BCU*, a Monte-Carlo simulation was performed to create 100 random variations of the worldwide median pelite composition. Each oxide was varied at the same time and then re-normalized. The weight percentage of each oxide and the bulk $X_{Fe^{3+}}$ was allowed to vary within an amount characteristic of a natural assemblage following the example used in *Palin et al.* (2016) (see Table 3.7). In this scenario, the bulk composition is treated as if it were a total bulk derived via XRF. The reasons why it may not be applicable to other methods of deriving bulk composition is covered in Section 3.6.1.1.

Table 3.7 Standard deviation of each oxide mol% applied to the worldwide median pelite bulk composition used in the Monte-Carlo simulation.

Oxide	**SiO_2**	**TiO_2**	**Al_2O_3**	**FeO**	**O**	**MnO**	**MgO**	**CaO**	**Na_2O**	**K_2O**
Mean	57.00	0.61	10.29	4.58	0.25	0.06	3.19	0.62	1.19	2.24
SD	0.52	0.09	0.26	0.46	0.02	0.02	0.22	0.24	0.12	0.15

Forward models were created for each of the 100 bulk compositions in a 75 x 75 grid. The range of these models therefore represent the uncertainty in the forward model predicted data from the variation of the bulk composition. The "true" bulk composition is assumed to lie within this model distribution. The synthetic input data, defined for the previously outlined variables, was constructed at each *P-T* point within the 75 x 75 grid using the recorded composition of the worldwide median pelite. The synthetic data were then passed through a grid-search routine for each of the 100 forward models, and the spread of the best-fit *P-T* solutions was analysed. The solution uncertainty for each variable type is shown in Fig. 3.7A–F and the median uncertainty over the modeled *P-T* space is shown in Fig. 3.7G, H.

The difference between the composition variables and the modal volume variables are larger for *BCU* than for *MMU*. For temperature, the use of composition variables results in an uncertainty of 11 °C, whereas the modal volume variables result in an uncertainty of 35 °C (Fig. 3.7G). This pattern is also observed in the pressure domain,

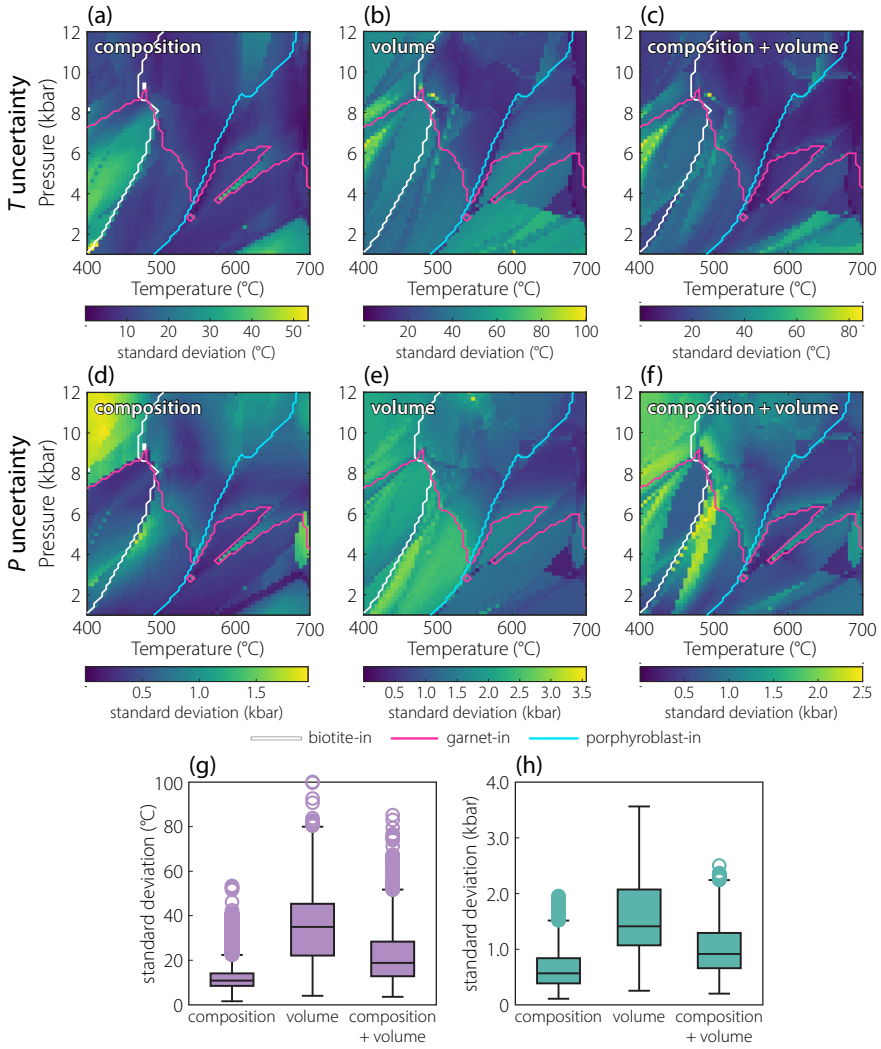

Fig. 3.7 Uncertainty (1 σ) in P-T estimate as a result of bulk composition uncertainty (BCU). (a) Uncertainty in T using composition variables. (b) Uncertainty in P using composition variables. (c) Uncertainty in T using modal volume variables. (d) Uncertainty in P using modal volume variables. (e) Uncertainty in T using both composition and modal volume variables. (f) Uncertainty in P using both composition and modal volume variables. (g) The distribution of T uncertainty over modeled P-T space. (h) The distribution of P uncertainty over modeled P-T space. Composition = composition variables only. Volume = modal volume variables only. Combined = composition and modal volume variables together. Bt = biotite, Grt = garnet, and Porph = porphyroblast (cordierite/andalusite/staurolite/kyanite).

with an increase in from 0.6 kbar to 1.4 kbar when modal volume variables are used (Fig. 3.7H). The P-T uncertainty derived from BCU, using composition and modal volume variables together, is 19 °C and 0.9 kbar.

3.5.3 The impact of observational uncertainty, *OU*

The impact of OU (which comprises both BCU and MMU) was examined using a combined approach of the sample bootstrapping and the Monte-Carlo variation in bulk composition. Two-hundred synthetic observation datasets for each point on the P-T grid were constructed for each variable via repeated sampling of a normal distribution with a standard deviation set to 10 % of the mean. The forward modeled data from the worldwide median pelite served as the sample mean for the resampling distribution. A bulk composition was then randomly selected from the 100 available forward models for each of the 200 bootstrap resamples. A grid-search inversion was then applied to calculate the best-fit solution for each of the 200 re-sampled datasets at each P-T point. The spread of the best-fit solutions therefore represents the P-T uncertainty introduced by both MMU and BCU. The solution uncertainty for each variable type is shown in Fig. 3.8A–F and the median uncertainty over the modeled P-T space is shown in Fig. 3.8G, H.

Using composition variables produces a lower temperature and pressure uncertainty (16 °C, 0.7 kbar) than for modal volume variables alone (36 °C, 1.4 kbar; Fig. 3.8G, H). The temperature uncertainty using composition and modal volume variables together is 21 °C and the pressure uncertainty is 1.0 kbar (Fig. 3.8G, H). When using the composition and the modal volume variables together, the addition of biotite to the stable assemblage increases pressure and temperature uncertainty by 27 % and 44 % respectively. The presence of garnet in the equilibrium phase assemblage also has a significant impact on the temperature uncertainty (28 °C garnet absent, 14 °C garnet present) but a negligible impact on pressure uncertainty (0.9 kbar garnet absent, 1.0 kbar garnet present).

3.5.4 The impact of uncertainty source and variable type across P-T space

The results from the analyses in Section 3.5.1, Section 3.5.2, and Section 3.5.3 have been binned into different domains (Fig. 3.9; **??**) to compare the impact of the uncertainty source and the variable type on the solution uncertainty across P-T space. The “chl/bt”, “grt”, “porph”, and “sil” denote metamorphic zones—respectively, the chlorite/biotite zone (temperatures up to 425 °C), garnet zone (425–550 °C), porphyroblast zone (comprising cordierite/andalusite/staurolite/kyanite, 550–625 °C), and sillimanite zone (625–700 °C). In contrast, “crd”, “st”, and “ky” define the pressure-dependent facies series: the cordierite series (cordierite–andalusite–sillimanite, 0–3.5 kbar), the staurolite series (staurolite–andalusite–sillimanite, 3.5–6.5 kbar), and the kyanite series (staurolite–kyanite–sillimanite, above 6.5 kbar). The distribution of these metamorphic zones and facies series is illustrated in Fig. B.3. The temperature and pressure ranges do not strictly denote the stability of the aforementioned minerals, and should therefore be used solely to inform the broader changes in metamorphic grade.

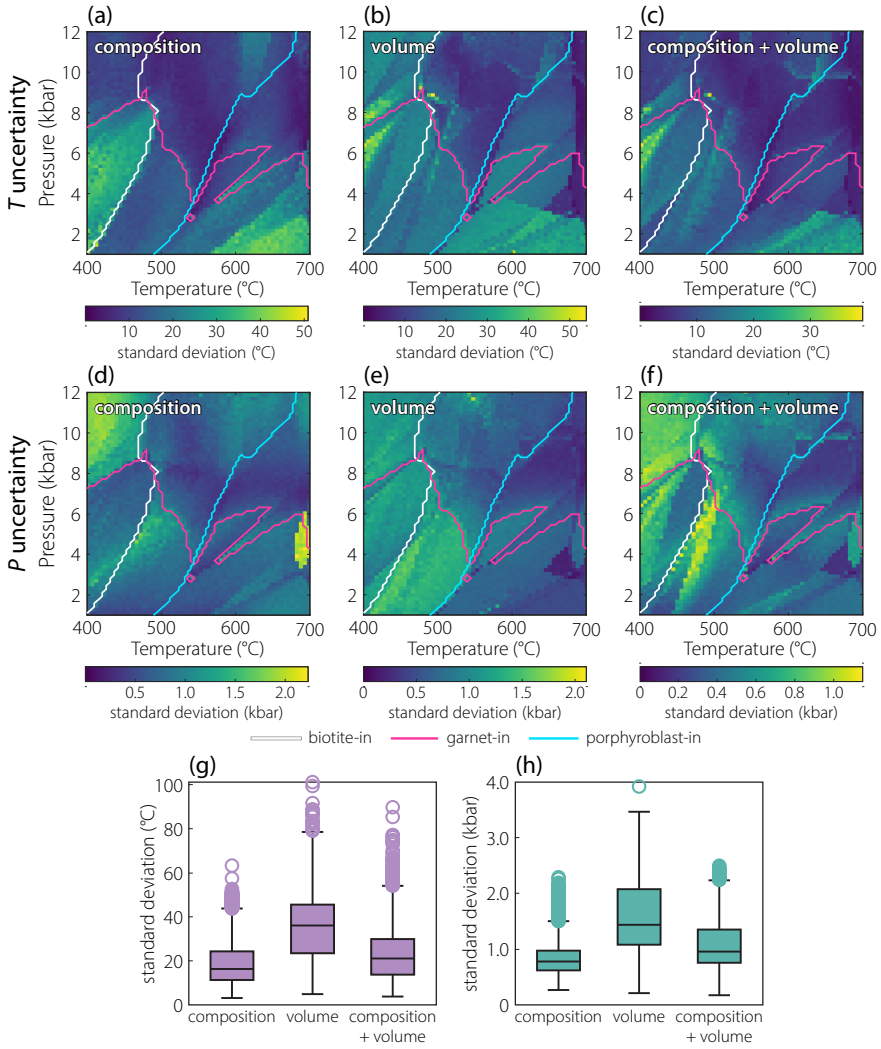

Fig. 3.8 Uncertainty (1 σ) in P-T estimate as a result of observational uncertainty (OU, mineral measurement uncertainty and bulk composition uncertainty combined). (a) Uncertainty in T using composition variables. (b) Uncertainty in P using composition variables. (c) Uncertainty in T using modal volume variables. (d) Uncertainty in P using modal volume variables. (e) Uncertainty in T using both composition and modal volume variables. (f) Uncertainty in P using both composition and modal volume variables. (g) The distribution of T uncertainty over modeled P-T space. Composition relates to composition variables only. Volume relates to modal volume variables only. (h) The distribution of P uncertainty over modeled P-T space. Composition = composition variables only. Volume = modal volume variables only. Combined = composition and modal volume variables together. Bt = biotite, Grt = garnet, and Porph = porphyroblast (cordierite/andalusite/staurolite/kyanite).

Using composition variables, the uncertainty in both temperature and pressure derived from OU decreases from the biotite zone to the porphyroblast zone and then minorly increases from the porphyroblast zone into the sillimanite zone (Fig. 3.9A, D).

For example, the pressure uncertainty shows the following trend: 1.0 kbar (biotite zone), 0.8 kbar (garnet zone), 0.7 kbar (porphyroblast zone) and 0.8 kbar (sillimanite

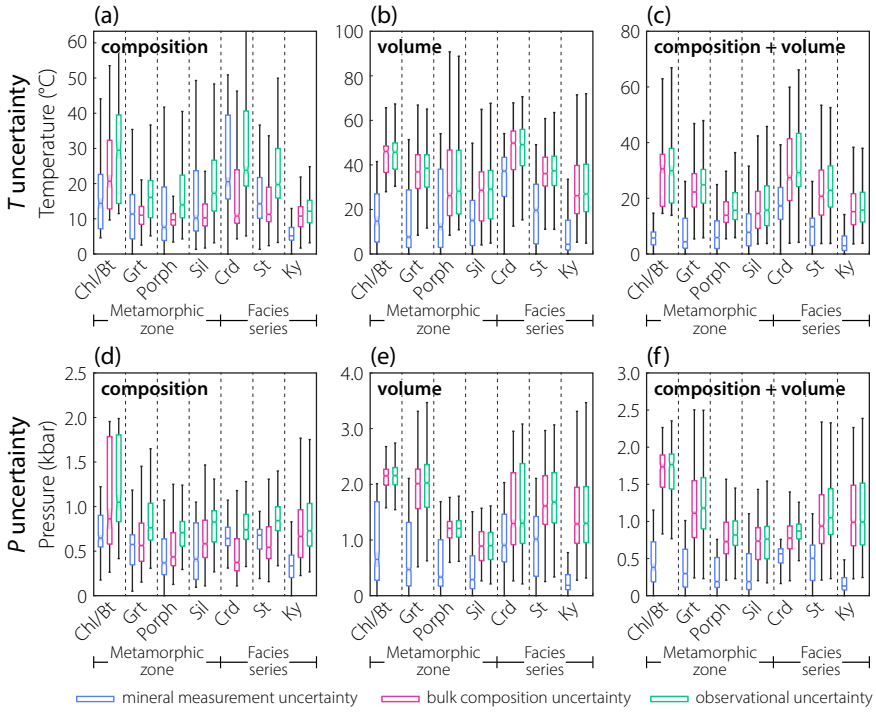

Fig. 3.9 The distribution of uncertainty in T and P binned into different metamorphic zones and facies series. (a) T uncertainty only using composition variables. (b) P uncertainty only using composition variables. (c) T uncertainty only using modal volume variables. (d) P uncertainty only using modal volume variables. (e) T uncertainty using both composition and modal volume variables. (f) P uncertainty using both composition and modal volume variables.

zone). This pattern is mirrored when using *MMU* and *BCU* separately, with the *BCU* producing the higher uncertainty of the two. This is notable in the chlorite/biotite zone, where accounting for *BCU* produces uncertainties of 21 °C and 0.9 kbar, compared to *MMU*, which produces an uncertainties of 14 °C and 0.6 kbar. For *OU*, temperature uncertainty decreases with increasing pressure conditions from the cordierite series to the kyanite series. This is largely driven by effects of *MMU*, for which the temperature uncertainty decreases significantly between the two series (21 °C, 14 °C, and 5 °C, respectively) whereas the temperature uncertainty attributed to *BCU* is largely constant. For *OU*, pressure uncertainty varies between 0.7—0.8 kbar. From lower to higher facies series, the pressure uncertainty derived from *MMU* decreases, but increases for *BCU* .

When only using modal volume variables, the most notable trend is the low solution uncertainties derived from *MMU*, relative to the higher uncertainties derived when applying *BCU* (Fig. 3.9B, E). This discrepancy is present across all metamorphic zones and facies series. For example, in the garnet zone the uncertainty derived from *MMU* is 8 °C and 0.5 kbar compared to the uncertainty from *BCU* of 37 °C and 2.0 kbar. In the kyanite series, the uncertainty for the *MMU* approach is 4 °C and 0.2 kbar compared to the uncertainty for the *BCU* approach of 26 °C and 1.3 kbar. For *BCU*, the calculated temperature and pressure uncertainty decreases with increasing metamorphic grade and

facies series. The uncertainty in the biotite zone is 46 °C and 2.1 kbar compared to 15 °C and 0.9 kbar in the sillimanite zone. The exception to this is the transition from the cordierite series to the kyanite series.

When the mineral composition and modal volume variables are used together, the calculated uncertainties show a similar pattern to that of the modal volume-only results (Fig. 3.9C, F), suggesting uncertainty in modal volumes has the largest impact on the uncertainty in estimated *P-T* conditions. *BCU* produces decreasing pressure and temperature uncertainties moving from lower to higher metamorphic zone and facies series. This is also observed for uncertainties derived from *OU*: in the biotite zone, the uncertainty is 30 °C and 1.8 kbar, whereas the porphyroblast zone has an uncertainty of 16 °C and 0.8 kbar. An exception to this pattern is the facies series, which shows the expected decrease in temperature uncertainty but a modest increase in pressure uncertainty from lower to higher facies. When accounting for *OU*, the cordierite series has an uncertainty of 29 °C and 0.9 kbar, whereas the kyanite series has an uncertainty of 16 °C and 1.0 kbar.

It is also worth noting the relative magnitude of the uncertainties when using composition variables compared to using modal volume variables. Each metamorphic zone and facies series shows an increased uncertainty when using modal volume variables in comparison to composition variables and is irrelevant of the uncertainties applied to the inversion calculation (*MMU*, *BCU*, or *OU*). In the garnet zone, the *OU* when using composition variables is 16 °C and 0.7 kbar (Fig. 3.9A, D) in contrast to 38 °C and 2.0 kbar when modal volume variables are used (Fig. 3.9B, E). In the porphyroblast zone, the uncertainty is 14 °C and 0.7 kbar when using composition variables, in comparison to 28 °C and 1.2 kbar when using modal volume variables. In the cordierite series, there is an uncertainty of 24 °C and 0.7 kbar when using composition variables, compared to 49 °C and 1.3 kbar when using modal volume variables. Across the total modeled *P-T* space modal volume variables approximately double the uncertainty of composition variables (220 % higher T uncertainty and 185 % higher P uncertainty; Fig. 3.8).

The impact of *MMU*, *BCU*, and *OU* for temperature and pressure uncertainties has also been quantified for each individual composition and modal volume variable (Fig. 3.10). The resulting uncertainties vary quite significantly between those associated with different phases and even between different composition variables from the same phase. For example, the behaviour of the four garnet variables (X_{Alm}, X_{Prp}, X_{Grs}, X_{Sps}) is relatively varied. X_{Prp} shows the lowest temperature uncertainty of the four, with a *OU* temperature uncertainty of 32 °C. X_{Alm} is particularly sensitive to *MMU* relative to *BCU*, with temperature uncertainties of 81 °C and 60 °C, respectively. Given almandine is commonly the largest mole fraction in a constant-sum composition, variation from other phase components more strongly influence the absolute value (*Kohn and Spear*, 1991b; *Waters*, 2019). For the composition variables, uncertainties from *MMU* are slightly higher than those derived from *BCU*. For example, *MMU* for X_{Ab} in

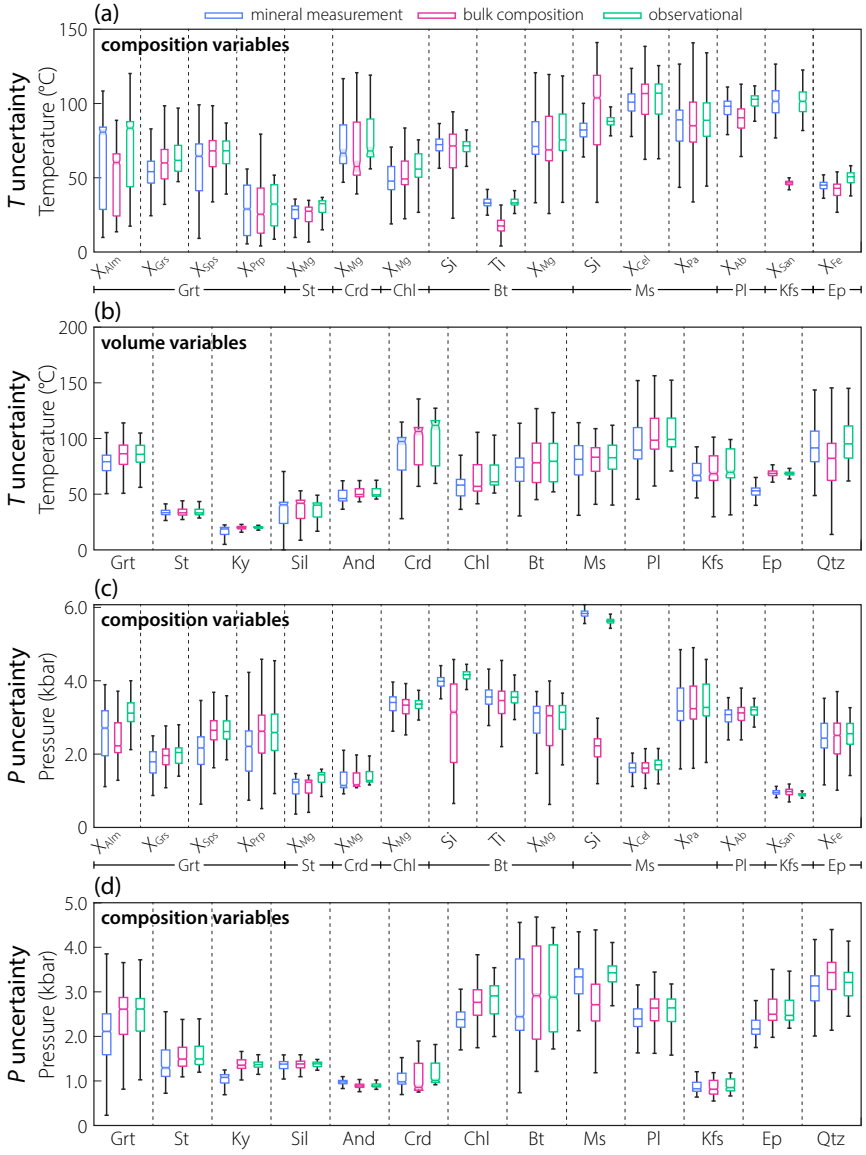

Fig. 3.10 The uncertainty in T and P for each variable as a result of mineral measurement uncertainty (MMU), bulk composition uncertainty (BCU), and observational uncertainty (OU, MMU and textitBCU combined). (a) T uncertainty for composition variables. (b) P uncertainty for composition variables. (c) T uncertainty for modal volume variables. (d) P uncertainty for modal volume variables.

plagioclase results in a temperature uncertainty of 98 °C, compared to 90 °C for BCU. Indeed, some variables show a significant lack of sensitivity to BCU. For example, Ti in biotite has a temperature uncertainty of only 17 °C for BCU. However, some are notably more sensitive, for example X_{Mg} in biotite has a temperature uncertainty of 69 °C. Finally, the modal volume variables for the Al-rich phases (staurolite, kyanite, sillimanite, and andalusite) can be used to constrain the calculated temperature and pressure conditions with low uncertainties across any uncertainty approach applied to the inversion. However, it should be noted that the low uncertainty displayed by kyanite (20 °C) is likely an artifact of the model limits and/or nature of the worldwide

pelite composition, for which kyanite only joins the assemblage at high P-T conditions. The modal volume of cordierite and K-feldspar are also notable for their low pressure uncertainties of 1.0 and 0.8 kbar (OU), yet higher temperature uncertainties of 112 and 70 °C (OU), respectively.

3.5.5 A comparison between uncertainty sources along a geotherm

The effects of *MMU*, *BCU*, and OU were also examined at 75 points along a typical continental-crust geotherm from *Copley and Weller* (2022). The distribution of this geotherm is shown in Fig. B.4. Bootstrap re-sampling (*MMU*) was performed on mineral measurements at 10 % and 20 % of the mean values predicted by the forward models. The *BCU* analysis was performed using the Monte-Carlo approach as outlined in Section 3.5.2, and the OU analysis was performed combing the above approaches, using bootstrapping at 10 % of the mean. The results of this analysis are presented in Fig. 3.11.

For the composition variables, the OU is dominantly controlled by the effects of the *BCU* (Fig. 3.11A, D). For example, before biotite becomes part of the stable assemblage, the temperature uncertainty derived from *BCU* exceeds that from the 10 % bootstrapped *MMU*. This is also consistent after garnet joins the assemblage, but prior to growth of staurolite. At chlorite-grade conditions, pressure uncertainty derived from *MMU* exceeds that from *BCU*. However, once biotite joins the stable assemblage, the pressure uncertainty derived from *BCU* is consistently greater than that from the 10 % bootstrapped *MMU*. Notably, P-T uncertainties from the 20 % bootstrapped *MMU* exceed those from OU at all points along the geotherm, suggesting that when relying solely on compositional variables, a high bootstrap threshold may be sufficient to estimate the "total" OU without requiring Monte Carlo bulk composition analysis.

When using modal volume variables alone, the P and T uncertainties derived from *BCU* are consistently in excess of the uncertainty from the 10 % bootstrapped *MMU*, and near consistently greater than the 20 % bootstrapped *MMU* (Fig. 3.11B, E). The bootstrapping on mineral measurements at 20 % is therefore unable to account for uncertainty in the bulk composition. This is particularly true near phase boundaries (e.g., biotite-in and staurolite-in), where the P and T uncertainties derived from the *MMU* are significantly lower than that derived from the *BCU*.

Where both mineral composition and volume variables are used, the trend of P and T uncertainties derived from *MMU* and *BCU* is often directly opposing across the modeled geotherm (Fig. 3.11C, F). The combined OU more closely follows the trend of the *BCU*, again suggesting the overall uncertainty stemming from the observations is most strongly impacted by *BCU* rather than *BCU*. P and T uncertainties shows a marked increase at biotite-in with another marked decrease at garnet-in. The addition of staurolite results in a minor increase in temperature uncertainty, but appears to

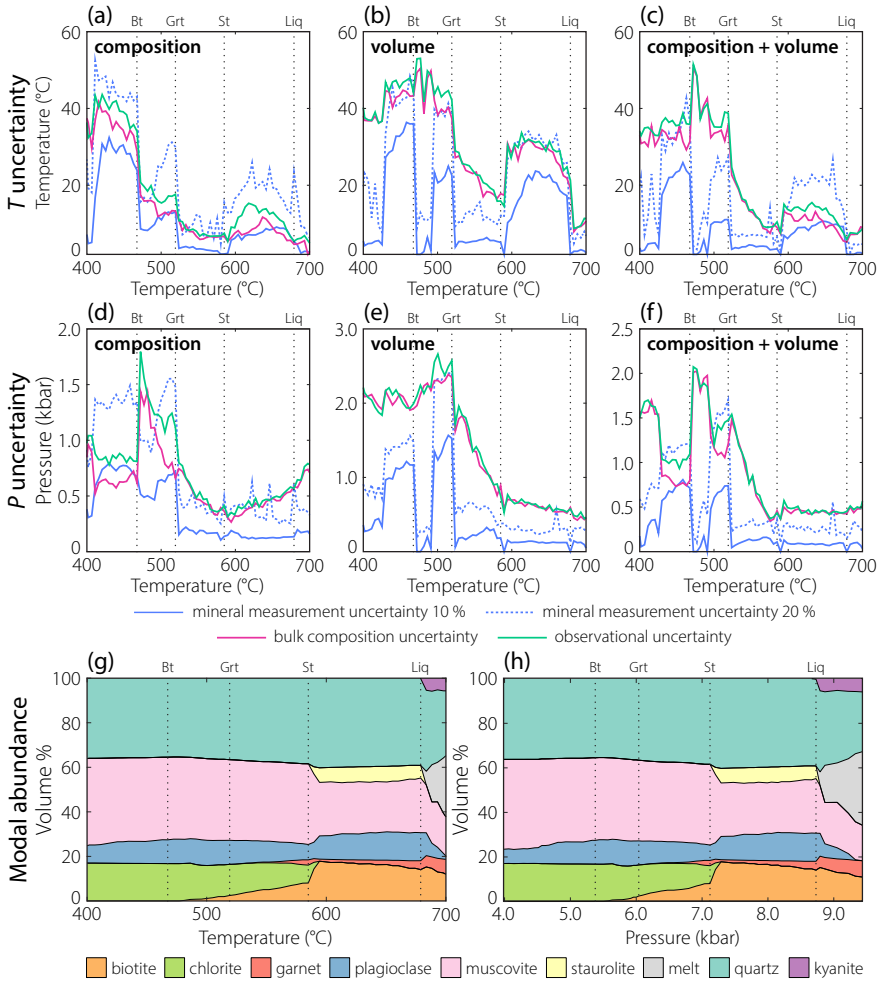

Fig. 3.11 The change of uncertainty in T and P along a geotherm as a result of mineral measurement uncertainty (MMU) at 10 % of the mean, MMU at 20 % of the mean, bulk composition uncertainty (BCU), and observational uncertainty (OU, a combination of MMU at 10 % of the mean and BCU). (a) Uncertainty in T using composition variables. (b) Uncertainty in T using modal volume variables. (c) Uncertainty in T using both composition and modal volume variables. (d) Uncertainty in P using composition variables. (e) Uncertainty in P using modal volume variables. (f) Uncertainty in P using both composition and modal volume variables. (g, h) Modal abundance of phases along the geotherm.

stabilise pressure uncertainty as the geotherm progresses to higher-grade conditions (Fig. 3.11C, F). As in previous sections, the results demonstrate that calculated uncertainties vary significantly across P-T space, as does the relative importance of MMU and BCU.

3.6 Discussion

The techniques used to examine the P-T evolution of metamorphic sequences have made considerable advances over recent decades. Despite a long-standing appreciation of the importance of uncertainty in P-T analyses (e.g., *Hodges and McKenna*, 1987;

Powell and Holland, 1988, 1994; *Kohn and Spear*, 1991a,b; *Worley and Powell*, 2000; *Powell and Holland*, 2008; *Palin et al.*, 2016), the majority of studies employ qualitative comparisons between predicted and observed phase information without accounting for, or quantifying, uncertainty within the system. Therefore, this discussion evaluates (1) the relative impact of different uncertainty sources and variable types on inverse solution uncertainties, (2) explores systematic controls on uncertainty in natural systems, (3) compares our results to previous uncertainty estimates, and (4) examines the benefits and limitations of the new grid-search inversion technique for metamorphic studies.

3.6.1 Uncertainty estimates in pelitic systems

The data presented in this study demonstrate that both mineral measurement uncertainty and bulk composition uncertainty can have a significant impact on *P-T* estimates, and that the magnitude of the impact varies with *P-T* grade and the type of observational variables used in the inversion (mineral composition, mineral modal volume, or both).

3.6.1.1 The impact of uncertainty source

Bootstrapping of mineral measurements (mineral measurement uncertainty) at an appropriate percentage (σ = mean × ~20%) and using solely mineral composition variables will generally account for the total observational uncertainty (e.g., Fig. 3.11A, D). However, when applying mineral measurement uncertainty using mineral modal volume variables the pressure and temperature uncertainties locally drop to zero or near-zero at phase boundaries (Fig. 3.11B, C, E, F). These pressure and temperature uncertainties show that bulk composition uncertainty has a significant impact on pseudosection topology (e.g., *Stuwe*, 1997; *Guevara and Caddick*, 2016; *Palin et al.*, 2016; *Lanari and Engi*, 2017). Therefore, when using modal volume variables near phase stability boundaries, bulk composition uncertainty should be accounted for in order to constrain a solution uncertainty that characterizes the total observational uncertainty in the system.

It should be noted that the impact of the uncertainty in bulk composition depends on how the bulk composition was measured (e.g., total vs effective) and what type of variables are used for the inversion. The effective (also termed reactive) bulk composition can be calculated from the observed phase assemblage by using the measured oxide composition of each phase (X_{ij}) in equilibrium within the assemblage and the observed modal abundance of each phase (v_j; Equation 3.8).

$$X_i^{bulk} = \sum_{j=1}^{p} X_{ij} \cdot v_j \tag{3.8}$$

Where X_i^{bulk} is the bulk composition of the rock, with a weight percent for each oxide (i). There are a total of p phases in the rock. Assuming that the phase compositions (X_{ij}) are well known, then the only source of uncertainty in the calculated bulk composition is the phase abundance (v_j). In this case, assuming an equilibrium scenario (a single P-T point) and no model uncertainty, the uncertainty in the bulk composition has no impact on the predicted phase compositions and assemblages (see Model 2A in **?**). In this case, the use of phase compositions for the inversion are significantly preferred to phase abundance (modal volumes). However, if there is significant uncertainty in the observed phase composition, equilibrium assemblage, and/or thermodynamic models (as is likely when investigating a natural system), then this will propagate through to uncertainty in both the predicted phase modal volume and phase composition. In this case, including mineral modal volumes in conjunction with other variables may aid in stabilising the complex non-linear nature of P-T analysis. The scenario outlined here does not apply if P–T conditions change, as is the case for a pseudosection, as the position of many reactions is controlled by the effective bulk composition (*Palin et al.*, 2016; *Lanari and Duesterhoeft*, 2019). If the bulk composition has been derived by XRF (total bulk composition), it represents the overall oxide abundances measured independently from observed phase composition and modal volume. This is the type of bulk composition measurement simulated in Section 3.5.2 of this study, and was shown to have a clear impact on the uncertainty in the predicted composition and modal volumes of phases throughout P-T space.

3.6.1.2 The impact of variable type

Using mineral composition variables generally produces lower median pressure and temperature uncertainties than using modal volume variables (Fig.s 3.6, 3.7, and 3.8). Each mineral composition and modal volume variable shows distinct sensitivity to uncertainties in mineral measurements and bulk composition (Fig. 3.10). Broadly mineral composition variables are notably less sensitive to bulk composition than mineral modal volumes or phase stability boundaries. This makes mineral composition variables valuable tools for calculating P-T estimates, providing constraints that are less dependent on one of the largest sources of uncertainty within modelling (bulk rock composition; Fig. 3.10). For example, Ti in biotite is relatively insensitive to bulk composition uncertainty (1 σ = 17 °C), which aligns with natural observations where systematic Ti variations correlate with metamorphic grade despite variation in bulk rock composition (*Henry and Guidotti*, 2002). However, a notable exception is that the X_{Mg} of biotite (1 σ = 69 °C, from bulk composition uncertainty). Therefore, although the calibration of the Ti-X_{Mg} relationship is based on a natural dataset (*Henry et al.*, 2005), and although a-X models may not perfectly reproduce the natural system (e.g., *Guevara and Caddick*, 2016; *Kendrick and Indares*, 2018; *Waters*, 2019; *Gervais and Trapy*,

2021), the variation of calculated temperatures from the thermometer will likely reflect not only metamorphic grade but also the significant influence of bulk composition.

Given the differing *P-T* uncertainty associated with the variables it may be tempting to select those that produce the most certain solution. The use of pseudosection stability fields combined with preferential isopleth or isomodes can offer impressively precise results *P-T* estimates (Fig. 3.2). However, in order to provide an estimate of both the *P-T* conditions and associated uncertainty that is representative of the modeled system, the widest and most diverse possible range of robust variables should be incorporated during the inversion (whilst allowing for a degree of freedom). Care must be taken to exclude variables with significant model error, as these may degrade the result (*Powell and Holland*, 2008), though as the L1-norm function is robust to outliers (*Claerbout and Muir*, 1973), the impact of this should be lessened. This approach enables an assessment of the overall model performance, which may provide insights into other characteristics of the system such as the degree of equilibrium.

3.6.1.3 The impact of metamorphic grade

The "total" observational uncertainty (derived from OU using both mineral composition and modal volume variables) was found to vary across *P-T* space (Table 3.8), with a particular difference between the lower-temperature biotite and garnet zone (1 σ = 25–30 °C, 1.2–1.8 kbar) and the higher-temperature porphyroblast and sillimanite zone (1 σ = 16 °C, 0.8 kbar). The lowest-grade conditions therefore exhibit approximately

Table 3.8 Median temperature and pressure uncertainty across different metamorphic zones and facies series. "C" is composition variables. "V" is modal volume variables.

		Median T uncertainty (1 σ, °C)			Median P uncertainty (1 σ, kbar)		
		$C + V$	C	V	$C + V$	C	V
Metamorphic zone	Biotite zone	30	29	46	1.8	1.0	2.2
	Garnet zone	25	16	38	1.2	0.8	2.0
	Porphyroblast zone	16	14	28	0.8	0.7	1.2
	Sillimanite zone	16	17	29	0.8	0.8	0.9
Facies series	Cordierite series	29	24	49	0.9	0.7	1.3
	Staurolite series	23	20	37	1.1	0.8	1.7
	Kyanite series	16	12	27	1.0	0.7	1.3
P-T space	All zones and series	21	16	36	1.0	0.8	1.4

double the uncertainty in *P-T* compared to the highest-grade conditions. This pattern is partly reflected across the facies series, with the highest-temperature uncertainty found at the lowest-pressure cordierite series (1 σ = 29 °C), and lowest-temperature uncertainty in the highest-pressure kyanite series (1 σ = 16 °C), whereas the the pressure uncertainty remains nearly constant across all facies series (1 σ = 0.9–1.1 kbar). The higher uncertainty at lower grades is predominantly caused by the impact of bulk composition uncertainty on the inversion of modal volume variables (Fig. 3.9B, E). This result, is perhaps unsurprising given low grades are dominated by hydrous sheet

silicates with broad compositional ranges, fewer assemblage changes over small P-T spaces, and a lack of aluminous porphyroblasts.

3.6.1.4 Tectonometamorphic controls on uncertainty in natural systems

The synthetic uncertainty analysis performed in this study used the median worldwide pelite composition from *Forshaw and Pattison* (2023), which represents a compilation of 5729 pelite compositions from 11 different orogens or regions. Such a broad dataset provides generalised insights into the metamorphic reactions and processes operating in pelitic systems. However, it does not fully account for uncertainties that may systematically vary specific to changing tectonometamorphic environments in natural systems. Different tectonic settings impart systematic compositional differences to deposited sedimentary units, which can be discriminated using major-element geochemical proxies (e.g., *Bhatia*, 1985; *Roser and Korsch*, 1988; *Verma and Armstrong-Altrin*, 2016). In addition, the degree of sediment reworking can impact compositions systematically (e.g., *McLennan et al.*, 1993). Upon metamorphism, these compositional differences influence the metamorphic equilibria, thereby affecting the observed mineral assemblages, phase proportions, and compositions within the resulting metamorphic sequence (*Bucher and Frey*, 1994). For example, mature pelites, which are often depleted in plagioclase, can exhibit large pressure uncertainties due to the loss of key barometric equilibria. Consequently, different depositional environments and their resulting metamorphic sequence may inherently exhibit different levels of uncertainty during petrological investigation (e.g., *Caddick and Thompson*, 2008). Furthermore, tectonometamorphic environments differ in heat sources, radiogenic heating levels, and rates of crustal thickening or erosion (*Waters and Lovegrove*, 2002; *Copley and Weller*, 2022) which may influence the degree to which reactions occur at or near-equilibrium conditions. Prograde metamorphism is governed by heating rates, with regional metamorphism typically occurring near equilibrium conditions(e.g., *Yardley*, 1977), whereas contact metamorphism often preserves evidence of disequilibrium processes (e.g., *Hollister*, 1969; *Voll et al.*, 1991; *Wheeler et al.*, 2004). The scale and effect of such processes vary considerably across individual metamorphic sequences and are not quantifiable in a generalised sense. Given these considerations, the synthetic uncertainty values presented in this study should be considered more as guidelines than actual rules when assessing real rock systems.

3.6.1.5 Comparison with prior uncertainty estimates

The uncertainty estimates reported in this study differ from those reported in previous studies in that they are separated as a function of metamorphic zone and facies series, emphasising the impact of the changing assemblage (i.e., the phases present or absent). Previous studies have reported various estimates of system uncertainty for conventional

thermobarometry: ± 100 °C and ± several kbar (geological uncertainty, analytical uncertainty, and thermobarometer calibration error; *Hodges and McKenna*, 1987); ± 0.60–3.25 kbar (geological uncertainty, analytical uncertainty, and thermobarometer calibration error; 1 σ; *Kohn and Spear*, 1991b); > ± 50 °C and > ± 1 kbar (2 σ; *Powell and Holland*, 2008), > ± 50 °C and > ± 1 kbar (*Spear et al.*, 2016); and for phase equilibrium modelling ± ~1 kbar (geological uncertainty, 20 % variation from mean, 2 σ; *Palin et al.*, 2016). This study reports an estimate for median observational uncertainty (Fig. 3.1) in subsolidus pelitic systems of 22 °C and 1.0 kbar at the 1 σ level (10 % variation from mean, Table 3.8). This is equivalent to 44 °C and 2.0 kbar at 2 σ level (thereby 20 % variation from the mean). This uncertainty is even higher where only modal volume variables are considered, 1 σ = 36 °C and 1.4 kbar (2 σ = 72 °C, 2.9 kbar).

3.6.2 Quantitative petrological modelling

3.6.2.1 Comparison to other quantitative workflows

Using petrological data to quantitatively invert for pressure and temperature is well established. The avPT function of THERMOCALC (*Powell and Holland*, 1994) uses the activities of phases involved in balanced independent chemical reactions from an internally consistent thermodynamic dataset to calculate the temperature and/or pressure. An iterative, least-squares inversion is used to find the optimal P-T condition which maximises the consistency between each independent chemical reaction involved within the inversion (*Powell and Holland*, 1994). The same approach applies for avP and avT calculations, although these are calculated directly without iteration (*Powell and Holland*, 1988). This approach calculates "predictive" uncertainties (specifically those stemming from model uncertainty), in contrast to observational uncertainties considered in the inversion method present in this study (Fig. 3.1). TWEEQU (Thermobarometry With Estimation of EQUilibration state) follows a similar multi-equilibrium approach, calculating all possible equilibria implied by selected phase components from an internally consistent thermodynamic database (*Berman*, 1991). The subsequent TWQ software (*Berman*, 2007), introduced a refinement by prioritizing an independent set of equilibria considered more robust, particularly those directly constrained by experimental data. While these methods are powerful and have been widely used, they remain independent from phase equilibrium modelling.

Most recently, Bingo-Antidote uses the forward models calculated by a Gibbs Free Energy Minimizer to perform inversions (*Duesterhoeft and Lanari*, 2020). Bingo-Antidote performs a global optimization of P and T as a function of the observed phase assemblage, mineral modes, and mineral composition. Bingo-Antidote incorporates all this information into a "global evaluation criterion" (Q_{total}). This method is particularly powerful due to its integration with XMapTools (*Lanari et al.*, 2019) and thus its

ability to link directly to compositional phase maps, and examine the impact of local bulk composition variation on resulting P-T estimates. Some key differences between Bingo-Antidote and the new workflow proposed here are discussed in Appendix B. Most notably, Bingo-Antidote and this workflow treat uncertainty estimates quite differently. Bingo-Antidote incorporates measurement uncertainties into its definition of its objective function, in a similar way to the chi-squared objective function. As such, lower values of Q_{total} indicate that the inversion is closer to the mean observed value for any given data variable. The uncertainty estimate provided in Bingo-Antidote is the area in P-T space with a Q_{total} score within 2 % of the maximum Q_{total} value. This can be thought of the goodness-of-fit error, which quantifies how well different potential solutions describe the mean value for each variable. However, this approach does not consider how the P-T solution might change as a result of uncertainty in the measurements or the impact of uncertainty in the forward models. In contrast, our new workflow uses bootstrap resampling for uncertainty propagation, showing how observational uncertainties affect the distribution of possible P-T solutions.

3.6.2.2 Advantages and limitations of the new workflow

Grid-search inversion The grid-search inversion offers a systematic approach to identify the global minimum of the misfit function and determine the best-fit solution within the selected model space. By discretizing P-T space into a grid of forward models and calculating the misfit at each grid point (Fig. 3.3A), this method ensures the global minimum is located, provided the grid range and precision are appropriate. The grid-search is also advantageous because it is adaptable to various combinations of model parameters, such as T-X and P-X, making it applicable across a broad range of petrological modelling scenarios. Furthermore, the workflow is equally applicable to higher-dimensional analyses (e.g., P-T-X). However, the grid-search approach introduces computational challenges as the number of trial solutions increases exponentially with increasing dimensionality. Advances in forward modelling software (e.g., *Riel et al.*, 2022) have significantly reduced the computational time required for these calculations, thereby opening up the extension of this workflow to higher dimensions and reducing the need for assigning parameters a priori (e.g., $X_{Fe^{3+}}$, $a H_2O$).

Misfit/objective function The workflow employs the L1-norm misfit function, a robust measure of fit that is widely used across scientific disciplines because of its resilience to outliers, outperforming L2-norm (least-squares) or chi-squared functions in this regard (*Claerbout and Muir*, 1973; *Li et al.*, 2015; *Ibraheem et al.*, 2021). This makes the method particularly well-suited for petrological systems where significant outliers are common.

The inversion does not directly identify the stable phase assemblage, unless the variables are set to accommodate this. Rather, the misfit function seeks solutions in which all phases included in the selected variables are of the correct composition and/or modal abundance, thereby defined by where these phases are predicted to be stable. Therefore the boundaries of the result are inherently dependent on the variables employed in the inversion. The lack of strict relationship between the misfit function and a user-defined peak assemblage field has several benefits: (1) The assemblage field corresponding to a mineral assemblage in a pseudosection may be smaller than the estimated uncertainty (*Powell and Holland*, 2008; *Waters*, 2019); (2) field boundaries defined by small modal volume or accessory phases may not be reliable (*Weller et al.*, 2024); and (3) assemblage field boundaries, mineral mode contours, and mineral compositional isopleths show relatively decreasing uncertainties and increasing precision (*Waters*, 2019).

The misfit function does not inherently penalize inversions using a small number of variables. Instead, the impact of the number of variables is best understood by analysing the standard error (SE). The number of variables will also have a significant impact on the P-T uncertainty derived from bootstrap resampling, discussed below. A notable feature of this workflow is its deliberate avoidance of variable weighting, such that all variables are treated as equally valid in the inversion. This approach is advantageous in scenarios where the relative importance of variables is difficult to determine or where weighting would introduce significant bias into the results.

Uncertainty analysis Formal error propagation is generally unsuitable for non-linear problems such as inverting for P-T conditions, because the combined effects of various random and systematic errors are impossible to calculate directly (*Menke*, 1984). Instead, Monte Carlo methods, such as bootstrap resampling, are particularly well suited. The application of bootstrap resampling to the observed data allows users to estimate the uncertainty of the inverse solution (Fig. 3.3B). It may also be used to identify any significant local minima that may provide alternative hypotheses and to evaluate the sensitivity of the final result to the different input variables (Fig. 3.4E).

Although the workflow incorporates multiple sources of uncertainty stemming from the observations, not all quantifiable and semi-quantifiable uncertainties are fully addressed (Fig. 3.1). Uncertainty in the parameters used during modelling and the underlying thermodynamic end-member datasets and a-X relations are not directly examined by bootstrap resampling and may unduly influence the forward modeled values. Nevertheless, the method inherently incorporates some of these uncertainties due to reliance on Monte Carlo-style methods (Fig. 3.1). The impact of these uncertainties on the solution could be more directly analyzed by performing Monte-Carlo simulations of the forward problem with varying input parameters, solution models and databases.

3.7 Conclusions

Accurately constraining the P-T history of metamorphic rocks is crucial for understanding a broad range of processes in both the solid and surficial Earth, including identifying geothermal gradients in the subsurface and sources of economically valuable raw materials (e.g., critical metals), understanding climate and Earth system feedbacks, reconstructing the tectonometamorphic evolution of terrains, and informing broader geodynamic models. The ability to understand and quantify uncertainties in the calculation of P-T conditions is essential to ensuring that results can be interpreted within a defined confidence range. This is particularly important in scenarios where geological or petrological interpretations hinge on relatively small variations in pressure and/or temperature (e.g., *Pattison and DeBuhr*, 2015). Although many sources of uncertainty in phase equilibrium modelling cannot be propagated or are difficult to quantify, for those that can be, there should be an attempt to do so (*Powell and Holland*, 2008). The key conclusions of this study are:

1. The new workflow, LinaForma, provides quantitative constraints on optimal P-T conditions and associated uncertainties for a given rock system. The technique identifies the best-fit solution by comparing observed data, such as mineral compositions and/or modal volumes, with forward model predictions across a user-defined P-T grid. Bootstrap resampling (repeated sampling with replacement) quantifies the uncertainty of the inverse solution and assesses its sensitivity to input variable uncertainty. Three diagnostic metrics—quality of data fit, variable sensitivity, and standard error—are incorporated to validate and refine the results.

2. Application to natural samples demonstrates that peak P-T conditions and uncertainty estimates for both pelitic and metabasic compositions align with classical thermobarometric methods. Local discrepancies help assess model limitations.

3. In a synthetic pelitic system, uncertainty varies across P-T space with lower-temperature biotite- and garnet-zone conditions showing approximately double the uncertainty (1σ = 25–30 °C, 1.2–1.8 kbar) compared to higher-temperature sillimanite-zone conditions (1σ = 16 °C, 0.8 kbar). Across facies series, temperature uncertainty is highest in the low-pressure cordierite series (1σ = 29 °C) and lowest in the high-pressure kyanite series (1σ = 16 °C), whilst pressure uncertainty remains consistent (1σ = 0.9–1.1 kbar). The higher uncertainty at lower grades is mainly due to the impact of bulk composition uncertainty affecting inversions using modal volumes. Assemblage changes produces marked differences in uncertainty.

4. The source of uncertainty propagated and choice of input variables significantly impacts P-T estimates. Mineral composition variables generally yield lower uncertainties than modal volume variables. Accounting for mineral measurement uncertainty (bootstrapped at an appropriate percentage, σ = mean × ~20%) can

capture the total quantifiable uncertainty stemming from the observations when using mineral composition variables. However, when modal volume variables are included, bulk composition uncertainty must also be accounted for, as it strongly influences phase stability boundaries. Where applicable, combining both variable types and propagating both mineral measurement and bulk composition uncertainties (observational uncertainty) may provide a more complete estimate of uncertainty in the system.

5. Given the varying sensitivities of different variables to uncertainty, selecting only those that minimize uncertainty may be misleading. Instead, the inversion should incorporate the largest and most diverse set of robust variables possible to ensure P-T estimates are representative of the natural system. This approach also enables an assessment of the overall model performance, which may provide insights into other characteristics of the system such as the degree of equilibrium.

3.8 Software Availability

The outlined workflow, `LinaForma`, is available at the GitHub repository: `https://github.com/TMackay-Champion/LinaForma`.

Chapter 4

The Metamorphic and Structural History of the Kansanshi Cu-Au Mine, and Its Implications for the Tectonics of the Zambian Copperbelt.

Abstract

The Kansanshi Cu–Au Mine in North-Western Zambia is Africa's third-largest copper deposit, yet its tectonic evolution and mineralisation history remain poorly constrained. Located within the Neoproterozoic Katangan Basin of the Central African Copperbelt, Kansanshi displays mineralisation styles and host lithologies that differ markedly from typical Copperbelt deposits. This study integrates new geological mapping, structural analysis, metamorphic pressure–temperature (P–T) paths, and pre-existing geochronological data to develop a new tectonic model for Kansanshi and the surrounding Solwezi area. Fieldwork focused on characterising metamorphic grade rather than correlating with regional stratigraphy, allowing for improved clarity regarding the metamorphic and thus tectonic evolution of this area. Our results indicate that Kansanshi is located above a thick autochthonous sequence of Roan Group sediments within a Tonian-age sub-basin. Convergence between the Congo and Kalahari plates during the Ediacaran Period resulted in the formation of a significant orogenic wedge, with peak metamorphic conditions of approximately 550–620 °C and 7.5–9.5 kbar. This corresponds to burial depths of ∼26–33 km, assuming a lithostatic gradient of 3.5 km/kbar. Garnet- and biotite-grade rocks of the wedge were thrust over the Kansanshi sub-basin during the mid- to late-Cambrian. The Cu-rich veins of Kansanshi are interpreted to result from remobilisation of pre-existing mineralisation during overthrusting. The proposed model provides the first coherent framework for understanding the structural and thermal evolution of the Kansanshi deposit. It also raises new questions about the role of Lufilian granitic magmatism in the mineral system, offering a foundation for future exploration and geochemical studies.

4.1 Introduction

The Kansanshi Cu-mine of North-West (NW) Zambia is the third largest copper mine in Africa, with a resource of 982.3 Mt of Cu (using a cut-off grade of TCu 0.2 %) and 0.11g/tonne of Au as of December 2023. Despite the economic and societal importance of this deposit, the tectonic evolution and the mechanism behind mineralisation at

Kansanshi is unresolved. This significantly hampers the exploration for further deposits like Kansanshi. The mine is situated in the Neoproterozoic Katangan Basin of the Central African Copperbelt, which primarily hosts Cu as disseminated and sediment-parallel veinlets of copper sulfides within low-grade to unmetamorphosed sediments. By contrast, large portions of the Kansanshi endowment occur in metal-rich, metre-wide veins that crosscut a wide range of lithologies from amphibolite-grade metamorphosed pelites to unmetamorphosed sediments. Kansanshi has been the focus of numerous studies, and yet a coherent tectonic model for Kansanshi and the NW region of the Zambian Copperbelt remains elusive. Several geological mapping programs have been conducted through Kansanshi and the neighbouring Solwezi Dome, helping to constrain the structural evolution of the mine and its country rock. However, there are few quantitative constraints on the pressure–temperature (P–T) evolution of the metamorphic rocks that widely crop out in the area. Previous mapping efforts have attempted to identify and map sedimentary units that are common to the Katangan Basin as a whole. However, metamorphism and deformation in the area around Kansanshi makes this challenging and prone to error (*MacIntyre*, 2019). Recent work by *Eglinger et al.* (2016) provided the first modern assessment of the metamorphic evolution of the rocks from the Solwezi area but the lack of structural constraints prevented a coherent model from being formulated. In this study, we integrate new field observations and structural analysis with calculated metamorphic P–T paths and geochronological constraints from the literature to create a new tectonic model for the Kansanshi Cu-mine. Outcrop mapping was performed on lithological units, paying particular attention to the metamorphic grade, rather than trying to fit the regional Katangan stratigraphy. This approach provides renewed clarity on the tectonic evolution of Kansanshi and NW Zambia, as well as a new starting point for assessing the validity of mineralisation models for the area.

4.2 Geological Setting and previous tectonic models

The Central African Copperbelt is hosted within the Neoproterozoic Katangan Basin, bordered to the north by the Archaean Congo Craton, to the east by the Paleoproterozoic Banguweulu Block and the Mesoproterozoic Irumide Belt, and to the south by the Archaean Kalahari Craton (Fig. 4.1). The Katangan Basin documents two phases of rifting and thermal subsidence (*Purkiss*, 2025). The Upper and Lower Roan Group sediments, deposited sometime after 880 Ma (*Armstrong et al.*, 2005), transition from syn-rift clastics to carbonate-dominated facies indicative of deposition in an epicontinental sea (*Purkiss*, 2025). The overlying Mwashia Group represents a second phase of rifting starting at *ca* 765 Ma, and is predominantly expressed as distal, sediment-starved facies (*Key et al.*, 2001). This is followed by the Nguba Group, which was accommodated by post-rift thermal subsidence (*Purkiss*, 2024). Finally, the Kundelungu Group of

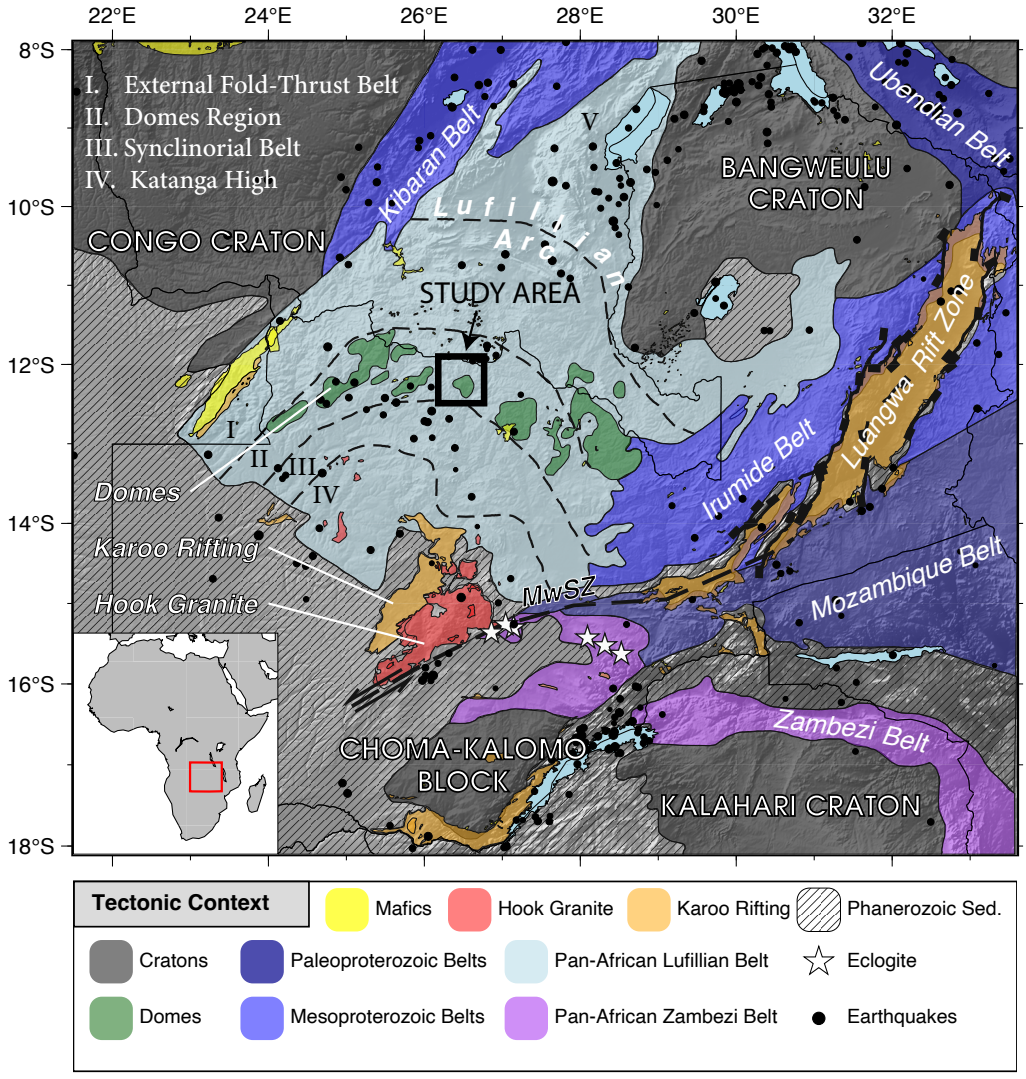

Fig. 4.1 Simplified geological map of Zambia, after *Kounoudis et al.* (2024).

predominantly carbonate-bearing siltstones records formation in a quiescent tectonic regime prior to and during basin inversion.

The exact timing of basin inversion is debated, although it is clear that peak Barrovian-style regional metamorphism occurred at *ca.* 530 Ma during the Lufilian Orogeny as a result of the convergence between the southern Kalahari Craton and the northern Congo Craton (*John et al.*, 2004). It is during this period that the metamorphic rocks surrounding Kansanshi experienced peak deformation and metamorphism (*Eglinger et al.*, 2016; *John et al.*, 2004). This Barrovian event is best preserved in the Domes Region of NW Zambia, named after five large antiformal domes of Mesoproterozoic basement rocks that crop out along strike from one another in the region. The Domes Region is an arcuate zone approximately 50 km across strike and features the highest levels of deformation and metamorphism of the entire basin. *Eglinger et al.* (2016) postulated it to be the site of the suture zone between the Congo and Kalahari cratons, in contrast *Daly et al.* (2024) argue it represents a completely closed and inverted, hyper-extended local basin, of the order of 100 km wide within a broad inter-cratonic zone separating the two cratons. The Domes Region preserves rocks increasing from sub-greenschist facies on its outer margins up to upper amphibolite facies (kyanite and sillimanite-grade) in the centre of the region (*Cosi et al.*, 1992; *Eglinger et al.*, 2016), indicating burial (and later exhumation) of pelitic material to middle crustal depths.

The Kansanshi Mine lies approximately 10 km north of the Solwezi basement dome outcrop, the easternmost-bar-one of the five basement domes (Fig. 4.2). The mine comprises a gentle NE-SW facing antiform of garnet- to kyanite- grade metasediments overlying undeformed Katangan sediments (*MacIntyre*, 2019), including a significant thickness (*ca.* 1.5 km) of Lower Roan clastics (*Daly and Tosca*, 2020). This represents a significant metamorphic inversion. The sole coherent tectonic model for Kansanshi was presented by *Daly and Tosca* (2020), in which they proposed that the sediments underlying Kansanshi represent a northern sub-basin of the main Katangan Basin to the south. In this model, the Lufilian Orogeny drove inversion of the Katangan Basin and northward expulsion of the sediments from the main Katangan Basin on top of the relatively undeformed, autochthonous Kansanshi sub-basin. Despite the novel insights provided by this model, such as its appreciation of the significant undeformed sediment thickness underlying Kansanshi, the model does not account for the formation of high-grade metamorphic rocks in the area.

4.3 Field relationships and structural analysis

New geological mapping was carried out at a scale of 1:55,000 over a ∼60 km by ∼30 km area, building on previous detailed work by *Arthurs* (1974) and *Barron* (2003). This new mapping had a renewed focus on identifying and mapping metamorphic units that have received little prior attention. The resulting geological map, with an accompanying

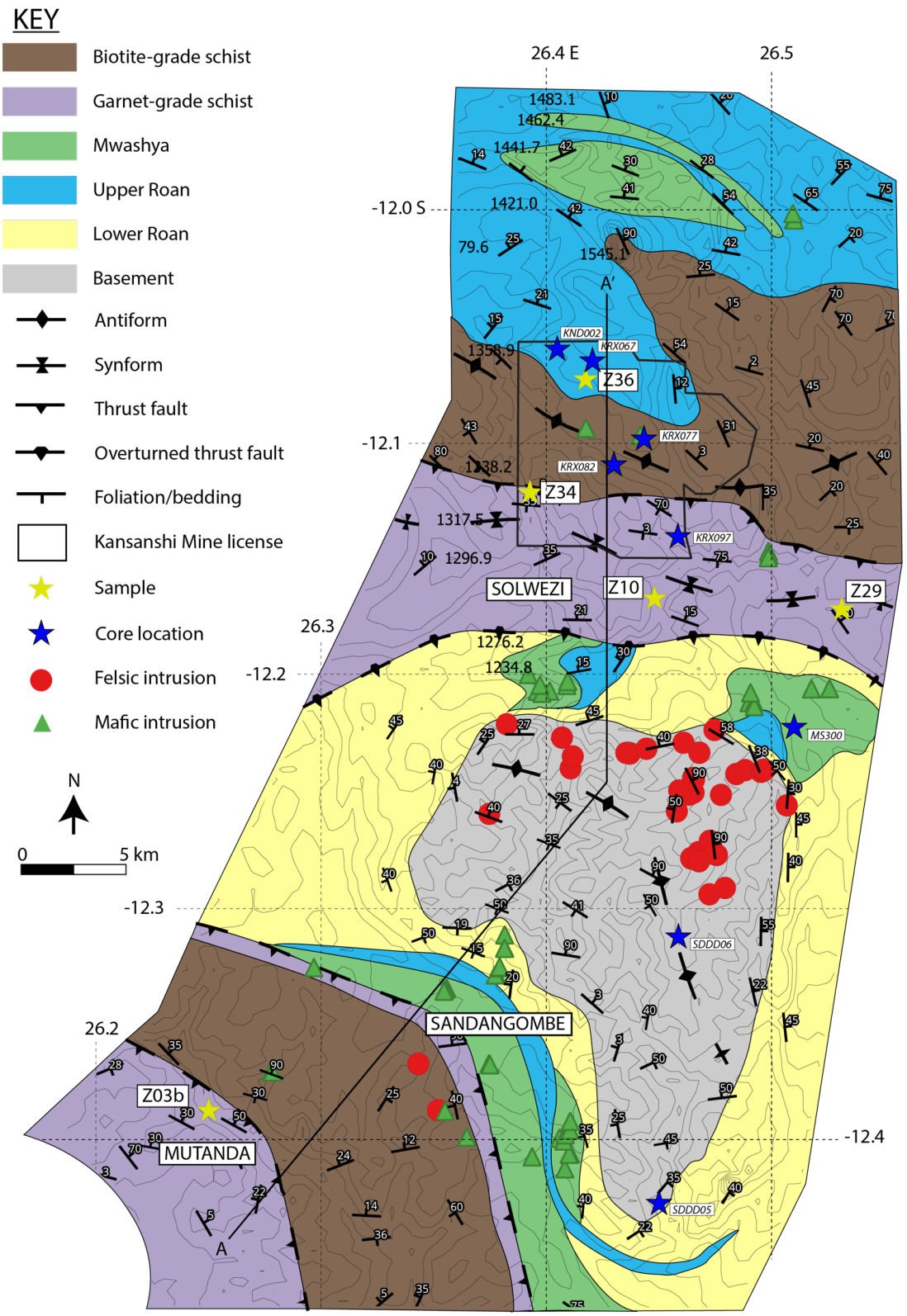

Fig. 4.2 1:50,000 Geological map of Solwezi and Kansanshi.

cross-section, restoration, and tectonostratigraphic column can be found in Fig. 4.2, Fig. 4.3, and Fig. 4.5. The main lithological units and field relationships are outlined below.

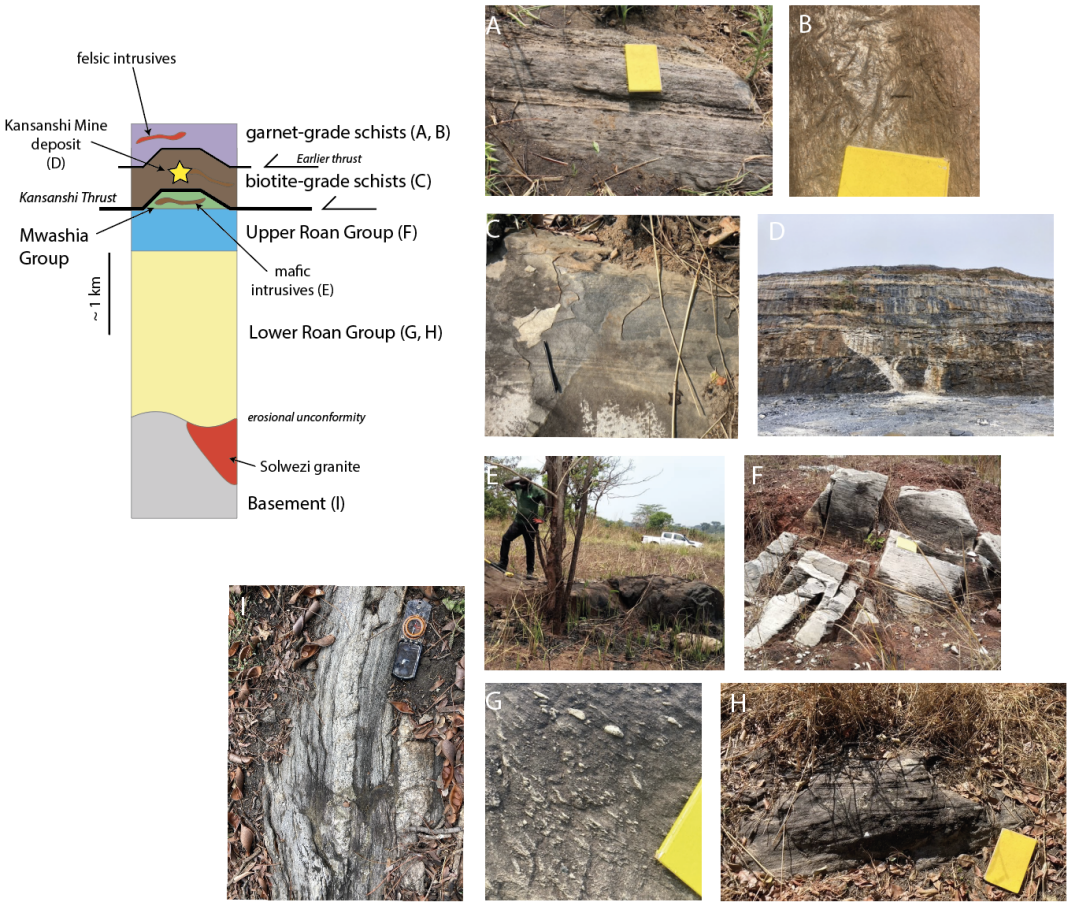

Fig. 4.3 Tectonostratigraphic column for Solwezi and Kansanshi.

4.3.1 The Paleoproterozoic - Mesoproterozoic basement

The basement rocks to the Katangan Supergroup are exposed in the core of the Solwezi Dome, which is located south of the town of Solwezi (Fig. 4.3I). For simplicity, we considered the basement lithologies as a single mappable unit due to the > 200 Myr age difference between it and the overlying sediments (*kang Xu et al.*, 2022)). However, the basement shows significant lithological variation. *Arthurs* (1974) divided it into the Gneiss Group, comprising biotite gneisses, schists, and minor amphibolites, and the Granite Group, comprising massive to gneissic granites, migmatites and late pegmatites.

The biotite gneisses of the Gneiss Group are fine- to medium-grained, and composed of quartz, biotite, muscovite, K-feldspar, plagioclase feldspar, and albite (*Barron*, 2003). The quartz forms medium-grained granoblastic bands, alternating with bands of fine-grained biotite which define a weakly crenulated schistosity (*Barron*, 2003). Interbedded with the gneisses are well-foliated, biotite schists with minor quartz, garnet,

and scapolite. Minor amphibolite schists are also present within the Gneiss Group. These amphibolites are strongly foliated, medium-grained, and comprise hornblende, plagioclase and biotite with minor quartz and epidote (*Arthurs*, 1974). The age of the Gneiss Group is currently unknown, although the group likely represents a northern equivalent of the Paleoproterozoic (*ca.* 1874–1980 Ma) metasedimentary Lufubu Schists and Gneisses which crop out in the Copperbelt to the south-east (*Rainaud et al.*, 2005). The younger Granite Group crops out particularly in the north-east and south of the Solwezi Dome and is comprised of 1178 ± 15 Ma, I-type, K-feldspar granites and 1109 ± 7 Ma, A-type, biotite monzogranites (*kang Xu et al.*, 2022). The texture of both lithologies ranges from porphyritic to gneissic, and the biotite monzogranite often contains Cu-mineralisation in the form of chalcopyrite (*kang Xu et al.*, 2022). The granites of the Granite Group are separated from the Gneiss Group by a zone of migmatites. The granite lithologies can be seen grading into quartz-feldspar-biotite migmatites from north to south along the Chisalala River in the NE of the Dome (*Arthurs*, 1974). Lensoid leucosomes of quartz and feldspar, up to 30 cm thick, grade into metre-wide pegmatitic segregations with abundant biotite-rich paleosomes, and finally into biotite-free, quartz-K-feldspar-muscovite granitoids (*Arthurs*, 1974). In the south of the Dome, late quartz-microcline pegmatites can be observed cutting both the granites and the migmatites. The age of these pegmatites is not known, but they likely represent a late stage of melting in the Mesoproterozoic granite system (*Arthurs*, 1974).

4.3.2 The Neoproterozoic Katangan Supergroup sediments

The Katangan Supergroup sediments were deposited sometime after 880 Ma (*Armstrong et al.*, 2005) and unconformably overly the Solwezi Dome, although the actual contact is not clearly defined (*Arthurs*, 1974). The lowermost sediments of the Katangan Supergroup belong to the Lower Roan Group, which is characterised by undeformed, cross-bedded, arenitic to wacke sandstones (Fig. 4.3H). This package of sediments is locally known as the Basal Clastic Sequence (*Barron*, 2003) and grades from immature conglomerates at its base (Fig. 4.3G) to more mature quartz-rich beds at the top of the sequence (*MacIntyre*, 2019). Despite this local heterogeneity, the Lower Roan Group was defined as a single mappable unit at the scale of mapping used in this study. Fluid-alteration is relatively widespread, with an abundance of muscovite and chlorite observed at certain outcrops. *Barron* (2003) characterised these muscovite-bearing outcrops as quartz-muscovite schist. This study mapped the quartz-muscovite schist and the less altered sandstones as a single unit—the Lower Roan Group—based on the continuity between adjacent outcrops, which range from muscovite-bearing to non-muscovite-bearing, and the presence of common sedimentary structures such as cross-bedding. We interpret the variation in mica content to represent variation in clay content within the protolith. The unit locally contains kyanite-talc schists, which are interpreted to represent late metasomatic alteration of the sediments (*Lefebvre*

and Patterson, 1982; *Williams and Nisbet*, 2017). These schists crop out in a 0.5–2 km envelope around the margin of the Solwezi Dome (*Arthurs*, 1974), and have been intersected by several drill cores below the Kansanshi Mine (see below for drill core KRX082).

The Lower Roan Group is conformably overlain by the carbonate-bearing sediments of the Upper Roan Group. Limestones and dolostones dominate the sequence (Fig. 4.3F), although lower portions of the sequence contain abundant anhydrite as well as horizons of biotite schist (+/- carbonate) and large (> 300m thick) mafic bodies (*Barron*, 2003). The carbonates display a varying degree of recrystallisation from the original sedimentary structures to marble. *MacIntyre* (2019) split this sequence into a lower Evaporitic Sequence and an upper Dolomitic Sequence, while *Broughton et al.* (2002) split the sequence into the Upper Roan and the Lower Dolomite sequences. This study defines the Upper Roan Group as a single mappable unit, following *Barron* (2003). This unit crops out extensively in the Kansanshi Mine as well as to the north of the mine as a southward-propagating back-thrust sheet. The unit can also be seen in irregular, thin zones around the margin of the Solwezi Dome. Whether these irregular outcrop patterns represent original stratigraphic relationships, or are the result of Lufilian deformation (*Arthurs*, 1974) remains unclear due to the poor exposure. Together, the basement lithologies and the Lower and Upper Roan Groups constitute the Footwall Domain of the Kansanshi deposit (*MacIntyre*, 2019).

In the classical Copperbelt, the Upper Roan sequence is overlain by the *ca.* 765 Ma Mwashia Group sediments characterised by mudstones, carbonates as well as ironstones and abundant mafic bodies (*Key et al.*, 2001; *Selley et al.*, 2005; *Master and Wendorff*, 2011). Around Solwezi, this group often contains biotite schists, slates and minor marbles indicative of a higher grade of deformation and metamorphism (*Arthurs*, 1974). *Arthurs* (1974) also defined an uppermost unit of dolomitic marbles termed the Chafugoma Marble Formation, and mapped them cropping out north of Kansanshi. However, the thickness of this unit greatly exceeds the maximum thickness of the Mwashia Group reported by *Purkiss* (2025). This, as well as the structural position of the unit at the base of a backthrust sheet (see Section 4.3.5), led us to interpret these carbonates as part of the Upper Roan Group. In this study, the Mwashia Group is a mappable unit often defined by the presence of ironstones and the presence of strike-parallel gabbroic intrusions in areas which are otherwise well constrained to host Katangan sediments (Fig. 4.3E). This is particularly clear around the northern and western margin of the Dome, in which several elongate mafic bodies have been mapped. It should be noted that *MacIntyre* (2019) does not recognise the Mwashia as a sedimentary group, but rather a subgroup within the Roan Group. Following the work by *Purkiss* (2025), this study categorised the Mwashia as separate group because it is underlain by a justifiable maximum flooding surface which can be correlated across much of the Katangan Basin.

The Mwashia Group is also interpreted to represent a second basin-wide extension event on account of it being associated with abundant mafic suits (*Purkiss*, 2025).

The relationships between each of the three aforementioned groups (Lower Roan, Upper Roan, Mwashia) cannot be readily examined in outcrop due to limited exposure. However, multiple drill cores in the area have provided a greater understanding of these units and their stratigraphic configuration prior to and after deformation. A detailed description of KRX082 is provided below. Other drill cores (KRX067, KRX077, KRX097, MS300) are also used to constrain the structure of the Kansanshi area, after *Daly and Tosca* (2020).

4.3.2.1 KRX082 drill core

The KRX082 core is one of the deepest drill cores in the Katangan basin of Zambia. It is 2511 m long, intersecting a 1185 m thick intensely folded and sheared section of metasedimentary and metamorphic units, which overlie a 1326 m thick clastic section, without reaching crystalline basement (*Daly et al.*, 2024). A summary log of the KRX082 core can be found in Figure 4.4. The basal clastic section comprises ∼500 m of medium to thickly bedded, texturally immature, medium to coarse-grained, laminated and cross-stratified sandy facies. These are intercalated with thin to medium-bedded pebble conglomerate units. The basal section is overlain by ∼150 m thick heterolithic succession comprising thinly bedded, and laminated, mud units interbedded with fine to coarse-grained sandy units. The heterolithic succession is overlain by a ∼500 m thick section of texturally immature, medium to coarse-grained, laminated and cross-stratified sandy facies. In the upper parts of the clastic section of the core dolomite occurs in the matrix, its proportion increasing upwards. The upper 200 m of the clastic section of the core show pronounced tectonic fabric that obscures most primary sedimentary structures (*Purkiss*, 2024).

The metasedimentary and metamorphic units that comprise the upper half of the core are separated from the clastic lower half by a dm-scale interval of rapidly increasing metamorphic grade and fabric, with a possible detachment surface being identifiable. The upper section of the core comprises intensely sheared and isoclinally folded garnet-bearing pelites, marbles, schists, mafic units, metasandstones and metadiamictites. The lower portions of the metamorphic section show duplication of sets of units (e.g., breccia - pelitic - carbonate - mafic). However, these even-numbered repetitions of units are lost higher up in the core, with, for example, two ∼30 m thick metadiamitictite units underlying one ∼140 m thick metadiamictite unit, making restoration of the section difficult.

The lower half of the KRX082 is interpreted to have been predominantly deposited in a fluvial, possibly braid plain, setting, with possible minor deepening into intertidal settings. Dolomite occurring in the upper portion of the clastic section indicates

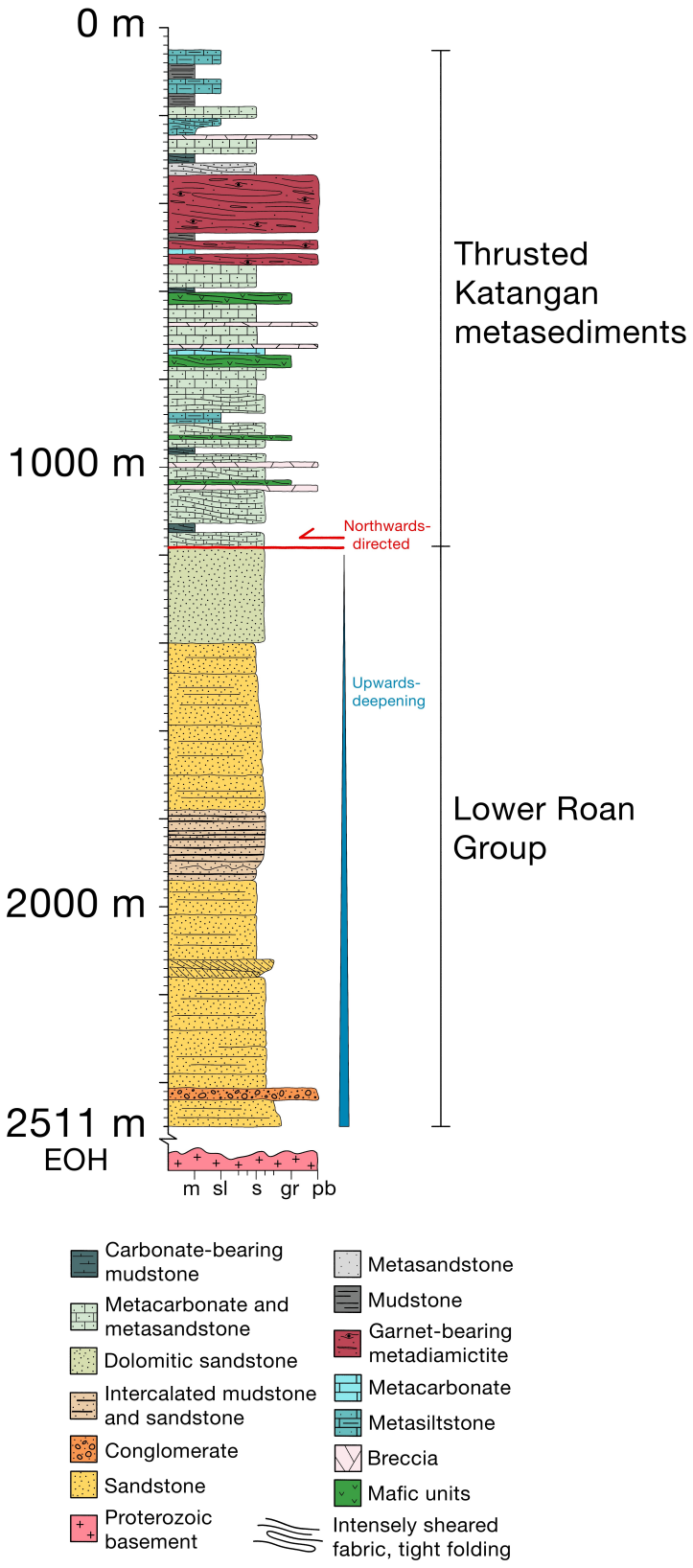

Fig. 4.4 Sedimentary log of Core KRX082 from *Purkiss* (2024).

increasing marine influence and deepening. The clastic lower half of the core is interpreted to belong to the terrestrial syn-rift fill of the Lower Roan Group, on account of highly amplified aggradational fluvial successions, textural immaturity, as well as thinning and onlap of the sediments onto the Solwezi Dome to the South. Localised structurally controlled sedimentation, showing highly aggradational facies stacking, is characteristic of rift-basin stratigraphy (*Gawthorpe and Leeder*, 2000). Monotonous aggradational fluvial successions, showing little deepening in the facies, indicates an overfilled basin in which sediment supply could match or exceed the accommodation space generation rate (A≤S) (*Nottvedt et al.*, 1995). (*MacIntyre*, 2019), *Barron* (2003), and *Arthurs* (1974) interpret the upper half of the core, above the interpreted detachment surface, to represent autochthonous Nguba or Kundelungu Group sediments. However, given the step-change in the grade of deformation and metamorphism as well as the structural relationships to the lithologies identified outside the mine, we interpret the upper half of the core to be allochthonous. The degree of deformation and metamorphism of this upper half precludes a precise correlation with traditional Katangan stratigraphy (*Purkiss*, 2024).

4.3.3 The metamorphic sheet

Structurally overlying the Katangan Supergroup is a sheet of metamorphic rocks, defined by penetrative metamorphic foliations that obliterate the original sedimentary structures and the development of metamorphic mineral porphyroblasts such as garnet, kyanite and biotite. This unit has previously been mapped as the Solwezi Biotite Quartzite Formation (*Hatfield*, 1937; *Arthurs*, 1974), or the Spangled Schist (*Barron*, 2003) with lithological descriptions including "biotite-garnet-hornblende schist", "biotite quartzose schist", and "quartzose biotitic dolomite". This previous aggregation of different lithologies and metamorphic grades has made interpretation of this unit difficult. In contrast, this study identified two distinct mappable units based on index minerals in pelitic bulk compositions: a garnet-bearing unit dominated by garnet-biotite metapelites (Fig. 4.3A, B) and a garnet-free unit dominated by well-foliated biotite-muscovite-chlorite metapelites (Fig. 4.3C). There is lithological variation within the two units, from standard Al-rich pelitic compositions to quartzites to carbonates, but our focus on the mapping of metamorphic index minerals allows the identification of units at a 10s-kilometre scale and thus an improved structural understanding. The original stratigraphic relationships between the different lithologies are unknown. The garnet-bearing lithologies are characterised by coarse porphyroblastic garnet, which have been heavily retrogressed to biotite, quartz, muscovite and chlorite in places (Section 4.4). The unit often contains a crenulated schistosity, as well as coarse-grained, unoriented hornblende laths overprinting the schistosity (Fig. 4.3B). The biotite-grade lithologies are predominantly mica-rich schists, phyllites, and quartzites with abundant fine to coarser grained biotite, muscovite, chlorite, as well as calcite in places. The metamorphic

sheet crops out to the south of the Solwezi Dome around the town of Mutanda and to the north of the town of Solwezi. The sheet is characterised by a well-defined foliation, varying from a penetrative cleavage to a true schistosity, and complex folding at a thin-section, outcrop, and even kilometre scale. This deformation can be clearly observed at the centre of the Kansanshi Mine, where the thrust contact between the metamorphic sheet and the underlying Katangan sediments can also be observed (see Section 4.3.2.1). *Daly and Tosca* (2020) report this contact to be heavily mylonitised, which would indicate temperatures of at least c. 300 °C (*Kohn and Northrup*, 2009) and a depth in the crust of around 10 km or more. The contact between the garnet-bearing unit and the garnet-free unit is not preserved in outcrop, and no clear transitional unit was identified. Although bulk-composition variation undoubtably plays a role in the presence or absence of indicator porphyroblasts (e.g., *Forshaw and Pattison*, 2023), the garnet-free unit is solely found structurally beneath the garnet-bearing unit. This metamorphic inversion indicates the presence of an original thrust contact.

4.3.4 Felsic and mafic intrusions

Felsic and mafic intrusive rocks are located throughout the study area. As discussed in Section 4.3.1, the Solwezi basement dome hosts the Mesoproterozoic Solwezi granite of monzogranitic to syenogranitic composition (*kang Xu et al.*, 2022). Mafic intrusives, including medium- to coarse-grained ophitic gabbro and pyroxene cumulates, can be found within the Katangan sediments around the Solwezi Dome and within the metamorphic sheet. Most of these mafic intrusions have been weakly recrystallized to an assemblage of hornblende, epidote, plagioclase and quartz. *Barron* (2003) analysed zircons and zircon overgrowths from two samples of meta-gabbro using the SHRIMP II U-Pb method and found concordant ages stretching between 752.6 ± 8.6 Ma and 510.9 ± 7.8 Ma. These are interpreted to represent the initial crystallisation of the gabbro, which is consistent with the age of Mwashia volcanism (*Key et al.*, 2001), and a later thermal event associated with the Lufilian Orogeny. Several felsic intrusions have been identified within the metamorphic sheet, including an alkali-feldspar granite and a monzogranite. The age of the felsic material within the metamorphic sheet is unknown, although a syn- to post-tectonic timing is likely based on the intrusive field relationships (e.g., Fig. 4.11B). This interpretation is not without precedence in the Domes Region - *Eglinger et al.* (2016) interpreted there to be Lufilian-age granitoids within the Mwombezhi Dome (c. 120 km along strike) based on intrusive field relationships relative to Lufilian-age (529 ± 2 Ma) amphibolites.

4.3.5 Structural analysis

The resulting map, cross-section and associated restoration clearly show the multi-phase evolution of the Solwezi area (Fig. 4.5). The Solwezi Dome formed the basement to the

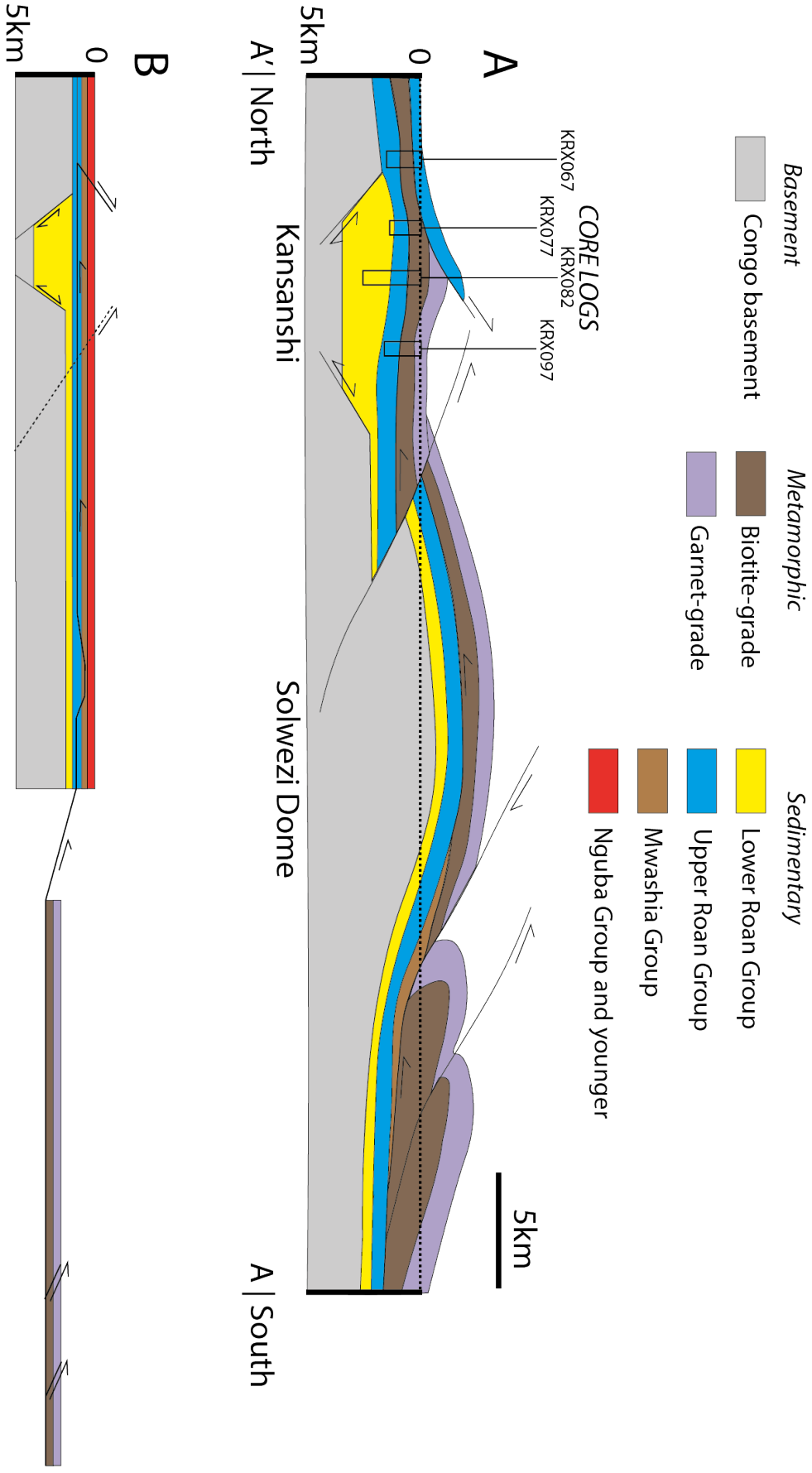

Fig. 4.5 A) Cross-section from A-A'. The profile length is approximately 50 km. B) Semi-schematic restoration of the cross-section.

overlying Katangan sediments at the time of deposition. The Lower Roan thickness sampled in drill core KRX082 of 1.36 km is significantly greater than the <0.5 km thickness preserved immediately north of the Solwezi Dome (*Arthurs*, 1974), suggesting a Lower Roan depocenter beneath the Kansanshi Mine. We call this the Kansanshi sub-basin. The lack of Lower Roan in core KRX067 and in outcrop to the north of the mine suggests that the Lower Roan stratigraphically pinches out to the north and is replaced by the Upper Roan carbonates.

We propose three phases of deformation (D0, D1, D2) following deposition of the Katangan sediments. D0 is characterised by the formation of the mica-defined foliation within the allochthonous metamorphic sheet. As discussed in Section 4.4, the metamorphic *P-T* conditions preserved by these rocks are indicative of significant burial (to garnet-grade conditions) and consequent deformation far afield from the location of Kansanshi. The garnet, kyanite and biotite porphyroblasts grew during this phase of deformation, which was dated at *ca.* 530 Ma by U-Pb monazite analysis (*John et al.*, 2004).

Deformation episode D1 was characterised by northward-verging folds of the foliations within the metamorphic sheet, formed as a result of north-eastward thin-skinned thrusting of the sheet over the Katangan sediments. The deformation fabrics preserved in core KRX082 indicate that the sole thrust (the Kansanshi thrust of Fig. 4.3) was located within the Upper Roan, likely utilising the relatively weak evaporite-rich horizons. The presence of the Mwashia Group surrounding the Solwezi Dome, structurally underneath the metamorphic sheet but above the Upper Roan Group, indicates that the thrust cut both up and down section. The extent of this is difficult to quantify as the thickness of the Mwashia Group cannot easily be constrained in the area. D1 also resulted in the formation of a southward-direct backthrust to the north of the mine, comprising Upper Roan carbonates and Mwashia sediments. The basal thrust of this backthrust sheet also lay within the Upper Roan, and placed the Katangan metasediments structurally above the metamorphic sheet to the south. The recumbent folds observed within the Kansanshi Mine formed during this phase of deformation (*MacIntyre*, 2019).

D2 was characterised by out-of-sequence, thick-skinned, northward thrusting of the Solwezi Dome and accompanied low-amplitude folding with east-west trending axes. The Solwezi Dome overthrusts the Katangan sediments and the metamorphic sheet to the north. The orientation of the bedding within the Lower Roan Group, in particular, show that the Katangan sediments dip northward and southwards off the edges of the Solwezi Dome, defining a basement-cored anticline. The basement itself displays a broadly NW-SE trending anticline, overprinting previous deformation fabrics. *Arthurs* (1974) reported isoclinal folding of the Lower Roan, which likely represents parasitic folding on the limbs of the antiform. *Barron* (2003) proposed that the NW-SE trending, gently dipping (10–20 °C) Kansanshi antiform is a thick-skinned, thrust-tip anticline which formed during D2 deformation. However, the antiform could also be the

result of thin-skinned deformation along the same Upper Roan basal décollement as the southward-directed backthrust. The undulating upper surface of the Lower Roan may simply reflect sediment expulsion beneath the mine as a result of basin inversion. *MacIntyre* (2019) proposed that the antiform resulted from post-orogenic collapse and extension, based on extensional boudinage observed within certain siliciclastic horizons within the mine. Kansanshi may have experienced some limited post-orogenic extension, but the predominant structures within the area are compressional and a significant degree of thrusting is required to create the significant metamorphic inversion preserved within KRX082.

4.4 Pressure-temperature evolution of metamorphism

4.4.1 Methods

4.4.1.1 Approach

Determining the metamorphic evolution of the metamorphic sheet is an essential step in the formulation of a coherent tectonic model for the Kansanshi area. Fives samples were chosen from the metamorphic sheet representing a range in mineral assemblage, bulk composition, and structural position. Multiple independent techniques were used to quantify the pressure-temperature conditions experienced by each sample.

Initially, we applied the fluid-independent Ti-in-biotite geothermometer (*Henry et al.*, 2005) to determine peak temperatures, as biotite appeared to be a part of the peak metamorphic assemblage in all lithologies. While this thermometer is calibrated for pressures of 3–6 kbar for peraluminous metapelites, many studies have applied this to higher-pressure (e.g. kyanite-grade) rocks and have determined geologically sensible and independently verifiable results (e.g., *Palin et al.*, 2018), indicating its suitability here. This geothermometer is reported to have an uncertainty of ±12–24 °C (1. S.D.).

In addition, we applied the average P-T method (avPT) of *Powell and Holland* (1994) using THERMOCALC (*Powell and Holland*, 1988) and dataset 5.5 (*Holland and Powell*, 1998) to determine the pressures and likely fluid composition during peak metamorphism. Here, we considered a binary composition fluid (H2O-CO2) and adjusted the composition to statistically fit the temperature window determined by the Ti-in-biotite fluid composition-independent thermometer. Given the abundance of evaporite and carbonate deposits within the Katangan Basin (*Jackson et al.*, 2003), we consider it likely that metamorphic fluids present within the crust during the Lufilian Orogeny were not pure H_2O.

The above-described techniques were applied to constrain individual *P-T* points, specifically for peak metamorphism; however, a complete examination of the metamorphic history of the Katangan Basin requires additional constraints on the burial and

exhumation paths of the sampled lithologies. As such, we also applied petrological modelling using the thermodynamic modelling software MAGEMin (*Riel et al.*, 2022) in conjunction with the *White et al.* (2014a) metapelite set of activity-composition (a-X) relations and the thermodynamic dataset ds-6 *Holland and Powell* (2011) to produce bulk-rock specific phase diagrams (pseudosections) for each lithology. These calculations were performed in the 11-component MnO-Na_2O-CaO-K_2O-FeO-MgO-Al_2O_3-SiO_2-H_2O-TiO_2-O_2 (MnNCKFMASHTO) system over 300–750 °C and 2–12 kbar. Point-wise forward models where then computed for a 75 x 75 grid over an equivalent area in P-T space using THERIAK-DOMINO (*de Capitani and Brown*, 1987; *de Capitani and Petrakakis*, 2010). The modelling was performed using a converted version of ds6.2 (*Holland and Powell* (2011), version td-ds62-mp50-v05 from 11th March 2022, modified by D. Tinkham) in the same 11-component MnNCKFMASHTO system as the pseudosections. The bulk compositions used for modelling were determined via X-ray fluorescence (XRF) and the XFe3+ content of each sample was determined by titration. THERIAK-DOMINO and MAGEMin are both examples of Gibbs Energy Minimizers, and thus their results should be comparable given the similarities in input database. All bulk-compositions were saturated with 30 mol% H_2O, and the activity of water for each sample was taken to be 0.8, following the results of avPT calculations (see below)

The 2D grid of forward models calculated using THERIAK-DOMINO were compared to the measured mineral chemistry data for each sample using the LinaForma inversion workflow (Chapter 3). This workflow provides a quantitative assessment of the best-fit pressure-temperature conditions for each rock, as well as the associated uncertainty. The results are shown over a P-T range from 400–700 °C and 5–11 kbar for the sake of clarity, but the inversion was performed over the full parameter range mentioned above.

4.4.1.2 Data collection

Mineral compositional analysis was performed on a Cameca SX5-Fe electron microprobe with a tungsten tipped field emission gun at the Department of Earth Sciences, University of Oxford, using an accelerating voltage of 15 keV, electron beam current of 20 nA and a beam diameter of 10 μm. Primary and secondary standards included albite (Na, Si, Al), MgO, sanidine (K), wollastonite (Ca), TiO2, Mn, fayalite (Fe), Durango apatite (P), Cr, Zn.

Poor quality analyses were removed from the data following an examination of the oxide weight % totals, following Kohn (2014), and if the weight % for any oxide from a particular analysis lay outside the upper or lower adjacent values for that dataset. Raw microprobe-derived mineral analyses (oxide wt. %) were then recalculated using the MINPLOT program (*Walters*, 2022) to a standard number of oxygens per formula unit for each mineral. The bulk composition of each sample and the associated bulk rock $X\mathrm{Fe}^{3+}$ was determined by XRF analysis, and titration, respectively, at Franklin and

Marshall College, Pennsylvania, USA. Where a measured $X\mathrm{Fe}^{3+}$ was not available, a value of 0.1 was chosen in line with the median global pelite composition (*Forshaw and Lanari*, 2024). The composition of each sample is provided in Table C.4.

4.4.2 Results

4.4.2.1 Z03b: garnet-kyanite schist

ZO3B is a garnet-kyanite schist collected south of the village of Mutanda (Fig. 4.6). The bulk composition contains CaO wt.% of 2.81, which is greater than the upper adjacent value for the global median pelite database (2.5 wt.%). This suggests a relatively carbonate-rich mudstone protolith. The total iron (11.62%) is also relatively high.

Table 4.1 Inversion fit values for sample lithologies.

Sample	Variable	Phase	Predicted	Mean	1σ	Fit Score
Z29	Ti	biotite	0.07400	0.07630	0.00380	0.30263
Z29	XMg	biotite	0.47700	0.52000	0.02600	0.82692
Z29	Si	muscovite	3.02000	3.10000	0.16000	0.25000
Z29	Xpa	muscovite	0.09800	0.09740	0.00940	0.03191
Z10	Ti	biotite	0.09100	0.09140	0.00490	0.04082
Z10	XMg	biotite	0.55330	0.54900	0.00430	0.50000
Z10	Xab	plagioclase	0.58970	0.56400	0.05200	0.24712
Z10	Xcz	epidote	0.63160	0.44800	0.09900	0.92727
Z03b	Xalm	garnet	0.69130	0.70000	0.00540	0.80556
Z03b	Xgr	garnet	0.13730	0.15300	0.01100	0.71364
Z03b	Xprp	garnet	0.14150	0.13500	0.00550	0.59091
Z03b	Si	biotite	2.69380	2.71000	0.02000	0.40500
Z03b	Ti	biotite	0.07650	0.08520	0.00440	0.98864
Z03b	Xab	plagioclase	0.63800	0.65200	0.01100	0.63636

The sample contains a peak metamorphic assemblage of garnet, biotite, kyanite, muscovite, plagioclase, and quartz. A spaced schistosity is observed, with microlithons of quartz and biotite and a foliation defined by muscovite. There are three tiers of grain size: coarse, granoblastic quartz and biotite in the microlithons (1–2 mm), fine-grained mica and quartz in the foliation ($<$ 0.25 mm), and large poikioblastic garnet crystals (2.0–2.5 mm). Garnet occurs as rounded to subangular poikiloblasts, with spiral inclusion trials (Fig. 4.6C). This is suggestive of a syntectonic timing of formation. The garnets display normal zoning, with compositions varying from rim to core as follows: Xalm = 0.62–0.71, Xpy = 0.07–0.14, Xgrs = 0.26–0.13 and Xspss = 0.05–0.003 (Appendix C). The kyanite grains occur as highly cleaved, 0.5–1.5 mm grains wrapped

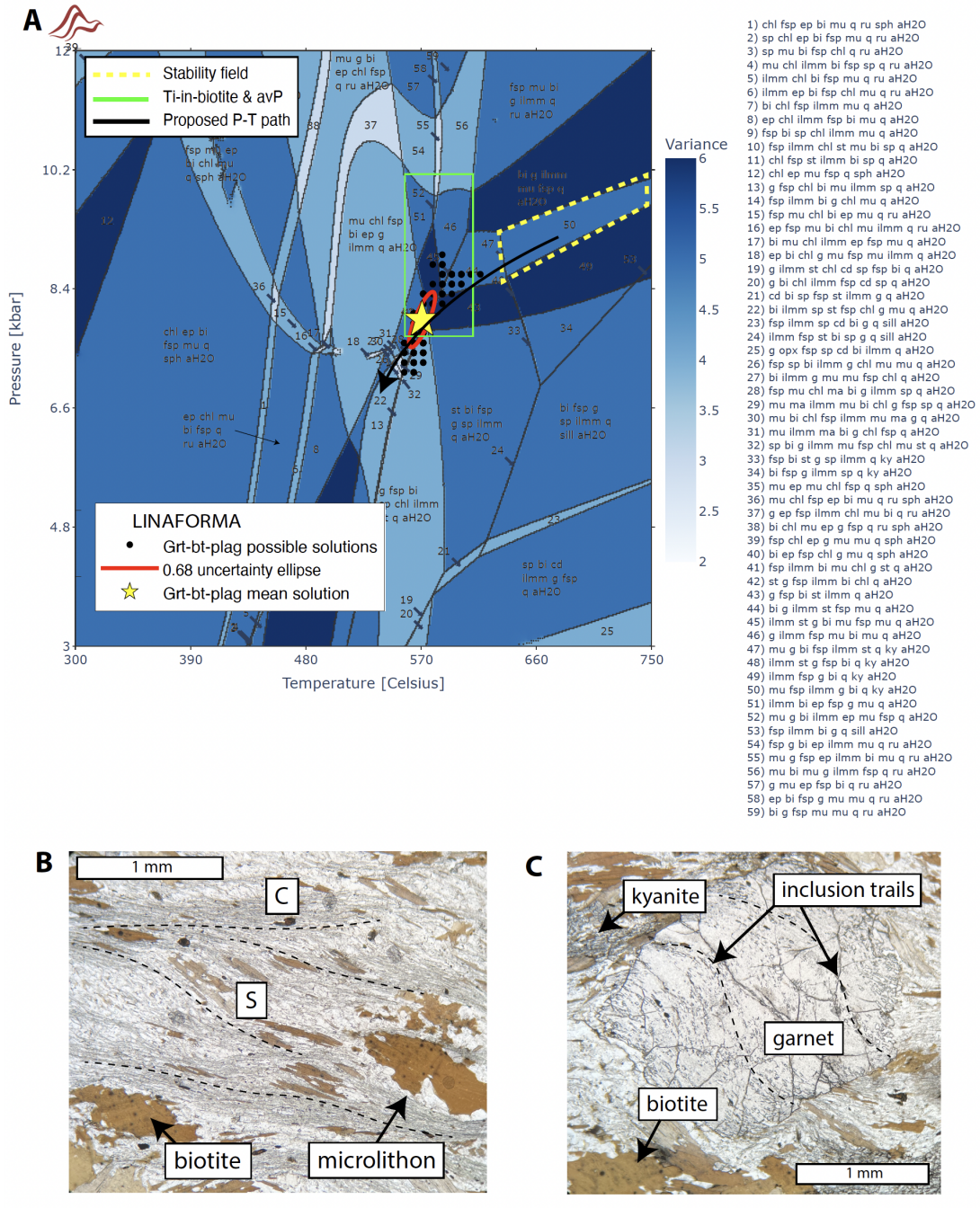

Fig. 4.6 A) P-T results for Z03b. B) and C) Photomicrographs of Z03b.

within the foliation, and are found most commonly neighbouring the garnet poikiloblasts. Muscovite defines a C-S fabric (Fig. 4.6B), although there is no compositional variation between microstructural locations (Xmu = 0.70–0.73). The sample contains two textural populations of biotite: tabular grains (0.5–2mm) preferentially aligned with the schistosity, and anhedral grains intergrown with quartz in the coarse-grained microlithons (Ti per 11 oxygen = 0.08–0.1, XMg = 0.54–0.58). Fine-grained plagioclase is observed within the rock matrix, with an andesine composition (Xab = 0.64–0.67). All phases are interpreted to be in equilibrium.

Compositions from nine biotite grains were used for the Ti-in-biotite thermometer, resulting in a temperature range of 572–613 °C. When combined with avP results, this gave a fluid-independent estimate of peak metamorphic conditions of 8.9 ± 0.63 (1σ) kbar at 595 °C. The pseudosection and forward models were calculated using an XFe3+ of 0.1 and an activity of water of 0.8. The observed peak assemblage garnet, biotite, kyanite, muscovite, quartz and ilmenite is calculated to be stable at temperatures of at least *ca.* 630 °C and a pressure of *ca.* 8.6–10.1 kbar (yellow outline in Fig. 4.6A).

The LinaForma grid-search inversion was performed by jointly inverting the measured garnet rim compositions (Xalm = 0.70 X), biotite chemistry (Si per formula unit (p.f.u.), xTi per 11 oxygens, XMg), and plagioclase chemistry (Xalbite) for pressure and temperature using a sum of absolute residuals objective function. The definition of these parameters can be found in Table 3.1. Parametric bootstrapping was performed assuming a Gaussian distribution. Each variable was assigned a standard deviation equal to either the standard deviation of the actual measurements or 5% of the mean values (following Palin et al., 2016), which ever was larger. The inversion results were only kept if the forward model predicted values fell within 2 standard deviations of the observed value (Table 4.1). The inversion produces a result of 575 °C (Inter-Quartile Range (IQR) = 565–575 °C) and 7.8 kbar (IQR = 7.7–8.0 kbar). The results from the Ti-in-biotite thermometry, avP analysis, and the LinaForma inversion agree within error, but are displaced down temperature and down pressure from the calculated equilibrium assemblage field. The lower temperature bound of the pseudosection stability field corresponds with the low temperature bound of kyanite, below which it is predicted to be replaced by staurolite. At lower temperatures, the muscovite would be replaced by chlorite. These results suggest that Sample Z03b experienced peak metamorphism at temperatures of at least 680 °C and at least 8.6 kbar, before experiencing a retrogression to conditions of approximately 575 °C and 7.8 kbar.

4.4.2.2 Z10: biotite-epidote-kyanite schist

Z10a is a biotite-epidote-kyanite schist collected approximately 2.5 km south of the Kansanshi Mine license (Fig. 4.7). The bulk composition is elevated in CaO (4.38 wt.%) relative to the median pelite, as is MgO (4.13 wt.%). The sample contains a

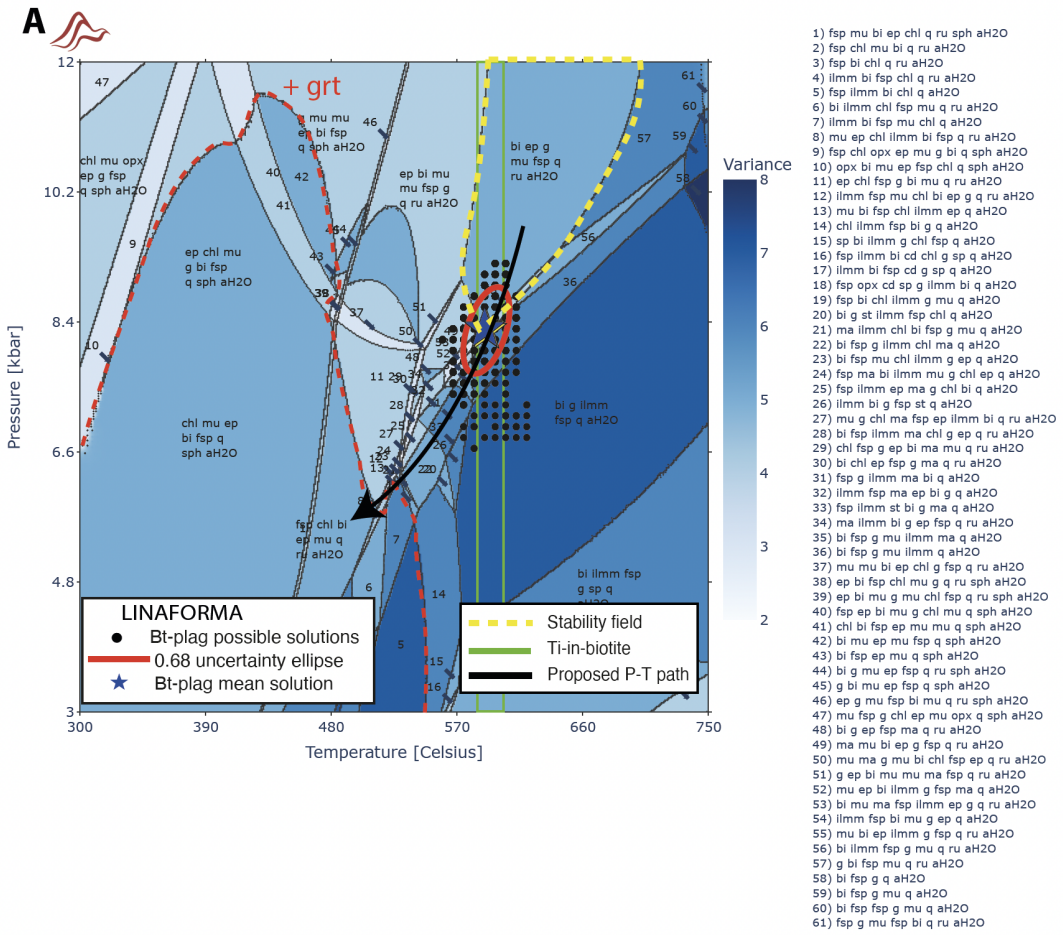

Fig. 4.7 A) P-T results from Z10. B) and C) Photomicrographs of Z10.

primary assemblage of kyanite, biotite, epidote, muscovite, quartz and plagioclase, with a discontinuous schistosity defined by aligned biotite, muscovite and epidote. There are two populations of biotite grains: fine-grained anhedral grains which help define the foliation, and very coarse porphyroblasts up to 5 mm. These porphyroblasts commonly show intergrowths with quartz. Despite the textural variation, the biotite composition is relatively homogeneous (Ti per 11 oxygen = 0.09–0.1, XMg = 0.54–0.56). Epidote is found throughout the sample, with a foliation-parallel preferred orientation. The grain size varies up to 0.5 mm and the composition varies within the range $X\mathrm{Fe}^{3+}$ = 0.53–0.86. Muscovite is fine grained and defines the schistosity. Quartz grains vary up to 0.25 mm, with some coarsening observed in zones with less muscovite or when neighbouring biotite porphyroblasts. Plagioclase feldspar is found within the matrix, with an andesine to minorly labradoritic composition (Xab = 0.43–0.64). Kyanite is present as centimetre-scale anhedral crystals encompassing the surrounding biotite and quartz grains, as well as smaller (∼1mm) subhedral grains in contact with large (3 mm) biotite grains. The kyanite is interpreted to represent a breakdown product with biotite and quartz after garnet (Fig. 4.7B). This relationship is common in the retrogression of metapelites (e.g., *Yardley*, 1977; *Searle et al.*, 1992).

The Ti-in-biotite thermometer was applied to 17 grains of biotite, resulting in a temperature estimate of 587–606 °C, with a mean of 596 °C. The avP analysis was inconclusive because the inversion was forced to use an incomplete set of reactions. Given the interpretation of kyanite as a breakdown product after garnet, the equilibrium phase assemblage at time of peak metamorphism would have been garnet, biotite, epidote, muscovite, quartz, plagioclase and rutile. This is found to be stable at conditions of *ca.* 575–705 °C and at least 8.4 kbar (Fig. 4.7A). Kyanite is not predicted anywhere within this pressure-temperature range, which is perhaps unsurprising given that the sample is relatively poor in Al_2O_3 wt.%. The presence of kyanite is perhaps best explained by the lack of mobility of the Al ion, resulting in a significant local enrichment of Al at the sites of garnet breakdown relative to the bulk rock as a whole. The biotite chemistry (xTi, XMg) and plagioclase chemistry (Xab) were jointly inverted for pressure and temperature using LinaForma. The forward models were calculated using an $X\mathrm{Fe}^{3+}$ of 0.1 (*Forshaw and Lanari*, 2024). The resulting best-fit solution is 590 °C (IQR = 580–595 °C) and 8.7 kbar (IQR = 8.4–9.0 kbar)(Fig. 4.7). This overlaps with the temperature estimate of the Ti-in-biotite geothermometer and is within error of the lowest region of the pseudosection stability field. Sample Z10 must therefore have equilibrated at these conditions, losing the garnet to biotite and kyanite along the retrograde path. However, the biotite and plagioclase largely preserve a high-pressure chemistry, suggesting that garnet must have made up only a minor proportion of the total rock volume.

4.4.2.3 Z36: garnet-biotite schist

Sample Z36 is a garnet-biotite-chlorite schist collected from the northern margin of the Kansanshi Mine pit (Fig. 4.8). The bulk composition is enriched in TiO_2 and FeO^T, with a measured $X Fe^{3+}$ of 0.23. The rock also contains 1.16% SO_3 in the form of disseminated Fe sulfides. The age of the mineralization at Kansanshi is 512–502 Ma, and thus post-dates the 530 Ma peak of metamorphism. Considering this, and the position of the sample as the hanging wall rock to the Kansanshi Mine deposit, which experienced infiltration by post-tectonic Cu-S-rich fluids (*MacIntyre*, 2019), the sulfur in this sample is considered post-tectonic. As such, it is not included within the model system. The primary assemblage includes garnet, biotite, muscovite, chlorite and quartz, with abundant Fe sulfide opaques (Fig. 4.8C). The sample features a continuous schistosity defined by muscovite and quartz, with minor crenulations in places. The garnet occurs as 1–2.5 mm porphryoblasts with spiral inclusion trails of predominantly quartz. The inclusion trails are continuous with the gross foliation of the rock. The garnet displays normal zoning (Xalm = 0.75–0.8, Xprp = 0.04–0.11, Xspss = 0.065–0.002, Xgrs = 0.17–0.09) (Appendix C), although some of the garnets have been significantly retrogressed to muscovite and chlorite (Fig. 4.8B). The alteration is often focused in fine-grained veinlets which cross-cut the garnet. Chlorite, muscovite (Xmuscovite = 0.61–0.66) and biotite (Ti per 11 oxygen = 0.07–0.08, XMg = 0.39–0.40) occur as foliation-parallel tabular grains varying from < 0.5 mm up to 2.5 mm. Coarse-grained anhedral chlorite and granoblastic quartz form distinct layers within the sample. The chlorite displays a relatively large compositional variation (XMg = 0.46–0.54), likely related to differing degrees of retrogression. The opaques vary from fine-grained, shaped-aligned grains within the muscovite-rich matrix, and coarser (though still < 0.5mm) anhedral grains within the chlorite-quartz layers. The sample is largely interpreted to represent an equilibrium assemblage, except for the muscovite-chlorite breakdown products after garnet.

The Ti-in-biotite thermometer was used on three biotite grains from sample Z36 and produced temperatures of 493–523 °C. Fluid-independent equilibria in avP resulted in a statistically significant result of 5.5 ± 1.76 (1σ) kbar at 510 °C, and a fluid-dependent result of 3.4 ± 2.7 (1σ) kbar when using an activity of water equal to 0.8. Activities of 0.9 and 1 failed to produce acceptable results. Z36 was the only sample in this study to provide a reliable constraint on the activity of water, and so aH2O = 0.8 was used for the petrological modelling of all the remaining samples.

Garnets in Z36 preserve a clear prograde zoning profile. Linear transects where performed across four garnets, with forty EPMA points each. The compositions of each analysis (Xalm, Xgr, Xpy) were inverted for pressure and temperature using LinaForma (scatter points in Fig. 4.8A, line profiles of Fig. 4.9). The garnets each show a relatively clear trend from *ca.* 6.7 kbar at the centre of the garnet up to *ca.* 8.5 kbar at the

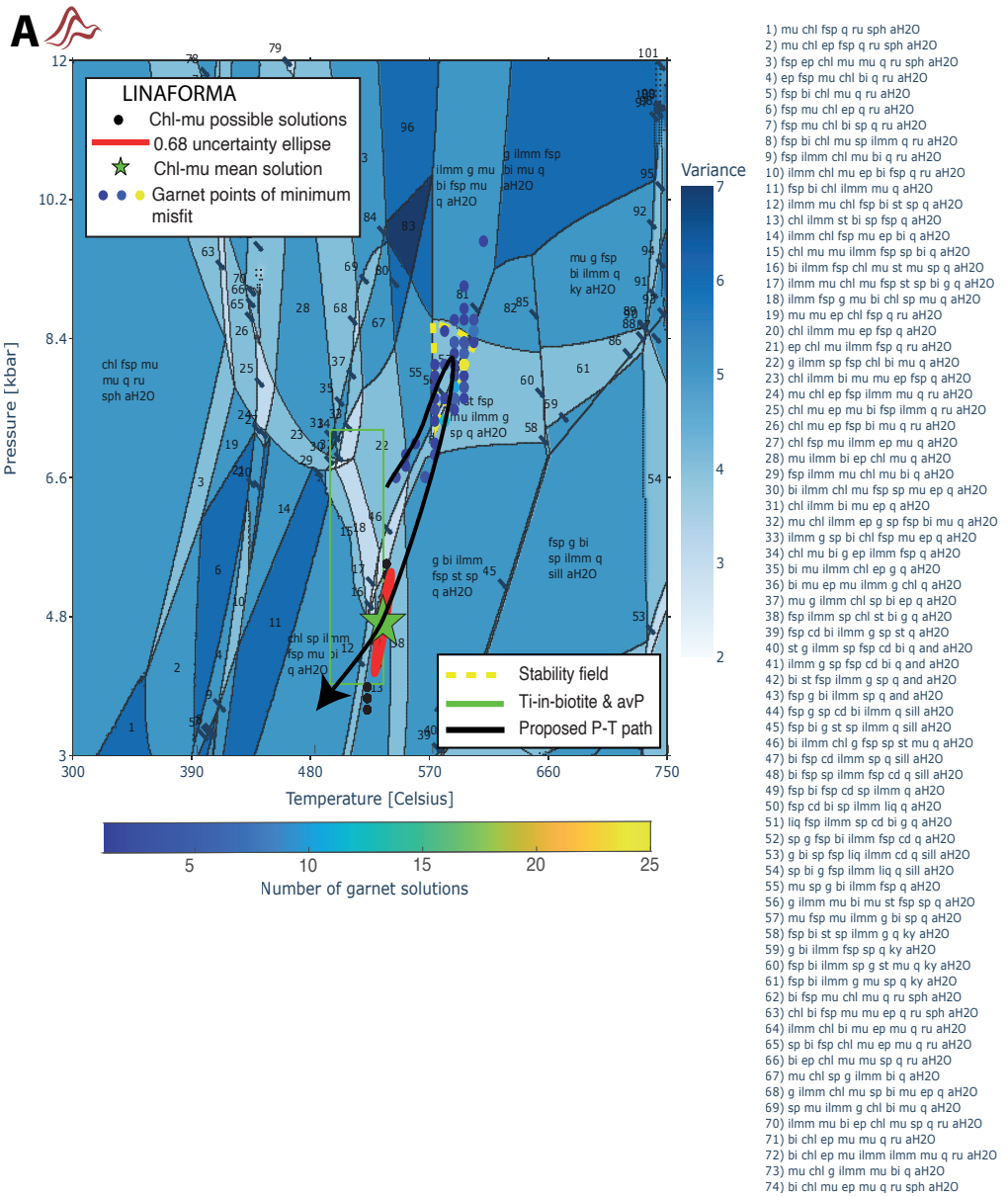

Fig. 4.8 A) P-T results from Z36. B) and C) Photomicrographs of Z36.

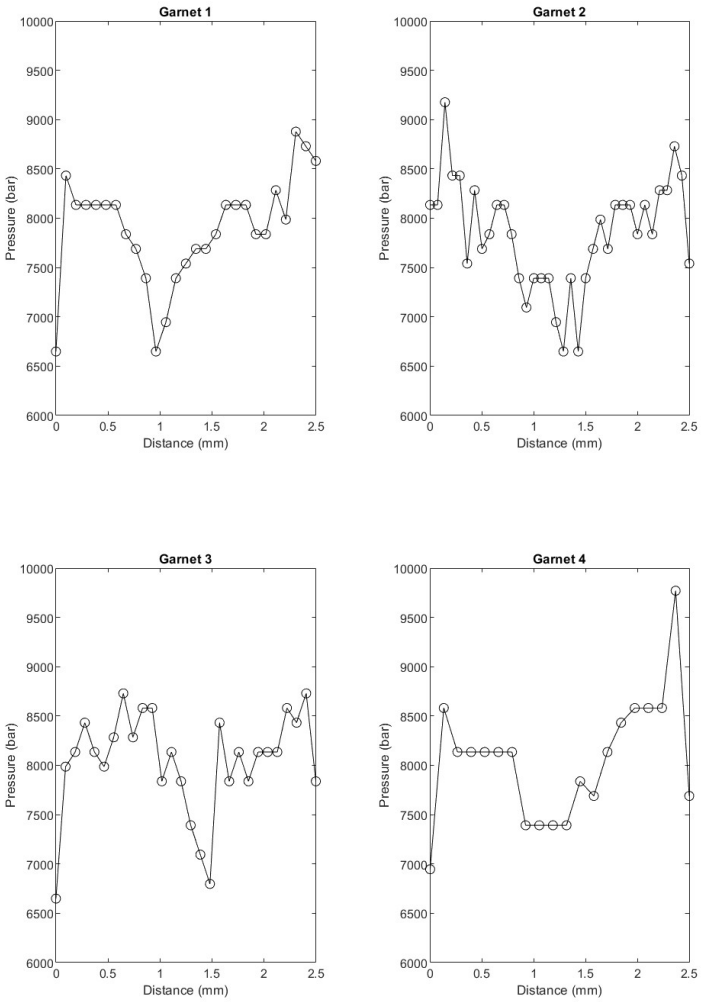

Fig. 4.9 Garnet pressure paths for Sample Z36, inverted for using LinaForma.

rim, before a steep decrease in pressure at the rim of the garnet. This is interpreted to represent a prograde increase in pressure (and accompanying increase in temperature) to a maximum of around 8.5 ± 0.5 kbar, followed by a retrogression to lower pressures (Fig. 4.8A).

The peak pressure estimate lies within the stability field of garnet, feldspar, muscovite, sphene, ilmenite, biotite, quartz and H2O (yellow field in Fig. 4.8A). This field suitably matches the assemblage of Z36. The chlorite observed in the sample is interpreted as a retrogressive phase after biotite and garnet, and the feldspar has been largely altered during retrogression and the post-tectonic influx of S-rich fluids. The chlorite (XMg) and muscovite (Si p.f.u., Xmu) compositions were then inverted for pressure and temperature, resulting in a best-fit solution of 535 °C (IQR = 530–535) and 4.7 kbar (IQR = 4.4–5.0 kbar). This agrees with the constraints provided by avP and the Ti-in-biotite thermometry, and must represent equilibrium along the retrograde path.

4.4.2.4 Z29: biotite-muscovite schist

Z29 is a biotite-muscovite schist collected approximately 7.5 km to the south-east of the Kansanshi Mine license (Fig. 4.10). The bulk composition is enriched in MgO (4.81 wt.%) and CaO (2.69 wt.%) relative to a typical pelite, although SiO2 (56 wt.%) is low. The primary assemblage is biotite, muscovite, quartz, with minor opaques. The foliation of Z29 is defined by fine-grained muscovite, which wraps around very coarse (up to 5mm) subhedral porphyroblasts of biotite and quartz (Fig. 4.10C). In places these porphyroblasts display complex intergrowths of biotite and granoblastic quartz. In other areas of the sample, the grains are predominantly poikiloblastic biotite with multiple quartz inclusions. Fine grained anhedral biotite and quartz are found within the matrix, as are subhedral opaque grains which vary up to 0.25 mm in diameter. These opaque grains are preferentially located near or within coarse biotite crystals. The biotite and quartz porphyroclasts are interpreted to represent pseudomorphs after garnet because of the similarity in shape, the complex intergrowths of the biotite and quartz and the clear rheological contrast between the clasts and the surrounding quartz-muscovite matrix.

Using 24 biotite point analyses, the Ti-in-biotite thermometer calculated temperatures of 535–574 °C, with a mean of 558 °C. The biotite (Ti per 11 O, XMg) and muscovite (Si p.f.u., Xpa) were inverted for pressure and temperature, yielding a result of 545 °C (IQR = 535–550 °C) and 2.5 kbar (IQR = 2.2–2.9 kbar) (Fig. 4.10A). This result overlaps with the stable assemblage field of biotite, muscovite, quartz, ilmenite, feldspar, rutile and H2O. However, there is no evidence for feldspar or andalusite in Z36 despite both phases being predicted throughout wide areas of P-T space. This is thought to be the result of andalusite + Kfs + H2O reacting to muscovite + quartz on retrogression, which is a well-documented reaction in low-grade metapelites (Berman, 1988). The reaction is often interpreted to proceed in the opposition direction (i.e.,

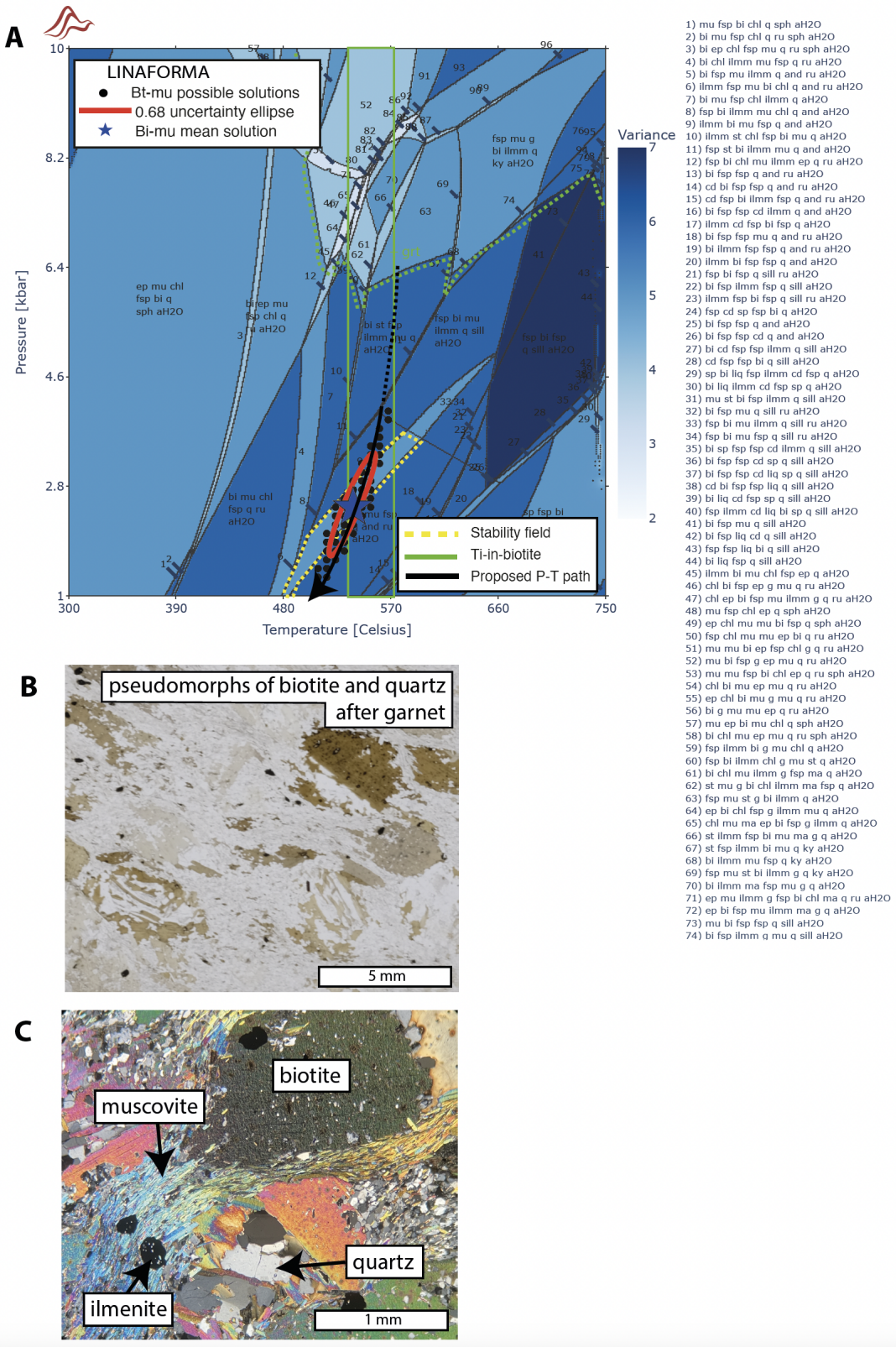

Fig. 4.10 A) P-T results from Z29. B) and C) Photomicrographs of Z29.

muscovite reacting to andalusite) as a result of contact metamorphism (*Pattison and Goldsmith*, 2022). This lower assemblage field is interpreted as a retrograde equilibrium, as it lacks the required garnet after which biotite and quartz are pseudomorphs (Fig. 4.10B). The exact location of the peak field is unknown, although it must lie above the garnet-in line which exhibits a minimum pressure of *ca.* 5.8 kbar.

4.4.2.5 Z34: garnet-biotite schist with felsic intrusions

Sample Z34 is a garnet-biotite-muscovite schist containing veins of K-feldspar-rich melt (Fig. 4.11). The sample was collected from the western edge of the Kansanshi Mine

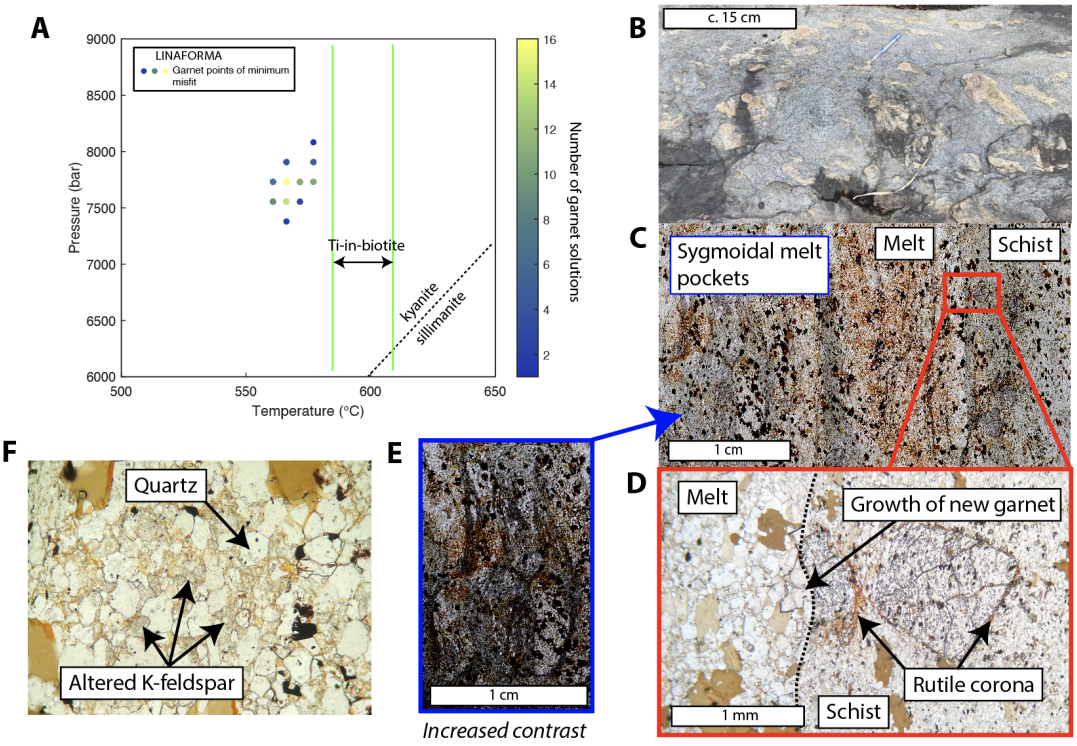

Fig. 4.11 A) P-T results from Z34. B) Photograph of outcrop from where Z34 was collected. C) Photograph of Z34 thin section. D) Photomicrograph of Z34. E) Photograph of Z34 thin section. F) Photomicrograph of Z34.

license. At outcrop, hand-sample and thin-section scale, Z34 can be separated into a red, K-feldspar bearing granitic unit and a grey schistose unit (Fig. 4.11B, C). At thin-section scale, the subsolidus schistose unit is characterised by a primary assemblage of garnet, biotite, plagioclase, quartz, and muscovite. The garnet occurs as quartz- and rutile-rich poikiloblasts (< 2 mm) with spiral inclusion trails and displays little chemical zoning (Xalm = 0.71–0.74, Xprp = 0.07–0.11, Xgr = 0.19–0.13, Xspss = 0.04–0.02) (Appendix C). In some cases, the garnets are relatively skeletal and feature a rutile-rich amorphous corona. The garnet grain in Fig. 4.11D is clearly divided between an inclusion-rich section which grew within the schistose unit, and an inclusion-free section

which grew within the melt unit. This is interpreted as two different stages of garnet growth: one prior to the intrusion of the felsic material (inclusion-rich), and one after the intrusion while the rock was still within the garnet stability field (inclusion-poor). The biotite occurs as 0.25–0.5 mm tabular grains throughout the matrix, with a slight shape-preferred orientation. In a similar way to the garnet, the biotite displays little chemical variation (Ti per 11 O = 0.10–0.11, XMg = 0.50–0.52). The matrix also comprises fine quartz and abundant shape-aligned fine muscovite (Xmu = 0.65–0.68). The melt veins are characterized by coarse, granoblastic quartz with intergrown, anhedral biotite and abundant pinite alteration of K-feldspar (Fig. 4.11F). The veins contain minor muscovite, and only minor, skeletal garnet. The boundaries between the finer-grained schistose unit and the coarser-grained melt unit vary throughout the sample. In some areas, the boundary is sharply defined with clear variations in grain-size and mineralogy across the divide (Fig. 4.11D), whereas in other areas the melt pockets are sigmoidal and appear wrapped within the foliation (Fig. 4.11E). This textural difference is attributed to variations in competence and melt volume fraction between different parts of the sample. This is unlikely to represent a primary igneous intrusive relationship, and more probably represents a syn-tectonic intrusion. The lack of sillimanite and melt-structures in the schist, paired with the abundance of micas, prevents a migmatite interpretation.

Following this preliminary analysis, it was clear that the XRF-determined bulk composition of the sample was unsuitable for use in petrological modelling due to the introduction of granitic material. As such, the analysis of this sample was limited to the Ti-in-biotite thermometer, avP, and garnet isopleth modelling using the global median pelite as the bulk composition. Garnet isopleths are relatively unperturbed by minor changes in bulk composition (*Waters and Lovegrove*, 2002). The Ti-in-biotite thermometer was applied to eight biotite grains, giving a temperature of 586–609 °C. Linear transects of EMP point analyses were performed on five garnets, and the composition of each point analysis (Xalm, Xpy, Xgr) was inverted for pressure and temperature using LinaForma. The resulting solutions cluster strongly around 560–580 °C and 7.5–8.0 kbar, which aligns well with the results from the other samples (Fig. 4.11). This is slightly lower temperature than the Ti-in-biotite thermometry. Although not plotted in Fig. 4.11A, the LinaForma inversion analysis was also performed assuming a bulk composition equal to the other garnet-bearing samples in the sample set (Z36 and Z03b). For each of these analyses, the garnet temperatures clustered around *ca.* 550 °C. As such, it is unlikely that the lower temperature of the garnets relative to the biotite represents an incorrect bulk-composition used for forward modelling. Instead, it suggests that biotite grew at an earlier stage in the *P-T* evolution of the rock. The felsic material intruded sometime after peak metamorphism, but the microstructures suggest this was before the cessation of deformation (Fig. 4.11E) and while the rock was still within the garnet stability field (Fig. 4.11D).

4.4.3 Metamorphic Synthesis

A comparison of our five samples with analyses available in the literature for the Domes Region is presented in Fig. 4.12. The samples documented in this study record clockwise

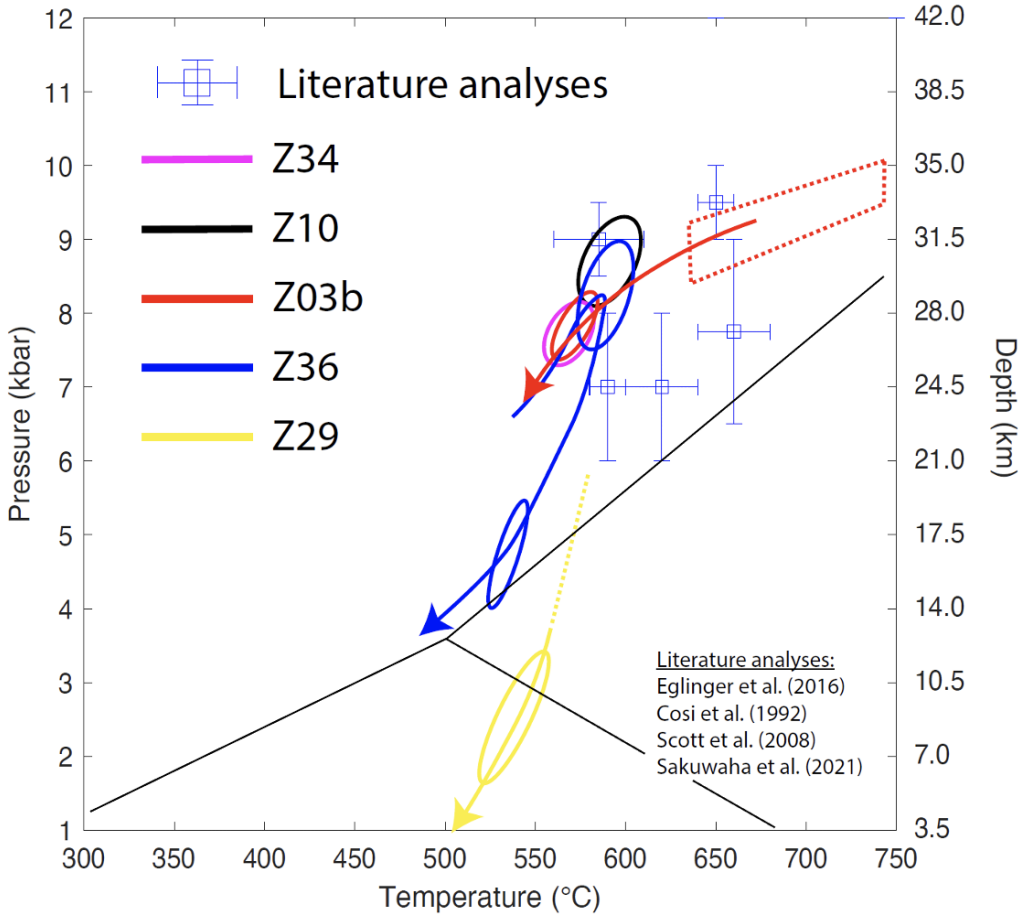

Fig. 4.12 P-T estimates from this study and from the literature.

P-T paths with peak metamorphic conditions of approximately 550–620 °C and 7.5–9.5 kbar, fitting expected conditions for classical models of Barrovian metamorphism (e.g., *Kohn*, 2014). This corresponds to burial depths of ~26–33 km, assuming a lithostatic gradient of 3.5 km/kbar. The peak conditions of samples Z03b and Z29 are relatively unconstrained, although sample Z03b likely records peak metamorphic conditions higher than 640 °C and 8.5 kbar (red dotted field in Fig. 4.12). Our samples record broadly similar conditions to those in the literature, in particular a garnet-kyanite amphibolite preserved within the core of the Mwombezhi Dome (585 ± 25 °C, 9 ± 0.5 kbar). This amphibolite was dated at 530 ± 2 Ma using Lu-Hf garnet (*Eglinger et al.*, 2016). This age overlaps with a 529 ± 2 Ma monazite age from a garnet-kyanite schist to the south of the Solwezi Dome (*John et al.*, 2004). As such, we expect that our samples experienced the same metamorphic event as those documented by *John et al.* (2004) and *Eglinger et al.* (2016).

The conditions of retrograde metamorphism have been reliably constrained in samples Z03b, Z36, and Z29, although sample Z03b records evidence of high-pressure conditions that likely document a very early stage in the retrograde path. Of particular note is the difference in temperature gradient preserved in samples Z36 and Z29. Z36 records retrograde conditions of 535 °C (IQR = 530–535) at 4.7 kbar (IQR = 4.4–5.0 kbar), whereas Z29 records conditions of 545 °C (IQR = 535–550 °C) at 2.5 kbar (IQR = 2.2–2.9 kbar). This difference is thought to be reliable because the difference is recorded by both conventional thermobarometry and phase diagram-based techniques. For example, garnet is preserved within sample Z36 and sample Z203b, but has been entirely replaced by biotite and quartz in sample Z29. There are two main interpretations that match this observation:

1. All the samples experienced the same *P-T* evolution, and therefore the same conditions on the retrograde path. However, each sample has undergone a slightly different extent of retrograde transformation. This may have been controlled by the bulk-composition and the availability of internally hosted water. If this is the case, the samples must have experienced near isothermal decompression from ∼525 °C at 5 kbar (Z36) to ∼525 °C at 2.5 kbar (Z29).

2. The rocks are recording a significantly different retrograde path. Sample Z29 preserves a higher thermal gradient, which could either be attributed to (a) a high-temperature, relatively low-pressure overprint on the retrograde path due to the intrusion of hot granitic material, or (b) Z29 experienced a higher grade of peak metamorphism and a higher temperature retention during exhumation.

Given the low number of samples analysed here, we cannot ascertain which of these scenarios is most probable. However, *Eglinger et al.* (2016) reported the presence of syn-tectonic melting proximal to the Mwombezhi Dome based on intrusive field relationships, with deformed granitic veins wrapped around the Lufilian amphibolites (Fig. 6 of *Eglinger et al.*, 2016). Felsic material is also observed within the metamorphic sheet around Solwezi, and is clearly intrusive (Fig. 4.11B). It is therefore possible that samples Z29 and Z34 record the elevated thermal gradient associated with the intrusion of magmas at the base of the thrust stack after peak metamorphism. The growth of garnet over the felsic material in Z34 (Fig. 4.11D) points towards intrusion while the rocks were within the garnet stability field. However, Z29 lay outside the garnet stability field when it experienced the high T - low P conditions. Detailed geochronological analysis of the felsic material and further pressure-temperature analysis of the metamorphic sheet is required to properly distinguish between these options.

4.5 Tectonic Synthesis

Based on our results, we present a new model for the tectonic evolution of the Kansanshi Mine and NW Zambian Copperbelt (Fig. 4.13). There are few ages constraints available for Solwezi, so the presented model makes use of ages from the entirety of the Domes Region which is assumed to have undergone the same geodynamic evolution. This is supported by the similarity in the P-T evolution of the rocks (see Section 4.4.3) and the similarity in ages where available. Nonetheless, there is a sparsity of available geochronological data, so age constraints are relatively wide.

The onset of continental extension between the Congo Craton to the north and the Kalahari Craton to the south led to the deposition of the Lower Roan continental red beds during the Tonian Period, < 840 Ma (*Turlin et al.*, 2016). The Kansanshi sub-basin formed via extension on the northern edge (modern-day reference frame) of the main Katangan rift basin at this time. Subsidence continued throughout the Tonian, leading to the deposition of the Upper Roan carbonates and evaporites in a shallow-marine setting. This was followed by a second stage of rifting, marked in the basin by the onset of deposition of the Mwashia Group (*Purkiss*, 2025). Metagabbros within the Kansanshi Mine and surrounding the Solwezi Dome formed between 753 ± 9 Ma and 742 ± 8 Ma (*Barron*, 2003) during this stage of rifting. Alkaline and mafic magmas are commonly associated with regions of crustal extension. The basin continued to deepen, leading to the deposition of the Nguba Group sediments during the Cryogenian. The metamorphic sheet within Kansanshi contains detrital zircons with a minimum age of 698 ± 7 Ma, indicating that the protoliths to the sheet were deposited during Nguba times at the earliest (*MacIntyre*, 2019). The youngest shales in the Katangan basin were deposited at < 573 Ma (*Master et al.*, 2005; *Cailteux and Putter*, 2019).

The basin began to close during the late stages of the Ediacaran (Fig. 4.13A), although the driving force for closure remains uncertain. *John et al.* (2003) reported 595 ± 10 Ma oceanic high-P, low-T eclogites from the Zambezi Belt, suggesting that the Katangan basin had become truly oceanic, and a period of oceanic subduction had been instigated. The oceanic subduction resulted in ocean closure and the collision of the Congo and Kalahari cratons during the late Ediacaran to early Cambrian period (*John et al.*, 2003). This collision is locally known as the Lufilian Orogeny but is an expression of the wider Pan-African orogeny. However, it has been debated whether the Zambezi Belt is tectonically linked to the Copperbelt. *Daly et al.* (2024) considers the Mwembeshi Shear Zone to mark the southern edge of the Katangan Basin, and thus separates the Domes Region to the north from the Zambezi Belt to the south. *Daly et al.* (2024) argue that the metamorphism is the result of complete inversion of a marine transitional basin and partial continental subduction of the lower northern plate beneath the Southern Rift basin of the Katangan basin. Regardless of the mechanism, it is clear from the abundance of Cambrian monazite ages (e.g., 530 ± 2 Ma; *Johns et*

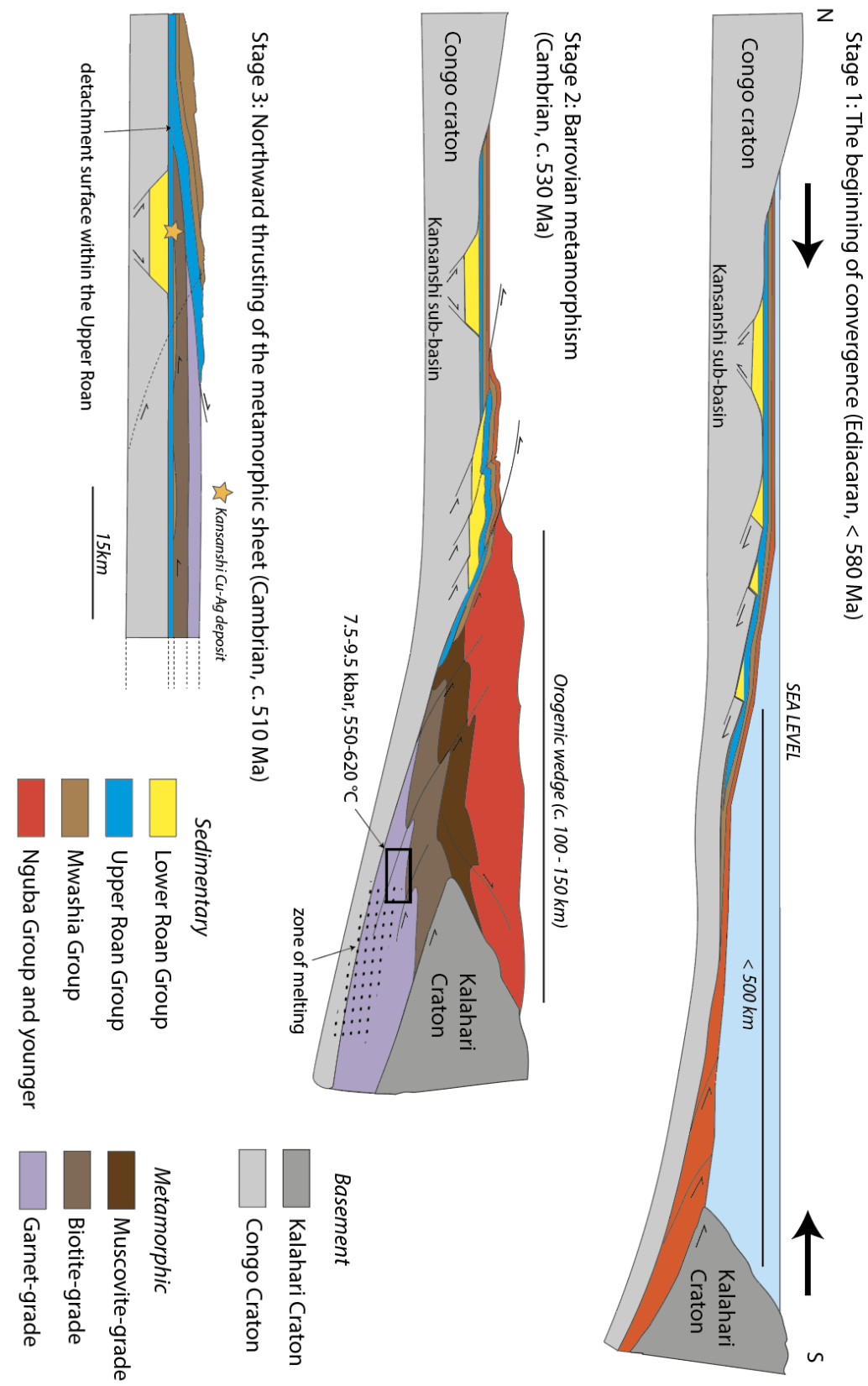

Fig. 4.13 Tectonic model for Kansanshi and the NW Zambian Copperbelt.

al., 2004) that a significant orogenic wedge had formed because of the collision between the Congo craton and the Kalahari craton. The metamorphic sheet at Kansanshi experienced garnet and kyanite-grade metamorphism and accompanying deformation (D0) within this wedge, with peak metamorphic conditions of approximately 550–620 °C and 7.5–9.5 kbar (Fig. 4.13B). This corresponds to burial depths of ∼26–33 km, assuming a lithostatic gradient of 3.5 km/kbar. These metamorphic conditions are typical of a medium-pressure, medium-temperature Barrovian sequence, such as those found in the Greater Himalayan Sequence or the Barrow Zones of Scotland (e.g., *Vorhies et al.*, 2013). It is proposed that crustal thickening led to the syn-tectonic generation of crustal granitic melts, as observed throughout the Solwezi area (e.g., sample Z34) and the Mwombezhi Dome (*Eglinger et al.*, 2016). The age of these granitic melts has not been determined analytically, but the field constrains suggest a syn-tectonic timing of formation. The source of these melts is unclear - they could be sourced from deeper structural levels within the orogenic wedge or perhaps sourced from melting of the down-going Congo plate. It is probable that the metamorphic inversion observed in the metamorphic sheet (garnet-grade structurally above biotite-grade rocks) resulted from ductile thrusting in the orogenic wedge during peak metamorphism, as seen in the Greater Himalayan Sequence (e.g., *Beaumont et al.*, 2001; *Kohn*, 2008). The orogenic wedge must have developed to the south of Kansanshi, in the modern-day reference frame, to allow for the northward thrusting of the metamorphic sheet over the Kansanshi sub-basin.

Following peak metamorphism, significant lateral transport of the metamorphic sheet was facilitated by thin-skinned thrusting above a regional decollement located in the Upper Roan unit (D1 deformation, Fig. 4.13C). This transport saw the overthrusting of garnet and biotite grade rocks over the semi-autochthonous to autochthonous sediments of the Congo passive margin, including those of the Kansanshi sub-basin (Fig. 4.13C). This overthrusting was followed by minor northwards out-of-sequence thrusting of the underlying basement blocks, truncating the expected litho-stratigraphic sequences (D2 deformation). The timing of D1 and D2 are not well constrained. Zircon overgrowths on a metagabbro north of the Solwezi Dome indicate a thermal event at 510.9 ± 7.8 Ma (*Barron*, 2003), while the Kansanshi Cu-Au vein-hosted mineralisation occurred in two stages at 512 ± 1.2 Ma and 502 ± 1.2 Ma (*Torrealday et al.*, 2000). This is notably later than most of the mineralisation within the Domes Region, which predominantly overlaps with peak metamorphism at c. 530 (*Sillitoe et al.*, 2015). D1 and the subsequent D2 events are assumed to be roughly contemporaneous with the vein mineralisation and the zircon overgrowth thermal event.

Finally, post-orogenic uplift and cooling of the Roan group sediments below 250 °C is known to have occurred between approximately 500 - 410 Ma based on zircon fission-track thermochronometry (*Purkiss*, 2024). The extensional boudins observed within Kansanshi (*MacIntyre*, 2019) likely formed at this time.

4.6 Discussion

4.6.1 Comparison to previous tectonic models

The tectonic model presented in Section 4.5 is the first all-encompassing model for the NW Zambian Copperbelt that is consistent with sedimentary, metamorphic and structural information available in the literature and collected in this study. It has some important similarities to existing models, most notably the recognition of a Lower Roan depocenter beneath the Kansanshi Mine (*MacIntyre*, 2019; *Daly and Tosca*, 2020). These red-bed sediments are thought to be a key source of copper for the overlying deposit (*Hitzman et al.*, 2012). The general structure of Kansanshi and Solwezi is also an area of broad agreement, with multiple studies recognising the importance of the Kansanshi antiform, the out-of-sequence motion along the Solwezi Dome, the decollement within the Upper Roan, as well multiple phases of deformation (*Arthurs*, 1974; *Barron*, 2003; *MacIntyre*, 2019; *Daly and Tosca*, 2020). The Kansanshi antiform likely proved an important structural trap for the Cu-bearing fluids. A notable point of different between our model and the current models in the literature, however, is our interpretation of the significance and evolution of the metamorphic sheet. *MacIntyre* (2019) and *Barron* (2003) interpreted the "Spangled Schist" as a separate stratigraphic unit and mapped the lithologies exposed within the Kansanshi Mine as belonging to either the Nguba or Kundelungu Group respectively. Neither study is particularly clear about the formation mechanism of the schistose units, and it is uncertain how the various grades of metamorphism were achieved. Without this understanding, it is impossible to provide a coherent model. *Daly and Tosca* (2020) suggest that the Kansanshi Mine formed from an allochthonous series of nappes thrust above the Upper Roan Group sediments during the Lufilian Orogeny. They proposed that the sheet was derived from the expulsion of sediments from a neighbouring rift basin to the south of Kansanshi (in a modern-day reference frame). Their model did not provide a mechanism for the formation of the metamorphic sheet, although the general kinematics agree with those proposed in this study. This study is the frist to provide an interpretation of the metamorphic sheet that is consistent with its P-T conditions of formation. It is also the first to speculate that significant crustal thickening during the Lufilian Orogeny drove granitic magmatism near the Solwezi area. This is consistent with observations made in the Mwombezhi Dome by *Eglinger et al.* (2016), but more work is needed to provide geochronological constraints on the age of intrusion of these felsic bodies.

4.6.2 Sediment thickness beneath Kansanshi

According to the sedimentary copper formation model proposed by *Hitzman et al.* (2012), the Lower Roan depocenter beneath the Kansanshi Mine is likely a key source of copper for the overlying deposit. However, due to the limited availability of deep drill core

data and the absence of comprehensive geophysical surveys, the size and geometry of this sedimentary body remain poorly constrained. Gaining a clearer understanding of its characteristics is critical—not only for assessing its contribution to the Kansanshi deposit but also for evaluating the importance of locating similar sediment bodies in mineral exploration. Moreover, insights into the geometry of this unit could help predict the potential presence of additional large deposits in the vicinity of Kansanshi. Given these implications, further investigation of this sediment body represents an important avenue of research, which will be addressed in detail in Chapter 5.

4.7 Conclusions

This study presents the results of new geological mapping and structural analysis of the Solwezi area in NW Zambia, including the Kansanshi Cu-Au Mine, integrated with a detailed examination of the P-T evolution of five garnet-grade metamorphic rock samples from the area. These new data allow us to propose a revised model for the tectonic evolution of the Kansanshi Mine and the surrounding area of the NW Zambian Copperbelt, both prior to and during the Lufilian Orogeny. Rifting between the Congo and Kalahari cratons during the Tonian Period led to the formation of a rift basin now situated beneath the Kansanshi Mine. Due to the limited availability of deep drill core data and the absence of comprehensive geophysical surveys, the size and geometry of this sedimentary body remain poorly constrained. Convergence between the Congo and Kalahari cratons, beginning in the Ediacaran Period, resulted in the formation of a significant orogenic wedge atop the underlying Congo plate. Allochthonous rocks, thrust over the Kansanshi sub-basin at approximately 510 Ma, experienced burial to depths of 26-33 km in this orogenic wedge by around 530 Ma. Granitic magmatism, driven by crustal thickening and pelitic partial melting, is thought to have occurred during this period.

This new geodynamic model offers the first coherent framework for testing mineralization hypotheses in the NW Zambian Copperbelt. A detailed investigation of the sedimentary body underlying Kansanshi will be presented in Chapter 5, while the implications of this model for the Kansanshi mineral system will be discussed in Chapter 6.

Chapter 5

Ambient Noise Tomography for Local to Regional Mineral Exploration Using Nodal MEMS Accelerometers: A Case Study from the Kansanshi Cu-Au Mine, Zambia.

Abstract

Metals are essential to the success of the energy transition, but the discovery rate of deposits has been in decline. Innovative new methods of exploration are required. In recent years, Ambient Noise Tomography (ANT) using passive seismic wavefields recovered from the background noise recorded by seismometers has gained increasing popularity as a tool in mineral explorations. Many studies have demonstrated its efficacy in mapping the local geological structure of mineral deposits, but have been limited to depths of a few hundred meters to a few kilometers and have focused on small lateral scales. The application of ANT for regional to local/sub-regional (tens of kilometers) exploration has remained untested. In this study, a network of 30 Sercel WiNG MEMS accelerometers was deployed along a c. 50 km NE-SW line through the Kansanshi copper (Cu) – gold (Au) mine. The Kansanshi mine is the third largest copper mine in Africa, with a resource of 982.3 Mt of Cu (using a cut-off grade of TCu 0.2 %) and 0.11g/tonne of Au as of December 2023. Here we show that ANT performed with cost-effective MEMS accelerometers can identify a significant body of metal source sediments beneath Kansanshi, with a thickness of multiple kilometres, as well as structures consistent with the expulsion of mineralizing fluid through focused zones. These results demonstrate that ANT performed with MEMS accelerometers would be a valuable tool for local- to regional-scale mineral exploration of greenfield sites.

5.1 Introduction

The fundamental importance of metals such as copper (Cu), nickel, lithium, and cobalt to electricity transmission and battery technology has seen them become critical components of the energy transition to a Net Zero future. However, S&P Global Market Intelligence has estimated a 20 million tonne deficit in Cu by 2035 as global electrification increases demand. This problem is exacerbated by the declining effectiveness of mineral exploration programs. The discovery rate of deposits has been in decline over the past thirty years (*Okada*, 2021), and the recent growth of exploration budgets has not led

to a meaningful increase in the number of major discoveries (*White and Hook*, 2023; *McKeith et al.*, 2010). Given these circumstances, developing innovative methods for metal exploration and advancing tools and techniques for discovering and defining subsurface deposits is essential (*Wood and Hedenquist*, 2019; *Watzel*, 2023). In recent years, ambient noise tomography has been increasing in popularity as a tool in mineral exploration. A number of studies have proved its efficacy for understanding the local geological structure of mineral deposits (e.g., *Colombero et al.*, 2022) and the significant role this technique will play in mineral exploration was recently documented by *Reid et al.* (2025). However, up until now these studies have focused on the upper 100s metres to the top couple of kilometres and on a limited lateral scale. While this provides valuable insights into the formation mechanisms of a deposit on a local scale, it is of limited use when exploring for new deposits or attempting to understand the geological systems controlling the location of deposits at a regional to local/sub-regional (10s kilometres) scale.

In this study, we propose that ambient noise tomography using nodal Micro-ElectroMechanical System (MEMS) accelerometers can be used to understand the crustal structure of a local- to regional-scale area and thus to vector towards areas which show promise for mineral exploration. To test this hypothesis, a network of 30 Sercel WiNG MEMS accelerometers was deployed along a c. 50 km NE-SW line through the Kansanshi copper (Cu) – gold (Au) mine for 188 days. The Kansanshi mine, owned by First Quantum Minerals (Ltd.), is the third largest copper mine in Africa, with a resource of 982.3 Mt of Cu (using a cut-off grade of TCu 0.2 %) and 0.11g/tonne of Au as of December 2023. It is therefore classified as a supergiant deposit (i.e., $>$ 24 Mt contained Cu). The mine is located approximately 10 km north of Solwezi, Zambia, and is hosted within the Central African Copperbelt (CACB). The CACB comprises the Neoproterozoic Katangan Basin, which is one of three basins worldwide to host supergiant Cu deposits, the two others being the Permian Zechstein basin of Europe (*Vaughan et al.*, 1989), and the Paleoproterozoic Kodaro-Udokan basin of Siberia (*Bakun et al.*, 1966). The CACB contributes about 14% and 60% of the world's supply of copper and cobalt (*Selley et al.*, 2005).

Kansanshi is a sediment-hosted Cu deposit. Sediment-hosted Cu deposits currently account for $\sim$ 23% of the world's Cu production (*Hitzman et al.*, 2005) and largely comprise relatively thin ($<$ 30 m) zones of disseminated and veinlet Cu-sulphides that occur concordant with lithological layering within sedimentary basins (*Hitzman et al.*, 2010). The deposits occur within a variety of sedimentary rock types but are generally found at or near the contact between red-bed sequences and overlying shales, siltones or carbonates (*Hitzman et al.*, 2010). *Hitzman et al.* (2010) described four important controls on the formation of significant sediment-hosted metal deposits: 1) the presence of metal source sediments, 2) the presence of reduced sediments to serve as chemical traps, 3) saline brines for leaching and transporting metals, and 4) the expulsion of

mineralizing fluids through focused zones. However, it is unclear how important these four controls were for the formation of Kansanshi, as the deposit is atypical of deposits in the CACB for two reasons. Firstly, the deposit is hosted within relatively high-grade, garnet- and kyanite-bearing metasediments as opposed to undeformed sediments (Barron, 2003). Secondly, the deposit contains metre-wide, cross-cutting, high-grade veins which contain approximately 30% of the resource.

Consequently, this study seeks to answer two key questions: (1) To what extent does the Kansanshi deposit align with the conditions outlined in the *Hitzman et al.* model? (2) Could Ambient Noise Tomography (ANT) have located the Kansanshi deposit without any prior constraints?

5.1.1 Instrumentation

Ambient Noise Tomography was first employed to understand the crustal structure of the western United States of America (*Shapiro et al.*, 2005). Since that study, it has been used at a variety of scales from continental down to experiments on the 100s metres scale (e.g., *Stork et al.*, 2018). Broadly, the larger-scale ANT studies have relied upon conventional broadband seismometers such as Guralp ESPCDs which are expensive ($>$ £10,000 per unit), highly technical and only ever deployed in relatively low numbers (typically n $<$ 30). These large-scale studies use low frequency seismic waves ($<$ 0.1 Hz) to which these conventional instruments are particularly sensitive. Smaller scale studies have predominantly relied upon simple induction geophones and used relatively high frequencies ($>$ 1 Hz). The corner frequencies of these geophones are often approximately 4–10 Hz and as such, are typically not deployed to examine frequencies below 1 Hz. MEMS accelerometers operate using electronic force-balance systems, which function by measuring the voltage required to maintain a positive electrode in a fixed position between two negative electrodes (*Herrmann et al.*, 2021). These sensors measure acceleration and offer several advantages over conventional instruments. Their lightweight and compact design facilitates the deployment of large networks or arrays, while their sensitivity to external factors like temperature is an order of magnitude lower than that of standard geophones (*Laine and Mougenot*, 2014). Additionally, MEMS accelerometers do not exhibit the data jitter commonly observed in geophones (*Herrmann et al.*, 2021), and the instrument response remains constant across the frequency spectrum (*Tellier et al.*, 2020). They are cost-effective and can be relied upon to record signals $<$ 1 Hz (*Fougerat et al.*, 2018). For this reason, the advent of MEMS accelerometers with low noise floors provides the opportunity for low frequency, large-scale studies with larger numbers of stations and logistically easy deployments. These characteristics make MEMS accelerometers ideal for the exploration industry and is why these instruments were used in this study.

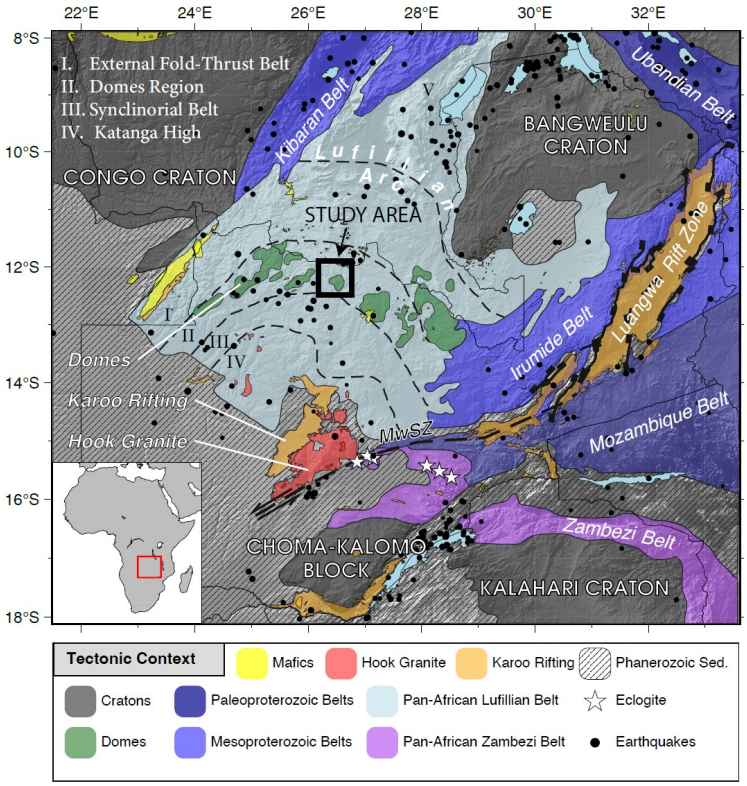

Fig. 5.1 Tectonic map of the Central African Copperbelt after *Kounoudis et al.* (2024). The black polygon demarcates the study area.

5.1.2 Geological Setting of the Kansanshi deposit

The Kansanshi deposit is a sediment-hosted Cu deposit. Sediment-hosted Cu deposits account for c. 23 % of the world's Cu production (*Hitzman et al.*, 2005). The deposit is hosted within the Domes Region of the Neoproterozoic Katangan Basin which crops out in Zambia and southern Democratic Republic of the Congo. The basin is bordered to the north by the Archaean Congo Craton, to the east by the Paleoproterozoic Banguweulu Block and the Mesoproterozoic Irumide Belt, and to the south by the Archaean Kalahari Craton (Figure 5.1).

The Domes Region of the basin is characterised by amphibolite-facies metamorphism and recumbent folding (*Cosi et al.*, 1992). The rocks at Kansanshi can be divided into two key domains, following *Daly and Tosca* (2020): (1) an para-autochthonous package of gneissic and schistose basement overlain by 1-2 km of Lower Roan quartzites, metaconglomerates and Upper Roan metacarbonates, (2) an overlying allochthonous metamorphic sheet containing biotite- and garnet-grade schists. The base of this allochthonous sheet is the Kansanshi Thrust, which runs along the contact of Mwashia Group sediments and underlying Upper Roan metacarbonates. The Kansanshi deposit is found within the allochthonous metamorphic sheet and comprises two main types of mineralization: stratabound and vein. The statabound mineralization hosts the majority

of Kansanshi's copper metal and is predominantly found as bedding-parallel disseminated chalcopyrite within phyllites, accompanied by lesser amounts of bornite and molybdenite. Vein mineralization hosts more than 30 % of the Cu metal and are typically composed of quartz or carbonate with accessory chalcopyrite, malachite, and chalcocite. The veins can be up to several metres wide and typically exhibit sub-vertical, cross-cutting orientations (*Kansanshi Operations, NI 43-101 Technical Report,* July 2024). The metamorphic character of the rocks in Kansanshi is at odds with traditional sediment-hosted deposits, which typically occur at the contact between unmetamorphosed red-bed sequences and overlying shales, siltones or carbonates (*Hitzman et al.*, 2010).

5.2 Ambient Noise Tomography Method

Ambient Noise Tomography (ANT) uses the difference in phase between ambient surface waves travelling through a network to seismometers to examine the 3-D seismic velocity structure within the network. These surface waves can be generated by distant earthquakes, by the oceans, or by more local sources such as mine-blasts. The phase difference of these surface waves between different pairs of stations is calculated using cross-correlations of the ambient recordings of each station within the network. The range of surface-wave frequencies recorded by the network is important. The depth of highest resolution for a given surface wave is proportional to its frequency - a lower frequency wave will have sensitivity to greater depths. This study follows the ANT method outlined in *Harmon and Rychert* (2016). Here we use Rayleigh Waves revealed by ambient noise cross-correlations to create a 44 km long, 2-dimensional (2-D) shear-wave velocity cross-section through the Kansanshi Mine and the surrounding terrain. Towards these ends, we perform a two-step inversion: the initial inversion generates phase velocity maps for surface waves at specific periods within the study area using the cross-correlations. The second inversion generates 1-dimensional (1-D) shear-wave (S-wave) velocity models from the 1-D phase velocity dispersion curves created using the phase velocity maps. These 1-D S-wave models are stitched together to create a final 2-D cross-section. The workflow is outlined below.

5.2.1 Deployment, cross-correlations, and phase velocity measurements

A network of 30 Sercel WiNG nodal MEMS accelerometers was deployed along a c. 50 km long, linear transect through the Kansanshi Cu-mine and Solwezi, Zambia between October 2021 and May 2022, for a total of 188 days (Figure 5.2). Each station was approximately 1.5-2 km from its nearest neighbour. The WiNG instrument contains a vertical-component Micro ElectroMechanical Systems (MEMS) accelerometer and an internal GPS and battery system. Each instrument weighs approximately 780 g, has

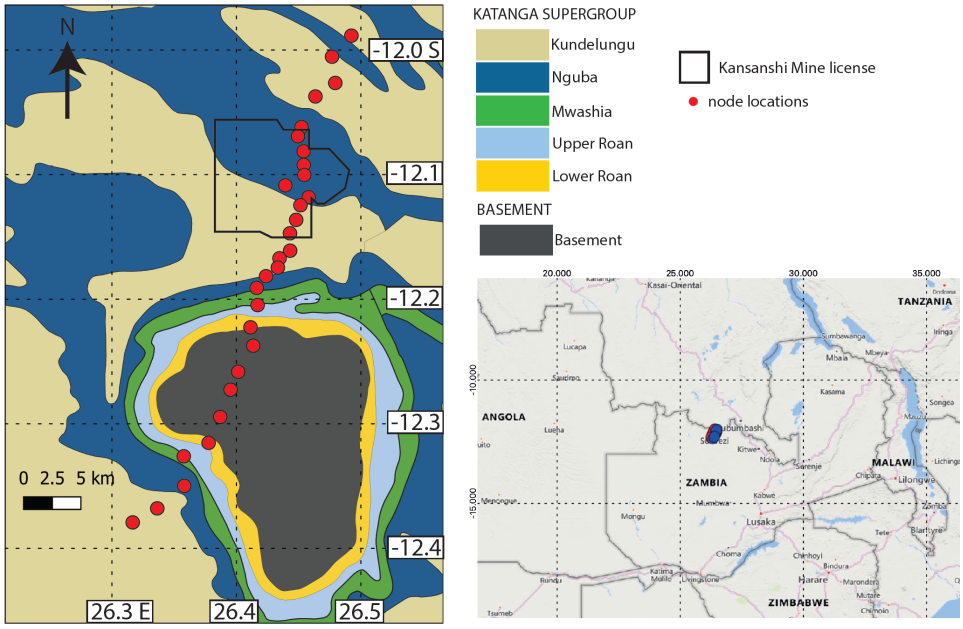

Fig. 5.2 Deployment map. The geological basemap is after *Barron* (2003).

a battery life of 40-50 days, and is well suited to recording seismic data below 1 Hz (Chapter 2).

The ambient recordings of each accelerometer were down sampled from the original sample rate of 500 Hz to 4 Hz. One-bit amplitude normalization and spectral whitening were then performed on the down-sampled data, following *Bensen et al.* (2007). Finally, the processed data were binned into 4-hour time windows. The cross-correlation of the seismograms for every possible pair of stations in the network was then calculated for each time window, followed by a linear stack across all of the time windows. For a network of 30 stations, this resulted in 420 final cross-correlation pairs. The cross-correlations provide an estimate of the empirical Green's function and therefore provide information on the velocity structure between each pair of stations.

For each frequency of interest, the average surface-wave phase velocity within the array, $\bar{c}$, was calculated by finding the phase velocity with the lowest data residual between the phase calculated for a zero-order Bessel Function of the first kind and the observed phase of the real (symmetric) component of all the cross-correlations. The Bessel function is a component of the empirical Green's Function for a surface wave (*Sánchez-Sesma and Campillo*, 1991; *Harmon et al.*, 2008). This was performed for periods of 2.5s, 3.5s, 4.5s, 5.5s, 6.5, and 7.0s.

The total phase, ϕ_T, for each pair of stations was then estimated by unwrapping the phase of the Fourier transformed cross-correlations, using the average phase velocity calculated above to provide an initial estimate of the total number of wavelengths between the pair of stations (Equation 5.1). It is assumed that the "true" total phase

lies within a single wavelength of the total phase calculated with the average phase velocity.

$$\phi_T = \phi_{cc} + 2\pi N + \frac{\pi}{4} \tag{5.1}$$

$$\left| \phi_T - \frac{2\pi s}{\bar{c}p} \right| < 2\pi \tag{5.2}$$

Where N is the integer number of wavelengths between the pair of stations, ϕ_{cc} is the phase of the cross-correlation, $\pi/4$ is the phase correction required for the great circle path (*Harmon et al.*, 2008), s is the interstation distance, and p is the period of interest.

5.2.2 Phase Velocity Inversion

The total phase from all useable station pairs is inverted for network-wide 2-D phase velocity maps using an iterative damped, weighted least-squares inversion, following *Forsyth and Li* (2005), and further studies such as *Harmon and Rychert* (2016) and *Schlaphorst et al.* (2021).

The total phase is converted into an observed phase residual relative to the calculated phase assuming the average phase velocity, $\bar{c}$. This observed residual, $\delta\phi$, is the data used within the tomography (Equation 5.3).

$$\delta\phi = \phi_T - \frac{2\pi s}{\bar{c}p} \tag{5.3}$$

Where p is the period of interest and s is the inter-station distance. We treat the data as a normally distributed random variable with uncorrelated uncertainty. As such, the *a priori* data covariance matrix, C_d, is a diagonal matrix with a constant value of 0.2, following *Forsyth and Li* (2005) and *Harmon and Rychert* (2016).

A gridded nodal parameterisation was used for the model, m. The resulting phase velocity map is a weighted average of the phase velocities at each model node. The initial model, m_0, is uniformly set to the average phase velocity, $\bar{c}$. Damping of the inversion is achieved using the *a priori* model covariance matrix, C_m, which uses a minimum length criterion and thus contains only diagonal terms (*Marquardt*, 1970).

$$C_m = \epsilon^2 W_m \tag{5.4}$$

Where W_m is a diagonal weighting matrix quantifying the relative importance of the solution length for each point in the velocity model and ϵ is a damping parameter controlling the balance between prediction error and the solution length. We employ

a uniform variance for all points in the interior of the grid. An outer boundary layer of nodes is also included with a ten-fold higher variance, such that these essentially undamped outer nodes can "absorb" variations that represent additional deviations from the idealized modeling assumptions (*Forsyth and Li*, 2005). The damping parameter ϵ was assigned a value of 0.2 using an L-curve analysis (Appendix D). The observations (observed residual phase) are related to the model (phase velocity) assuming the following model:

$$d = \delta\phi = \iint K \frac{\delta c}{c} dxdy \tag{5.5}$$

$$G = \iint K dxdy \tag{5.6}$$

Where K is the 2-D finite frequency phase sensitivity kernels of *Zhou et al.* (2004) and $\delta c = c - \bar{c}$ (i.e., the change in phase velocity relative to the starting model at a particular point in x and y). In essence, the inversion determines the change in phase velocity, δc, needed from the initial model to account for the observed phase residual, $\delta\phi$. This is achieved by iterating (i) over Equations 5.7-5.9.

$$\Delta d = d - G(m_i - m_0) \tag{5.7}$$

$$\Delta m = (G^T C_d^{-1} G + C_m^{-1})^{-1} (G^T C_d^{-1} \Delta d) \tag{5.8}$$

$$m_{i+1} = m_i + \Delta m \tag{5.9}$$

We find that the best-fit model is typically found after 11 iterations, as defined by a plateauing in the variance of the residuals ($\epsilon = d - G\Delta m$). Following the inversion, a smoothing is performed using a 2-D Gaussian weighting function, in which the phase velocity values within a high-resolution grid are defined as the weighted average of the phase velocities at each point in the model grid (m_k). This follows the method of *Forsyth and Li* (2005). The Gaussian functions are scaled with distance, such that proximal model nodes exert more weight on the value than distal model node. This smoothing allows the velocity to be continuously described everywhere in the area of interest, rather than solely at discrete model nodes. The length-scale of the smoothing is controlled by the "characteristic length", L_w, which controls the width of the Gaussian function. There is no absolute criterion for selecting the characteristic length, which causes a trade-off between data misfit and model length. Instead, a conventional trade-off curve analysis was performed, and a value of 5.5 km was assigned for L_w. The error, amplitude resolution, spatial resolution, and phase velocity residuals for each inversion were calculated using the methods outlined in Appendix D.

5.2.3 S-wave Velocity Inversion

Shear wave (S-wave) velocity models were created by first generating 1-D dispersion curves at all points of interest. The dispersion curves were created using the 2-D phase velocity tomography maps. These curves were then inverted for 1-D S-wave velocity models with depth using an iterative non-linear least-squares approach. We use Computer Programs in Seismology to forward calculate, $F(m)$, the dispersion and sensitivity kernels for each model (*Herrmann*, 2013). The density and V_p/V_s of the inversion are fixed at 2.7 kg/m^3 and 1.7 respectively.

The iterative non-linear least-squares approach iteratively updates the S-wave model, m, through Equations 5.10-5.13, to minimize the misfit between the observed phase velocities are those predicted for the model (Δd). We perform 100 iterations for each model.

$$\Delta d = d^{\text{obs}} - d^{\text{pred}} \tag{5.10}$$

$$\Delta m = (G^T C_d^{-1} G + C_m^{-1})^{-1} (G^T C_d^{-1} \Delta d) \tag{5.11}$$

$$m_{i+1} = m_i + \Delta m \tag{5.12}$$

$$[d_{i+1}^{\text{pred}}, G_{i+1}] = F(m_{i+1}) \tag{5.13}$$

At the end of each loop, the forward model dispersion curves and sensitivity kernels are re-calculated because the sensitivity kernels are a function of the model (hence the inversion is non-linear). This follows the method of *Tarantola and Valette* (1982) as employed in *Harmon and Rychert* (2016). The problem is damped using diagonal terms in the model covariance matrix (C_m) equal to 0.1, following a trade-off curve analysis between the spread of the resolution matrix and the solution length (Appendix D). The quality of the model is quantified using a chi-squared objective function (Equation 5.14).

$$\chi = \frac{1}{N} \sum_{i=1}^{N} \left(\frac{d_i^{\text{obs}} - d_i^{\text{pred}}}{2\sigma_i} \right) \tag{5.14}$$

Where N is the number of periods included in the inversion. A value above 1 indicates that the average forward modelled data lies outside 2 standard deviations, $2\sigma_i$, from the observed phase velocity, d^{obs}. The starting model was a 60 by 0.33km layers, reaching a maximum depth of 20 km. Bootstrap resampling of the observations was then used to assess the uncertainty of the solution by randomly selecting observed phase velocities within the range defined by the mean and standard deviation. The distribution of the re-sampled solutions is used to estimate the uncertainty of the 1-D S-wave model.

5.3 Results

5.3.1 Cross-correlations and phase velocity

The cross-correlations of the ambient noise recorded at each station-pair within the network shows a clear ∼ 3km/s moveout, which is indicative of Rayleigh waves moving across the network (Figure 5.3). Phase velocity analysis was performed at periods of 2.5s, 3.5s, 4.5s, 5.5s, 6.5s, and 7s (Figure 5.4). The median phase velocities for this selection of periods are 3.20 km/s, 3.16 km/s, 3.20 km/s, 3.19 km/s, 3.23 km/s, 3.21 km/s respectively (Figure 5.5). The decrease in phase velocity from 2.5s to 3.5s suggests the presence of a velocity inversion (i.e., a layer of rocks with a higher S-wave velocity above a layer with a slower velocity).

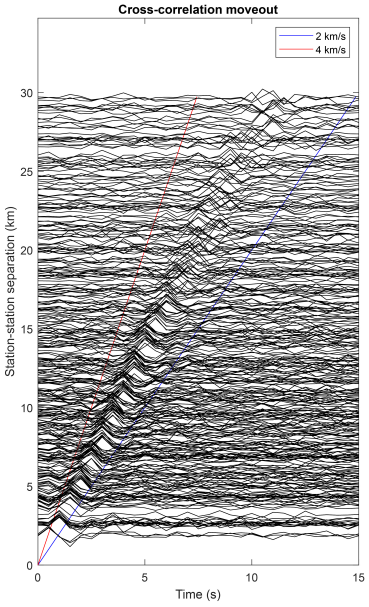

Fig. 5.3 Station-pair cross-correlation moveout.

5.3.2 2-D Phase Velocity Maps

Phase velocity tomography was performed for each period above. A selection of these phase velocity maps, with accompanying error estimates, are displayed in Figure 5.6. The phase velocities are plotted relative to the average phase velocity for the given period (e.g., 3.17 km/s for a period of 3.5 s). The resolution maps and residual plots for each period can be found in Appendix D. The phase velocity maps reveal lateral velocity variations that correspond with surface geology. For example, the phase velocity of a 2.5s wave shows a clear low velocity zone within the Kansanshi Mine of -0.27 ± 0.08 (2σ) km/s relative to the average phase velocity of 3.21km/s (Figure 5.6A). This is contrasted with higher phase velocities immediately to the south of the mine. A velocity low is also seen within the mine at periods of 3.5s and 5.5s, with velocities of -0.22 ± 0.06 km/s and -0.12 ± 0.09 km/s respectively (Figure 5.6C, E). The area south of the mine is characterized by both velocity highs and velocity lows. This is particularly prevalent at a 5.5s period, with phase velocities ranging from -0.19 ± 0.09 to +0.05 ± 0.09 when moving south down the network, relatively to an average velocity of 3.18 km/s (Figure 5.6E). The average absolute amplitude bias along the network is 7.5 % at 2.5s, with an average of 7.0 % at 4.5s and 4.5 % at 7s. The average spatial resolution along the network is 2.4 km at 2.5s, rising to an average of 2.71 km and 3.6 km at 4.5s and 7s respectively (see Appendix D).

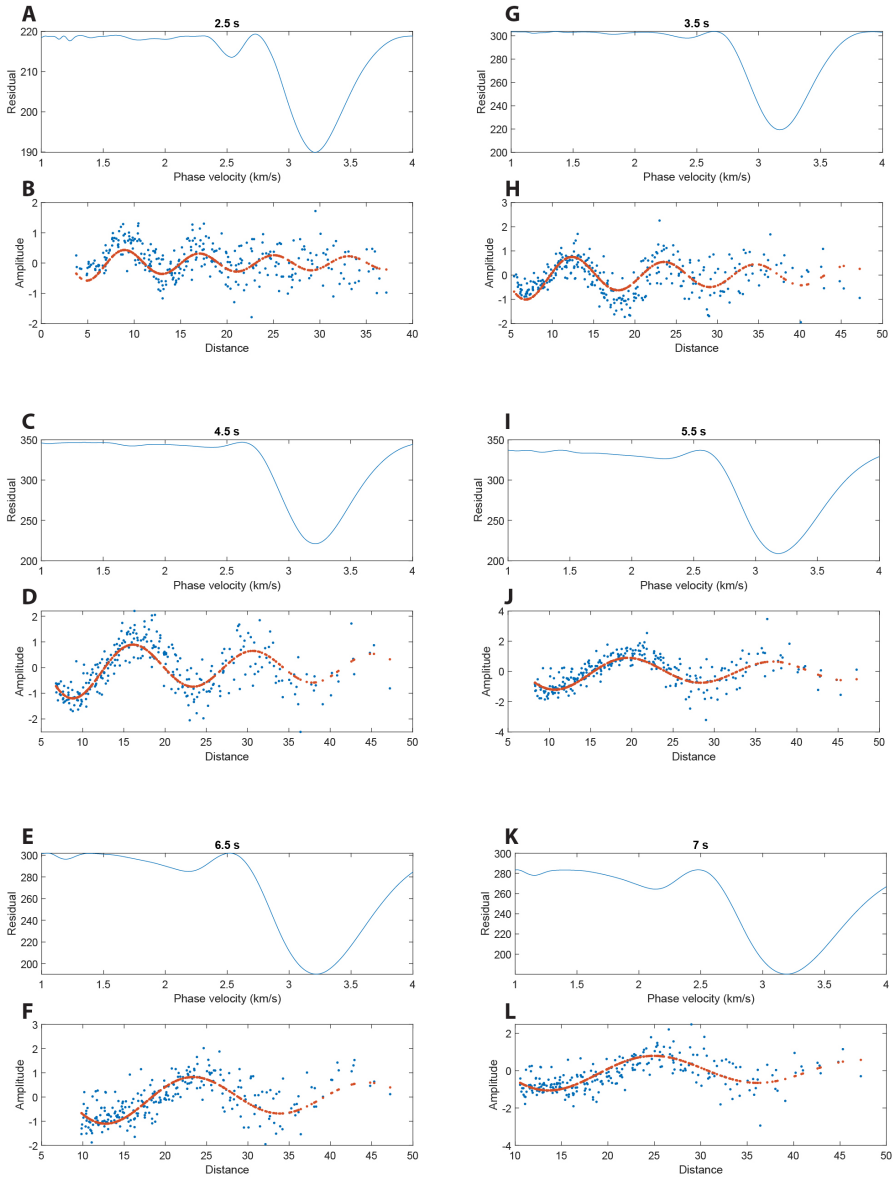

Fig. 5.4 Average phase velocities for each period of interest and a comparison between the phase calculated for a zero-order Bessel Function (red dots) of the first kind and the observed phase of the real (symmetric) component of all the cross-correlations (blue dots). (A) Residuals plot for 2.5s, (B) Bessel Function comparison for 2.5s. (C, D) for 3.5s. (E, F) for 6.5s, (G, H) for 3.5s, (I,J) for 5.5s, (K,L) for 7s.

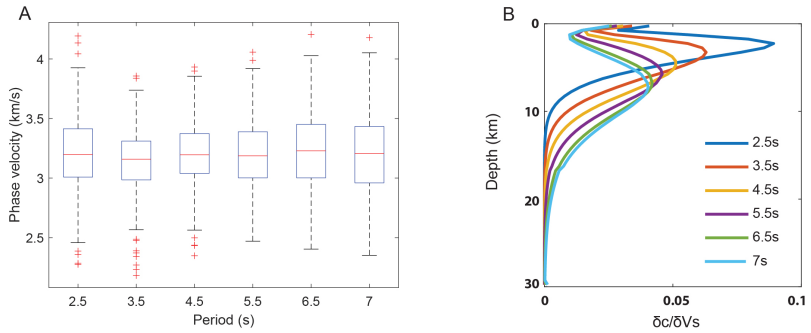

Fig. 5.5 (A) Distribution of phase velocities at each period. Boxplots show the median value, the interquartile range and maximum and minimum values defined as 1.5 times the interquartile range away from the bottom or top of the box. (B) Depth sensitivity kernels for the surface waves of interest.

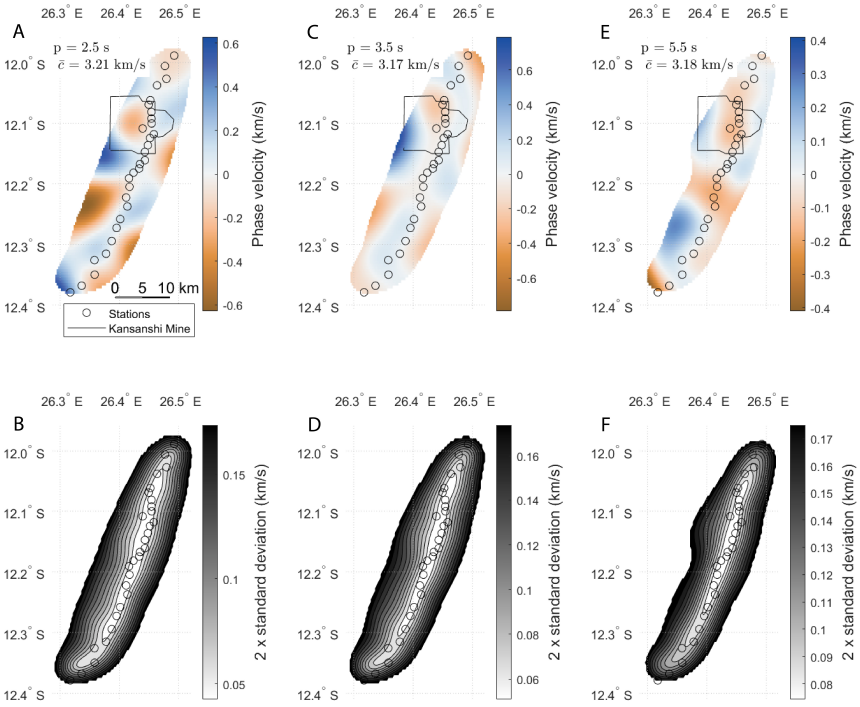

Fig. 5.6 2-D phase velocity models. The phase velocities are plotted relative to the average phase velocity ($\bar{c}$) for the given period. (A) Phase velocity map for a period of 2.5s. (B) Phase velocity error map for a period of 2.5s. (C, D) for a period of 3.5s. (E, F) for a period of 5.5s.

5.3.3 2-D S-wave Cross-section

The phase velocity maps were compiled into 60 dispersion curves along the X-X' profile of Figure 5.7A, each of which was inverted for a 1-D S-wave velocity profile. The sensitivity kernels of the included surface waves (2.5–7 s) demonstrate that the surface waves are

sensitive to variations in S-wave velocity (∼ lithology) down to depths well in excess of 10 km (Figure 5.5B). Bootstrap resampling of the dispersion curves was conducted over

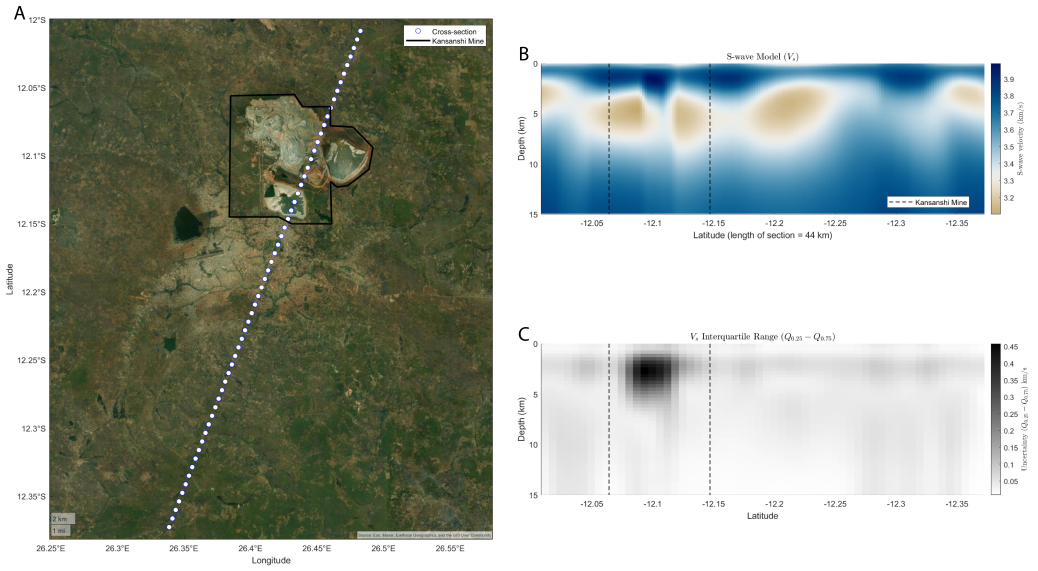

Fig. 5.7 2-D S-wave model. (A) Location of points along the profile. (B) S-wave velocity model corresponding to the points in (A). (C) S-wave velocity uncertainty defined as the interquartile range.

500 iterations to evaluate the spread of potential S-wave models at each point along the profile. The re-sampling assumed a Gaussian distribution with a mean and standard deviation equal to that calculated in the phase velocity tomography for each period. The resulting S-wave cross-section displays the median and interquartile range of the distribution of solutions from the bootstrap re-samples. Given the non-Gaussian nature of the probability density function in non-linear problems, percentile-based confidence intervals such as the interquartile range are often more informative than the standard deviation (*Menke*, 1984).

The cross-section shows clear variations in S-wave velocity vertically and laterally along the profile. Beneath Kansanshi Mine at 12.1°S, the S-wave velocity drops from a high of 4.0 km/s at a depth of 1.5 km to a 3.11 km/s at a depth of 4.5 km. This low velocity zone is laterally continuous but rises to a shallower depth of 3.0 km and 3.2 km in the north and south respectively. The southern section of the profile is characterized by higher velocities. For example, between latitudes of 12.25°S and 12.34°S, the average velocity at 4.5 km depth is 3.45 km/s while inside the Kansanshi Mine license, the average velocity at that depth is 3.22 km/s. However, the southern-most end exhibits another low velocity zone of 3.2 km/s at a depth of 2.2 km. These velocity contrasts are deemed robust because their velocity values remain distinct even when accounting for uncertainty (Figure 5.7C). The highest uncertainty is found within the Kansanshi Mine license, with an interquartile range of 0.45 at a depth of 2.3 km at -12.1°S. The average interquartile range above 10 km is 0.06 km/s.

5.4 Discussion

5.4.1 The Geological Structure of the Kansanshi Cu-Au Mine

The S-wave cross-section demonstrates that the tomography successfully differentiates rock units with varying S-wave velocities, resulting in geologically realistic structures. Although the interpretation of S-wave velocities is non-unique, we assume that Katangan sediments have S-wave velocities up to 3.2 km/s as sandstones and mudstones have been measured to have S-wave velocities up to and exceeding this value (e.g., 3.26 ± 0.18 km/s for fine sandstone in *Zhang et al.*, 2009). In contrast, lithologies with S-wave velocities above 3.3 km/s are interpreted as either basement or Lufilian-age metamorphics, because crystalline rocks—including granites, gneisses, and high-grade metamorphics—typically exhibit S-wave velocities ranging from 3.3 to 4.5 km/s (*Christensen*, 1996). Some overlap in S-wave velocities between Katangan sediments, basement, and metamorphic units is expected due to variations in composition, alteration, metamorphism, and deformation intensity. Therefore, lithologies with S-wave velocities between 3.2 km/s and 3.3 km/s could readily correspond to either sedimentary or basement/metamorphic units. We assign a velocity of 3.3 km/s as the pivot point in the color scheme of Figure 5.7A, 5.8A. This approach provides a practical balance, allowing for an approximate yet visually effective differentiation between these lithological categories. It should be noted that

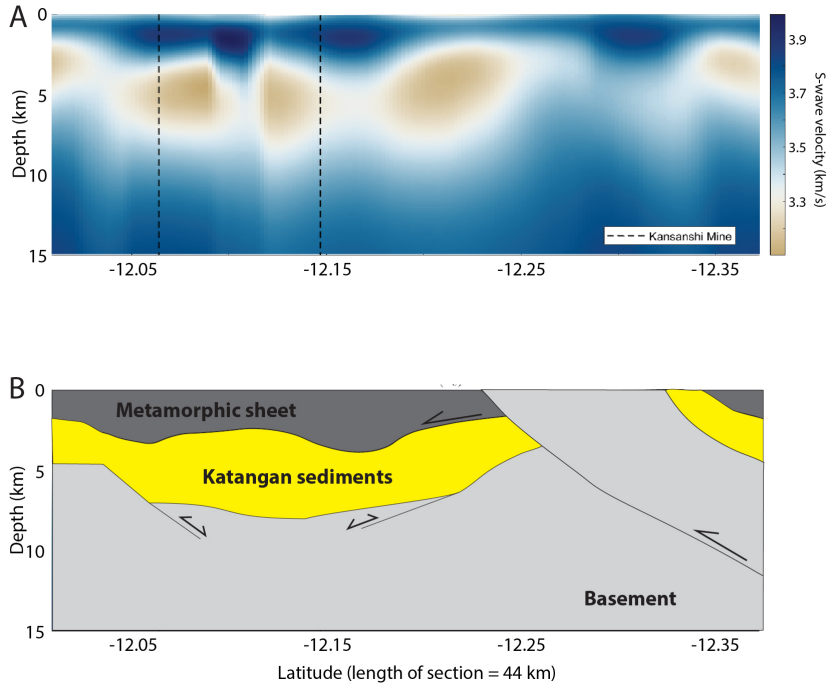

Fig. 5.8 Tectonic interpretation. (A) 2-D S-wave velocity model. (B) Geological interpretation.

surface waves have a relatively poor vertical resolution (Figure 5.5B). The S-wave models

vary smoothly with depth, and therefore no discrete interfaces are observed. As such, the depths to structures such as the sediment-basement contact are poorly understood. However, the models do robustly show a large accumulation of sediments beneath Kansanshi. This is in good agreement with *MacIntyre* (2019) and *Daly and Tosca* (2020) who previously identified significant sediment thickness (> 1.5 km) beneath Kansanshi on the basis of deep sedimentary core logs. The sediment package appears to thin to the north and the south, with the depth of the sediment-basement contact decreasing away from the mine. This indicates the existence of a Lower Roan depocentre beneath the mine. The thinning of the sediments to the south is observed by *Arthurs* (1974) and is corroborated by the MS300 core log (*Daly and Tosca*, 2020). These lateral thickness variations are best explained by a graben system beneath Kansanshi (Figure 5.8B). The modern-day topography of the interface is likely controlled by original basin structures, such as normal faults, and later thrust faulting. To the south of the mine between -12.25°S and -12.35°S there are no velocities of 3.2 km/s and below. We interpret this area as a block of basement brought up along an out-of-sequence thrust, cutting the Katangan sediments and overlying metamorphic sheet. This is in good agreement with the surface geology, with the basement Solwezi Dome cropping out in this area (Figure 5.2). Sitting structurally above the sediments in much of the model is a layer of high-Vs rocks which we interpret as belonging to an overthrust metamorphic sheet. This is in good agreement with the field observations, with garnet-biotite schists cropping out within the Kansanshi Mine and surrounding area (*Barron*, 2003; *Daly and Tosca*, 2020).

5.4.1.1 A comparison with the results from Chapter 4

I concluded in Chapter 5, on the basis of field constraints and core logs alone, that the Kansanshi sat a thick autochthonous sequence of Roan Group sediments within a Tonian-age sub-basin. This sequence is overlain by a Lufilian-age allochthonous metamorphic sheet. Both of these units are then cut by the later thrust fault exhuming the Solwezi Dome. The limitations of the outcrop and core longs meant that the extent of this sub-basin was entirely unconstrained, with questions remaining regarding its depth, geometry, and lateral extent. The results shown in Figure 5.8 provide first-order constraints on all these parameters. Crucially, the geophysical model is a good agreement with the geological cross-section (Figure 4.5) with each unit and their structural relationships clearly preserved. However, the sediment interface inferred from the geophyical section is slightly deeper than that expected from the core logs (e.g., KRX082, Figure 4.4). As will be discussed in Section 5.4.3, surface-waves provide poor resolution on the depths of geological interfaces, so this mild discrepancy is not a surprise. The power of the ANT technique is in imaging the lateral contrasts in S-wave velocity, through which we get a clear understanding of the sub-basin geometry (Figure 5.8B).

5.4.2 The Mineral System at Kansanshi

As previously noted, *Hitzman et al.* (2010) notes four fundamental controls on the formation of sedimentary metal deposits: 1) the presence of metal source sediments, 2) the presence of reduced sediments to serve as chemical traps, 3) saline brines for leaching and transporting metals, and 4) the expulsion of mineralizing fluids through focused zones. The Kansanshi deposit exhibits some key characteristics outlined in the *Hitzman et al.* (2010) model for sediment-hosted copper deposits but also diverges from the model in significant ways. The ANT method does not provide direct evidence for reduced sediments acting as chemical traps, nor does it confirm the presence of saline brines, which are typically essential for metal transport. However, the S-wave model shows a large body of sediments beneath the Kansanshi Mine. This significant thickness of sediments could have provided a source of copper for scavenging and subsequent deposition to create the Kansanshi deposit. This aligns with the idea that a large volume of metal-rich sediments is a prerequisite for forming a major copper deposit, following the red-bed source model of *Hitzman* (2000). The volume from which metal is sourced is a fundamental control on the probability of forming a large metal deposit (*McCuaig and Hronsky*, 2014). The ANT results also reveal fault systems and an antiformal structure beneath Kansanshi, which could have served as conduits for mineralizing fluids. Faults are well-documented pathways for hydrothermal fluids, and the structural geometry detected in this study suggests that faults may have played a key role in localizing mineralization. The largest fault zone is the thrust fault bounding the Solwezi Dome. This fault may have been a conduit for the metasomatic fluids responsible for the formation of the whiteschists found at the boundary between the sediments and the Dome (*Eglinger et al.*, 2014). Normal faulting and subsequent reactivation as thrust faults are interpreted beneath the Kansanshi Mine in order to explain the significant thickness of sediments which are not observed in outcrop to the south of the mine. These faults may well have acted as significant fluid pathways. The S-wave model also suggests the presence of a mild antiform directly beneath Kansanshi. This is consistent with the surface geology, as Kansanshi comprises a weakly dipping, NW-SE trending dome (e.g., *MacIntyre*, 2019). This antiformal structure would have provided the perfect trap structure for metal-bearing fluids. Finally, the S-wave model predicts the presence of an overlying metamorphic sheet which is clearly observed in the field. *Daly and Tosca* (2020) proposed that the overthrusting of the metamorphic sheet resulted in overpressuring of the underlying Katangan sediments in response to the increased overburden. This increase in pressure is calculated to have increased the solubility of chalcopyrite in the pore fluids and thus driven a significant Cu-enrichment in the circulating fluid. Upon orogenic collapse and uplift, the overpressuring would have driven critical failure in the overlying sediments and the deposition of the Cu-rich veins for which Kansanshi is famous.

5.4.3 Limitations of the approach

Although the S-wave cross-section demonstrates that ANT successfully differentiates rock units with varying S-wave velocities, resulting in geologically realistic structures, the approach has several limitations of import:

The two-step inversion: The methodology relies on a two-step inversion process—phase velocity tomography followed by an S-wave inversion. It is difficult/impossible to reliably understand 3-D uncertainty and resolution using a two-step method (*Latallerie et al.*, 2024). Additionally, each step introduces its own set of assumptions and potential sources of error. For example, the phase velocity inversion relies upon sensitivity kernels that assume linear changes in velocity through space (*Zhou et al.*, 2004). This means that discrete structures like fault zones are poorly resolved. The S-wave inversion is affected by the inherent non-uniqueness of the non-linear inversion process, meaning that multiple subsurface models could explain the observed data.

The noise sources: Cross-correlations provide an estimate of the empirical Green's Function when the noise sources are homogeneously distributed around the station pair (*Weaver and Lobkis*, 2001). As such, heterogeneous noise sources can be a source of bias in the phase velocity calculations. This may be of particular importance in areas around mine sites where several large noise sources (such as mine blasts) occur. In our case, the noise of Kansanshi Mine was a useful source as it lay along strike of the linear array. In a more 3-D network, this may not have been the case. However, some studies have estimated that heterogenous noise sources impart only a small bias onto the phase velocity calculations (< 1 % in the case of *Yao and van der Hilst*, 2009).

Vertical resolution of surface waves: One of the fundamental limitations of ANT is the relatively poor vertical resolution of surface waves compared to body-wave methods and the difficulty in reliably understanding this resolution. Surface waves provide excellent lateral coverage, but their depth resolution is inherently limited by the frequency content of the recorded ambient noise and the breadth of the sensitivity kernels with depth (Figure 5.5B). This makes it challenging to distinguish between closely spaced geological layers or to precisely define geological contacts and the thickness of rock units.

5.5 Conclusions

At the outset of this study, we posed two key questions: (1) To what extent does the Kansanshi deposit align with the conditions outlined in the *Hitzman et al.* (2010) model? (2) Could Ambient Noise Tomography (ANT) have identified the Kansanshi

deposit without prior geological constraints? To address these questions, a network of 30 Sercel WiNG MEMS accelerometers was deployed along a c. 50 km long, linear transect through the Kansanshi Cu-Au mine and surrounding area of Solwezi, Zambia, from October 2021 to May 2022, over a period of 188 days. The resulting shear-wave model revealed key geological structures, including a depocenter of Katangan sediments beneath the Kansanshi Mine, an uplifted basement section south of the mine, and an overlying metamorphic sheet. We conclude that Kansanshi shares some fundamental characteristics with sediment-hosted copper deposits, particularly in terms of its metal source and structural controls. Furthermore, ANT could have played a crucial role in identifying the Kansanshi deposit as a promising exploration target, even in the absence of prior geological constraints. The implications of these findings, alongside their integration with the geological datasets of Chapter 4, are explored in greater detail in Chapter 6.

Chapter 6

Conclusions

6.1 Thesis conclusions

This thesis explored two key methodological developments and their application to understanding the tectonic evolution and structural configuration of the Kansanshi Cu-Au deposit, with implications for the broader Central African Copperbelt mineral system. First, I assessed the suitability of MEMS accelerometers for low-frequency (< 1 Hz) passive seismic studies (Chapter 2). Second, I presented a novel workflow for quantitatively determining the best-fit pressure-temperature (P–T) conditions and their associated uncertainties in metamorphic rocks (Chapter 3). These methods were then applied in two complementary studies. In Chapter 4, the metamorphic workflow was integrated with new field mapping and structural analysis to examine the tectonic evolution of the Kansanshi Cu-Au deposit. This was followed by a passive seismic study (Chapter 5), in which I used a network of MEMS accelerometers and ambient noise tomography to investigate the subsurface structural configuration of the deposit.

6.1.1 The application of MEMS accelerometers to regional-scale passive seismology

This thesis has shown that the WiNG nodes reliably record over 100 Hz to 0.03 Hz, with a -136 dB broadband noise-floor between 100–1 Hz, and a $1/f$ noise-floor at frequencies below 1 Hz. The nodes reliably recorded a range of earthquakes with epicentral distances from 72° to 40 km. In particular, the low-period (*ca.* 10–30 s) surface waves of two teleseismic earthquakes were clearly resolved above the sensor's noise floor. The cross-correlation of pairs of nodes provided information on ambient surface waves down to a period of at least 7.5 s, which provided sensitivity to seismic velocities down to a depth of 20 km. The 7.5 s limit represents the limit enforced by the maximum station separations within the array and not the instruments themselves. A set of three WiNG nodes deployed in a 3-component configuration provided an accurate estimate of the crustal thickness beneath Oxford of 39.0 ± 2.0 km using the H-k stacking technique of *Ogden et al.* (2019) on a calculated receiver function from a teleseismic MW 7.0 earthquake in Alaska. This estimate is in error of the estimate provided by the conventional 3-component ESPCD of 37.9 ± 1.3 km and aligns well with previous results in the literature. The nodal systems have a number of clear advantages over conventional

systems, including speed of deployment, cost, and small size. These advantages mean a large array of MEMS sensors could be deployed inexpensively, easily, and in a short time frame. The disadvantages include the restricted depth of burial, which reduces coupling and increases noise levels, and the limited life of the internal battery system. In conclusion, the strong performance of the WiNG nodes at frequencies above and below 1 Hz, in both ambient noise and earthquake analysis, shows that MEMS-based nodes are well-suited for passive seismology studies at a local, regional, and potentially larger scale.

6.1.2 Towards Optimal Estimates of P-T Conditions and Uncertainty

Accurately constraining the P-T history of metamorphic rocks is crucial for understanding a broad range of processes in both the solid and surficial Earth, including identifying geothermal gradients in the subsurface and sources of economically valuable raw materials (e.g., critical metals), understanding climate and Earth system feedbacks, reconstructing the tectonometamorphic evolution of terrains, and informing broader geodynamic models. The ability to understand and quantify uncertainties in the calculation of P-T conditions is essential to ensuring that results can be interpreted within a defined confidence range. This is particularly important in scenarios where geological or petrological interpretations hinge on relatively small variations in pressure and/or temperature (e.g., *Pattison and DeBuhr*, 2015).

The new workflow presented in Chapter 4, *LinaForma*, provides quantitative constraints on optimal P-T conditions and associated uncertainties for a given rock system. The technique identifies the best-fit solution by comparing observed data, such as mineral compositions and/or modal volumes, with forward model predictions across a user-defined P-T grid. Bootstrap resampling (repeated sampling with replacement) quantifies the uncertainty of the inverse solution and assesses its sensitivity to input variable uncertainty. Three diagnostic metrics—quality of data fit, variable sensitivity, and standard error—are incorporated to validate and refine the results. Given the varying sensitivities of different variables to uncertainty, selecting only those that minimize uncertainty may be misleading. Instead, the inversion should incorporate the largest and most diverse set of robust variables possible to ensure P-T estimates are representative of the natural system. This approach also enables an assessment of the overall model performance, which may provide insights into other characteristics of the system such as the degree of equilibrium.

6.1.3 The tectonic evolution of the Kansanshi Cu-Au mine and the use of MEMS accelerometers in mineral exploration

Chapters 4 and 5 presented a multi-disciplinary understanding of the Kansanshi Cu-Au deposit in northwestern Zambia, addressing both the tectonic context of mineralisation and the practical applicability of geophysical tools—specifically Ambient Noise Tomography (ANT)—for mineral exploration in sediment-hosted copper systems.

Chapter 4 established a new tectono-stratigraphic framework for the Solwezi region, based on detailed geological mapping, core logging, and thermobarometric analysis of five garnet-bearing metamorphic rock samples. This study concluded that the Kansanshi deposit is situated atop a thick sequence of autochthonous Lower Roan sandstones. These were deposited in a Tonian-age sub-basin at the northern margin of the Katangan Rift, and are conformably overlain by Upper Roan Group carbonates and Mwashia Group siliciclastic sediments. Together, these units represent a complete rift basin stratigraphy, with sedimentation continuing well into the Cryogenian.

During the Ediacaran, convergence between the Congo and Kalahari cratons initiated the Lufilian Orogeny, resulting in the development of an orogenic wedge which experienced Barrovian metamorphism during the early Cambrian, with peak conditions of 550–620 °C and 7.5–9.5 kbar. Assuming a lithostatic pressure gradient of 3.5km/kbar, this equates to burial depths of 26–33 km. Granitic magmatism is inferred to have occurred coevally with peak metamorphism, driven by crustal thickening and pelitic partial melting. The garnet- and biotite-grade rocks produced during the Lufilian Orogeny now comprise the autochthonous high-grade metamorphic sheet structurally overlying the Kansanshi mine. This allochthonous metamorphic sheet was emplaced via southward-directed thrusting during the mid- to late-Cambrian, utilising a detachment horizon within the Upper Roan Group. Late-stage, out-of-sequence thrusting then exhumed the Solwezi Dome. Although the precise timing of this exhumation remains uncertain, its tectonic significance is clear—it disrupted the earlier structural architecture and may have remobilised fluids, as evidenced by the formation of whiteschists around the dome margin.

While the tectonic model developed in Chapter 4 is a significant improvement on pre-existing models for NW Zambia, considering both metamorphic and tectonic constraints, key uncertainties remained—particularly regarding the geometry, depth, and lateral continuity of the Lower Roan sub-basin underlying Kansanshi. These uncertainties were addressed in Chapter 5, which used Ambient Noise Tomography (ANT) to assess whether such sedimentary architectures could be reliably imaged using passive seismology and whether this method could support regional mineral exploration in the absence of extensive outcrop or drilling data. To this end, a network of 30 Sercel WiNG MEMS accelerometers was deployed along a ∼50 km transect crossing the Kansanshi mine and extending into the surrounding Solwezi region. The deployment

spanned 188 days between October 2021 and May 2022. ANT processing followed a two-stage approach: first, phase velocity maps were generated following the method of *Forsyth and Li* (2005), then converted to S-wave velocity models via inversion using the framework of *Harmon and Rychert* (2016). The final model achieved resolvable structure to depths of ∼10 km, with lateral resolution sufficient to distinguish features on the order of a few kilometres.

The ANT results confirm the presence of a major sedimentary depocenter beneath Kansanshi, consistent with the Tonian-age sub-basin described in Chapter 4. This depocenter is characterised by relatively low S-wave velocities (< 3.2 km/s), sharply contrasting with the higher velocities of the underlying and surrounding basement. The basin comprises a thick central package of sediment that thins laterally to the north and south. While the model's vertical resolution is limited, the strength of ANT lies in resolving lateral velocity contrasts which provide robust constraints on the sub-basin geometry. In addition to the sedimentary depocentre, the ANT model also resolved an uplifted basement block south of the mine and a high-velocity sheet overlying the basin—interpreted as the autochthonous metamorphic sheet described in Chapter 4.

Together, the two studies demonstrate that Kansanshi possesses many hallmarks of a sediment-hosted copper system, including a thick Roan Group depocenter as a potential metal source, structurally-controlled fluid pathways, and evidence of basin inversion. However, both datasets also highlight significant complexities in Kansanshi's formation history—particularly the role of late-stage deformation, fluid remobilisation, and magmatic inputs. The presence of cross-cutting Cu-rich veins suggests that post-orogenic processes were essential in concentrating ore. Importantly, the ANT results indicate that Kansanshi could have been identified as a prospective exploration target even without prior geological constraints. This underscores the potential of passive seismic techniques in greenfield exploration. However, due to its documented limitations (see Section 5.4.3), the effectiveness of ANT is maximized when used in concert with detailed geological studies and complementary geophysical methods. Future work should focus on integrating ANT with gravity, ellipticity, and receiver function datasets to improve vertical resolution and further refine deposit models.

6.1.4 The Kansanshi Cu-Au mineral system

The Kansanshi deposit is unique among the mines within Zambia because it contains a significant concentration of gold (0.11 g/t) and the copper (∼11 Mt) predominantly occurs as chalcopyrite within quartz-carbonate-pyrite veins up to 5 m thick (Fig. 4.3D), although disseminated and stratabound Cu-sulfides are also present. This markedly contrasts with the sediment-hosted stratiform copper seen in mines such as Sentinel (∼5 Mt Cu) and Lumwana (∼6 Mt Cu), which are proximal to the Kabompo and Mwombezhi basement domes respectively. The age of the mineralisation at Kansanshi

(512 Ma and 502 Ma; *Torrealday et al.*, 2000) is also younger than the mineralisation at Sentinel (> 530 Ma; *Sillitoe et al.*, 2015).

The largest veins in Kansanshi are interpreted to be post-tectonic and cut carbonaceous phyllites of the local Monwezi Formation (*MacIntyre*, 2019), which is located within the allochthonous metamorphic sheet. *MacIntyre* (2019) proposed that mineralization occurred during post-orogenic collapse and extension, with mineralizing fluids concentrating in the crest of the antiform, although no mechanism for the formation of super enriched Cu-bearing ore fluids was provided. *Daly and Tosca* (2020) proposed that the overthrusting of the metamorphic sheet resulted in overpressuring of the Lower Roan sediments in response to the increased overburden. This increase in pressure is calculated to have increased the solubility of chalcopyrite in the pore fluids, and thus driven a significant Cu-enrichment in the circulating fluid (*Daly and Tosca*, 2020). Upon orogenic collapse and uplift, the overpressuring of the Lower Roan drove critical failure in the overlying sediments and the deposition of Cu-rich veins in the fracture space. This model does not address the abundance of carbonate within the veins. Secondly, the model suggests that hydraulic fracturing by overpressure-induced fluids has carried the saline fluids through nearly 1 km of overlying metamorphic nappe. Given the veins in today's pit are ∼1 m, thick this model would likely require a much thicker and dense advective hydrothermal system at depth being drawn to the low pressure of the Kansanshi Dome. Such a linkage has not yet been detected but provides an interesting avenue for future study.

An alternative interpretation is that the veins formed as a result of fluid and metal remobilisation from a Lufilian-age (*ca.* 530 Ma) pre-existing deposit in Kansanshi during the overthrusting of the metamorphic sheet at around 510 Ma. Given the thickness of Lower Roan beneath Kansanshi, it is likely that Kansanshi hosted a significant pre- to syn-Lufilian stratiform Cu-mineralisation like that seen at the Sentinel mine. This would have formed as a result of syn-diagenetic to syn-metamorphic oxidising fluids leaching Cu from the Lower Roan and depositing it in overlying, reduced sediments of the Mwashia Group (Hitzman et al., 2000). During overthrusting of the metamorphic sheet, this pre-existing deposit at Kansanshi would have experienced an increase in temperature, pressure, and deviatoric stress. This is recorded by the 510.9 ± 7.8 Ma zircon overgrowths on metagabbros to the north of the Solwezi Dome (*Barron*, 2003). These changing P-T-σ conditions may have caused significant fluid re-mobilization, and the recrystallisation and dissolution of the existing chalcopyrite, creating a fluid significantly enriched in Cu. Given the abundance of carbonates in the sedimentary succession, and the carbonate within the veins themselves, it is likely this fluid was also highly enriched in CO_2. Fluids enriched in CO_2 have the capacity to transport a significant concentration of Cu and Au (*Lai and Chi*, 2007). This ore-fluid would have precipitated in any accommodation space created during shearing (e.g., en echelon fractures, boudins) or later extension. More work is needed to test this hypothesis.

Finally, the new tectonic model also raises the question of whether Lufilian-age granitic magmatism provided any input to the mineral system, either as a source of heat or an additional source of metal. Fundamental questions such as the location and age of melting relative to the Kansanshi deposit, and the original metal content of the granites remain unanswered and would be the focus for future work

6.2 Summary

In conclusion, this thesis has: 1) Demonstrated the suitability of novel MEMS accelerometers for regional-scale geophysics. 2) Presented a new method for quantifying the best-fit pressure-temperature solution for a metamorphic rock of interest and estimating the uncertainty in the solution. 3) Created a new geodynamic model for the Kansanshi Cu-Au deposit and the NW Zambian Copperbelt, informed by both geophysical and geological observations. This model provides a coherent framework in which mineralisation models for northwest Zambia can be tested in the future. 4) Demonstrated the suitability of ambient noise tomography, performed using MEMS accelerometers, for mineral exploration. Integrating diverse geophysical and geological approaches in terms of technology and process has resulted in new insights into the formation of one of the world's premier sediment-hosted Cu mines. In addition, it has added a new tool to the sedimentary Cu exploration tool kit and insight into the formation of the Central African Copperbelt regionally.

6.3 Future work

This research also presents several opportunities for further work, a few of which are outlined below.

6.3.1 Ambient noise tomography

1. Chapter 5 demonstrated that ANT is well suited to sedimentary-Cu environments. In these environments, the S-wave velocity contrasts between underlying crystalline basement and overlying undeformed sediments is often relatively strong. More work needs to be done to assess how applicable the ANT method is to areas where the S-wave velocity contrasts may be weaker.

2. ANT relies upon the calculation of cross-correlations between the seismograms of pairs of stations. The seismograms are binned into short time periods (e.g., hours or days) and the resulting cross-correlations are stacked to increase the signal to noise ratio. This process is computationally expensive, and often results in low signal to noise ratios in areas with a high degree of incoherent noise. It would be worth assessing whether machine-learning can be used to improve this

process, making it faster and better able to select the pertinent data to attain an improved signal to noise ratio. The DAS-N2N algorithm from *Lapins et al.* (2023), which was developed for de-noising Distributed Acoustic Sensing (DAS) data, could likely be modified for this purpose.

3. For making business decisions, it is important to provide an uncertainty alongside any geophysical results. In Chapter 5, this was approached using a bootstrap re-sampling method for the surface wave to S-wave inversion. However, this could potentially be done more thoroughly using Backus-Gilbert techniques to optimise the inversions and maximise the sensitivity to a particular property of interest. This would increase the utility of ambient noise tomography.

6.3.2 Metamorphic methodology

1. The metamorphic method presented in Chapter 3 assumes equilibrium between the observed variables. However, different variables in a rock may be recording different sections of the pressure-temperature evolution of the rock. Could these different sections of P-T space be identified using a clustering methodology similar to the one adopted by *Ogden et al.* (2019) for receiver function analysis?

2. This work has highlighted the potential importance of Cu mobility during metamorphism and structural re-organisations. Little is known about this topic, so future work would involve detailed petrological modelling and experimentation to understand the stability of Cu ore minerals in different geodynamic environments.

6.3.3 Kansanshi Cu-Au mine

Fundamental questions remain regarding the timing and mechanism of mineralisation at Kansanshi relative to the tectonic and structural events identified in Chapter 5. These are crucial for understanding the mineral system of Kansanshi and how to locate similar deposits.

1. I would recommend detailed petro-chronological analysis of the allochthonous metamorphic sheet and the mineralisation at Kansanshi. In particular, mica cooling ages of the metamorphic sheet should be combined with high-resolution Re-Os sulphide ages of the veins and disseminated mineralisation to understand the relative timings of metamorphism, cooling, and mineralisation. This should be integrated with field observations to constrain the structural regime during mineralisation.

2. Another question pertains to why Kansanshi hosts a significant endowment of gold. Given the limited lateral extent of gold mineralisation in the Domes Region,

it is likely that the gold was concentrated in a local depocentre, and perhaps originally sourced from the Mesoproterozoic basement of the Kansanshi sub-basin itself. *Rainaud et al.* (2005) have previously proposed that the basement of the Copperbelt was an extinct porphyry-Cu system, which may explain the hypothesised Au within the basement of Kansanshi. Detailed petrological analysis of the Solwezi Dome may help clarify this.

6.4 Finding the next Copperbelt

Finding new greenfield sites for copper exploration is essential for the Energy Transition. Sedimentary basins cover ∼75 % of the continental surface, and features such as evaporite deposition essential for brine formation, thick packages of clastic sediments, and reducing layers of shale are commonplace and therefore do not sufficiently reduce the search space (*Hoggard et al.*, 2020). Acquiring large-scale geophysics datasets is essential for meeting this challenge. Recent studies have shown remarkable correlations between the depth of the lithosphere-asthenosphere boundary and the occurrence of sediment-hosted deposits at a global scale (e.g., *Hoggard et al.*, 2020), as well as the correlation between particular seismic velocities and deposits at a continental and regional scale (e.g., *Chen et al.*, 2023). The collection and joint inversion of large-scale (> regional), high-resolution, multi-method geophysical datasets is therefore surely essential for locating new greenfield sites, especially those under significant cover.

The NERC-funded Copper Basin Exploration Science project has recently acquired a multi-method (gravity, MT, passive seismology) geophysics dataset across Zambia. The joint inversion of this dataset will be an interesting test of the power of this approach – can it identify the features controlling the different mineral systems in Zambia? Future work might include expanding this network into a 3-D, country-wide array across Zambia. Exploration methods developed during this experiment should then be applied to areas under cover in the west of Zambia, through to Angola and Namibia and northwards deep into the DRC.

References

Alessio, B. L., A. S. Collins, P. Siegfried, S. Glorie, B. D. Waele, J. Payne, and D. B. Archibald (2019), Neoproterozoic tectonic geography of the south-east Congo Craton in Zambia as deduced from the age and composition of detrital zircons, *Geoscience Frontiers*, *10*, 2045–2061, doi:10.1016/j.gsf.2018.07.005.

Armstrong, R., S. Master, and L. Robb (2005), Geochronology of the Nchanga Granite, and constraints on the maximum age of the Katanga Supergroup, Zambian Copperbelt, *Journal of African Earth Sciences*, *42*, 32–40, doi:10.1016/j.jafrearsci.2005.08.012.

Arthurs, J. W. (1974), Geology of the Solwezi Area, Degree Sheets 1226, NW Quarter and 1126 SW Quarter, report 36.

Bakun, N., R. Volodin, and F. Krendelev (1966), Genesis of Udokansk cupriferous sandstone deposit (Chitinsk oblast), *International Geology Review*, *8*(4), 455–466, doi:10.1080/00206816609474302.

Barmin, M. P., M. H. Ritzwoller, and A. L. Levshin (2001), A fast and reliable method for surface wave tomography, *Pure and Applied Geophysics*, *158*(8), 1351–1375, doi:10.1007/978-3-0348-8264-4_3.

Barron, J. W. (2003), The Stratigraphy, Metamorphism, and Tectonic History of the Solwezi Area, Northwest Province, Zambia: Integrating Geological Field Observations and Airborne Geophysics in the Interpretation of Regional Geology, Ph.D. thesis.

Beaumont, C., R. A. Jamieson, M. H. Nguyen, and B. Lee (2001), Himalayan tectonics explained by extrusion of a low-viscosity crustal channel coupled to focused surface denudation, *Nature*, *414*, 738–742, doi:10.1038/414738a.

Belsley, D. A., E. Kuh, and R. E. Welsch (1980), *Regression Diagnostics: Identifying Influential Data and Sources of Collinearity*, Wiley, New York.

Bensen, G. D., M. H. Ritzwoller, M. P. Barmin, A. L. Levshin, F. Lin, M. P. Moschetti, N. M. Shapiro, and Y. Yang (2007), Processing seismic ambient noise data to obtain reliable broad-band surface wave dispersion measurements, *Geophysical Journal International*, *169*, 1239–1260, doi:10.1111/j.1365-246X.2007.03374.x.

Berman, R. G. (1991), Thermobarometry Using Multi-Equilibrium Calculations; a New Technique, with Petrological Applications, *The Canadian Mineralogist*, *29*, 833–855.

Berman, R. G. (2007), winTWQ (Version 2.3): A Software Package for Performing Internally-Consistent Thermobarometric Calculations, Geological Survey of Canada, Open File, 5462.

Bhatia, M. R. (1985), Rare Earth Element Geochemistry of Australian Paleozoic Graywackes and Mudrocks: Provenance and Tectonic Control, *Sedimentary Geology*, *45*(1), 97–113, doi:10.1016/0037-0738(85)90025-9.

Bidgood, A., and M. Hitzman (2023), New models to aid the discovery of critical raw material deposits for the Green Stone Age, *Geological Society, London, Special Publications*, *526*, 183–191, doi:10.1144/SP526-2022-79.

Blannin, R., M. Frenzel, L. Tuşa, S. Birtel, P. Ivăşcanu, T. Baker, and J. Gutzmer (2021), Uncertainties in Quantitative Mineralogical Studies Using Scanning Electron Microscope-Based Image Analysis, *Minerals Engineering*, *167*, 106,836, doi:10.1016/j.mineng.2021.106836.

Broughton, D. W., M. W. Hitzman, and A. J. Stephens (2002), *Exploration History and Geology of the Kansanshi Cu(-Au) Deposit, Zambia*, Society of Economic Geologists, doi:10.5382/SP.09.07.

Bucher, K., and M. Frey (1994), Metamorphism of Pelitic Rocks (Metapelites), in *Petrogenesis of Metamorphic Rocks*, edited by K. Bucher and M. Frey, pp. 191–232, Springer, Berlin, Heidelberg, doi:10.1007/978-3-662-03000-4_7.

Burke, K. (1977), Aulacogens and continental breakup, *Annual Review of Earth and Planetary Sciences, Vol. 5, p. 371*, *5*, 371.

Caddick, M. J., and A. B. Thompson (2008), Quantifying the Tectono-Metamorphic Evolution of Pelitic Rocks from a Wide Range of Tectonic Settings: Mineral Compositions in Equilibrium, *Contributions to Mineralogy and Petrology*, *156*(2), 177–195, doi:10.1007/s00410-008-0280-6.

Cailteux, J. L., and T. D. Putter (2019), The Neoproterozoic Katanga Supergroup (D. R. Congo): State-of-the-art and revisions of the lithostratigraphy, sedimentary basin and geodynamic evolution, *Journal of African Earth Sciences*, *150*, 522–531, doi:10.1016/j.jafrearsci.2018.07.020.

Caliński, T., and J. Harabasz (1974), A dendrite method for cluster analysis, *Communications in Statistics-theory and Methods*, *3*(1), 1–27.

Carlson, W. D., D. R. Pattison, and M. J. Caddick (2015), Beyond the Equilibrium Paradigm: How Consideration of Kinetics Enhances Metamorphic Interpretation, *American Mineralogist*, *100*(8-9), 1659–1667, doi:10.2138/am-2015-5097.

Cawood, I., M. St-Onge, O. Weller, M. Searle, D. Waters, and T. Ahmad (2024), Structural and metamorphic architecture of the Zanskar Himalaya, Suru Valley region, NW India: Implications for the evolution of the Himalayan metamorphic core, *Geological Society of America Bulletin*, doi:10.1130/B37241.1.

Cawood, I. P. (2024), Structural and Metamorphic Evolution of the Zanskar Himalaya, Suru Valley Region, NW India, Ph.D. thesis, University of Oxford.

Chen, Y., E. Saygin, B. Kennett, M. T. Qashqai, J. Hauser, D. Lumley, and M. Sandiford (2023), Next-generation seismic model of the Australian crust from synchronous and asynchronous ambient noise imaging, *Nature Communications*, *14*(1), 1192, doi:10.1038/s41467-023-36514-z.

Christensen, N. I. (1996), Poisson's ratio and crustal seismology, *Journal of Geophysical Research: Solid Earth*, *101*, 3139–3156, doi:10.1029/95JB03446.

Claerbout, J. F., and F. Muir (1973), Robust Modeling With Erratic Data, *Geophysics*, *38*(5), 826–844, doi:10.1190/1.1440378.

Cline, J. S., A. H. Hofstra, J. L. Muntean, R. M. Tosdal, and K. A. Hickey (2005), *Carlin-Type Gold Deposits in Nevada: Critical Geologic Characteristics and Viable Models*, Society of Economic Geologists, doi:10.5382/AV100.15.

Colombero, C., M. Papadopoulou, T. Kauti, P. Skyttä, E. Koivisto, M. Savolainen, and L. V. Socco (2022), Surface-wave tomography for mineral exploration: a successful combination of passive and active data (Siilinjärvi phosphorus mine, Finland), *Solid Earth*, *13*, 417–429, doi:10.5194/se-13-417-2022.

Comte, D., G. Palma, J. Vargas, D. Calle-Gardella, M. Peña, S. García-Fierro, J. D'Andres, S. Roecker, and S. Pichott (2023), Imaging the subsurface architecture in porphyry copper deposits using local earthquake tomography, *Scientific Reports*, *13*, 6812, doi:10.1038/s41598-023-33820-w.

Connolly, J. (2005), Computation of Phase Equilibria by Linear Programming: A Tool for Geodynamic Modeling and Its Application to Subduction Zone Decarbonation, *Earth and Planetary Science Letters*, *236*(1-2), 524–541, doi:10.1016/j.epsl.2005.04.033.

Connolly, J. A. D. (1990), Multivariable phase diagrams; an algorithm based on generalized thermodynamics, *American Journal of Science*, *290*, 666–718, doi:10.2475/ajs.290.6.666.

Copley, A., and O. Weller (2022), The controls on the thermal evolution of continental mountain ranges, *Journal of Metamorphic Geology*, *40*, 1235–1270, doi:10.1111/jmg.12664.

Cosi, M., A. D. Bonis, G. Gosso, J. Hunziker, G. Martinotti, S. Moratto, J. Robert, and F. Ruhlman (1992), Late proterozoic thrust tectonics, high-pressure metamorphism and uranium mineralization in the Domes Area, Lufilian Arc, Northwestern Zambia, *Precambrian Research*, *58*, 215–240, doi:10.1016/0301-9268(92)90120-D.

Coward, M., and M. Daly (1984), Crustal lineaments and shear zones in Africa: Their relationship to plate movements, *Precambrian Research*, *24*(1), 27–45, doi:10.1016/0301-9268(84)90068-8.

Crotwell, H. P., and T. J. Owens (2005), Automated Receiver Function Processing, *Seismological Research Letters*, *76*(6), 702–709, doi:10.1785/gssrl.76.6.702.

d'Alessandro, A., D. Luzio, and G. D'Anna (2014), Urban MEMS based seismic network for post-earthquakes rapid disaster assessment, *Advances in Geosciences*, *40*, 1–9, doi:10.5194/adgeo-40-1-2014.

Daly, M., and N. Tosca (2020), A Geodynamic Model of the Kansanshi Cu-Au System, Zambia., *SEG Mwale Symposium 2020: New Insights in Sediment-Hosted Copper*.

Daly, M., S. Chakraborty, P. Kasolo, M. Musiwa, P. Mumba, B. Naidu, C. Namateba, O. Ngambi, and M. Coward (1984), The Lufilian arc and Irumide belt of Zambia: Results of a geotraverse across their intersection, *Journal of African Earth Sciences (1983)*, *2*(4), 311–318, doi:10.1016/0899-5362(84)90003-4.

Daly, M. C. (1986), The intracratonic Irumide Belt of Zambia and its bearing on collision orogeny during the Proterozoic of Africa, *Geological Society, London, Special Publications*, *19*(1), 321–328, doi:10.1144/GSL.SP.1986.019.01.18.

Daly, M. C., M. Zimba, M. Purkiss, and F. Chibesakunda (2024), Lithospheric Thickness, Rift and Inversion Tectonics: The Formation and Deformation of the Neoproterozoic Katangan Basin of Central Africa., doi:10.22541/essoar.171412711.12959313/v1.

Davies, R. J., S. A. Stewart, J. A. Cartwright, M. Lappin, R. Johnston, S. I. Fraser, and A. R. Brown (2004), 3D Seismic Technology: Are We Realising Its Full Potential?, *Geological Society, London, Memoirs*, *29*, 1–10, doi:10.1144/GSL.MEM.2004.029.01.01.

de Capitani, C., and T. H. Brown (1987), The Computation of Chemical Equilibrium in Complex Systems Containing Non-Ideal Solutions, *Geochimica et Cosmochimica Acta*, *51*(10), 2639–2652, doi:10.1016/0016-7037(87)90145-1.

de Capitani, C., and K. Petrakakis (2010), The Computation of Equilibrium Assemblage Diagrams with Theriak/Domino Software, *American Mineralogist*, *95*(7), 1006–1016, doi:10.2138/am.2010.3354.

De Swardt, A., A. R. Drysdall, and P. Garrard (1964), Precambrian geology and structure in central Northern Rhodesia, *Northern Rhodesia, geological Survey, Memoir*, (2).

Demaison, G., and B. J. Huizinga (1991), Genetic Classification of Petroleum Systems, *AAPG Bulletin*, *75*, doi:10.1306/0C9B29BB-1710-11D7-8645000102C1865D.

Diener, J. F. A., and R. Powell (2010), Influence of Ferric Iron on the Stability of Mineral Assemblages, *Journal of Metamorphic Geology*, *28*(6), 599–613, doi:10.1111/j.1525-1314.2010.00880.x.

Dominish, E., N. Florin, and S. Teske (2019), Responsible Minerals Sourcing for Renewable Energy, *Tech. rep.*, Institute for Sustainable Futures, University of Technology Sydney.

Doukkari, S. A., J. F. Diener, K. Ouzegane, and J.-R. Kienast (2018), Mineral Equilibrium Modelling and Calculated Chemical Potential Relations of Reaction Textures in the Ultrahigh-Temperature In Ouzzal Terrane (In Hihaou Area, Western Hoggar, Algeria), *Journal of Metamorphic Geology*, *36*(9), 1175–1198, doi:10.1111/jmg.12441.

Droop, G. T. R. (1987), A General Equation for Estimating Fe3+ Concentrations in Ferromagnesian Silicates and Oxides from Microprobe Analyses, Using Stoichiometric Criteria, *Mineralogical Magazine*, *51*(361), 431–435, doi:10.1180/minmag.1987.051.361.10.

Drysdall, A., R. Johnson, T. Moore, and J. Thieme (1972), Outline of the geology of Zambia, *Geol. Mijnbouw*, *51*(3), 265–276.

Dubacq, B., and J. B. Forshaw (2024), The Composition of Metapelitic Biotite, White Mica, and Chlorite: A Review with Implications for Solid-Solution Models, *European Journal of Mineralogy*, *36*(4), 657–685, doi:10.5194/ejm-36-657-2024.

Duda, R. O., and P. E. Hart (1973), Pattern classification and scene analysis, *A Wiley-Interscience Publication.*

Duesterhoeft, E., and P. Lanari (2020), Iterative Thermodynamic Modelling—Part 1: A Theoretical Scoring Technique and a Computer Program (Bingo-Antidote), *Journal of Metamorphic Geology*, *38*(5), 527–551, doi:10.1111/jmg.12538.

d'Alessandro, A., S. Scudero, and G. Vitale (2019), A Review of the Capacitive MEMS for Seismology, *Sensors*, *19*, 3093, doi:10.3390/s19143093.

Efron, B. (1979), Bootstrap Methods: Another Look at the Jackknife, *The Annals of Statistics*, *7*, doi:10.1214/aos/1176344552.

Eglinger, A., A. Tarantola, C. Durand, C. Ferraina, O. Vanderhaeghe, A.-S. André-Mayer, J.-L. Paquette, and E. Deloule (2014), Uranium mobilization by fluids associated with Ca–Na metasomatism: A P–T–t record of fluid–rock interactions during Pan-African metamorphism (Western Zambian Copperbelt), *Chemical Geology*, *386*, 218–237, doi:10.1016/j.chemgeo.2014.07.028.

Eglinger, A., O. Vanderhaeghe, A. S. André-Mayer, P. Goncalves, A. Zeh, C. Durand, and E. Deloule (2016), Tectono-metamorphic evolution of the internal zone of the Pan-African Lufilian orogenic belt (Zambia): Implications for crustal reworking and syn-orogenic uranium mineralizations, *Lithos*, *240-243*, 167–188, doi:10.1016/j.lithos.2015.10.021.

Evans, C. L., and T. J. Napier-Munn (2013), Estimating Error in Measurements of Mineral Grain Size Distribution, *Minerals Engineering*, *52*, 198–203, doi:10.1016/j.mineng.2013.09.005.

Faber, K., and P. Maxwell (1997), Geophone spurious frequency: What is it and how does it affect seismic data quality?, *Canadian Journal of Exploration Geophysics*, *3*, 46–54.

Forshaw, J., and P. Lanari (2024), Neglected elements: carbon, hydrogen, sulphur, fluorine, chlorine, and ferric iron in metapelites., *Metamorphic Studies Group Research-in-Progress Meeting*.

Forshaw, J. B., and D. R. Pattison (2023), Major-element geochemistry of pelites, *Geology*, *51*, 39–43, doi:10.1130/G50542.1.

Forshaw, J. B., and D. R. M. Pattison (2021), Ferrous/Ferric (Fe2+/Fe3+) Partitioning among Silicates in Metapelites, *Contributions to Mineralogy and Petrology*, *176*(9), 63, doi:10.1007/s00410-021-01814-4.

Forshaw, J. B., D. J. Waters, D. R. Pattison, R. M. Palin, and P. Gopon (2019), A comparison of observed and thermodynamically predicted phase equilibria and mineral compositions in mafic granulites, *Journal of Metamorphic Geology*, *37*, 153–179, doi:10.1111/jmg.12454.

Forsyth, D. W., and A. Li (2005), Array Analysis of Two-Dimensional Variations in Surface Wave Phase Velocity and Azimuthal Anisotropy in the Presence of Multipathing Interference, in *Seismic Earth: Array Analysis of Broadband Seismograms*, pp. 81–97, American Geophysical Union (AGU), doi:https://doi.org/10.1029/157GM06.

Fougerat, A., L. Guérineau, and N. Tellier (2018), High-quality signal recording down to 0.001 Hz with standard MEMS accelerometers, *SEG Technical Program Expanded Abstracts 2018*, pp. 196–200, doi:10.1190/segam2018-2995544.1.

François, A. (1973), *L'Extrémité occidentale de l'arc cuprifére shabien: Etude géologique*, Éditeur non identifié.

Fuławka, K., P. Mertuszka, M. Szumny, L. Stolecki, and K. Szczerbiński (2022), Application of MEMS-Based Accelerometers for Near-Field Monitoring of Blasting-Induced Seismicity, *Minerals*, *12*(5), 533, doi:10.3390/min12050533.

Gawthorpe, R. L., and M. R. Leeder (2000), Tectono-sedimentary evolution of active extensional basins, *Basin Research*, *12*, 195–218, doi:10.1111/j.1365-2117.2000.00121.x.

Gerstoft, P., M. C. Fehler, and K. G. Sabra (2006), When Katrina hit California, *Geophysical Research Letters*, *33*, doi:10.1029/2006GL027270.

Gervais, F., and P.-H. Trapy (2021), Testing solution models for phase equilibrium (forward) modeling of partial melting experiments, *Contributions to Mineralogy and Petrology*, *176*, 4, doi:10.1007/s00410-020-01762-5.

González-Barros, M., and J. A. Espí (2019), The returns on mining exploration investments, *Boletín Geológico y Minero*, *130*, 161–180, doi:10.21701/bolgeomin.130.1.010.

Gordon, T. M. (1992), Generalized Thermobarometry: Solution of the Inverse Chemical Equilibrium Problem Using Data for Individual Species, *Geochimica et Cosmochimica Acta*, *56*(5), 1793–1800, doi:10.1016/0016-7037(92)90310-F.

Goscombe, B., D. A. Foster, D. Gray, and B. Wade (2020), Assembly of central Gondwana along the Zambezi Belt: Metamorphic response and basement reactivation during the Kuunga Orogeny, *Gondwana Research*, *80*, 410–465, doi:10.1016/j.gr.2019.11.004.

Green, E. C. R., R. W. White, J. F. A. Diener, R. Powell, T. J. B. Holland, and R. M. Palin (2016), Activity–Composition Relations for the Calculation of Partial Melting Equilibria in Metabasic Rocks, *Journal of Metamorphic Geology*, *34*(9), 845–869, doi:10.1111/jmg.12211.

Guevara, V. E., and M. J. Caddick (2016), Shooting at a moving target: phase equilibria modelling of high-temperature metamorphism, *Journal of Metamorphic Geology*, *34*, 209–235, doi:10.1111/jmg.12179.

Guiraud, M., R. Powell, and G. Rebay (2001), H2O in Metamorphism and Unexpected Behaviour in the Preservation of Metamorphic Mineral Assemblages, *Journal of Metamorphic Geology*, *19*(4), 445–454, doi:10.1046/j.0263-4929.2001.00320.x.

Halford, D. (1968), A general mechanical model for |f| spectral density random noise with special reference to flicker noise 1/|f|, *Proceedings of the IEEE*, *56*, 251–258, doi:10.1109/PROC.1968.6269.

Hanson, R. E., T. J. Wilson, and M. S. Wardlaw (1988), Deformed batholiths in the Pan-African Zambezi belt, Zambia: Age and implications for regional Proterozoic tectonics, *Geology*, *16*(12), 1134, doi:10.1130/0091-7613(1988)016<1134:DBITPA>2.3.CO;2.

Harmon, N., and C. A. Rychert (2016), Joint inversion of teleseismic and ambient noise Rayleigh waves for phase velocity maps, an application to Iceland, *Journal of Geophysical Research: Solid Earth*, *121*, 5966–5987, doi:10.1002/2016JB012934.

Harmon, N., P. Gerstoft, C. A. Rychert, G. A. Abers, M. S. de la Cruz, and K. M. Fischer (2008), Phase velocities from seismic noise using beamforming and cross correlation in Costa Rica and Nicaragua, *Geophysical Research Letters*, *35*, doi:10.1029/2008GL035387.

Hatfield, W. C. (1937), The Geology of the Solwezi District, Northern Rhodesia, *Quarterly Journal of the Geological Society of London*, *93*(1-4), 127–155, doi:10.1144/GSL.JGS.1937.093.01-04.08.

Havskov, J., and G. Alguacil (2016), *Seismic Sensors*, pp. 13–100, Springer International Publishing, doi:10.1007/978-3-319-21314-9_2.

Hawthorne, F., R. Oberti, G. Harlow, W. Maresch, R. Martin, J. Schumacher, and M. Welch (2012), Nomenclature of the Amphibole Supergroup, *American Mineralogist*, *97*, 2031–2048.

Henry, D. J., and C. V. Guidotti (2002), Titanium in biotite from metapelitic rocks: Temperature effects, crystal-chemical controls, and petrologic applications, *American Mineralogist*, *87*, 375–382, doi:10.2138/am-2002-0401.

Henry, D. J., C. V. Guidotti, and J. A. Thomson (2005), The Ti-saturation surface for low-to-medium pressure metapelitic biotites: Implications for geothermometry and Ti-substitution mechanisms, *American Mineralogist*, *90*, 316–328, doi:10.2138/am.2005.1498.

Herrmann, P., S. Laroche, H. Wang, and N. Tellier (2021), Land Acquisition without Data Jitter Made Possible with MEMS Sensors, *82nd EAGE Annual Conference Exhibition*, pp. 1–5, doi:10.3997/2214-4609.202112510.

Herrmann, R. B. (2013), Computer Programs in Seismology: An Evolving Tool for Instruction and Research, *Seismological Research Letters*, *84*, 1081–1088, doi:10.1785/0220110096.

Hitzman, M. (2000), Source basins for sediment-hosted stratiform Cu deposits: implications for the structure of the Zambian Copperbelt, *Journal of African Earth Sciences*, *30*, 855–863, doi:10.1016/S0899-5362(00)00056-7.

Hitzman, M., R. Kirkham, D. Broughton, J. Thorson, and D. Selley (2005), *The Sediment-Hosted Stratiform Copper Ore System*, Society of Economic Geologists, doi:10.5382/AV100.19.

Hitzman, M. W., D. Selley, and S. Bull (2010), Formation of Sedimentary Rock-Hosted Stratiform Copper Deposits through Earth History, *Economic Geology*, *105*, 627–639, doi:10.2113/gsecongeo.105.3.627.

Hitzman, M. W., D. Broughton, D. Selley, J. Woodhead, D. Wood, and S. Bull (2012), *The Central African Copperbelt: Diverse Stratigraphic, Structural, and Temporal Settings in the World's Largest Sedimentary Copper District*, Society of Economic Geologists, doi:10.5382/SP.16.19.

Hodges, K. V., and L. W. McKenna (1987), Realistic propagation of uncertainties in geologic thermobarometry, *American Mineralogist*, *72*, 671–680.

Hofer, H. E., G. P. Brey, B. Schulz-Dobrick, and R. Oberhänsli (1994), The Determination of the Oxidation State of Iron by the Electron Microprobe, *European Journal of Mineralogy*, pp. 407–418, doi:10.1127/ejm/6/3/0407.

Hoggard, M. J., K. Czarnota, F. D. Richards, D. L. Huston, A. L. Jaques, and S. Ghelichkhan (2020), Global distribution of sediment-hosted metals controlled by craton edge stability, *Nature Geoscience*, *13*(7), 504–510, doi:10.1038/s41561-020-0593-2.

Holland, T., and J. Blundy (1994), Non-Ideal Interactions in Calcic Amphiboles and Their Bearing on Amphibole-Plagioclase Thermometry, *Contributions to Mineralogy and Petrology*, *116*(4), 433–447, doi:10.1007/BF00310910.

Holland, T., and R. Powell (1996a), Thermodynamics of Order-Disorder in Minerals; I, Symmetric Formalism Applied to Minerals of Fixed Composition, *American Mineralogist*, *81*(11-12), 1413–1424, doi:10.2138/am-1996-11-1214.

Holland, T., and R. Powell (1996b), Thermodynamics of Order-Disorder in Minerals: II. Symmetric Formalism Applied to Solid Solutions, *American Mineralogist*, *81*(11-12), 1425–1437, doi:10.2138/am-1996-11-1215.

Holland, T., and R. Powell (2003), Activity–Composition Relations for Phases in Petrological Calculations: An Asymmetric Multicomponent Formulation, *Contributions to Mineralogy and Petrology*, *145*(4), 492–501, doi:10.1007/s00410-003-0464-z.

Holland, T. J. B., and R. Powell (1998), An internally consistent thermodynamic data set for phases of petrological interest, *Journal of Metamorphic Geology*, *16*, 309–343, doi:10.1111/j.1525-1314.1998.00140.x.

Holland, T. J. B., and R. Powell (2011), An improved and extended internally consistent thermodynamic dataset for phases of petrological interest, involving a new equation of state for solids, *Journal of Metamorphic Geology*, *29*, 333–383, doi:10.1111/j.1525-1314.2010.00923.x.

Holland, T. J. B., E. C. R. Green, and R. Powell (2022), A Thermodynamic Model for Feldspars in KAlSi3O8-NaAlSi3O8-CaAl2Si2O8 for Mineral Equilibrium Calculations, *Journal of Metamorphic Geology*, *40*(4), 587–600, doi:10.1111/jmg.12639.

Hollis, D., J. McBride, D. Good, N. Arndt, F. Brenguier, and G. Olivier (2018), Use of ambient-noise surface-wave tomography in mineral resource exploration and evaluation, *SEG Technical Program Expanded Abstracts 2018*, pp. 1937–1940, doi:10.1190/segam2018-2998476.1.

Hollister, L. (1969), Contact Metamorphism in the Kwoiek Area of British Columbia: An End Member of the Metamorphic Process, *GSA Bulletin*, *80*(12), 2465–2494, doi:10.1130/0016-7606(1969)80[2465:CMITKA]2.0.CO;2.

Hoschek, G. (2004), Comparison of Calculated P-T Pseudosections for a Kyanite Eclogite from the Tauern Window, Eastern Alps, Austria, *European Journal of Mineralogy*, pp. 59–72, doi:10.1127/0935-1221/2004/0016-0059.

Hudson, T. S., J. M. Kendall, J. D. Blundy, M. E. Pritchard, P. MacQueen, S. S. Wei, J. H. Gottsmann, and S. Lapins (2023), Hydrothermal Fluids and Where to Find Them: Using Seismic Attenuation and Anisotropy to Map Fluids Beneath Uturuncu Volcano, Bolivia, *Geophysical Research Letters*, *50*, doi:10.1029/2022GL100974.

Ibraheem, I. M., B. Tezkan, and R. Bergers (2021), Integrated Interpretation of Magnetic and ERT Data to Characterize a Landfill in the North-West of Cologne, Germany, *Pure and Applied Geophysics*, *178*(6), 2127–2148, doi:10.1007/s00024-021-02750-x.

Jackson, M., O. Warin, G. Woad, and M. Hudec (2003), Neoproterozoic allochthonous salt tectonics during the Lufilian orogeny in the Katangan Copperbelt, central Africa, *Geological Society of America Bulletin*, *115*, 314–330, doi:10.1130/0016-7606(2003)115<0314:NASTDT>2.0.CO;2.

John, T., V. Schenk, K. Haase, E. Scherer, and F. Tembo (2003), Evidence for a Neoproterozoic ocean in south-central Africa from mid-oceanic-ridge–type geochemical signatures and pressure-temperature estimates of Zambian eclogites, *Geology*, *31*, 243, doi:10.1130/0091-7613(2003)031<0243:EFANOI>2.0.CO;2.

John, T., V. Schenk, K. Mezger, and F. Tembo (2004), Timing and PT Evolution of Whiteschist Metamorphism in the Lufilian Arc–Zambezi Belt Orogen (Zambia): Implications for the Assembly of Gondwana, *The Journal of Geology*, *112*, 71–90, doi:10.1086/379693.

Jones, T., G. Olivier, B. Murphy, L. Cole, C. Went, S. Olsen, N. Smith, M. Gal, B. North, and D. Burrows (2024), Real-Time Ambient Seismic Noise Tomography of the Hillside Iron Oxide–Copper–Gold Deposit, *Minerals*, *14*, 254, doi:10.3390/min14030254.

Kampunzu, A., and J. Cailteux (1999), Tectonic Evolution of the Lufilian Arc (Central Africa Copper Belt) During Neoproterozoic Pan African Orogenesis, *Gondwana Research*, *2*(3), 401–421, doi:10.1016/S1342-937X(05)70279-3.

kang Xu, K., W. Xie, K. Sun, J. ping Ren, P. hui Gong, S. fei He, Y. guan Lu, and H. Zhang (2022), Geochronology, geochemistry, and petrogenesis of I- and A-type granites in the Solwezi Dome of the Lufilian Arc: implications for the late-Mesoproterozoic magmatic and geodynamic evolution in northern Zambia, *Arabian Journal of Geosciences*, *15*, 1729, doi:10.1007/s12517-022-10971-0.

Kendrick, J., and A. Indares (2018), The Reaction History of Kyanite in High-P Aluminous Granulites, *Journal of Metamorphic Geology*, *36*(2), 125–146, doi:10.1111/jmg.12286.

Key, R., A. Liyungu, F. Njamu, V. Somwe, J. Banda, P. Mosley, and R. Armstrong (2001), The western arm of the Lufilian Arc in NW Zambia and its potential for copper mineralization, *Journal of African Earth Sciences*, *33*, 503–528, doi:10.1016/S0899-5362(01)00098-7.

Kobayashi, N., and K. Nishida (1998), Continuous excitation of planetary free oscillations by atmospheric disturbances, *Nature*, *395*, 357–360, doi:10.1038/26427.

Kohn, M. J. (2008), P-T-t data from central Nepal support critical taper and repudiate large-scale channel flow of the Greater Himalayan Sequence, *Geological Society of America Bulletin*, *120*, 259–273, doi:10.1130/B26252.1.

Kohn, M. J. (2014), Himalayan Metamorphism and Its Tectonic Implications, *Annual Review of Earth and Planetary Sciences*, *42*, 381–419, doi:10.1146/annurev-earth-060313-055005.

Kohn, M. J., and C. Northrup (2009), Taking mylonites' temperatures, *Geology*, *37*, 47–50, doi:10.1130/G25081A.1.

Kohn, M. J., and F. S. Spear (1991a), Error propagation for barometers: 2. Application to rocks, *American Mineralogist*, *76*, 138 – 147, cited by: 110.

Kohn, M. J., and F. S. Spear (1991b), Error Propagation for Barometers: 2. Application to Rocks, *American Mineralogist*, *76*, 138–147.

Kounoudis, R., J. M. Kendall, C. S. Ogden, S. Fishwick, C. Chifwepa, and M. C. Daly (2024), The tectonic development of the Central African Plateau: evidence from shear-wave splitting, *Geophysical Journal International*, *239*(3), 1694–1708, doi:10.1093/gji/ggae345.

Koymans, M. R., J. D. Ballesta, E. Ruigrok, R. Sleeman, L. Trani, and L. G. Evers (2021), Performance Assessment of Geophysical Instrumentation Through the Automated Analysis of Power Spectral Density Estimates, *Earth and Space Science*, *8*, doi:10.1029/2021EA001675.

Kuhn, S., M. J. Cracknell, and A. M. Reading (2019), Lithological mapping in the Central African Copper Belt using Random Forests and clustering: Strategies for optimised results, *Ore Geology Reviews*, *112*, 103,015, doi:10.1016/j.oregeorev.2019.103015.

Lai, J., and G. Chi (2007), CO2-rich fluid inclusions with chalcopyrite daughter mineral from the Fenghuangshan Cu–Fe–Au deposit, China: implications for metal transport in vapor, *Mineralium Deposita*, *42*, 293–299, doi:10.1007/s00126-006-0109-z.

Laine, J., and D. Mougenot (2007), Benefits of MEMS Based Seismic Accelerometers for Oil Exploration, *TRANSDUCERS 2007 - 2007 International Solid-State Sensors, Actuators and Microsystems Conference*, pp. 1473–1477, doi:10.1109/SENSOR.2007.4300423.

Laine, J., and D. Mougenot (2014), A high-sensitivity MEMS-based accelerometer, *The Leading Edge*, *33*, 1234–1242, doi:10.1190/tle33111234.1.

Lanari, P., and E. Duesterhoeft (2019), Modeling Metamorphic Rocks Using Equilibrium Thermodynamics and Internally Consistent Databases: Past Achievements, Problems and Perspectives, *Journal of Petrology*, *60*(1), 19–56, doi:10.1093/petrology/egy105.

Lanari, P., and M. Engi (2017), Local Bulk Composition Effects on Metamorphic Mineral Assemblages, *Reviews in Mineralogy and Geochemistry*, *83*, 55–102, doi:10.2138/rmg.2017.83.3.

Lanari, P., S. Ferrero, P. Goncalves, and E. G. Grosch (2019), Metamorphic Geology: Progress and Perspectives, *Geological Society, London, Special Publications*, *478*(1), 1–12, doi:10.1144/SP478-2018-186.

Langston, C. A. (1979), Structure under Mount Rainier, Washington, inferred from teleseismic body waves, *Journal of Geophysical Research: Solid Earth*, *84*(B9), 4749–4762.

Lapins, S., A. Butcher, J.-M. Kendall, T. S. Hudson, A. L. Stork, M. J. Werner, J. Gunning, and A. M. Brisbourne (2023), DAS-N2N: machine learning distributed acoustic sensing (DAS) signal denoising without clean data, *Geophysical Journal International*, *236*, 1026–1041, doi:10.1093/gji/ggad460.

Latallerie, F., C. Zaroli, S. Lambotte, A. Maggi, A. Walker, and P. Koelemeijer (2024), Towards surface-wave tomography with 3D resolution and uncertainty, doi:10.31223/X5FM79.

Lefebvre, J. J., and L. E. Patterson (1982), Hydrothermal assemblages of aluminian serpentine, florencite and kyanite in the Zairian Copperbelt.

Li, C.-N., Y.-H. Shao, and N.-Y. Deng (2015), Robust L1-norm Two-Dimensional Linear Discriminant Analysis, *Neural Networks*, *65*, 92–104, doi:10.1016/j.neunet.2015.01.003.

Ligorría, J. P., and C. J. Ammon (1999), Iterative deconvolution and receiver-function estimation, *Bulletin of the Seismological Society of America*, *89*(5), 1395–1400, doi:10.1785/BSSA0890051395.

Lobo-Guerrero Sanz, A. (2005), Pre-and Post-Katangan Granitoids of the greater Lufilian Arc—geology, geochemistry, geochronology and metallogenic significance, Ph.D. thesis.

Lognonné, P., W. B. Banerdt, W. T. Pike, D. Giardini, U. Christensen, R. F. Garcia, T. Kawamura, S. Kedar, B. Knapmeyer-Endrun, L. Margerin, F. Nimmo, M. Panning, B. Tauzin, J.-R. Scholz, D. Antonangeli, S. Barkaoui, E. Beucler, F. Bissig, N. Brinkman, M. Calvet, S. Ceylan, C. Charalambous, P. Davis, M. van Driel, M. Drilleau, L. Fayon, R. Joshi, B. Kenda, A. Khan, M. Knapmeyer, V. Lekic, J. McClean, D. Mimoun, N. Murdoch, L. Pan, C. Perrin, B. Pinot, L. Pou, S. Menina, S. Rodriguez, C. Schmelzbach, N. Schmerr, D. Sollberger, A. Spiga, S. Stähler, A. Stott, E. Stutzmann, S. Tharimena, R. Widmer-Schnidrig, F. Andersson, V. Ansan, C. Beghein, M. Böse, E. Bozdag, J. Clinton, I. Daubar, P. Delage, N. Fuji, M. Golombek, M. Grott, A. Horleston, K. Hurst, J. Irving, A. Jacob, J. Knollenberg, S. Krasner, C. Krause, R. Lorenz, C. Michaut, R. Myhill, T. Nissen-Meyer, J. ten Pierick, A.-C. Plesa, C. Quantin-Nataf, J. Robertsson, L. Rochas, M. Schimmel, S. Smrekar, T. Spohn, N. Teanby, J. Tromp, J. Vallade, N. Verdier, C. Vrettos, R. Weber, D. Banfield, E. Barrett, M. Bierwirth, S. Calcutt, N. Compaire, C. Johnson, D. Mance, F. Euchner, L. Kerjean, G. Mainsant, A. Mocquet, J. A. R. Manfredi, G. Pont, P. Laudet, T. Nebut, S. de Raucourt, O. Robert, C. T. Russell, A. Sylvestre-Baron, S. Tillier, T. Warren, M. Wieczorek, C. Yana, and P. Zweifel (2020), Constraints on the shallow elastic and anelastic structure of Mars from InSight seismic data, *Nature Geoscience*, *13*, 213–220, doi:10.1038/s41561-020-0536-y.

MacIntyre, T. J. (2019), Geology and Geochemistry of the Kansanshi Cu-(Au) deposit, North-Western Province, Zambia, Ph.D. thesis.

Mahar, E. M., J. M. Baker, R. Powell, T. J. B. Holland, and N. Howell (1997), The Effect of Mn on Mineral Stability in Metapelites, *Journal of Metamorphic Geology*, *15*(2), 223–238, doi:10.1111/j.1525-1314.1997.00011.x.

Maier, W. (2005), Platinum-group element (PGE) deposits and occurrences: Mineralization styles, genetic concepts, and exploration criteria, *Journal of African Earth Sciences*, *41*, 165–191, doi:10.1016/j.jafrearsci.2005.03.004.

Marquardt, D. W. (1970), Generalized Inverses, Ridge Regression, Biased Linear Estimation, and Nonlinear Estimation, *Technometrics*, *12*(3), 591, doi:10.2307/1267205.

Master, S., and M. Wendorff (2011), Chapter 12 Neoproterozoic glaciogenic diamictites of the Katanga Supergroup, Central Africa, *Geological Society, London, Memoirs*, *36*, 173–184, doi:10.1144/M36.12.

Master, S., C. Rainaud, R. Armstrong, D. Phillips, and L. Robb (2005), Provenance ages of the Neoproterozoic Katanga Supergroup (Central African Copperbelt), with implications for basin evolution, *Journal of African Earth Sciences*, *42*, 41–60, doi:10.1016/j.jafrearsci.2005.08.005.

McCuaig, T. C., and J. M. A. Hronsky (2014), *The Mineral System Concept: The Key to Exploration Targeting*, Society of Economic Geologists, doi:10.5382/SP.18.08.

McKeith, T. D., R. C. Schodde, and E. J. Baltis (2010), Gold Discovery Trends, *SEG Discovery*, pp. 1–26, doi:10.5382/SEGnews.2010-81.fea.

McLennan, S. M., S. Hemming, D. K. McDaniel, and G. N. Hanson (1993), Geochemical Approaches to Sedimentation, Provenance, and Tectonics, *Processes Controlling the Composition of Clastic Sediments*, p. 0, doi:10.1130/SPE284-p21.

McNamara, D. E., and R. Buland (2004), Ambient Noise Levels in the Continental United States, *Bulletin of the Seismological Society of America*, *94*, 1517–1527, doi:10.1785/012003001.

Menke, W. (1984), *Geophysical Data Analysis: Discrete Inverse Theory*, Elsevier, doi:10.1016/B978-0-12-490920-5.X5001-7.

Milani, L., J. Lehmann, K. V. Naydenov, K. Saalmann, J. A. Kinnaird, J. S. Daly, D. Frei, and A. Lobo-Guerrero Sanz (2015), A-type magmatism in a syn-collisional setting: The case of the Pan-African Hook Batholith in Central Zambia, *Lithos*, *216-217*, 48–72, doi:10.1016/j.lithos.2014.11.029.

Naydenov, K. V., J. Lehmann, K. Saalmann, L. Milani, J. A. Kinnaird, G. Charlesworth, D. Frei, and W. Rankin (2014), New constraints on the Pan-African Orogeny in Central Zambia: A structural and geochronological study of the Hook Batholith and the Mwembeshi Zone, *Tectonophysics*, *637*, 80–105, doi:10.1016/j.tecto.2014.09.010.

Naydenov, K. V., J. Lehmann, K. Saalmann, L. Milani, J. Poterai, J. A. Kinnaird, G. Charlesworth, and J. D. Kramers (2016), The geology of the Matala Dome: an important piece of the Pan-African puzzle in Central Zambia, *International Journal of Earth Sciences*, *105*(3), 695–712, doi:10.1007/s00531-015-1222-y.

Nottvedt, A., R. Gabrielsen, and R. Steel (1995), Tectonostratigraphy and sedimentary architecture of rift basins, with reference to the northern North Sea, *Marine and Petroleum Geology*, *12*, 881–901, doi:10.1016/0264-8172(95)98853-W.

Ogden, C. S., I. D. Bastow, A. Gilligan, and S. Rondenay (2019), A reappraisal of the H– stacking technique: implications for global crustal structure, *Geophysical Journal International*, *219*, 1491–1513, doi:10.1093/gji/ggz364.

Ohmoto, H., and D. M. Kerrick (1977), Devolatilization equilibria in graphitic systems, *American Journal of Science*, *277*, 1013–1044, doi:10.2475/ajs.277.8.1013.

Okada, K. (2021), A Historical Overview of the Past Three Decades of Mineral Exploration Technology, *Natural Resources Research*, *30*, 2839–2860, doi:10.1007/s11053-020-09721-4.

Palin, R. M., O. M. Weller, D. J. Waters, and B. Dyck (2016), Quantifying geological uncertainty in metamorphic phase equilibria modelling; a Monte Carlo assessment and implications for tectonic interpretations, *Geoscience Frontiers*, *7*, 591–607, doi:10.1016/j.gsf.2015.08.005.

Palin, R. M., P. J. Treloar, M. P. Searle, T. Wald, R. W. White, and R. Mertz-Kraus (2018), U-Pb monazite ages from the Pakistan Himalaya record pre-Himalayan Ordovician orogeny and Permian continental breakup, *GSA Bulletin*, doi:10.1130/B31943.1.

Pattison, D. R., and S. A. Goldsmith (2022), Metamorphism of the Buchan type-area, NE Scotland and its relation to the adjacent Barrovian domain, *Journal of the Geological Society*, *179*, doi:10.1144/jgs2021-040.

Pattison, D. R. M., and C. L. DeBuhr (2015), Petrology of metapelites in the Bugaboo aureole, British Columbia, Canada, *Journal of Metamorphic Geology*, *33*, 437–462, doi:10.1111/jmg.12128.

Pattison, D. R. M., and F. S. Spear (2018), Kinetic control of staurolite–Al2SiO5 mineral assemblages: Implications for Barrovian and Buchan metamorphism, *Journal of Metamorphic Geology*, *36*, 667–690, doi:10.1111/jmg.12302.

Pattison, D. R. M., and D. K. Tinkham (2009), Interplay between Equilibrium and Kinetics in Prograde Metamorphism of Pelites: An Example from the Nelson Aureole, British Columbia, *Journal of Metamorphic Geology*, *27*(4), 249–279, doi:10.1111/j.1525-1314.2009.00816.x.

Peterson, J. (1993), Observations and modeling of seismic background noise.

Pike, W. T., A. K. Delahunty, A. Mukherjee, G. Dou, H. Liu, S. Calcutt, and I. M. Standley (2014), A self-levelling nano-g silicon seismometer, *IEEE SENSORS 2014 Proceedings*, pp. 1599–1602, doi:10.1109/ICSENS.2014.6985324.

Porada, H. (1989), Pan-African rifting and orogenesis in southern to equatorial Africa and eastern Brazil, *Precambrian Research*, *44*(2), 103–136, doi:10.1016/0301-9268(89)90078-8.

Porada, H., and V. Berhorst (2000), Towards a new understanding of the Neoproterozoic-Early Palaeozoic Lufilian and northern Zambezi Belts in Zambia and the Democratic Republic of Congo, *Journal of African Earth Sciences*, *30*(3), 727–771, doi:10.1016/S0899-5362(00)00049-X.

Powell, R. (1985), Geothermometry and Geobarometry: A Discussion, *Journal of the Geological Society*, *142*(1), 29–38, doi:10.1144/gsjgs.142.1.0029.

Powell, R., and T. Holland (1988), An internally consistent dataset with uncertainties and correlations: 3. Applications to geobarometry, worked examples and a computer program, *Journal of Metamorphic Geology*, *6*, 173–204, doi:10.1111/j.1525-1314.1988.tb00415.x.

Powell, R., and T. Holland (1993a), The Applicability of Least Squares in the Extraction of Thermodynamic Data from Experimentally Bracketed Mineral Equilibria, *American Mineralogist*, *78*(1-2), 107–112.

Powell, R., and T. Holland (1993b), On the Formulation of Simple Mixing Models for Complex Phases, *American Mineralogist*, *78*(11-12), 1174–1180.

Powell, R., and T. Holland (1994), Optimal geothermometry and geobarometry, *American Mineralogist*, *79*, 120–133.

Powell, R., and T. J. B. Holland (2008), On thermobarometry, *Journal of Metamorphic Geology*, *26*, 155–179, doi:10.1111/j.1525-1314.2007.00756.x.

Purkiss, M. (2024), Basin analysis of the Katangan Basin of Zambia: subsidence mechanisms, dynamic stratigraphy, and mineral systems, Ph.D. thesis.

Purkiss, M. (2025), Facies and sequence stratigraphy of the Katangan Basin in Zambia, *Journal of African Earth Sciences*, *227*, 105,617, doi:10.1016/j.jafrearsci.2025.105617.

Rainaud, C., S. Master, R. Armstrong, and L. Robb (2005), Geochronology and nature of the Palaeoproterozoic basement in the Central African Copperbelt (Zambia and the Democratic Republic of Congo), with regional implications, *Journal of African Earth Sciences*, *42*, 1–31, doi:10.1016/j.jafrearsci.2005.08.006.

Reid, A., G. Olivier, and T. Jones (2025), Ambient Noise Tomography: A Sensitive, Rapid, Passive Seismic Technique for Mineral Exploration, *SEG Discovery*, (140), 17–26, doi:10.5382/SEGnews.2025-140.fea-01.

Riel, N., B. J. P. Kaus, E. C. R. Green, and N. Berlie (2022), MAGEMin, an Efficient Gibbs Energy Minimizer: Application to Igneous Systems, *Geochemistry, Geophysics, Geosystems*, *23*, doi:10.1029/2022GC010427.

Ritzwoller, M. H., N. M. Shapiro, M. P. Barmin, and A. L. Levshin (2002), Global surface wave diffraction tomography, *Journal of Geophysical Research: Solid Earth*, *107*(B12), ESE 4–1–ESE 4–13, doi:https://doi.org/10.1029/2002JB001777.

Roser, B. P., and R. J. Korsch (1988), Provenance Signatures of Sandstone-Mudstone Suites Determined Using Discriminant Function Analysis of Major-Element Data, *Chemical Geology*, *67*(1), 119–139, doi:10.1016/0009-2541(88)90010-1.

Sánchez-Sesma, F. J., and M. Campillo (1991), Diffraction of P, SV, and Rayleigh waves by topographic features: A boundary integral formulation, *Bulletin of the Seismological Society of America*, *81*(6), 2234–2253.

Schaeffer, A. J., and S. Lebedev (2013), Global shear speed structure of the upper mantle and transition zone, *Geophysical Journal International*, *194*(1), 417–449, doi:10.1093/gji/ggt095.

Schlaphorst, D., N. Harmon, J. M. Kendall, C. A. Rychert, J. Collier, A. Rietbrock, and S. Goes (2021), Variation in Upper Plate Crustal and Lithospheric Mantle Structure in the Greater and Lesser Antilles From Ambient Noise Tomography, *Geochemistry, Geophysics, Geosystems*, *22*, doi:10.1029/2021GC009800.

Schorn, S., and J. F. Diener (2019), Seemingly Disparate Temperatures Recorded in Coexisting Granulite Facies Lithologies, *Journal of Metamorphic Geology*, *37*(8), 1049–1078, doi:10.1111/jmg.12500.

Schumacher, J. C. (1991), Empirical Ferric Iron Corrections: Necessity, Assumptions, and Effects on Selected Geothermobarometers, *Mineralogical Magazine*, *55*(378), 3–18, doi:10.1180/minmag.1991.055.378.02.

Searle, M. P., D. J. Waters, D. C. Rex, and R. N. Wilson (1992), Pressure, temperature and time constraints on Himalayan metamorphism from eastern Kashmir and western Zanskar, *Journal of the Geological Society*, *149*, 753–773, doi:10.1144/gsjgs.149.5.0753.

Selley, D., D. Broughton, R. Scott, M. Hitzman, S. Bull, R. Large, P. McGoldrick, M. Croaker, N. Pollington, and F. Barra (2005), *A New Look at the Geology of the Zambian Copperbelt*, Society of Economic Geologists, doi:10.5382/AV100.29.

Shapiro, N. M., M. Campillo, L. Stehly, and M. H. Ritzwoller (2005), High-Resolution Surface-Wave Tomography from Ambient Seismic Noise, *Science*, *307*, 1615–1618, doi:10.1126/science.1108339.

Sillitoe, R. H. (2010), Porphyry Copper Systems, *Economic Geology*, *105*, 3–41, doi:10.2113/gsecongeo.105.1.3.

Sillitoe, R. H., J. Perelló, R. A. Creaser, J. Wilton, and T. Dawborn (2015), Two Ages of Copper Mineralization in the Mwombezhi Dome, Northwestern Zambia: Metallogenic Implications for the Central African Copperbelt, *Economic Geology*, *110*, 1917–1923, doi:10.2113/econgeo.110.8.1917.

Sleeman, R., A. van Wettum, and J. Trampert (2006), Three-Channel Correlation Analysis: A New Technique to Measure Instrumental Noise of Digitizers and Seismic Sensors, *Bulletin of the Seismological Society of America*, *96*, 258–271, doi:10.1785/0120050032.

Spear, F. S., D. R. Pattison, and J. T. Cheney (2016), The Metamorphosis of Metamorphic Petrology, in *The Web of Geological Sciences: Advances, Impacts, and Interactions II: Geological Society of America Special Paper 523*, edited by M. Bickford, The Geological Society of America, doi:10.1130/2016.2523(02).

Starr, P. G., and D. R. M. Pattison (2019), Equilibrium and Disequilibrium Processes across the Greenschist–Amphibolite Transition Zone in Metabasites, *Contributions to Mineralogy and Petrology*, *174*(2), 18, doi:10.1007/s00410-019-1553-y.

Starr, P. G., D. R. M. Pattison, and D. E. Ames (2020), Mineral Assemblages and Phase Equilibria of Metabasites from the Prehnite–Pumpellyite to Amphibolite Facies, with the Flin Flon Greenstone Belt (Manitoba) as a Type Example, *Journal of Metamorphic Geology*, *38*(1), 71–102, doi:10.1111/jmg.12513.

Steltenpohl, M. G., and J. M. Bartley (1987), Thermobarometric profile through the Caledonian nappe stack of Western Ofoten, North Norway, *Contributions to Mineralogy and Petrology*, *96*, 93–103, doi:10.1007/BF00375530.

Štípská, P., and R. Powell (2005), Constraining the P–T Path of a MORB-type Eclogite Using Pseudosections, Garnet Zoning and Garnet-Clinopyroxene Thermometry: An Example from the Bohemian Massif, *Journal of Metamorphic Geology*, *23*(8), 725–743, doi:10.1111/j.1525-1314.2005.00607.x.

Stork, A. L., C. Allmark, A. Curtis, J.-M. Kendall, and D. J. White (2018), Assessing the potential to use repeated ambient noise seismic tomography to detect CO2 leaks: Application to the Aquistore storage site, *International Journal of Greenhouse Gas Control*, *71*, 20–35, doi:10.1016/j.ijggc.2018.02.007.

Stuwe, K. (1997), Effective bulk composition changes due to cooling: a model predicting complexities in retrograde reaction textures, *Contributions to Mineralogy and Petrology*, *129*, 43–52, doi:10.1007/s004100050322.

Stüwe, K., and R. Powell (1995), PT Paths from Modal Proportions: Application to the Koralm Complex, Eastern Alps | Contributions to Mineralogy and Petrology, *Contributions to Mineralogy and Petrology*, *119*, 83–93.

Tarantola, A., and B. Valette (1982), Generalized nonlinear inverse problems solved using the least squares criterion, *Reviews of Geophysics*, *20*, 219–232, doi:10.1029/RG020i002p00219.

Tellier, N., and P. Herrmann (2020), True Vertical and Orthogonal OBN Sensing with 3C MEMS Sensors, in *Second EAGE Marine Acquisition Workshop*, pp. 1–4, European Association of Geoscientists Engineers, doi:10.3997/2214-4609.202034022.

Tellier, N., S. Laroche, and P. Herrmann (2020), Native true amplitude and phase broadband sensing now available with the latest MEMS sensors, *SEG Technical Program Expanded Abstracts 2020*, pp. 111–115, doi:10.1190/segam2020-3423114.1.

Thompson, A. B. (1986), The Role of Mineral Kinetics in the Development of Metamorphic Microtextures, in *Fluid—Rock Interactions during Metamorphism*, vol. 5, edited by S. K. Saxena, J. V. Walther, and B. J. Wood, pp. 154–193, Springer New York, New York, NY, doi:10.1007/978-1-4612-4896-5_7.

Tinkham, D. K., C. A. Zuluaga, and H. H. Stowell (2001), Metapelite Phase Equilibria Modeling in MnNCKFMASH: The Effect of Variable Al2O3 and MgO/(MgO + FeO) on Mineral Stability, *Geological Materials Research*, *3*(1), 1–42.

Tomlinson, J. P., P. Denton, P. K. H. Maguire, and D. C. Booth (2006), Analysis of the crustal velocity structure of the British Isles using teleseismic receiver functions, *Geophysical Journal International*, *167*, 223–237, doi:10.1111/j.1365-246X.2006.03044.x.

Torrealday, H. I., M. W. Hitzman, H. J. Stein, R. J. Markley, R. Armstrong, and D. Broughton (2000), Re-Os and U-Pb dating of the vein-hosted mineralization at the Kansanshi copper deposit, Northern Zambia., *Economic Geology*, *95*, 1165–1170, doi:10.2113/gsecongeo.95.5.1165.

Turlin, F., A. Eglinger, O. Vanderhaeghe, A.-S. André-Mayer, M. Poujol, J. Mercadier, and R. Bartlett (2016), Synmetamorphic Cu remobilization during the Pan-African orogeny: Microstructural, petrological and geochronological data on the kyanite-micaschists hosting the Cu(–U) Lumwana deposit in the Western Zambian Copperbelt of the Lufilian belt, *Ore Geology Reviews*, *75*, 52–75, doi:10.1016/j.oregeorev.2015.11.022.

Unrug, R. (1988), Mineralization controls and source of metals in the Lufilian fold belt, Shaba (Zaire), Zambia, and Angola, *Economic Geology*, *83*(6), 1247–1258, doi:10.2113/gsecongeo.83.6.1247.

Van der Plas, L., and A. C. Tobi (1965), A Chart for Judging the Reliability of Point Counting Results, *American Journal of Science*, *263*(1), 87–90, doi:10.2475/ajs.263.1.87.

Vance, D., and E. Mahar (1998), Pressure-Temperature Paths from P-T Pseudosections and Zoned Garnets: Potential, Limitations and Examples from the Zanskar Himalaya, NW India, *Contributions to Mineralogy and Petrology*, *132*, 225–245.

Vaughan, D. J., M. A. Sweeney, G. Friedrich, R. Diedel, and C. Haranczyk (1989), The Kupferschiefer; an overview with an appraisal of the different types of mineralization, *Economic Geology*, *84*(5), 1003–1027, doi:10.2113/gsecongeo.84.5.1003.

Verma, S. P., and J. S. Armstrong-Altrin (2016), Geochemical Discrimination of Siliciclastic Sediments from Active and Passive Margin Settings, *Sedimentary Geology*, *332*, 1–12, doi:10.1016/j.sedgeo.2015.11.011.

Voll, G., J. Töpel, D. R. M. Pattison, and F. Seifert (Eds.) (1991), *Equilibrium and Kinetics in Contact Metamorphism*, Springer, Berlin, Heidelberg, doi:10.1007/978-3-642-76145-4.

Vorhies, S. H., J. J. Ague, and A. K. Schmitt (2013), Zircon growth and recrystallization during progressive metamorphism, Barrovian zones, Scotland, *American Mineralogist*, *98*, 219–230, doi:10.2138/am.2013.4240.

Walker, C. B., M. P. Searle, and D. J. Waters (2001), An Integrated Tectonothermal Model for the Evolution of the High Himalaya in Western Zanskar with Constraints from Thermobarometry and Metamorphic Modeling, *Tectonics*, *20*(6), 810–833, doi: 10.1029/2000TC001249.

Walters, J. B. (2022), MinPlot: A mineral formula recalculation and plotting program for electron probe microanalysis, *Mineralogia*, *53*, 51–66, doi:10.2478/mipo-2022-0005.

Wang, Y., F.-C. Lin, and K. M. Ward (2019), Ambient noise tomography across the Cascadia subduction zone using dense linear seismic arrays and double beamforming, *Geophysical Journal International*, *217*, 1668–1680, doi:10.1093/gji/ggz109.

Ward, K. M., R. C. Porter, G. Zandt, S. L. Beck, L. S. Wagner, E. Minaya, and H. Tavera (2013), Ambient noise tomography across the Central Andes, *Geophysical Journal International*, *194*, 1559–1573, doi:10.1093/gji/ggt166.

Ward, K. M., F. Lin, and B. Schmandt (2018), High-Resolution Receiver Function Imaging Across the Cascadia Subduction Zone Using a Dense Nodal Array, *Geophysical Research Letters*, *45*(22), 12,218–12,225, doi:https://doi.org/10.1029/2018GL079903.

Waters, D. J. (2019), Metamorphic constraints on the tectonic evolution of the High Himalaya in Nepal: the art of the possible, *Geological Society, London, Special Publications*, *483*, 325–375, doi:10.1144/SP483-2018-187.

Waters, D. J., and D. P. Lovegrove (2002), Assessing the extent of disequilibrium and overstepping of prograde metamorphic reactions in metapelites from the Bushveld Complex aureole, South Africa, *Journal of Metamorphic Geology*, *20*, 135–149, doi: 10.1046/j.0263-4929.2001.00350.x.

Watzel, R. (2023), Minerals for future technologies: how Germany copes with challenges, *Geological Society, London, Special Publications*, *526*(1), 13–24, doi: 10.1144/SP526-2022-12.

Weaver, R., and O. Lobkis (2001), On the emergence of the Green's function in the correlations of a diffuse field, *The Journal of the Acoustical Society of America*, *109*, 2410–2410, doi:10.1121/1.4744516.

Welch, P. (1967), The use of fast Fourier transform for the estimation of power spectra: A method based on time averaging over short, modified periodograms, *IEEE Transactions on Audio and Electroacoustics*, *15*, 70–73, doi:10.1109/TAU.1967.1161901.

Weller, O. M., M. R. St-Onge, D. J. Waters, N. Rayner, M. P. Searle, S. Chung, R. M. Palin, Y. Lee, and X. Xu (2013), Quantifying Barrovian metamorphism in the Danba Structural Culmination of eastern Tibet, *Journal of Metamorphic Geology*, *31*, 909–935, doi:10.1111/jmg.12050.

Weller, O. M., T. J. B. Holland, C. R. Soderman, E. C. R. Green, R. Powell, C. D. Beard, and N. Riel (2024), New Thermodynamic Models for Anhydrous Alkaline-Silicate Magmatic Systems, *Journal of Petrology*, *65*(10), egae098, doi:10.1093/petrology/egae098.

Wheeler, J., L. S. Mangan, and D. J. Prior (2004), Disequilibrium in the Ross of Mull Contact Metamorphic Aureole, Scotland: A Consequence of Polymetamorphism, *Journal of Petrology*, *45*(4), 835–853, doi:10.1093/petrology/egg113.

Wheller, C. J., and R. Powell (2014), A New Thermodynamic Model for Sapphirine: Calculated Phase Equilibria in K2O–FeO–MgO–Al2O3–SiO2–H2O–TiO2–Fe2O3, *Journal of Metamorphic Geology*, *32*(3), 287–299, doi:10.1111/jmg.12067.

White, Powell, Holland, and Worley (2000), The Effect of TiO2 and Fe2O3 on Metapelitic Assemblages at Greenschist and Amphibolite Facies Conditions: Mineral Equilibria Calculations in the System K2O–FeO–MgO–Al2O3–SiO2–H2O–TiO2–Fe2O3, *Journal of Metamorphic Geology*, *18*(5), 497–511, doi:10.1046/j.1525-1314.2000.00269.x.

White, E., and L. Hook (2023), Miner Rio Tinto to test 'new frontiers' as copper age dawns, *Financial Times*.

White, R. W., R. Powell, and T. J. B. Holland (2007), Progress Relating to Calculation of Partial Melting Equilibria for Metapelites, *Journal of Metamorphic Geology*, *25*(5), 511–527, doi:10.1111/j.1525-1314.2007.00711.x.

White, R. W., R. Powell, and T. E. Johnson (2014a), The effect of Mn on mineral stability in metapelites revisited: new a–x relations for manganese-bearing minerals, *Journal of Metamorphic Geology*, *32*, 809–828, doi:10.1111/jmg.12095.

White, R. W., R. Powell, T. J. B. Holland, T. E. Johnson, and E. C. R. Green (2014b), New Mineral Activity–Composition Relations for Thermodynamic Calculations in Metapelitic Systems, *Journal of Metamorphic Geology*, *32*(3), 261–286, doi:10.1111/jmg.12071.

Whitney, D. L., and B. W. Evans (2010), Abbreviations for Names of Rock-Forming Minerals, *American Mineralogist*, *95*(1), 185–187, doi:10.2138/am.2010.3371.

Williams, P., and B. Nisbet (2017), Structural framework of the Lufilian Fold Belt in the Domes region of North Western Province, Zambia from interpretation of geophysical data, *Journal of African Earth Sciences*, *129*, 542–557, doi:10.1016/j.jafrearsci.2017.01.029.

Winder, T., C. A. Bacon, J. D. Smith, T. Hudson, T. Greenfield, and R. S. White (2019), QuakeMigrate: a Modular, Open-Source Python Package for Automatic Earthquake Detection and Location.

Withers, M., R. Aster, C. Young, J. Beiriger, M. Harris, S. Moore, and J. Trujillo (1998), A comparison of select trigger algorithms for automated global seismic phase and event detection, *Bulletin of the Seismological Society of America*, *88*, 95–106, doi:10.1785/BSSA0880010095.

Wood, D., and J. Hedenquist (2019), Mineral Exploration: Discovering and Defining Ore Deposits, *SEG Discovery*, pp. 1–22, doi:10.5382/Geo-and-Mining-02.

Worley, and Powell (2000), High-precision relative thermobarometry: theory and a worked example, *Journal of Metamorphic Geology*, *18*, 91–101, doi:10.1046/j.1525-1314.2000.00239.x.

Wyborn, L. A. I., C. A. Heinrich, and A. L. Jaques (1994), Australian Proterozoic mineral systems: essential ingredients and mappable criteria, *The AusIMM annual conference*, *1994*, 109–115.

Yao, H., and R. D. van der Hilst (2009), Analysis of ambient noise energy distribution and phase velocity bias in ambient noise tomography, with application to SE Tibet, *Geophysical Journal International*, *179*(2), 1113–1132, doi:10.1111/j.1365-246X.2009.04329.x.

Yardley, B. W. D. (1977), The nature and significance of the mechanism of sillimanite growth in the Connemara schists, Ireland, *Contributions to Mineralogy and Petrology*, *65*, 53–58, doi:10.1007/BF00373570.

Zhang, X., L. L. H. Tsang, Y. Wang, and B. Zhao (2009), Petrologic composition model of the upper crust in Bohai Bay basin, China, based on Lamé impedances, *Applied Geophysics*, *6*, 327–336, doi:10.1007/s11770-009-0039-5.

Zhou, Y., F. A. Dahlen, and G. Nolet (2004), Three-dimensional sensitivity kernels for surface wave observables, *Geophysical Journal International*, *158*(1), 142–168, doi:10.1111/j.1365-246X.2004.02324.x.

Zhu, L., and H. Kanamori (2000), Moho depth variation in southern California from teleseismic receiver functions, *Journal of Geophysical Research: Solid Earth*, *105*, 2969–2980, doi:10.1029/1999JB900322.

Appendix A

The Application of MEMS Accelerometers to Regional-scale Passive Seismology.

Table A.1 Oxford Seismograph Network Details

Network	Station	Instrument	Latitude	Longitude	Elevation	Start date	End date
ONSTAGE	ON001	WiNG node	51.81420	-1.43495	140.06300	19/10/2020	16/11/2020
ONSTAGE	ON002	WiNG node	51.64410	-1.00110	113.09200	19/10/2020	16/11/2020
ONSTAGE	ON003	WiNG node	51.87430	-1.47404	139.47700	19/10/2020	16/11/2020
ONSTAGE	ON004	WiNG node	51.76480	-1.26606	63.10200	19/10/2020	16/11/2020
ONSTAGE	ON005	WiNG node	51.87160	-1.27593	101.09000	19/10/2020	16/11/2020
ONSTAGE	ON006	WiNG node	51.76480	-1.26606	63.10200	19/10/2020	16/11/2020
ONSTAGE	ON007	WiNG node	51.70940	-1.25095	95.34700	19/10/2020	16/11/2020
ONSTAGE	ON008	WiNG node	51.70750	-0.99896	90.40000	19/10/2020	16/11/2020
ONSTAGE	ON009	WiNG node	51.78220	-1.49869	83.08200	19/10/2020	16/11/2020
ONSTAGE	ON010	WiNG node	51.66520	-1.07804	72.33900	19/10/2020	16/11/2020
ONSTAGE	ON011	WiNG node	51.73110	-1.23392	75.92500	19/10/2020	16/11/2020
ONSTAGE	ON012	WiNG node	51.76480	-1.26606	63.10200	19/10/2020	16/11/2020
ONSTAGE	ON013	WiNG node	51.83010	-1.19692	64.47000	19/10/2020	16/11/2020
ONSTAGE	ON014	WiNG node	51.62410	-0.90301	184.55600	19/10/2020	16/11/2020
ONSTAGE	ON015	WiNG node	51.62410	-0.90283	187.23200	19/10/2020	16/11/2020
ONSTAGE	ON016	WiNG node	51.80540	-1.31276	66.93200	19/10/2020	16/11/2020
ONSTAGE	ON017	WiNG node	51.84690	-1.30629	62.48300	19/10/2020	16/11/2020
ONSTAGE	ON018	WiNG node	51.86530	-1.56440	108.04800	19/10/2020	16/11/2020
ONSTAGE	ON019	WiNG node	51.70350	-1.10643	78.29500	19/10/2020	16/11/2020
ONSTAGE	ON020	WiNG node	51.63770	-1.13921	48.08000	19/10/2020	16/11/2020
ONSTAGE	ESP1	60s-100 Hz Güralp CMG-ESPCD	51.76480	-1.26606	63.10200	19/10/2020	16/11/2020
ONSTAGE	ESP2	60s-50 Hz Güralp CMG-ESPCD	51.86530	-1.56440	108.04800	20/10/2020	16/11/2020
ONSTAGE	GEOPHONE1	GS-11D 4.5 Hz geophone - Reftek-RT130 datalogger	51.76480	-1.26606	63.10200	19/10/2020	16/11/2020

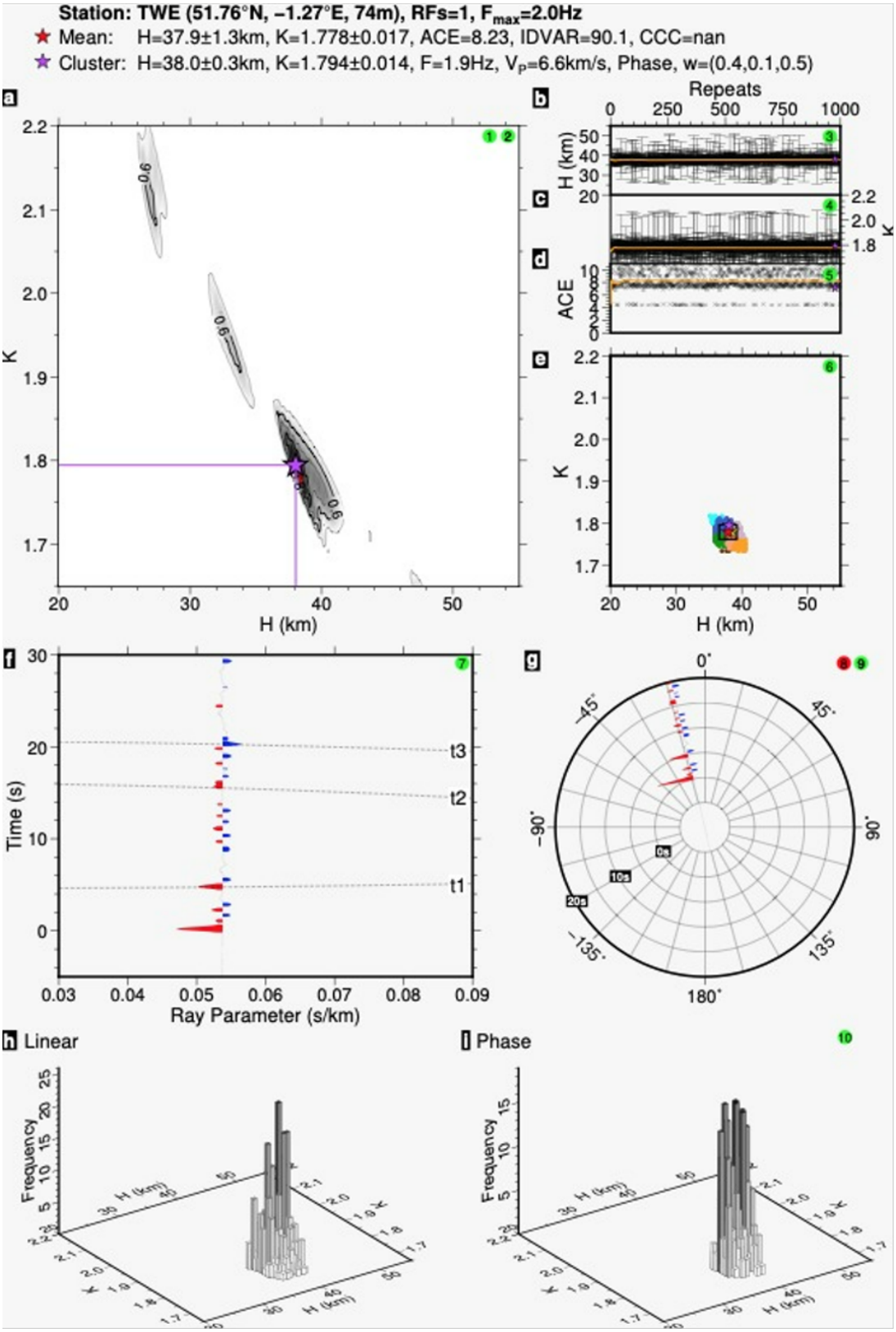

Fig. A.1 Full output from the H-k stacking routine of *Ogden et al.* (2019) for an Alaskan M7.6 earthquake recorded on a Guralp CMP-ESPCD.

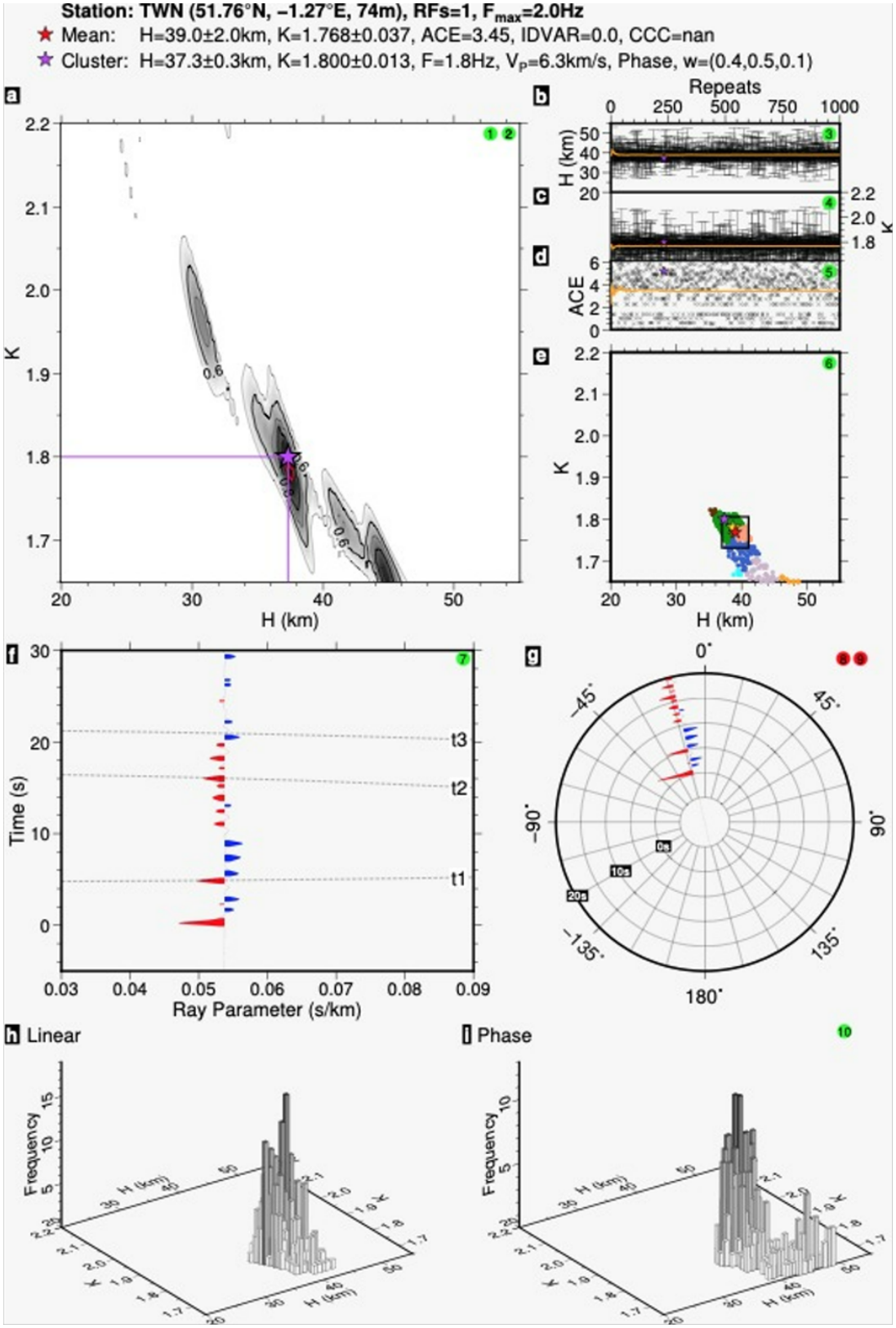

Fig. A.2 Full output from the H-k stacking routine of *Ogden et al.* (2019) for an Alaskan M7.6 earthquake recorded on a 3-component WiNG node system.

Table A.2 Values used for the STA/LTA analysis.

Earthquake	**Magnitude**	**Epicentral Distance ()**	**STA (s)**	**LTA (s)**	**Bandpass Max. (Hz)**	**Bandpass Min. (Hz)**
Stoke-on-Trent	1.3	1.26	3	40	4	12
Greece	7.0	24	4	50	0.01	3
Alaska	7.6	72	4	50	0.01	3

Appendix B

Towards Optimal Estimates of P-T Conditions and Uncertainty.

B.1 Methods: Natural Sample

B.1.1 Analytical setup and mineral recalculation

Mineral compositional analysis and element-distribution maps were completed on a Cameca SX5-Fe electron microprobe with a tungsten tipped field emission gun at the Department of Earth Sciences, University of Oxford. Analyses were conducted on carbon coated, polished thin sections, ~30 µm thick. Mineral compositional analyses were undertaken at an accelerating voltage of 15 keV, electron beam current of 20 nA and diameter of 10 µm. Primary and secondary standards included albite (Na, Si, Al), MgO, sanidine (K), wollastonite (Ca), TiO_2, Mn, fayalite (Fe), Durango apatite (P), Cr, Zn.

Table B.1 EPMA peak and background measurement parameters

Spectrometer	Elements	Crystal	Background position
Sp1	Na Kα	TAP	(-850, 850)
Sp1	Mg Kα	TAP	(-1750, 1400)
Sp2	K Kα	PET	(-650, 650)
Sp2	Ti Kα	PET	(-1000, 800)
Sp3	Ca Kα	LPET	(-800, 800)
Sp3	P Kα	LPET	(-800, 1300)
Sp4	Si Kα	TAP	(-750, 850)
Sp4	Al Kα	TAP	(-650, 800)
Sp5	Mn Kα	LLIF	(-800, 800)
Sp5	Fe Kα	LLIF	(-1000, 1000)
Sp5	Cr Kα	LLIF	(-1000, 1000)
Sp5	Zn Kα	LLIF	(-1000, 1000)

Wavelength dispersive spectrometer spot analyses were collected for each mineral in each thin section. Line profiles were used for porphyroblastic phases and individual spots were manually selected for different textural positions of the matrix phases. A population mean and 1 standard deviation was calculated for analyses from each matrix mineral phase. The garnet grain with the greatest X_{Sps} in the core was selected for modelling and a representative analysis was taken from the garnet rim. As there is not population uncertainty for a representative point, an estimate was taken using the

uncertainty from AX, propagated onto the endmember. Representative spot analyses were used for all phases for avP mode in THERMOCALC (*Powell and Holland*, 1994).

Raw microprobe-derived mineral analyses (oxide weight%) were recalculated using the program AX to a standard number of oxygens per formula unit for each mineral: garnet (12), staurolite (46), plagioclase (3), K-feldspar (8), biotite (11), muscovite (11), chlorite (14), amphibole (23), ilmenite-hematite (3). The proportion of Fe_3+/Fe_{total} and activities of mineral end-members was calculated using AX.

B.1.2 Thermobarometry

B.1.2.1 Conventional thermometry

The Ti-in-biotite thermometer of *Henry et al.* (2005) was selected for ICSV13 because biotite is abundant and the thermometer was specifically calibrated for graphitic pelites that contain either ilmenite or rutile as the Ti-dominant phase, both of which are present. Biotite compositions are also within the suggested calibration range of X_{Mg} = 0.275–1.000, Ti = 0.02–0.30 apfu, and T = 480–800 °C (*Henry et al.*, 2005). For metabasic compositions the hornblende-plagioclase NaSi-CaAl exchange thermometer was used as the independent thermometry result as pre-requisite composition is present, the minerals show textural equilibrium, and it has been successfully applied in calcic-amphibole bearing assemblages in numerous metamorphic and igneous studies. The thermometer calibration of *Holland and Blundy* (1994) was used with corrections from **?**. An in-house spreadsheet is used where half of the Ti substitution is treated as deprotonation (for compatibility with the *Green et al.* (2016) amphibole model) and allocates Mn preferentially to the M4 site, following the stoichiometry of *Hawthorne et al.* (2012). Thermometry results were averaged across compositional analyses and the relevant calibration error of ± 24 °C (Ti-in-biotite) and ± 40 °C (hornblende-plagioclase) are given with the respective results.

B.1.2.2 Multi-equilibrium barometry

Recalculated point analyses for the interpreted equilibrium phases were run through avP mode in THERMOCALC (version 3.37; (*Powell and Holland*, 1994)) using dataset 5.5 (*Holland and Powell*, 1998). An older dataset was used in order to provide a semi-independent P constraint in comparison to the pseudosection modelling which uses dataset 6.2 (*Holland and Powell*, 2011). Endmembers were sequentially removed until all indices conformed (the χ^2 test), following the procedure outlined in (*Powell and Holland*, 1994). Iteration to constrain aH_2O is explained in a subsequent section. The thermobarometer intersection was calculated based on the calibration error of the Ti-in-biotite thermometer or Hornblende-Plagioclase exchange thermometer and

1 σ error range of avP (defined by the propagated AX uncertainties) at the given thermometer result.

B.1.2.3 Phase equilibrium modelling

Forward modelling for both the pelitic natural sample and the synthetic pelite composition was performed in Theriak-Domino (*de Capitani and Brown*, 1987; *de Capitani and Petrakakis*, 2010, ICSV13: version 25th May 2021, modified by D. Tinkham; synthetics: : version 11th June 2023, modified by D. Tinkham2023.06.11) using a converted version of ds6.2 (*Holland and Powell*, 2011, version td-ds62-mp50-v05 from 11th March 2022, modified by D. Tinkham). Forward models were computed in the 11-component MnNCKFMASHTO system (MnO-Na_2-CaO-K_2-FeO-MgO-Al_2O_3-SiO_2-H_2O-TiO_2-O_2). MnO was added, as Mn has been shown to have a large effect on garnet stability (*Mahar et al.*, 1997; *White et al.*, 2014b). The following solid-solution models were used: silicate melt, garnet, biotite, muscovite, margarite, orthopyroxene, cordierite, staurolite, chlorite, chloritoid (*White et al.*, 2014a), feldspar (*Holland et al.*, 2022), stipnomelane, minnesotaite, prehnite, pumpellyite, epidote (*Holland and Powell*, 2011), sapphirine (*Wheller and Powell*, 2014), ilmenite and hematite, magnetite (subsolidus model; *White et al.*, 2000).

All metabasite pseudosections were constructed also in Theriak-Domino using a later version (version 11th June 2023) to incorporate the latest compositional models (e.g., FSP4TR; *Holland et al.*, 2022) integrated into ds6.2 (version td-ds62-mb50-v07 from 24th Dec 2022, modified by D. Tinkham). Forward models were computed in the 10-component NCKFMASHTO system (Na_2-CaO-K_2-FeO-MgO-Al_2O_3-SiO_2-H_2O-TiO_2-O_2). The following solid-solution models were used: silicate melt, hornblende, actinolite, glaucophane, jadeite-omphacite-diopside clinopyroxene, muscovite (*Green et al.*, 2016), feldspar (*Holland et al.*, 2022), epidote, olivine (*Holland and Powell*, 2011), garnet, biotite, orthopyroxene, chlorite (*White et al.*, 2014a), ilmenite and hematite, magnetite (subsolidus model; *White et al.*, 2000). Additional phases with no solid solution include H_2O, andalusite, kyanite, sillimanite, corundum, H_2O, quartz, rutile, and titanite.

The following modifications were made to the bulk composition for sample ICSV13: accounting for the presence of both apatite and monazite a half-P_2O_5 correction was made; a value of $X\mathrm{Fe}_{3+}$ was set at 6.25 % using Fe-Ti-oxide minerals present as a guide of oxidation state and informed from T-X and P-X pseudosections (*Diener and Powell*, 2010; *Forshaw and Pattison*, 2021); H_2O was set in excess for all sub-solidus regions (in this case $M H_2O$ was set to 20 %), to simulate prograde metamorphism (*Guiraud et al.*, 2001).

For sample ICSV117, Fe_2O_3 is distributed across multiple phases, making Fe-Ti-oxides less reliable for determining the oxidation state. Instead, the bulk rock $X_{\mathrm{Fe}^{3+}}$ was calculated as a mean of amphibole $X_{\mathrm{Fe}^{3+}}$, given that hornblende is the modally

dominant mineral. The $X_{Fe^{3+}}$ calculation uses the in-house spreadsheet adjustments detailed above, producing better alignment than AX calculations with the model of *Green et al.* (2016), making it the preferred choice. H_2O was set in excess for all sub-solidus regions (MH_2O = 20 %).

B.1.2.4 Constraining aH_2O

For modelled bulk compositions, initial pseudosection reconnaissance assuming dominant pure H_2O for a large proportion of the sample set resulted in no field match across large *P-T* ranges for the observed assemblage, or temperatures significantly in excess of conventional thermometry results (*Cawood*, 2024). Therefore thermometry and multiequilibrium barometry were used constrain aH_2O of the system (e.g., *Walker et al.*, 2001; *Powell and Holland*, 2008). The Ti-in-biotite and hornblende-plagioclase thermometers (*Henry et al.*, 2005; *Holland and Blundy*, 1994) are not constrained by aH_2O and are orthogonal to the system used for modelling. The results from these thermometers were used with an aH_2O-independent (ICSV13) or aH_2O-dependent (ICSV117) avP result. For ICSV13 where the avP result was constrained by reactions without a free fluid phase, the forward model was first calculated using $aH_2O = 1.0$, then iteration proceeded in decrements of 0.1 to achieve acceptable overlap between the thermobarometer intersection, peak assemblage field, and the median best-fit solution. For ICSV117 which used aH_2O-dependent calculations in avP, aH_2O was reduced in avP increments of 0.1 until all indices conformed within the thermometer error range. This aH_2O constraint then informed the input into the thermodynamic database for the forward model. For further details of the aH_2O-independent approach see *Cawood* (2024). aH_2O was set at 0.5 for ICSV13 and 0.7 for ICSV117 based on these results. To produce statistically significant avP results, the final run for ICSV13 excluded Mg-staurolite, Fe-staurolite, paragonite, and albite endmembers, and for ICSV117 excluded pargasite and glaucophane.

B.2 Comparison between LinaForma and Bingo-Antidote

In addition to the contrasting treatment of error discussed in the main manuscript, there are several other key differences between the Bingo-Antidote (*Duesterhoeft and Lanari*, 2020) and the LinaForma workflows. Three differences will be summarized below:

B.2.1 Integration with other software

Bingo-Antidote is fully integrated with Theriak-Domino (*de Capitani and Brown*, 1987; *de Capitani and Petrakakis*, 2010) and XMapTools (*Lanari et al.*, 2019), which provides

a number of advantages over the LinaForma workflow. In particular, Bingo-Antidote can inherently weight the inversion (via the assemblage scorer, Q_{asm}) to select areas in P-T space in which the appropriate stable phase assemblage is predicted, as measured by XMapTools. Additionally, the variation in the local bulk composition can be measured by XMapTools and then propagated through the Bingo-Antidote algorithm to assess the impact of bulk composition uncertainty on the resulting P-T estimate (Recipe 9). In comparison, LinaForma is a standalone piece of software which can be applied to a diverse range of geological or geophysical problems, so long as an appropriate forward model can be calculated.

B.2.2 The objective functions and diagnostics

Bingo-Antidote uses a number of objective functions which are unique to the software, including separate functions for the assemblage, the mineral modes, the mineral compositions and then a combined function to represent the global evaluation. These objective functions are highly optimized for their specific tasks. For example, the composition quality factor, Q_{cmp}, has been optimized for analysing the compositions of phases expressed in apfu (Equation B.1).

$$Q_{cmp} = \sum_{i} v_i^{norm} \sum_{j}^{N} \frac{100 \cdot (1 - \frac{(\Delta_{i,j} - \sigma_{i,j})}{6\sigma_{i,j}})^{X_{i,j}^{model}+1}}{N} \tag{B.1}$$

Where v_i^{norm} is the normalized volume fraction of phase i, $\Delta_{i,j}$ is the absolute difference in composition between the observations and model for element j in phase i, $X_{i,j}^{model}$ is the modeled composition, and $\sigma_{i,j}$ is the standard deviation of the observed composition.

In comparison, LinaForma uses a standard L1-norm objective function. This makes the LinaForma workflow robust to outliers and suitable for a diverse range of variables. This is a particularly attractive trait in complex geological systems. LinaForma also outputs a significant number of diagnostic tests, allowing the user to intuitively understand the model fit and the performance and sensitivity of each variable separately.

B.2.3 The inversion technique

Bingo-Antidote performs a coarse gird-search (10 x 10) in P-T space to identify the stability field with the best assemblage fit and then a second coarse multi-dimensional (P-T-X) grid-search within the best-fitting stability field. The bulk composition variables (X) include $a\mathrm{H_2O}$, $f\mathrm{O_2}$, H, C, and O. The parameters resulting in the lowest total fit are then used as a starting value for an iterative inversion known as the Nelder-Mead simplex algorithm. The solution to which the algorithm converges is taken as the final

solution. Relying on a coarse grid-search (10 x 10) to define the basin of attraction of the global minimum is appropriate when the stability fields are large as the field will likely be sampled by the coarse grid. In contrast, LinaForma relies on a single, fine-scale, grid-search inversion, performed on forward models provided by the user. The resolution of the inversion is controlled by the resolution of these forward models. A fine-scale grid-search will prevent global minima being missed (*Menke*, 1984), although it may be more computationally expensive to run depending on the computational cost of calculating the forward models.

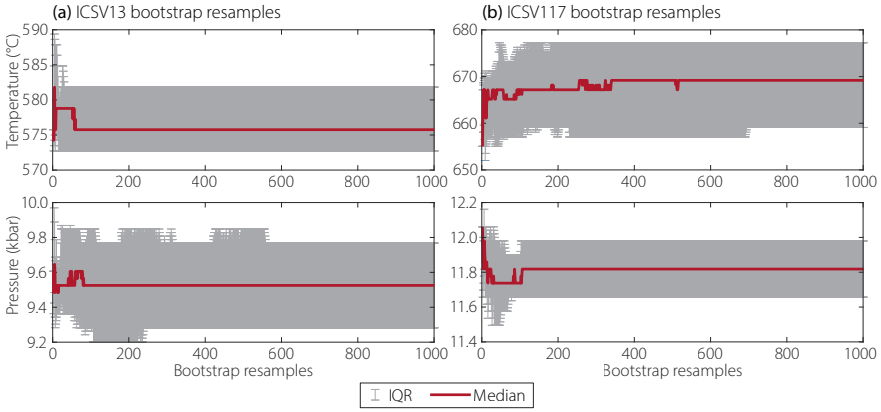

Fig. B.1 Number of bootstrap resamples relative to best-fit median and IQR for the temperature and pressure solution for ICSV13 and ICSV117.

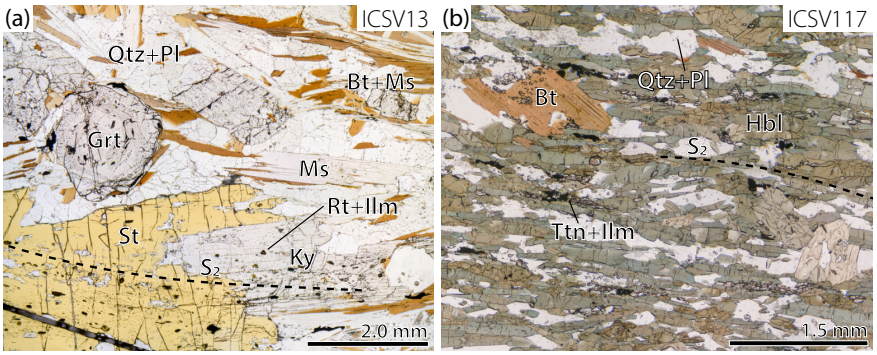

Fig. B.2 Petrographic images of characteristic mineral assemblages and textures in a) ICSV13 and b) ICSV117. S_2 refers to the main deformation fabric expressed in the sample. Mineral abbreviations follow *Whitney and Evans* (2010).

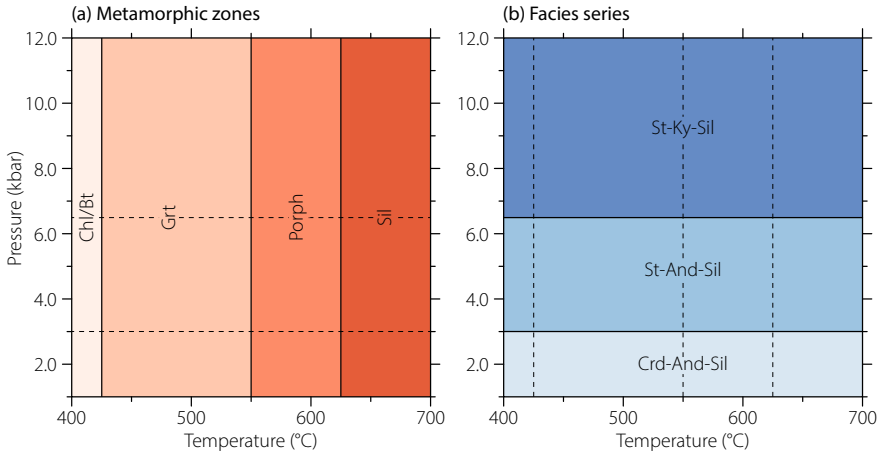

Fig. B.3 Binned temperature and pressure domains used in this study. Domains are separated into approximate a) metamorphic zones and b) facies series. The temperature and pressure domains do not strictly denote the stability of the minerals. Diagram modified from schematic in *Forshaw and Pattison* (2021).

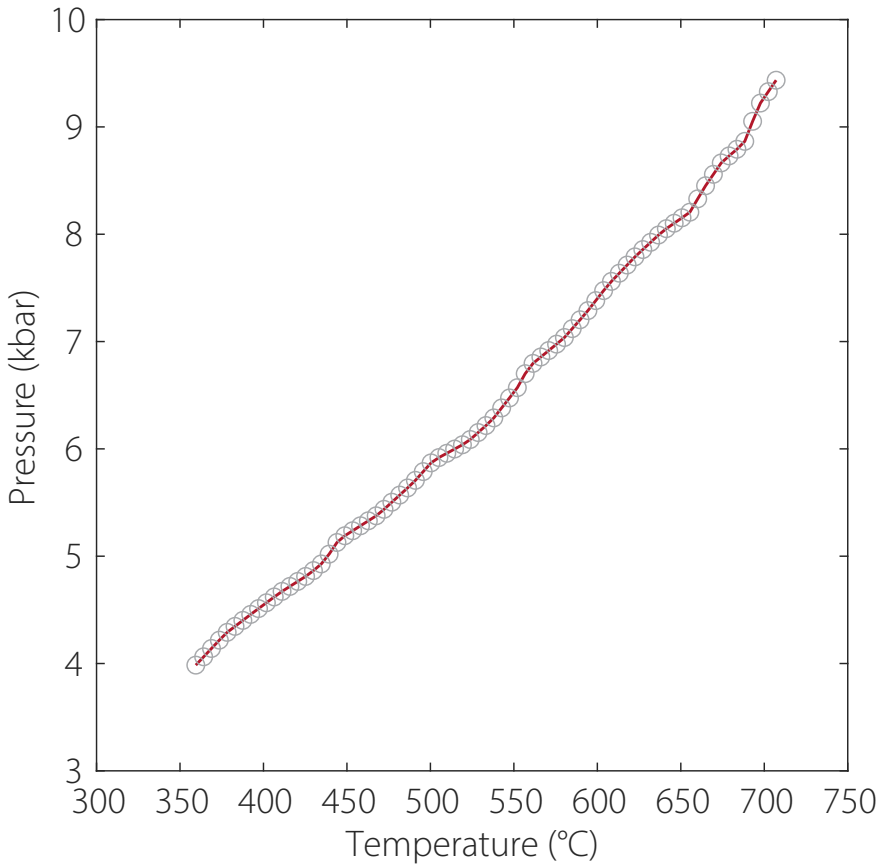

Fig. B.4 75 point geotherm from *Copley and Weller* (2022) along which the uncertainty in the worldwide median pelite composition of *Forshaw and Pattison* (2023) is quantified in Figure 3.11.

Appendix C

The Metamorphic and Structural Evolution of the Kansanshi Cu-Au Mine and NW Zambia

C.1 Outcrop locations

Table C.1 Solwezi outcrop locations. WGS84 co-ordinate system.

Lithology	Latitude	Longitude	Lithology	Latitude	Longitude
quartzite	-12.1496	26.4981	Katangan carbonate	-11.9889	26.3883
quartzite	-12.1025	26.5172	Katangan carbonate	-11.9799	26.3863
quartzite	-12.0948	26.5064	Katangan carbonate	-11.9953	26.3904
quartzite	-12.1303	26.5068	Katangan carbonate	-12.0051	26.3943
quartzite	-12.1478	26.4908	Katangan carbonate	-12.0127	26.3800
quartzite	-12.1511	26.4798	Katangan carbonate	-11.9979	26.3736
quartzite	-12.3677	26.3704	Katangan carbonate	-12.0268	26.3964
quartzite	-12.4148	26.3564	Katangan carbonate	-12.0208	26.3959
quartzite	-12.3852	26.3575	Katangan carbonate	-12.0087	26.4045
quartzite	-12.3625	26.3523	Katangan carbonate	-11.9993	26.4079
quartzite	-12.2585	26.3999	Katangan carbonate	-12.0004	26.3966
quartzite	-12.2595	26.4022	Katangan carbonate	-12.0095	26.4162
quartzite	-12.2556	26.4540	Katangan carbonate	-12.1992	26.4120
quartzite	-12.2690	26.3960	Katangan carbonate	-12.1932	26.4297
quartzite	-12.2980	26.4753	Katangan carbonate	-12.4022	26.3873
quartzite	-12.3531	26.4629	Katangan carbonate	-12.4031	26.3901
quartzite	-12.4059	26.4528	Katangan carbonate	-12.1517	26.3410
quartzite	-12.1076	26.5480	Katangan carbonate	-12.2337	26.4917
quartzite	-12.3859	26.2626	Katangan carbonate	-12.2286	26.4900
quartzite	-12.3939	26.3627	Katangan carbonate	-12.0497	26.3661
quartzite	-12.3747	26.3306	Katangan carbonate	-12.0388	26.3677
quartzite	-12.4149	26.4265	Katangan carbonate	-12.0344	26.3681
quartzite	-12.4108	26.4422	Katangan carbonate	-12.0497	26.3744
quartzite	-12.3878	26.4523	Katangan carbonate	-12.0489	26.3836
quartzite	-12.3851	26.4566	Katangan carbonate	-12.0466	26.3845
quartzite	-12.2780	26.3678	Katangan carbonate	-12.0500	26.3894
quartzite	-12.3282	26.3770	Katangan carbonate	-12.0424	26.3884
quartzite	-12.3886	26.4656	Katangan carbonate	-12.0314	26.3940
quartzite	-12.3904	26.4524	Katangan carbonate	-12.0372	26.3698
quartzite	-12.2811	26.4649	Katangan carbonate	-12.0337	26.3703
quartzite	-12.2975	26.4712	Katangan carbonate	-11.9919	26.4796

Continued on next page

Table C.1 – continued from previous page

Lithology	Latitude	Longitude	Lithology	Latitude	Longitude
quartzite	-12.2838	26.4775	Katangan carbonate	-12.0006	26.4872
quartzite	-12.2591	26.4112	Katangan carbonate	-11.9919	26.4796
quartzite	-12.2304	26.4037	Katangan carbonate	-11.9910	26.4811
quartzite	-12.2652	26.3693	Katangan carbonate	-12.0293	26.3697
quartzite	-12.2684	26.3687	Katangan carbonate	-12.0227	26.4299
quartzite	-12.3244	26.3645	Katangan carbonate	-11.9803	26.4688
quartzite	-12.2728	26.4773	Katangan carbonate	-11.9842	26.5120
quartzite	-12.2733	26.4804	Katangan carbonate	-11.9871	26.5136
quartzite	-12.3352	26.3866	Katangan carbonate	-12.0027	26.5306
quartzite	-12.3407	26.3896	Katangan carbonate	-11.9994	26.5285
quartzite	-12.4290	26.4809	Katangan carbonate	-11.9988	26.5281
quartzite	-12.4516	26.4634	Katangan carbonate	-12.0233	26.4291
quartzite	-12.2460	26.3577	Katangan carbonate	-12.0240	26.4295
quartzite	-12.3140	26.3525	Katangan carbonate	-12.0247	26.4309
quartzite	-12.4327	26.4494	Katangan carbonate	-11.9806	26.4701
quartzite	-12.4327	26.4494	Katangan carbonate	-11.9826	26.4706
quartzite	-12.4245	26.4378	Katangan carbonate	-11.9852	26.4733
quartzite	-12.4218	26.4291	Katangan carbonate	-11.9854	26.4747
quartzite	-12.4217	26.4336	Katangan carbonate	-12.0232	26.4284
quartzite	-12.4275	26.4414	Katangan carbonate	-12.0247	26.4287
quartzite	-12.4285	26.4431	Katangan carbonate	-11.9874	26.3955
quartzite	-12.4494	26.4533	Katangan carbonate	-11.9833	26.3888
quartzite	-12.4081	26.4498	Katangan carbonate	-11.9840	26.3915
quartzite	-12.4058	26.4434	Katangan carbonate	-12.0247	26.4309
quartzite	-12.3422	26.3895	Katangan carbonate	-12.0232	26.4310
biotite schist	-12.1398	26.5127	Katangan carbonate	-11.9912	26.5142
biotite schist	-12.1405	26.5293	Katangan carbonate	-12.0032	26.5318
biotite schist	-12.1403	26.5121	Katangan carbonate	-11.9984	26.3742
biotite schist	-12.1305	26.5384	Katangan carbonate	-12.4602	26.4643
biotite schist	-12.1352	26.5375	Katangan carbonate	-12.0657	26.3836
biotite schist	-12.1352	26.5375	Katangan siliciclastic	-12.3534	26.5010
biotite schist	-12.1352	26.5375	Katangan siliciclastic	-12.1974	26.4084
biotite schist	-12.1352	26.5375	Katangan siliciclastic	-12.2672	26.5117
biotite schist	-12.1163	26.3998	Katangan siliciclastic	-12.2882	26.5068
biotite schist	-12.1163	26.3998	Katangan siliciclastic	-12.3636	26.5169
biotite schist	-12.1480	26.5274	Katangan siliciclastic	-12.3603	26.5037
biotite schist	-12.0657	26.3858	Katangan siliciclastic	-12.3849	26.5023
biotite schist	-12.0344	26.5274	Katangan siliciclastic	-12.4337	26.4128
biotite schist	-12.0376	26.5243	Katangan siliciclastic	-11.9963	26.4534
biotite schist	-12.0501	26.5259	Katangan siliciclastic	-12.2298	26.3642
biotite schist	-12.0475	26.5283	Katangan siliciclastic	-11.9733	26.3984
biotite schist	-12.0486	26.5275	Katangan siliciclastic	-11.9776	26.3902
biotite schist	-12.1358	26.5353	Katangan siliciclastic	-11.9753	26.3831
biotite schist	-12.0177	26.4336	Katangan siliciclastic	-11.9740	26.3973

Continued on next page

Table C.1 – continued from previous page

Lithology	Latitude	Longitude	Lithology	Latitude	Longitude
biotite schist	-12.0205	26.4589	Katangan siliciclastic	-11.9722	26.4028
biotite schist	-12.0191	26.4601	Katangan siliciclastic	-11.9701	26.4098
biotite schist	-12.3109	26.4024	Katangan siliciclastic	-11.9704	26.4162
biotite schist	-12.3871	26.4591	Katangan siliciclastic	-11.9739	26.4276
biotite schist	-12.4124	26.4544	Katangan siliciclastic	-11.9614	26.4420
biotite schist	-12.4124	26.4533	Katangan siliciclastic	-11.9749	26.4467
biotite schist	-12.4294	26.4536	Katangan siliciclastic	-11.9765	26.4489
biotite schist	-12.4296	26.4546	Katangan siliciclastic	-11.9733	26.3997
biotite schist	-12.3220	26.4586	Katangan siliciclastic	-11.9726	26.4049
biotite schist	-12.3813	26.4623	Katangan siliciclastic	-11.9719	26.4125
biotite schist	-12.3742	26.4608	Katangan siliciclastic	-11.9722	26.4213
biotite schist	-12.4267	26.4536	Katangan siliciclastic	-11.9728	26.4245
biotite schist	-12.2276	26.4889	Katangan siliciclastic	-11.9745	26.4284
biotite schist	-12.2429	26.3438	Katangan siliciclastic	-11.9842	26.3951
biotite schist	-12.1117	26.3781	Katangan siliciclastic	-11.9842	26.3951
biotite schist	-12.1117	26.3781	Katangan siliciclastic	-11.9800	26.3908
biotite schist	-12.1165	26.3819	Katangan siliciclastic	-11.9823	26.3946
biotite schist	-12.1180	26.3815	Katangan siliciclastic	-11.9794	26.3898
biotite schist	-12.0665	26.3827	Katangan siliciclastic	-11.9810	26.3928
biotite schist	-12.0662	26.3829	Katangan siliciclastic	-11.9849	26.3964
biotite schist	-12.1053	26.3774	Katangan siliciclastic	-11.9834	26.3973
biotite schist	-12.3876	26.2657	Katangan siliciclastic	-11.9546	26.4004
biotite schist	-12.2438	26.3632	Katangan siliciclastic	-11.9745	26.4016
biotite schist	-12.2404	26.3658	Katangan siliciclastic	-11.9703	26.4069
biotite schist	-12.4221	26.4350	Katangan siliciclastic	-11.9722	26.4072
biotite schist	-12.4049	26.4528	Katangan siliciclastic	-11.9701	26.4132
biotite schist	-12.4050	26.4446	Katangan siliciclastic	-11.9710	26.4156
biotite schist	-12.3346	26.4003	Katangan siliciclastic	-11.9707	26.4189
biotite schist	-12.3340	26.4003	Katangan siliciclastic	-11.9710	26.4219
biotite schist	-12.3922	26.4531	Katangan siliciclastic	-11.9726	26.4229
biotite schist	-12.3904	26.4524	Katangan siliciclastic	-11.9726	26.4229
biotite schist	-12.3992	26.2633	Katangan siliciclastic	-11.9717	26.4236
biotite schist	-12.4354	26.3155	Katangan siliciclastic	-11.9739	26.4276
biotite schist	-12.4416	26.3290	Katangan siliciclastic	-11.9740	26.4297
biotite schist	-12.4136	26.3031	Katangan siliciclastic	-11.9753	26.4311
biotite schist	-12.3869	26.3255	Katangan siliciclastic	-12.0247	26.4129
biotite schist	-12.4647	26.3265	Katangan siliciclastic	-12.2076	26.3962
biotite schist	-12.4737	26.3210	Katangan siliciclastic	-12.2242	26.3760
biotite schist	-12.4670	26.2976	Katangan siliciclastic	-12.3041	26.3293
biotite schist	-12.3741	26.2750	Katangan siliciclastic	-12.3043	26.3294
biotite schist	-12.4683	26.3353	Katangan siliciclastic	-12.2258	26.3261
biotite schist	-12.4373	26.3369	Katangan siliciclastic	-12.2222	26.4182
biotite schist	-12.4346	26.3315	Katangan siliciclastic	-12.2106	26.4359
biotite schist	-12.4390	26.3540	Katangan siliciclastic	-12.2288	26.4560

Continued on next page

Table C.1 – continued from previous page

Lithology	Latitude	Longitude	Lithology	Latitude	Longitude
biotite schist	-12.4364	26.3542	Katangan siliciclastic	-12.4067	26.4138
biotite schist	-12.4065	26.3327	Katangan siliciclastic	-12.4012	26.4127
biotite schist	-12.3890	26.3539	Katangan siliciclastic	-12.4311	26.4756
biotite schist	-12.4614	26.3394	Katangan siliciclastic	-12.4258	26.4639
biotite schist	-12.4446	26.4451	Katangan siliciclastic	-12.4430	26.4542
biotite schist	-12.4448	26.4438	Katangan siliciclastic	-12.4530	26.4846
biotite schist	-12.4108	26.4478	Katangan siliciclastic	-12.4312	26.4582
biotite schist	-12.4112	26.4485	Katangan siliciclastic	-12.4337	26.4128
biotite schist	-12.4106	26.4482	Katangan siliciclastic	-12.2109	26.4346
biotite schist	-12.4081	26.4432	Katangan siliciclastic	-12.2103	26.4341
biotite schist	-12.4072	26.4664	Katangan siliciclastic	-12.2103	26.4341
biotite schist	-12.4050	26.4477	Katangan siliciclastic	-12.2103	26.4341
biotite schist	-12.4050	26.4472	Katangan siliciclastic	-12.2096	26.4334
biotite schist	-12.4048	26.4467	Katangan siliciclastic	-12.2106	26.4360
biotite schist	-12.3631	26.2211	Katangan siliciclastic	-12.4729	26.4845
biotite schist	-12.3845	26.2431	Katangan siliciclastic	-12.4602	26.4533
biotite schist	-12.3707	26.2362	Katangan siliciclastic	-12.4602	26.4597
biotite schist	-12.3656	26.2273	Katangan siliciclastic	-12.2288	26.4563
biotite schist	-12.3593	26.2321	Katangan siliciclastic	-12.2612	26.3467
biotite schist	-12.3452	26.2374	Katangan siliciclastic	-12.2269	26.4754
biotite schist	-12.1102	26.3657	Katangan siliciclastic	-12.2354	26.4914
biotite schist	-12.0946	26.3611	Katangan siliciclastic	-12.4130	26.4131
biotite schist	-12.1054	26.3475	Katangan siliciclastic	-12.4468	26.4514
biotite schist	-12.0849	26.3548	Katangan siliciclastic	-12.2894	26.3231
biotite schist	-12.2765	26.3979	Katangan siliciclastic	-12.2487	26.3428
biotite schist	-12.0351	26.4670	Katangan siliciclastic	-12.2501	26.3539
biotite schist	-12.3872	26.2648	Katangan siliciclastic	-12.3864	26.5045
biotite schist	-12.2954	26.3864	Katangan siliciclastic	-12.3477	26.5079
biotite schist	-12.3048	26.3744	Katangan siliciclastic	-12.2773	26.5091
biotite schist	-12.0814	26.4196	Katangan siliciclastic	-12.2445	26.5090
granitoid	-12.2975	26.4712	Katangan siliciclastic	-12.2304	26.4480
granitoid	-12.2811	26.4649	Katangan siliciclastic	-12.2261	26.4765
granitoid	-12.2818	26.4630	Katangan siliciclastic	-12.2366	26.4924
granitoid	-12.2790	26.4663	Katangan siliciclastic	-12.3424	26.3894
granitoid	-12.2798	26.4733	Katangan siliciclastic	-12.3175	26.3432
granitoid	-12.2540	26.4764	Katangan siliciclastic	-12.3168	26.3421
granitoid	-12.2256	26.4735	Katangan siliciclastic	-12.3165	26.3418
granitoid	-12.2798	26.4733	Katangan siliciclastic	-12.3147	26.3384
granitoid	-12.2768	26.4721	Katangan siliciclastic	-12.3109	26.3339
granitoid	-12.2623	26.3714	Katangan siliciclastic	-12.3140	26.3374
granitoid	-12.2424	26.4082	Katangan siliciclastic	-12.3191	26.3490
granitoid	-12.2830	26.4665	Katangan siliciclastic	-12.3191	26.3500
granitoid	-12.2816	26.4629	Katangan siliciclastic	-12.3192	26.3502
granitoid	-12.2530	26.4640	Katangan siliciclastic	-12.3192	26.3509

Continued on next page

Table C.1 – continued from previous page

Lithology	Latitude	Longitude	Lithology	Latitude	Longitude
granitoid	-12.2612	26.4564	Katangan siliciclastic	-12.3194	26.3511
granitoid	-12.2520	26.4575	Katangan siliciclastic	-12.3195	26.3521
granitoid	-12.2355	26.4666	Katangan siliciclastic	-12.3229	26.3583
granitoid	-12.2539	26.4620	Katangan siliciclastic	-12.3231	26.3587
granitoid	-12.2231	26.3793	Katangan siliciclastic	-12.3236	26.3592
granitoid	-12.2586	26.5063	Katangan siliciclastic	-12.3177	26.3437
granitoid	-12.2466	26.4637	Katangan siliciclastic	-12.3174	26.3426
granitoid	-12.2355	26.4666	Katangan siliciclastic	-12.2517	26.5076
granitoid	-12.2359	26.4351	Katangan siliciclastic	-12.2217	26.4019
granitoid	-12.2356	26.4335	Katangan siliciclastic	-11.9975	26.4933
granitoid	-12.2338	26.4426	Katangan siliciclastic	-12.4240	26.4717
granitoid	-12.2449	26.4833	Katangan siliciclastic	-12.4529	26.4524
granitoid	-12.2432	26.4874	Katangan siliciclastic	-12.4675	26.4818
granitoid	-12.2439	26.4946	mafic body	-12.2085	26.3988
granitoid	-12.2430	26.4957	mafic body	-12.3209	26.3783
granitoid	-12.2432	26.4961	mafic body	-12.3715	26.3713
granitoid	-12.2312	26.4594	mafic body	-12.3720	26.3717
granitoid	-12.3920	26.3481	mafic body	-12.3295	26.2918
granitoid	-12.2372	26.4092	mafic body	-12.3209	26.3783
granitoid	-12.2289	26.4043	mafic body	-12.3323	26.3746
granitoid	-12.3717	26.3392	mafic body	-12.3327	26.3740
granitoid	-12.2947	26.4782	mafic body	-12.3296	26.3760
granitoid	-12.2522	26.4581	mafic body	-12.3715	26.3713
granitoid	-12.2474	26.4642	mafic body	-12.3720	26.3717
granitoid	-12.2741	26.4714	mafic body	-12.1475	26.4979
granitoid	-12.2829	26.4665	mafic body	-12.0935	26.4152
granitoid	-12.3716	26.3392	mafic body	-12.0935	26.4152
granitoid	-12.2803	26.4746	mafic body	-12.1491	26.4983
granitoid	-12.2798	26.4734	mafic body	-12.0966	26.4399
garnet schist	-12.3911	26.2444	mafic body	-12.0023	26.5093
garnet schist	-12.3921	26.2441	mafic body	-12.0023	26.5097
garnet schist	-12.3919	26.2456	mafic body	-11.9995	26.5090
garnet schist	-12.4068	26.2184	mafic body	-12.2086	26.3931
garnet schist	-12.4216	26.1958	mafic body	-12.3152	26.3783
garnet schist	-12.1895	26.4372	mafic body	-12.2086	26.3931
garnet schist	-12.1300	26.4801	mafic body	-12.2095	26.3952
garnet schist	-12.1510	26.4800	mafic body	-12.2012	26.3891
garnet schist	-12.1517	26.4794	mafic body	-12.4175	26.4056
garnet schist	-12.1511	26.4782	mafic body	-12.3923	26.3512
garnet schist	-12.1513	26.4781	mafic body	-12.4041	26.4032
garnet schist	-12.1514	26.4786	mafic body	-12.4036	26.3612
garnet schist	-12.1526	26.4777	mafic body	-12.2043	26.4069
garnet schist	-12.3825	26.3581	mafic body	-12.2043	26.4069
garnet schist	-12.3577	26.3437	mafic body	-12.2075	26.5257

Continued on next page

Table C.1 – continued from previous page

Lithology	Latitude	Longitude	Lithology	Latitude	Longitude
garnet schist	-12.1681	26.4463	mafic body	-12.2076	26.5175
garnet schist	-12.1650	26.4002	mafic body	-12.2061	26.4065
garnet schist	-12.1656	26.3995	mafic body	-12.2043	26.4069
garnet schist	-12.1506	26.3976	mafic body	-12.2136	26.4891
garnet schist	-12.1730	26.5312	mafic body	-12.2135	26.4915
garnet schist	-12.4059	26.4447	mafic body	-12.2153	26.4915
garnet schist	-12.1935	26.3237	mafic body	-12.2093	26.4898
garnet schist	-12.1406	26.3969	mafic body	-12.2059	26.3943
garnet schist	-12.1442	26.3979	mafic body	-12.4122	26.3908
garnet schist	-12.1431	26.3933	mafic body	-12.1502	26.4978
garnet schist	-12.1431	26.3941	mafic body	-12.4109	26.4082
garnet schist	-12.1277	26.3866	mafic body	-12.4111	26.4075
garnet schist	-12.1218	26.3898	mafic body	-12.4053	26.4051
garnet schist	-12.1463	26.4863	mafic body	-12.4026	26.4058
garnet schist	-12.1503	26.5117	mafic body	-12.4005	26.4080
garnet schist	-12.1507	26.5123	mafic body	-12.3967	26.4081
garnet schist	-12.1501	26.5106	mafic body	-12.3386	26.3520
garnet schist	-12.1501	26.5103	mafic body	-12.3392	26.3515
garnet schist	-12.3610	26.3541	mafic body	-12.3398	26.3508
Katangan carbonate	-12.0478	26.3777	mafic body	-12.3750	26.2723
Katangan carbonate	-12.0678	26.4570	mafic body	-12.3751	26.2730
Katangan carbonate	-12.0470	26.4215	mafic body	-12.3211	26.3783
Katangan carbonate	-12.0080	26.3947		-12.3292	26.3761

C.2 Structural measurements

Table C.2 Foliation measurements. WGS84 co-ordinate system.

Dip (°)	Dip direction (°)	Latitude	Longitude
35.00	295.00	26.3391	-12.4730
54.00	41.00	26.4560	-12.0597
35.00	46.00	26.2270	-12.3664
35.00	46.00	26.2270	-12.3664
28.00	158.00	26.1999	-12.3750
3.00	195.00	26.1956	-12.4218
70.00	52.00	26.2088	-12.4118
30.00	28.00	26.2325	-12.3960
36.00	244.00	26.2550	-12.4124
22.00	281.00	26.2653	-12.4306
5.00	59.00	26.2431	-12.4407

Continued on next page

Table C.2 – continued from previous page

Dip	Dip direction	Latitude	Longitude
14.00	3.00	26.3158	-12.4366
24.00	339.00	26.3034	-12.4147
5.00	320.00	26.3217	-12.4750
36.00	174.00	26.3203	-12.4493
60.00	239.00	26.3547	-12.4372
12.00	350.00	26.3331	-12.4078
50.00	29.00	26.2562	-12.3974
25.00	123.00	26.3256	-12.3877
90.00	353.00	26.3547	-12.3621
40.00	258.00	26.3544	-12.3899
22.00	147.00	26.4401	-12.4459
35.00	131.00	26.4531	-12.4244
25.00	260.00	26.4281	-12.3980
50.00	353.00	26.4769	-12.3851
50.00	155.00	26.4463	-12.3723
3.00	287.00	26.4285	-12.3640
22.00	77.00	26.4923	-12.3399
3.00	41.00	26.4190	-12.3443
20.00	277.00	26.3799	-12.3366
19.00	182.00	26.3567	-12.3136
90.00	9.00	26.4063	-12.3227
41.00	212.00	26.4096	-12.3054
36.00	153.00	26.3806	-12.2944
90.00	28.00	26.4461	-12.2882
55.00	91.00	26.4960	-12.3137
90.00	83.00	26.4744	-12.2756
50.00	279.00	26.4539	-12.2599
25.00	217.00	26.4024	-12.2583
40.00	20.00	26.3715	-12.2624
4.00	260.00	26.3543	-12.2509
38.00	68.00	26.4929	-12.2378
58.00	31.00	26.4772	-12.2274
90.00	63.00	26.4645	-12.2473
40.00	349.00	26.4485	-12.2315
45.00	342.00	26.4164	-12.2202
25.00	305.00	26.3686	-12.2303
27.00	0.00	26.3852	-12.2262
30.00	304.00	26.4303	-12.1942
15.00	19.00	26.4606	-12.1767
75.00	185.00	26.4746	-12.1528
3.00	188.00	26.4408	-12.1405
70.00	212.00	26.4477	-12.1298

C.3 Sample locations and compositions

Table C.3 Sample locations. WGS84 co-ordinate system.

Sample	Latitude	Longitude
Z03b	-12.39212	26.24413
Z10	-12.16809	26.44632
Z29	-12.17295	26.53124
Z34	-12.12175	26.38981
Z36	-12.07223	26.41503

Table C.4 Water-saturated mole % composition of each sample.

Sample	SiO2	Al2O3	CaO	MgO	FeO	K2O	Na2O	TiO2	O	MnO	H2O
Z10	45.63	7.36	3.35	4.67	5.11	1.67	1.39	0.51	0.26	0.05	30.00
Z03b	44.57	7.45	2.03	4.58	7.44	1.36	1.63	0.53	0.37	0.05	30.00
Z29	43.29	8.69	1.97	5.53	5.91	2.46	1.16	0.56	0.30	0.05	30.00
Z36	47.27	7.71	0.49	2.62	7.78	1.25	1.59	0.87	0.39	0.04	30.00

C.4 Data from Electron Probe Microanalysis of samples

Table C.5 Sample Z03b EPMA analysis. Composition given in oxide weight percent.

Phase	**Na2O**	**MgO**	**SiO2**	**Al2O3**	**TiO2**	**K2O**	**CaO**	**MnO**	**FeO**	**Cr2O3**	**Total**	**Distance** μm
Garnet1/1	0.00940	3.52200	37.79070	21.69070	0.06300	0.02270	5.66070	0.20200	32.44070	0.02160	101.42340	0.00000
Garnet1/2	0.04230	3.41390	37.52220	21.60640	0.06080	-0.00410	5.98460	0.23030	32.44330	0.00110	101.30490	47.46000
Garnet1/3	0.07230	2.63000	38.92780	22.50420	0.05200	-0.00410	6.47500	0.24890	31.30190	0.01480	102.22700	94.93000
Garnet1/4	0.14490	1.43310	66.13540	9.89160	0.01590	0.11800	2.32860	0.10830	14.12560	0.01210	94.31350	142.39000
Garnet1/5	0.03520	3.20440	37.73010	21.65250	0.05420	0.01340	6.44000	0.33500	32.22190	0.01190	101.69860	189.84000
Garnet1/6	0.02590	3.07000	37.25390	21.39280	0.04210	-0.01850	6.27480	0.36840	32.36290	0.03100	100.82180	237.30000
Garnet1/7	0.01640	2.80910	37.19820	21.70590	0.07800	0.02670	6.94070	0.56540	31.40490	0.00630	100.75170	284.78000
Garnet1/8	0.08180	2.60720	37.25600	22.01080	0.04370	0.07600	7.18040	0.61790	30.88430	0.00960	100.76770	332.22000
Garnet1/9	0.04200	2.48540	38.44510	22.37970	0.07500	0.01130	7.64100	0.85010	30.68430	0.01410	102.62800	379.69000
Garnet1/10	0.04680	2.48240	37.24480	21.54850	0.04640	0.01430	7.71090	0.87000	30.80440	-0.00650	100.76850	427.15000
Garnet1/11	0.02570	2.38610	37.44580	21.58200	0.09180	0.00100	7.86820	1.04460	30.26660	0.01080	100.72280	474.61000
Garnet1/12	0.03280	2.38030	37.33700	21.51220	0.04590	-0.01430	8.01330	1.25310	30.46610	0.00650	101.04720	522.07000
Garnet1/13	0.07490	2.16560	37.21300	21.28390	0.05690	0.01640	8.17040	1.40030	29.89860	0.01680	100.29670	569.53000
Garnet1/14	0.01640	2.18010	37.52810	21.38090	0.04040	0.00510	8.03880	1.57040	30.20450	0.00720	100.97180	616.99000
Garnet1/15	0.04930	0.50440	91.12760	6.25620	-0.00090	0.00330	2.38660	0.37240	9.53140	0.01770	110.24870	664.45000
Garnet1/16	0.01170	2.10470	37.43760	21.31540	0.09460	0.00200	8.55030	1.61320	29.53290	0.00880	100.67130	711.91000
Garnet1/17	0.02100	2.01450	37.44830	21.38770	0.09100	-0.01120	8.37640	1.73190	29.87090	0.03460	100.97640	759.37000
Garnet1/18	0.02340	2.01520	37.32700	21.41850	0.09510	-0.01640	8.51270	1.63150	29.79080	0.01470	100.82880	806.83000
Garnet1/19	0.06790	2.00080	37.09570	21.14440	0.11940	0.02140	8.41850	1.75170	29.79100	0.01350	100.42420	854.29000
Garnet1/20	0.00230	1.85150	37.50520	21.45620	0.09480	0.00920	8.67070	1.89850	29.67170	0.03510	101.19530	901.75000
Garnet1/21	0.28910	1.94610	36.46320	21.18580	0.08760	0.26330	6.99820	1.46690	24.71190	0.01780	93.43000	949.21000
Garnet1/22	0.00470	1.84820	37.61040	21.33280	0.08360	0.00200	8.73800	1.93310	29.69830	0.03150	101.28260	996.67000
Garnet1/23	0.09580	1.70590	37.40210	21.30240	0.08840	0.00710	8.89040	1.93390	29.38020	0.02450	100.83060	1044.13000
Garnet1/24	-0.02740	0.00490	98.44570	0.05680	-0.00820	0.01770	0.07160	0.07630	0.63270	-0.00070	99.30560	1091.59000

Continued on next page

Table C.5 – continued from previous page

Phase	Na2O	MgO	SiO2	Al2O3	TiO2	K2O	CaO	MnO	FeO	Cr2O3	Total	Distance μm
Garnet1/25	0.02330	1.72160	37.42950	21.30690	0.11700	-0.00510	8.45730	2.12540	29.31640	0.00980	100.50730	1139.05000
Garnet1/26	0.04200	1.78170	37.55800	21.41240	0.10680	0.02240	8.43140	2.19430	29.52550	0.02220	101.09680	1186.51000
Garnet1/27	0.09710	1.61510	38.91020	23.25520	0.10580	0.01230	8.37280	2.20180	29.07500	0.02290	103.66820	1233.98000
Garnet1/28	0.04200	1.64250	36.99670	20.70020	0.09400	0.00610	9.87200	2.25400	28.81420	0.02580	100.44750	1281.44000
Garnet1/29	0.00700	1.69680	37.21960	21.47580	0.10790	-0.01120	8.79080	2.40180	29.44620	0.00680	101.15270	1328.90000
Garnet1/30	0.03530	0.79920	65.89270	8.95370	0.04180	0.00740	4.10330	1.22890	13.61740	0.00860	94.68850	1376.36000
Garnet1/31	0.00930	1.69110	37.44240	21.59820	0.11770	-0.00100	8.98330	2.13210	29.10490	0.02380	101.10280	1423.82000
Garnet1/32	0.04670	1.72880	37.29930	21.44530	0.09440	0.00410	8.40230	2.34640	29.43720	0.00420	100.80860	1471.28000
Garnet1/33	0.04190	1.71810	37.73890	21.45960	0.10700	-0.01120	8.77340	2.28060	29.29410	-0.00390	101.41360	1518.74000
Garnet1/34	0.01400	1.74650	37.49570	21.45400	0.07590	-0.00410	9.05230	2.11660	29.22610	-0.00080	101.18110	1566.20000
Garnet1/35	0.37370	1.69370	39.51930	23.65600	0.07510	0.14250	7.18630	1.57110	27.71610	0.01690	101.95060	1613.66000
Garnet1/36	0.15590	1.58750	36.81510	22.12750	0.11220	0.07340	7.74490	1.95440	29.38460	0.02540	99.98090	1661.12000
Garnet1/37	0.03270	1.85200	37.34370	21.53600	0.09610	0.00100	8.40870	1.81690	29.84860	0.01900	100.95470	1708.58000
Garnet1/38	0.01630	1.97230	37.38420	21.29390	0.08040	-0.00100	8.25780	1.80060	29.85590	0.02260	100.68400	1756.04000
Garnet1/39	0.03260	2.00710	37.46430	21.46890	0.06950	0.00810	8.32170	1.70140	29.91430	0.02210	101.01020	1803.50000
Garnet1/40	0.00470	2.26950	37.61630	21.59620	0.08680	-0.02040	7.40830	1.67610	30.91890	0.00910	101.58560	1850.96000
Garnet1/41	0.00700	2.19650	37.64630	21.55600	0.04320	-0.03260	7.91840	1.57000	30.48400	0.01910	101.44050	1898.42000
Garnet1/42	0.02560	2.36390	37.76310	21.65940	0.06390	0.00810	7.52600	1.31410	30.73900	0.03430	101.49750	1945.88000
Garnet1/43	0.02560	2.47630	37.42760	21.72760	0.06280	0.01020	7.39800	1.00540	30.91850	0.02870	101.08060	1993.35000
Garnet1/44	-0.01400	2.63790	37.46620	21.52120	0.07760	0.02140	7.73410	0.79030	30.78960	0.01750	101.05570	2040.81000
Garnet1/45	-0.00700	2.68030	37.52080	21.42360	0.07580	0.02240	7.32880	0.63600	31.35690	0.02900	101.07360	2088.26000
Garnet1/46	0.02100	2.76130	37.51290	21.41750	0.08330	0.01840	7.15320	0.54630	31.37110	0.02540	100.91040	2135.73000
Garnet1/47	0.02800	3.30890	37.48210	21.45650	0.08030	-0.00410	6.43300	0.33710	31.77700	-0.00310	100.90300	2183.19000
Garnet1/48	0.02560	3.25670	37.94430	21.73800	0.02530	0.00310	6.57930	0.20590	31.92080	-0.01940	101.69890	2230.65000
Garnet1/49	0.02820	0.90830	84.68690	8.90120	-0.01290	0.01510	1.85540	0.11710	13.40150	-0.00570	109.91380	2278.11000

Continued on next page

Table C.5 – continued from previous page

Phase	Na2O	MgO	SiO2	Al2O3	TiO2	K2O	CaO	MnO	FeO	Cr2O3	Total	Distance μm
Garnet1/50	0.08790	3.02140	35.67740	21.76970	0.26150	0.05320	6.59520	0.21150	29.63330	0.01480	97.32580	2325.57000
Garnet2/1	0.01170	3.57670	37.71480	21.38530	0.05670	0.00000	5.65630	0.17620	32.66050	0.00210	101.24020	0.00000
Garnet2/2	0.02340	3.37300	37.44160	21.34550	0.08560	0.00920	5.68380	0.21190	32.33040	0.01500	100.51950	55.40000
Garnet2/3	0.06060	3.20910	37.96740	21.70740	0.07460	-0.01020	6.15180	0.17120	32.16340	0.02120	101.52680	110.79000
Garnet2/4	0.00460	3.20810	37.61140	21.67900	0.06610	0.00820	6.79100	0.32440	31.50440	0.02390	101.22100	166.18000
Garnet2/5	-0.02270	2.83180	47.94760	18.70620	0.00570	0.00720	4.76960	0.25690	29.06190	-0.00520	103.58700	221.57000
Garnet2/6	0.03270	3.06390	37.46690	21.41570	0.01450	0.00000	6.52140	0.45450	31.82930	0.01920	100.81810	276.96000
Garnet2/7	-0.01400	2.84050	37.95720	21.07430	0.04270	0.00000	6.66390	0.53250	31.19670	0.00660	100.31460	332.35000
Garnet2/8	0.00930	2.79210	37.67250	21.57930	0.05390	-0.02240	7.35150	0.60930	31.33100	-0.00080	101.39900	387.75000
Garnet2/9	-0.00470	2.72270	37.75820	21.46480	0.05310	-0.01630	7.30960	0.66720	31.09430	0.00700	101.07680	443.14000
Garnet2/10	0.23250	2.38680	35.94420	22.83250	0.07880	0.05920	7.15330	0.76610	29.00430	0.03430	98.49210	498.53000
Garnet2/11	0.03250	2.63980	37.48370	21.53180	0.06090	-0.01940	7.43730	0.81300	30.80550	0.01650	100.82120	553.92000
Garnet2/12	0.02560	2.56650	37.39800	21.24110	0.07000	-0.00920	7.66090	0.91200	31.01910	0.03430	100.92760	609.31000
Garnet2/13	0.05110	2.44760	37.39960	21.17540	0.05280	0.00920	7.79940	1.01300	30.34370	0.00960	100.30130	664.71000
Garnet2/14	0.04870	2.42280	37.80830	21.48770	0.07720	0.00310	8.00530	1.10230	30.32650	0.01650	101.29830	720.10000
Garnet2/15	0.01860	2.37450	37.41060	21.59630	0.03150	0.02030	7.96850	1.29150	30.52360	0.00860	101.24400	775.49000
Garnet2/16	0.03030	2.31470	37.58920	21.44910	0.03240	-0.00810	7.47280	1.47520	30.46900	0.00050	100.83310	830.88000
Garnet2/17	-0.01850	2.17740	37.50580	21.66770	0.06420	0.03250	8.31130	1.45410	29.53240	0.02290	100.76820	886.27000
Garnet2/18	0.02090	2.18730	37.36060	21.51640	0.07230	0.00910	8.33500	1.49870	29.91710	0.00970	100.92720	941.67000
Garnet2/19	0.04410	2.09340	37.59640	21.50030	0.08180	0.01020	8.69940	1.54730	29.73350	0.01450	101.32090	997.06000
Garnet2/20	-0.00930	2.04480	37.54340	21.23990	0.05760	-0.01120	8.63560	1.57700	29.67670	0.03830	100.81330	1052.45000
Garnet2/21	0.00230	2.14350	37.44050	21.29480	0.04840	0.00200	8.75240	1.61300	29.88410	0.02110	101.20210	1107.84000
Garnet2/22	0.00460	2.02630	37.56270	21.48320	0.06960	0.00710	8.66810	1.54370	29.52110	0.02080	100.90720	1163.24000
Garnet2/23	0.06500	2.02340	37.43390	21.25990	0.06120	0.00100	8.47080	1.65570	29.72320	0.03490	100.72890	1218.63000
Garnet2/24	0.05810	2.00930	37.42660	21.51190	0.05240	-0.01620	8.29750	1.66320	29.99800	0.03480	101.05190	1274.02000

Continued on next page

Table C.5 – continued from previous page

Phase	Na2O	MgO	SiO2	Al2O3	TiO2	K2O	CaO	MnO	FeO	Cr2O3	Total	Distance μm
Garnet2/25	0.01160	2.04190	37.31880	21.30860	0.06020	-0.00510	8.02710	1.82830	30.33790	0.04090	100.97530	1329.41000
Garnet2/26	0.30640	1.74750	28.82800	23.02640	0.08080	0.14040	7.45420	1.26850	23.36810	-0.00070	86.22020	1384.81000
Garnet2/27	0.03010	1.86960	37.41660	21.76230	0.09340	-0.00610	8.48380	1.76600	29.55030	0.03050	101.00250	1440.20000
Garnet2/28	0.01390	1.93760	37.57670	21.25330	0.10340	0.00410	8.61400	1.72410	29.54060	0.03340	100.80100	1495.59000
Garnet2/29	0.03690	1.79680	37.23210	21.43870	0.12110	0.01420	9.33710	1.70720	28.73110	0.02990	100.44500	1550.98000
Garnet2/30	-0.00230	1.97020	37.44110	21.41550	0.06040	-0.02030	8.11150	1.76980	30.21870	0.01240	100.99960	1606.38000
Garnet2/31	0.00460	1.85060	37.72270	21.34100	0.10220	-0.02530	9.27380	1.67870	28.86530	0.01680	100.85580	1661.77000
Garnet2/32	0.02310	1.86410	37.54690	21.36000	0.11450	0.00810	9.32800	1.74580	29.18710	0.00410	101.18180	1717.16000
Garnet2/33	0.01850	2.02110	37.35970	21.25580	0.08780	0.01220	8.66290	1.73700	29.50020	0.01230	100.66740	1772.55000
Garnet2/34	0.13850	1.64930	35.19840	20.87300	0.09610	0.06380	8.51270	1.55440	27.64480	0.03380	95.76470	1827.95000
Garnet2/35	0.01450	-0.00170	100.06060	0.01920	-0.00370	-0.00770	0.04060	0.03120	0.60170	0.01160	100.77930	1883.34000
Garnet2/36	-0.05080	2.05990	37.78460	21.55740	0.08470	-0.01420	8.66590	1.56420	29.47860	0.02160	101.21690	1938.73000
Garnet2/37	0.06260	2.12980	37.38370	21.59050	0.07240	0.01720	8.22260	1.66850	30.07660	0.02280	101.24670	1994.12000
Garnet2/38	0.01160	2.11070	37.27950	21.59600	0.06360	0.02130	8.44620	1.61520	29.52950	0.04020	100.71370	2049.51000
Garnet2/39	0.04170	2.14550	37.91240	21.50290	0.07660	-0.00710	7.88660	1.35410	30.17490	0.01360	101.10820	2104.90000
Garnet2/40	0.05330	2.41330	37.59330	21.40100	0.07370	0.03140	7.88090	1.11990	30.59670	0.01440	101.17790	2160.30000
Garnet2/41	0.03750	0.70790	82.74910	7.13370	0.00680	0.03750	2.30360	0.26950	10.64820	-0.02260	103.89370	2215.69000
Garnet2/42	0.02090	2.55720	37.40870	21.47850	0.06400	-0.00710	7.50650	0.90590	30.91540	0.00480	100.86180	2271.08000
Garnet2/43	0.08470	2.46370	39.86480	19.07140	0.03210	0.02550	6.55800	0.72270	28.19390	-0.00890	97.01670	2326.47000
Garnet2/44	0.06020	2.74890	37.29330	21.75560	0.04810	-0.02030	7.32650	0.60510	31.27210	0.04040	101.15030	2381.87000
Garnet2/45	-0.00230	2.81480	37.63500	21.44030	0.05340	0.00510	6.92590	0.54120	31.46900	0.01870	100.90340	2437.26000
Garnet2/46	0.01860	2.90310	37.35960	21.41190	0.06010	-0.03450	6.76730	0.45940	31.73690	0.02620	100.74300	2492.65000
Garnet2/47	-0.00910	0.01550	100.03970	0.00810	-0.00410	0.00770	0.03510	0.02220	0.67740	0.01430	100.82010	2548.04000
Garnet2/48	0.04850	3.22450	37.42560	21.53980	0.07390	0.02240	6.46650	0.30090	31.24240	0.01330	100.35780	2603.43000
Garnet2/49	0.02780	3.23310	37.69600	21.50260	0.06680	0.01520	6.24910	0.20560	31.94850	0.03510	100.97980	2658.83000

Continued on next page

Table C.5 – continued from previous page

Phase	Na2O	MgO	SiO2	Al2O3	TiO2	K2O	CaO	MnO	FeO	Cr2O3	Total	Distance μm
Garnet2/50	-0.00460	3.49920	37.49550	21.37450	0.05000	-0.00810	5.72450	0.17110	32.14580	0.01350	100.47400	2714.22000
Garnet3/1	-0.01390	3.58370	37.70600	21.56000	0.06520	0.00810	5.62000	0.15860	31.87310	0.01570	100.59030	0.00000
Garnet3/2	1.68260	3.32740	20.35510	12.29440	0.06010	0.94810	4.93920	0.13020	25.31540	0.02050	69.07300	42.95000
Garnet3/3	0.04630	3.56300	37.85930	21.54780	0.08370	0.01730	5.78040	0.11790	32.28120	0.05070	101.34760	85.88000
Garnet3/4	0.18270	3.44540	37.41870	21.57030	0.06240	0.03760	5.86110	0.14500	31.92790	0.02340	100.67460	128.82000
Garnet3/5	0.03480	3.61180	37.62310	21.53550	0.04530	0.00200	5.35170	0.16660	32.86250	0.00370	101.23700	171.76000
Garnet3/6	0.00230	3.38790	37.53810	21.59700	0.05950	0.00810	6.05290	0.16690	32.20280	0.01700	101.03250	214.70000
Garnet3/7	0.07200	3.30760	37.28400	21.30980	0.06990	0.00810	6.06450	0.23780	32.19100	-0.00700	100.54460	257.64000
Garnet3/8	0.04640	3.26660	37.43640	21.62870	0.07430	0.01020	6.19280	0.23260	32.10530	0.01310	101.00640	300.59000
Garnet3/9	0.02080	3.30500	37.88800	21.42230	0.08570	-0.00710	6.24270	0.22960	31.82550	0.02390	101.04370	343.52000
Garnet3/10	0.02770	3.13390	37.68650	21.54620	0.08910	-0.00300	6.57070	0.24820	31.76780	0.01030	101.08040	386.46000
Garnet3/11	0.20990	2.26990	40.48470	23.57700	0.09250	0.07630	6.82350	0.32740	31.04080	0.02500	104.92710	429.40000
Garnet3/12	0.06250	2.97460	37.48230	21.42060	0.07120	-0.00710	6.87420	0.52410	31.48560	0.04180	100.93680	472.34000
Garnet3/13	0.00690	2.70240	37.49880	21.55090	0.07440	0.00300	6.95370	0.60420	31.27140	0.03630	100.70200	515.28000
Garnet3/14	-0.01160	2.71400	37.55280	21.44790	0.06310	0.00300	7.17960	0.63630	31.09620	0.03150	100.72450	558.22000
Garnet3/15	0.01150	2.53870	37.81850	21.42470	0.05230	0.01010	7.55450	0.76770	30.71670	0.02260	100.91730	601.17000
Garnet3/16	0.38290	0.27520	81.09330	3.03930	-0.00390	0.24600	1.01150	0.15550	3.60760	0.00920	89.82080	644.10000
Garnet3/17	0.10570	2.45760	37.12370	21.87370	0.07010	0.05670	7.56200	1.04820	29.63580	0.02070	99.95420	687.05000
Garnet3/18	0.05540	2.28950	37.83400	21.54210	0.04950	0.01110	8.18240	1.18150	30.28000	-0.01160	101.42550	729.98000
Garnet3/19	0.02540	2.14130	37.50800	21.35910	0.05960	0.01820	8.65010	1.48050	29.62830	0.02860	100.89890	772.92000
Garnet3/20	0.05550	2.01690	37.47260	21.43960	0.08180	-0.01010	8.36840	1.73970	29.83630	0.02980	101.04050	815.86000
Garnet3/21	0.25020	1.73650	38.13340	22.20710	0.09490	0.14680	7.92130	1.61210	29.27390	0.01750	101.39350	858.80000
Garnet3/22	0.01160	1.69290	37.29640	21.35550	0.08990	-0.00100	8.86540	1.94240	29.42260	0.02380	100.70040	901.74000
Garnet3/23	0.03460	1.73920	37.69260	21.37620	0.13710	-0.02620	8.86950	2.03490	29.28500	0.03620	101.20520	944.68000
Garnet3/24	0.03240	1.75120	37.38940	21.43360	0.10800	-0.00400	8.63360	2.11950	29.25110	0.03090	100.74960	987.62000

Continued on next page

Table C.5 – continued from previous page

Phase	Na2O	MgO	SiO2	Al2O3	TiO2	K2O	CaO	MnO	FeO	Cr2O3	Total	Distance μm
Garnet3/25	0.04160	1.77560	37.16750	21.29070	0.10190	-0.02520	8.49150	2.20900	29.16210	0.02250	100.26220	1030.56000
Garnet3/26	-0.01850	1.69330	36.06580	20.91400	0.07590	0.01110	8.07900	2.14810	28.78850	0.01730	97.79300	1073.50000
Garnet3/27	0.00460	1.78130	37.27250	21.19290	0.09550	0.01920	8.33550	2.32560	29.39970	0.01860	100.44530	1116.44000
Garnet3/28	0.03240	1.68460	37.37470	21.46830	0.09050	0.02020	8.49980	2.20430	29.69320	0.03200	101.10000	1159.38000
Garnet3/29	0.09500	1.75320	36.66350	21.15010	0.75490	0.07470	8.20640	2.27950	29.13650	0.01210	100.12610	1202.32000
Garnet3/30	0.00690	1.80310	37.39750	21.36590	0.09680	-0.00300	8.66850	2.01960	29.28280	0.02290	100.66400	1245.26000
Garnet3/31	0.00000	0.00980	99.77790	0.06840	0.00380	0.01090	0.03780	0.05330	0.68620	0.01030	100.65840	1288.20000
Garnet3/32	0.01610	1.74980	37.69390	21.58140	0.08030	0.01210	9.18290	2.02010	29.14690	0.02560	101.50910	1331.14000
Garnet3/33	0.01620	1.87170	37.41870	21.31480	0.07830	0.00710	7.95070	1.90120	29.93990	0.01770	100.51630	1374.08000
Garnet3/34	0.00690	1.88550	37.43260	21.48100	0.10820	0.01920	8.85520	1.94320	29.24360	0.04670	101.02200	1417.02000
Garnet3/35	0.01610	1.90780	37.49380	21.49950	0.10550	-0.00400	9.01710	1.72550	29.54910	0.03490	101.34930	1459.96000
Garnet3/36	0.02070	1.91880	37.53500	21.48960	0.09880	-0.01620	9.25770	1.62190	29.06470	0.02870	101.03570	1502.90000
Garnet3/37	0.03460	2.02870	37.55800	21.58870	0.05540	0.00910	8.74030	1.50520	29.56150	0.03370	101.11520	1545.85000
Garnet3/38	0.02310	2.26240	37.12270	21.49970	0.04300	0.01920	8.35990	1.47790	29.95940	0.03290	100.80020	1588.78000
Garnet3/39	0.43440	2.12280	32.97030	22.74220	0.06390	0.33520	7.24330	0.93380	27.55590	0.03880	94.44060	1631.72000
Garnet3/40	0.03480	2.50610	37.64830	21.57060	0.02470	0.00000	6.81100	0.96230	31.45210	0.00720	101.01700	1674.66000
Garnet3/41	-0.00690	2.67010	37.71880	21.72870	0.05610	0.00510	7.31360	0.72770	31.22190	0.01010	101.45200	1717.60000
Garnet3/42	0.02550	2.80260	37.63860	21.48710	0.07170	0.02230	7.13690	0.61620	31.57410	-0.00210	101.37490	1760.54000
Garnet3/43	0.00690	2.73920	37.82970	21.51720	0.06200	0.01220	7.04580	0.49340	31.38050	0.02730	101.11410	1803.48000
Garnet3/44	0.05780	3.02390	37.64730	21.68110	0.05860	-0.01320	6.49100	0.35810	31.99910	0.00300	101.31990	1846.42000
Garnet3/45	0.02540	3.18320	37.83400	21.72100	0.08750	0.01010	6.44340	0.26390	31.91240	0.01120	101.49220	1889.36000
Garnet3/46	0.01160	3.25090	37.84360	21.54790	0.03930	-0.01620	6.21750	0.22630	31.82900	0.01960	100.98560	1932.30000
Garnet3/47	0.09010	3.22820	37.10550	21.43760	0.06010	0.03550	6.00870	0.23630	31.61330	0.01420	99.82960	1975.24000
Garnet3/48	0.03240	3.45980	37.60770	21.56610	0.07480	0.02130	6.01950	0.18540	32.20100	0.00450	101.17250	2018.18000
Garnet3/49	0.02080	3.49580	37.76600	21.31820	0.06210	0.00100	5.98970	0.18420	31.95420	0.01330	100.80530	2061.12000

Continued on next page

Table C.5 – continued from previous page

Phase	Na2O	MgO	SiO2	Al2O3	TiO2	K2O	CaO	MnO	FeO	Cr2O3	Total	Distance μm
Garnet3/50	0.01850	3.50140	37.75080	21.50520	0.06250	-0.00300	5.50900	0.22370	32.58890	0.01040	101.17040	2104.06000
Garnet4/1	0.01390	3.59630	37.51990	21.64500	0.07190	-0.01520	5.08190	0.18900	32.76260	0.02900	100.90950	0.00000
Garnet4/2	0.01620	3.69750	37.54660	21.48980	0.07450	0.00000	5.15690	0.17460	32.58270	0.04290	100.78180	38.89000
Garnet4/3	0.00920	3.61220	37.84570	21.67420	0.07290	0.00810	5.56150	0.16230	32.43970	0.00780	101.39360	77.78000
Garnet4/4	0.06940	3.59630	37.24600	21.53790	0.08220	0.01620	5.23120	0.14750	32.40870	0.03810	100.37350	116.63000
Garnet4/5	0.01620	3.56920	37.37240	21.59910	0.06040	-0.00810	5.66610	0.16120	32.36410	0.06720	100.87600	155.53000
Garnet4/6	0.04160	3.53560	37.37290	21.50620	0.07980	0.02330	5.60930	0.18310	31.95310	0.04790	100.35270	194.38000
Garnet4/7	0.04970	2.46590	54.15470	13.05170	0.17950	0.23190	3.01630	0.20400	21.07880	0.02920	94.46170	233.27000
Garnet4/8	-0.00930	3.51220	37.39900	21.61880	0.06220	-0.00200	5.74080	0.15410	32.33530	0.02270	100.84510	272.14000
Garnet4/9	-0.00460	3.36230	37.66570	21.62870	0.02360	-0.01220	5.79000	0.26260	32.16090	-0.00940	100.89390	311.00000
Garnet4/10	-0.01250	1.65350	77.29590	11.54680	0.00150	0.04640	2.53110	0.10310	19.46600	-0.01690	112.64430	349.88000
Garnet4/11	0.00930	3.24040	37.56700	21.58990	0.03240	0.00610	6.26630	0.27720	31.95280	0.01780	100.95910	388.75000
Garnet4/12	-0.02540	3.07830	37.73500	21.58030	0.06020	-0.01520	6.78200	0.25440	31.44250	0.03710	100.96960	427.63000
Garnet4/13	0.04390	3.02860	37.68230	21.53890	0.06060	0.00100	6.65380	0.37610	31.71520	0.03510	101.13560	466.51000
Garnet4/14	0.05080	2.88640	37.31150	21.47970	0.05830	0.01210	7.13670	0.39700	31.31490	0.02010	100.66750	505.37000
Garnet4/15	0.03010	2.93570	37.57470	21.62450	0.03650	0.01620	6.53650	0.44770	31.94590	-0.00500	101.14790	544.26000
Garnet4/16	0.00460	2.73620	37.60580	21.36180	0.06690	0.00610	7.21480	0.47850	31.18740	0.03180	100.69380	583.13000
Garnet4/17	0.02310	2.70100	37.59870	21.55840	0.05500	0.00100	7.25430	0.58870	31.31860	0.02100	101.11990	622.00000
Garnet4/18	0.03240	2.73610	37.41440	21.38690	0.07090	-0.01310	7.35120	0.68260	31.15530	0.01800	100.84780	660.87000
Garnet4/19	0.00230	2.73690	37.53650	21.66020	0.02990	0.01310	6.72470	0.80130	31.47740	0.00300	100.98550	699.76000
Garnet4/20	-0.00690	2.55480	37.54350	21.40330	0.04530	0.00200	7.47070	0.89280	31.01740	0.00060	100.93040	738.63000
Garnet4/21	0.01390	2.38280	37.48850	21.49080	0.05810	-0.01820	7.70050	0.99990	30.54950	0.03430	100.71810	777.51000
Garnet4/22	0.06460	2.37850	37.45600	21.46610	0.04720	0.01310	7.45660	1.12980	30.57790	0.01210	100.60190	816.37000
Garnet4/23	0.06230	2.34280	37.37390	21.38270	0.05770	0.02120	7.63420	1.26120	30.43370	-0.00210	100.56960	855.25000
Garnet4/24	0.05540	2.24970	37.37300	21.32780	0.04540	0.03730	8.00810	1.37030	30.14500	0.01450	100.62650	894.12000

Continued on next page

Table C.5 – continued from previous page

Phase	Na2O	MgO	SiO2	Al2O3	TiO2	K2O	CaO	MnO	FeO	Cr2O3	Total	Distance μm
Garnet4/25	0.01380	2.25620	37.44620	21.67730	0.05140	-0.00610	8.10990	1.44300	30.07340	0.00340	101.07450	933.00000
Garnet4/26	0.00180	-0.00400	99.63570	0.00690	-0.00970	0.01200	0.01410	0.05870	0.51510	-0.00130	100.24440	971.87000
Garnet4/27	-0.03680	2.12790	37.32350	21.48850	0.06660	0.01820	8.58530	1.44500	29.47180	-0.00730	100.52680	1010.75000
Garnet4/28	0.04580	2.10200	36.91540	21.01460	0.08110	0.02120	9.16960	1.51590	28.22300	0.03080	99.11960	1049.63000
Garnet4/29	0.01380	2.00510	37.32600	21.40870	0.09590	0.00810	9.05450	1.60500	29.39160	0.02040	100.92920	1088.50000
Garnet4/30	0.02780	2.10250	37.19470	21.49110	0.10010	-0.00200	7.71120	1.73730	30.51330	0.03020	100.90820	1127.37000
Garnet4/31	0.02070	2.02760	37.59980	21.43290	0.09910	-0.02520	8.61220	1.70760	29.54520	0.01650	101.06150	1166.25000
Garnet4/32	0.02540	2.08730	37.17970	21.52130	0.07780	-0.00300	8.37230	1.68140	29.74090	0.01130	100.69720	1205.12000
Garnet4/33	0.05540	2.03350	37.09580	21.44580	0.08530	0.01710	8.37160	1.75750	29.86200	0.03720	100.76120	1244.00000
Garnet4/34	-0.01380	1.99920	37.34250	21.32580	0.11280	0.01710	8.71180	1.72440	29.59780	0.01970	100.85120	1282.87000
Garnet4/35	0.18550	2.37130	33.47360	18.85760	0.11090	0.09460	8.49340	1.60660	27.89020	0.03950	93.12330	1321.75000
Garnet4/36	0.03460	1.98160	37.43800	21.36300	0.08950	-0.00810	8.33260	1.76480	29.95900	0.03570	100.99870	1360.62000
Garnet4/37	0.03240	2.14350	36.99980	21.28030	0.04560	0.01310	7.58080	1.73660	30.31200	0.01910	100.16330	1399.49000
Garnet4/38	0.03230	2.00930	37.74630	21.49950	0.08290	0.01210	8.31170	1.52330	30.00950	0.02460	101.25150	1438.37000
Garnet4/39	-0.00230	2.18600	37.43510	21.28390	0.07840	-0.01010	7.87510	1.56980	30.30110	0.03600	100.76530	1477.24000
Garnet4/40	0.01850	2.11940	37.32180	21.71980	0.05280	0.01920	8.32490	1.58470	30.04050	0.03030	101.23190	1516.12000
Garnet4/41	0.00690	2.31350	37.52230	21.60000	0.05720	0.00500	7.99960	1.45500	30.44850	0.01350	101.42140	1555.00000
Garnet4/42	0.01850	2.37590	37.59240	21.32130	0.05930	0.01410	7.90580	1.10490	30.62720	0.02090	101.04030	1593.87000
Garnet4/43	0.06000	2.49460	37.39590	21.59320	0.07530	-0.00300	7.63620	0.93430	30.86780	0.01820	101.07540	1632.75000
Garnet4/44	-0.01620	2.64380	37.47120	21.73440	0.07400	0.01010	7.21350	0.80390	31.44730	0.00630	101.40430	1671.62000
Garnet4/45	0.01390	2.75160	37.58740	21.57320	0.06300	0.00400	6.93170	0.63100	31.36310	0.02230	100.94100	1710.49000
Garnet4/46	0.03230	2.86070	37.58520	21.52990	0.06770	0.00100	7.04530	0.48280	31.63040	0.02610	101.26160	1749.37000
Garnet4/47	0.03700	3.04890	37.56220	21.63820	0.06530	0.01420	6.60870	0.41520	31.95890	0.01550	101.36420	1788.24000
Garnet4/48	0.04390	3.10850	37.67860	21.46880	0.07550	0.00610	6.64630	0.33510	32.05210	0.04210	101.45700	1827.12000
Garnet4/49	0.04860	3.14680	37.45130	21.70090	0.08220	-0.02830	6.41730	0.21430	32.21400	0.01250	101.28780	1865.99000

Continued on next page

Table C.5 – continued from previous page

Phase	Na2O	MgO	SiO2	Al2O3	TiO2	K2O	CaO	MnO	FeO	Cr2O3	Total	Distance μm
Garnet4/50	0.00230	3.27500	37.50280	21.59540	0.06840	0.02230	6.35270	0.20190	31.96870	0.03120	101.02070	1904.87000
Garnet5/1	0.02780	3.67490	37.83450	21.61210	0.04380	0.01930	5.27800	0.17980	33.06990	0.01900	101.75890	0.00000
Garnet5/2	0.00230	3.59670	37.72990	21.64950	0.06700	0.01520	5.46860	0.15280	32.80320	0.02980	101.51510	30.01000
Garnet5/3	0.04400	3.44160	37.67910	21.46750	0.07030	0.00910	5.77760	0.16850	32.44110	0.01390	101.11250	60.03000
Garnet5/4	-0.00230	3.47990	37.61130	21.62860	0.05540	0.01110	5.70520	0.14960	32.63720	-0.00370	101.27830	90.04000
Garnet5/5	0.00920	3.43690	37.38010	21.54900	0.07920	-0.00610	5.74430	0.14530	32.30330	0.00800	100.65540	120.06000
Garnet5/6	0.02780	3.37920	37.16210	21.26200	0.05220	0.02130	5.91730	0.20260	32.24690	0.01360	100.28480	150.07000
Garnet5/7	0.01850	3.29720	37.74760	21.59940	0.06390	-0.01320	5.79110	0.22030	32.35020	0.00780	101.09600	180.09000
Garnet5/8	0.02900	0.06430	100.00890	0.49760	0.00690	0.00760	0.06800	-0.01990	1.07990	0.00660	101.76880	210.10000
Garnet5/9	0.05310	3.48570	37.17620	21.21620	0.07270	0.02430	6.04880	0.26100	31.79170	0.03180	100.16160	240.11000
Garnet5/10	0.04630	3.36350	37.02620	21.24930	0.04730	-0.00510	5.98000	0.22160	31.96550	0.02700	99.92660	270.13000
Garnet5/11	0.05310	3.34800	37.78630	21.72340	0.00900	0.02130	5.77590	0.23490	32.27420	0.00130	101.22740	300.14000
Garnet5/12	0.00430	1.93100	68.74870	12.64730	0.00610	-0.00730	2.80580	0.16640	22.13040	0.01750	108.45750	330.15000
Garnet5/13	-0.00460	3.31440	37.46770	21.36620	0.04990	-0.01420	5.83290	0.20090	32.05930	0.00930	100.30070	360.17000
Garnet5/14	0.00910	-0.01340	100.13830	0.10950	-0.00130	-0.00660	0.05790	0.02000	0.92390	-0.01190	101.25860	390.18000
Garnet5/15	0.03710	3.28190	36.86980	21.31340	0.06090	-0.00200	6.05520	0.25560	32.43630	0.00860	100.31880	420.20000
Garnet5/16	0.07410	3.22570	37.48800	21.53110	0.06240	0.01110	6.12750	0.27670	32.22340	0.01950	101.03940	450.21000
Garnet5/17	0.14910	2.33330	40.02110	23.22290	0.02210	0.16200	5.39840	0.29900	29.10380	0.01130	100.72300	480.22000
Garnet5/18	0.03010	3.12950	37.23690	21.47130	0.05410	0.00510	6.42660	0.32560	31.84170	0.00910	100.53000	510.24000
Garnet5/19	0.05990	2.98710	37.61120	21.40590	0.06620	0.00200	6.73750	0.33780	31.56810	0.01890	100.79450	540.25000
Garnet5/20	0.07570	3.03060	36.56660	22.27520	0.07400	0.02130	6.53420	0.30230	30.51020	0.00900	99.39910	570.27000
Garnet5/21	0.01250	1.66050	72.43210	12.27380	0.00370	0.00630	3.14140	0.14540	19.98980	-0.01060	109.66560	600.28000
Garnet5/22	0.02770	2.99610	37.32060	21.59930	0.07060	0.00610	6.57260	0.31130	31.51440	0.02430	100.44300	630.30000
Garnet5/23	0.09230	2.94700	37.34480	21.67540	0.06060	-0.00300	6.81200	0.37950	31.80630	0.00420	101.12210	660.31000
Garnet5/24	0.04640	2.84750	37.37000	21.17030	0.05320	-0.01210	6.54340	0.45740	32.14110	0.00770	100.63700	690.32000

Continued on next page

Table C.5 – continued from previous page

Phase	Na2O	MgO	SiO2	Al2O3	TiO2	K2O	CaO	MnO	FeO	Cr2O3	Total	Distance μm
Garnet5/25	0.22120	2.71920	35.88830	22.28890	0.07140	0.16000	5.99840	0.42570	30.82370	0.01570	98.61250	720.34000
Garnet5/26	0.01010	1.15260	81.66950	9.78390	0.00480	-0.00950	2.68630	0.14680	15.09240	-0.00340	110.54640	750.35000
Garnet5/27	0.00930	2.91410	37.27940	21.59210	0.04540	0.02530	6.55110	0.50760	31.98420	0.01920	100.92760	780.36000
Garnet5/28	0.00930	2.88430	37.39120	21.57220	0.07600	-0.00200	6.67440	0.49710	32.06550	-0.01090	101.16990	810.38000
Garnet5/29	0.08310	2.84740	37.42800	21.28290	0.08730	-0.01310	6.83190	0.55470	31.36040	0.01780	100.49350	840.39000
Garnet5/30	0.05100	2.90590	37.04950	21.66060	0.06500	0.01110	6.93080	0.46680	31.75560	0.02070	100.91690	870.41000
Garnet5/31	0.02310	2.90120	37.69050	21.50020	0.04490	0.01820	6.76460	0.41480	31.74510	0.01010	101.11280	900.42000
Garnet5/32	0.01850	2.84070	37.27600	21.42950	0.05610	-0.00200	6.68510	0.41720	31.95080	0.00820	100.68210	930.43000
Garnet5/33	0.06340	2.66710	47.42150	20.40400	0.02650	-0.00100	6.08690	0.39660	30.42820	0.02060	107.51470	960.45000
Garnet5/34	0.65620	3.83810	25.56100	16.16170	0.07750	0.34760	6.28700	0.29650	28.26000	0.01590	81.50140	990.46000
Garnet5/35	-0.02240	0.29100	97.20940	2.61660	-0.00640	-0.01300	0.41850	0.02980	4.19010	-0.00600	104.75540	1020.48000
Garnet5/36	-0.00930	3.17720	37.31720	21.51820	0.07680	-0.01930	6.38280	0.31470	31.81990	0.01200	100.61880	1050.49000
Garnet5/37	0.09410	2.96000	38.85050	22.18180	0.06890	0.02030	6.48390	0.32410	31.47200	0.02280	102.47830	1080.51000
Garnet5/38	0.02540	3.07940	37.55040	21.35050	0.05190	-0.00610	6.79870	0.27720	31.77090	0.01430	100.91870	1110.52000
Garnet5/39	0.03940	3.06600	37.56680	21.38770	0.07600	0.01110	6.42840	0.25900	32.16330	0.02480	101.02240	1140.53000
Garnet5/40	0.02310	3.22660	37.70780	21.72610	0.06330	-0.00510	6.45870	0.19690	32.05740	0.00960	101.46960	1170.55000
Garnet5/41	-0.03010	3.16490	37.35980	21.46600	0.06070	0.00510	6.40520	0.31840	32.19420	0.00420	100.97840	1200.56000
Garnet5/42	0.01850	3.21830	37.79210	21.65190	0.05520	0.00810	6.12970	0.20610	32.31230	-0.00100	101.39230	1230.57000
Garnet5/43	0.05330	3.32710	37.25610	21.50390	0.04870	0.02230	6.05110	0.19030	32.46560	0.00430	100.92270	1260.59000
Garnet5/44	-0.00540	-0.00120	99.79550	0.04150	0.01330	-0.01200	0.03910	-0.01110	0.73490	0.01440	100.63860	1290.60000
Garnet5/45	0.08790	3.71700	36.86200	20.91760	0.08340	0.05780	6.02190	0.21880	31.63730	0.01460	99.61830	1320.62000
Garnet5/46	0.00000	3.36080	37.82090	21.70000	0.06940	0.00200	5.94710	0.17280	32.25760	0.01900	101.34950	1350.63000
Garnet5/47	0.14970	3.57850	36.29910	21.97290	0.04860	0.17120	4.93200	0.11070	28.43840	0.00550	95.70640	1380.65000
Garnet5/48	0.05560	3.47150	37.58010	21.63470	0.04350	0.01010	5.65560	0.19460	32.54390	0.01790	101.20750	1410.66000
Garnet5/49	0.02320	3.55540	37.74070	21.58730	0.04600	0.00300	5.62920	0.20500	32.64950	0.01870	101.45810	1440.67000

Continued on next page

Table C.5 – continued from previous page

Phase	Na2O	MgO	SiO2	Al2O3	TiO2	K2O	CaO	MnO	FeO	Cr2O3	Total	Distance μm
Garnet5/50	0.03480	3.53990	37.55270	21.39700	0.04670	0.02840	5.52860	0.15790	32.75440	0.01510	101.05550	1470.69000
Biotite1	0.01620	3.55500	37.63930	21.69300	0.04810	-0.00510	5.39100	0.17360	32.50970	0.01340	101.03930	NaN
Biotite2	0.26010	12.14410	36.39940	19.30890	1.65380	9.58680	0.00070	-0.02980	16.08830	0.04420	95.48610	NaN
Biotite3	0.12260	11.92160	36.43470	19.10770	1.64270	9.80040	-0.00520	0.00000	16.54570	0.06020	95.63550	NaN
Biotite4	0.24370	12.05800	36.17280	19.30120	1.61080	9.46480	-0.01170	-0.00640	16.07020	0.04550	94.96680	NaN
Biotite5	0.21970	11.60810	36.05660	19.40630	1.54090	9.82410	0.01700	-0.02240	16.08990	0.02700	94.78950	NaN
Biotite6	0.23210	12.47560	35.31580	18.87060	1.74310	8.91710	0.05550	0.00210	15.92990	0.05180	93.59360	NaN
Biotite7	0.62970	10.23230	34.86020	20.34520	1.48970	8.54080	0.39740	0.01280	15.22960	0.05290	91.79060	NaN
Biotite8	0.22490	12.22350	37.40110	19.13880	1.71130	9.74580	0.00000	0.03100	15.59240	0.06670	96.13550	NaN
Biotite9	0.25950	12.43450	36.31200	19.38890	1.51680	9.54960	0.01500	0.02670	15.81930	0.05590	95.37810	NaN
Biotite10	0.19680	11.92360	36.21570	19.07980	1.74210	9.60810	0.01370	0.03090	15.65570	0.04420	94.51060	NaN
Biotite11	0.18200	12.14090	36.10030	19.28900	1.64740	10.00780	0.00330	0.00640	15.42080	0.03900	94.83700	NaN
Biotite12	0.26400	12.16450	36.20520	19.23470	1.82210	9.65180	0.00200	0.01070	15.77370	0.06030	95.18890	NaN
Biotite13	0.27800	12.30980	36.17360	19.05280	1.66540	9.71380	0.00260	0.00320	15.72470	0.03740	94.96120	NaN
Muscovite1	0.81210	1.34720	46.92330	33.54440	0.48120	10.51850	0.01550	-0.00330	1.05660	0.05870	94.75750	NaN
Muscovite2	0.94080	1.06350	45.80550	34.70090	0.52280	10.26700	0.01610	-0.02950	1.14430	0.05740	94.51820	NaN
Muscovite3	0.97070	0.87020	45.38780	34.83600	0.45750	10.24790	0.01480	0.01090	1.24230	0.06220	94.10040	NaN
Muscovite4	1.02600	0.89750	44.88020	34.43380	0.50340	10.05670	0.05180	0.02410	1.10930	0.04640	93.02900	NaN
Muscovite5	0.88380	1.24860	46.43710	33.94270	0.46680	10.84450	0.03030	0.01090	1.14410	0.05250	95.06120	NaN
Plagioclase1	7.80920	-0.00300	60.10260	25.46270	-0.00200	0.06490	6.83200	0.00660	0.04790	0.02060	100.34640	NaN
Plagioclase2	7.91460	0.06590	58.71010	25.11780	0.00120	0.10540	6.00040	0.02420	0.80450	0.00840	98.75240	NaN
Plagioclase3	7.31820	0.00100	59.26780	25.82730	-0.00490	0.07870	7.29440	0.00000	0.18840	-0.00520	99.97580	NaN
Plagioclase4	7.47540	-0.01990	59.42350	25.52710	0.01150	0.05740	7.15280	0.02530	0.04170	0.00480	99.71960	NaN
Plagioclase5	1.03520	1.97500	44.03070	33.78150	0.51730	8.52290	0.14590	-0.03380	2.02640	0.07200	92.10690	NaN
Plagioclase6	7.44180	-0.01240	58.17850	25.01540	0.01070	0.06380	7.17810	-0.02530	0.09880	-0.01490	97.98710	NaN

Continued on next page

Table C.5 – continued from previous page

Phase	Na2O	MgO	SiO2	Al2O3	TiO2	K2O	CaO	MnO	FeO	Cr2O3	Total	Distance µm
Plagioclase7	7.47760	0.01200	59.75120	25.49010	-0.00490	0.03830	7.18200	0.01320	0.04580	-0.00820	100.01020	NaN
Plagioclase8	6.65140	0.57640	57.09870	24.78920	-0.00680	0.52000	6.24520	0.00660	1.23820	-0.00540	97.12560	NaN
Plagioclase9	7.73140	0.00680	59.69020	25.22320	-0.00160	0.09160	6.82280	-0.02090	0.18740	0.00550	99.75900	NaN

Table C.6 Sample Z10 EPMA analysis. Composition given in oxide weight percent.

Phase	Na2O	MgO	SiO2	Al2O3	TiO2	K2O	CaO	MnO	FeO	Cr2O3	Total
Biotite1	0.26980	11.66090	35.24210	17.76070	1.63490	10.00090	-0.03380	0.14350	17.05960	0.03920	93.81170
Biotite2	0.26760	11.75030	36.28640	17.62610	1.67740	10.29910	0.00460	0.07770	17.19940	0.03500	95.22350
Biotite3	0.20950	11.88440	35.84510	17.45880	1.68080	9.97020	-0.02120	0.15860	17.34640	0.03560	94.58950
Biotite4	0.31510	11.80110	36.46790	17.88110	1.66360	10.13170	0.02050	0.12090	17.13040	0.02750	95.55970
Biotite5	0.23860	11.89870	35.96610	17.65860	1.71730	9.96290	-0.00930	0.13480	17.34940	0.01530	94.94170
Biotite6	0.30810	12.18470	35.77740	17.65650	1.62190	9.76920	-0.00400	0.15370	17.27030	0.01640	94.75820
Biotite7	0.23130	11.76130	36.27800	17.78260	1.68010	10.27610	-0.01530	0.14710	17.62080	0.02440	95.80170
Biotite8	0.32490	11.63070	36.77430	17.95170	1.74610	10.05310	0.00800	0.16880	17.32310	0.02170	96.00240
Biotite9	0.22620	11.60240	36.56450	17.77710	1.71070	10.15390	0.01320	0.16530	17.31320	0.03020	95.55670
Biotite10	0.22220	11.64850	36.51780	17.86230	1.72940	9.72470	0.01060	0.12850	17.50290	0.00430	95.35110
Biotite11	0.26990	11.89100	36.85970	17.60890	1.72700	10.18150	0.00330	0.10060	17.23920	0.01330	95.89460
Biotite12	0.21250	11.92350	36.07900	17.60940	1.72000	9.76050	0.00070	0.13720	17.79410	0.04300	95.27990
Biotite13	0.18040	11.87330	36.60390	17.74500	1.80700	10.05420	-0.01190	0.13510	17.46310	0.02360	95.88550
Biotite14	0.22630	11.93670	36.55450	17.55690	1.70260	10.15460	0.01590	0.13300	17.31640	0.02270	95.61960
Biotite15	0.30200	11.44410	36.20890	17.82210	1.70420	9.87660	0.02780	0.12430	17.30130	0.01470	94.82590
Biotite16	0.36340	11.74290	36.33740	17.73740	1.73820	9.96490	0.04180	0.17430	17.41970	0.02530	95.54540
Plagioclase1	5.96240	-0.01310	56.53220	27.78530	-0.01040	0.10730	9.64660	-0.00780	0.21590	-0.00240	100.24960
Plagioclase2	6.55480	0.01210	57.21140	27.28690	-0.00010	0.04410	9.12160	-0.01790	0.15100	0.00090	100.38290
Plagioclase3	6.33730	-0.00760	56.94200	27.61290	-0.00040	0.06450	9.32500	0.00890	0.06820	0.00420	100.36310
Plagioclase4	4.98880	-0.00030	53.80450	29.53790	0.01110	0.04060	11.78220	-0.01120	0.24470	0.00870	100.41880
Plagioclase5	4.39680	-0.01520	52.16340	30.71730	-0.00810	0.04480	13.08250	-0.00110	0.13740	0.00090	100.54300
Plagioclase6	7.06570	0.00040	58.54680	26.89580	-0.00390	0.05930	8.14570	0.01680	0.11480	-0.00780	100.84500
Plagioclase7	7.33610	-0.01290	59.90100	26.01900	0.00240	0.04230	7.45710	0.04710	0.06950	-0.00780	100.87450
Plagioclase8	7.01920	-0.01220	59.51200	26.07890	-0.01450	0.07140	7.62250	0.00670	0.05190	0.00620	100.36890

Continued on next page

Table C.6 – continued from previous page

Phase	Na2O	MgO	SiO2	Al2O3	TiO2	K2O	CaO	MnO	FeO	Cr2O3	Total
Plagioclase9	6.56700	0.00540	57.27880	26.74110	0.00040	0.03880	8.85050	-0.02580	0.07870	-0.01260	99.56060
Plagioclase10	6.22280	0.00820	56.68190	27.17960	0.00860	0.05280	9.12650	0.01010	0.06210	0.00330	99.35590
Plagioclase11	8.54270	-0.02170	61.16400	24.46800	-0.00210	0.08150	5.63970	0.01230	0.04350	-0.00470	99.95170
Plagioclase12	6.12400	-0.01130	56.15120	27.83550	-0.01460	0.05060	9.65520	-0.00450	0.07770	-0.00150	99.89420
Plagioclase13	7.12060	-0.00980	58.48350	26.14030	0.00320	0.06270	7.82590	-0.02350	0.15020	-0.00840	99.78640
Plagioclase14	6.78320	-0.01520	58.11730	26.58710	0.01760	0.07230	8.36970	-0.01010	0.04350	0.00460	99.99530
Plagioclase15	5.63620	0.03460	55.96380	28.20950	0.01680	0.45370	9.64960	0.01340	0.11590	-0.00820	100.09360
Plagioclase16	6.07920	-0.00310	56.20480	27.77510	-0.00270	0.05820	9.71060	0.01010	0.00930	0.00380	99.85110
Plagioclase17	6.70340	0.02090	56.88470	26.45790	0.00780	0.16510	8.37360	0.00780	0.11090	0.00980	98.74190
Epidote1	-0.03520	0.03070	37.84240	25.71660	0.05180	0.03580	23.32430	0.10990	9.87270	0.00830	96.99250
Epidote2	0.00610	0.06560	37.96560	26.78550	0.11250	0.03180	23.34000	0.27870	8.26160	0.02030	96.86780
Epidote3	0.02320	0.00880	37.38460	23.64330	0.06910	0.02760	22.39760	0.13920	11.71900	0.04100	95.45330
Epidote4	0.18180	0.09710	36.52020	25.48030	0.07880	0.16190	21.94370	0.12940	11.21800	0.03360	95.84480
Epidote5	0.04270	0.06380	69.74990	8.86900	0.03830	0.00430	9.53630	0.03350	4.20420	0.03210	92.57420
Epidote6	0.05770	0.58740	36.87860	23.09760	0.08400	0.05220	21.52350	0.18700	13.65990	0.03640	96.16420
Epidote7	-0.00210	0.01810	37.96370	24.93920	0.05430	0.00920	23.16020	0.12290	11.20990	0.03350	97.51100
Epidote8	0.05700	0.00650	37.20350	23.95690	0.05990	-0.01330	23.15480	0.12380	12.09670	0.02350	96.68260
Epidote9	0.00410	0.03690	37.48610	25.39480	0.10980	-0.01330	23.34120	0.18800	9.68630	0.02640	96.27370
Feldspar	0.75040	0.93070	45.23770	33.59320	0.54840	11.12450	0.01710	-0.01890	2.45910	0.03010	94.69110
Feldspar	0.79170	1.06610	45.63720	33.30430	0.47710	10.99040	0.02800	-0.01000	2.58880	0.04180	94.92540
Feldspar	0.82190	0.96440	45.19140	32.71230	0.62840	11.13460	0.04310	-0.02330	2.43370	0.15810	94.08770
Feldspar	0.79100	0.93670	45.62110	33.99510	0.41490	10.96000	0.01570	0.00330	2.52850	0.05080	95.31720
Feldspar	0.79250	1.25980	46.09430	33.02550	0.36890	11.11810	0.03560	0.01000	2.64060	0.04380	95.38900
Feldspar	0.81300	1.02680	45.42820	33.22660	0.51800	11.00730	0.04450	0.01780	2.57800	0.05410	94.71430
Feldspar	0.27300	11.97020	35.64240	17.63040	1.54360	10.00230	0.04510	0.14930	17.33380	0.08020	94.67040

Continued on next page

Table C.6 – continued from previous page

Phase	Na2O	MgO	SiO2	Al2O3	TiO2	K2O	CaO	MnO	FeO	Cr2O3	Total
Mica1	0.23010	11.78920	36.23440	17.89810	1.74430	10.17270	-0.00130	0.12540	17.08080	0.02860	95.30350
Mica2	0.21350	11.82650	36.33610	17.67520	1.70570	10.10570	0.00730	0.16440	17.08370	0.02580	95.14380
Mica3	0.21950	12.03630	36.05830	17.74960	1.60170	10.20420	0.03120	0.12540	17.04600	0.04040	95.11260
Mica4	0.18230	11.75040	35.80560	17.83460	1.74350	10.38950	-0.00200	0.16650	17.15070	0.03130	95.05430
Mica5	0.24210	12.10970	36.05270	17.81980	1.62950	10.07560	0.02380	0.11340	17.05740	0.04100	95.16510

Table C.7 Sample Z29 EPMA analysis. Composition given in oxide weight percent.

Phase	**Na2O**	**MgO**	**SiO2**	**Al2O3**	**TiO2**	**K2O**	**CaO**	**MnO**	**FeO**	**Cr2O3**	**Total**	**Distance** μm
Biotite1	0.04850	17.17710	25.53330	22.84590	0.09190	0.01260	0.00730	0.14170	21.63950	0.02950	87.52720	NaN
Biotite2	0.20380	11.14640	36.29990	18.43170	1.54060	8.91590	-0.01010	0.06250	18.25880	0.00700	94.86660	NaN
Biotite3	0.22990	10.84800	36.15570	18.40150	1.53280	8.91850	0.01210	0.04440	18.23520	0.04250	94.42070	NaN
Biotite4	0.25800	11.29430	35.57970	18.25700	1.46750	8.98160	0.02490	0.07930	18.29460	0.01230	94.24920	NaN
Biotite5	0.35140	10.93960	36.12420	18.49930	1.50950	8.56800	0.02420	0.05080	17.69870	0.03040	93.79600	NaN
Biotite6	0.23970	11.01840	35.82520	18.45290	1.47950	8.84720	0.01750	0.09100	17.73640	0.02050	93.72820	NaN
Biotite7	0.27660	11.03850	36.16050	18.37900	1.47520	8.95330	0.03020	0.07390	18.14270	0.02880	94.55850	NaN
Biotite8	0.27930	11.47630	35.47500	18.07430	1.54070	8.93660	0.00400	0.02750	18.29900	0.01860	94.13110	NaN
Biotite9	0.27250	11.20400	35.74480	18.68890	1.47330	9.08860	-0.00470	0.05070	18.25780	0.03870	94.81930	NaN
Biotite10	0.22810	11.02290	36.05500	18.22130	1.52350	9.10680	-0.00070	0.08340	17.93350	0.00660	94.18120	NaN
Biotite11	0.28930	11.19680	36.10850	18.23350	1.43100	8.82480	0.02720	0.08450	17.70550	-0.00030	93.90110	NaN
Biotite12	0.24050	11.17980	35.52460	18.57210	1.40320	8.75370	0.00130	0.08660	17.74940	0.02790	93.53920	NaN
Biotite13	0.27770	11.13170	35.61770	18.43640	1.49340	8.63640	0.05300	0.08850	18.31880	0.03240	94.08590	NaN
Biotite14	0.17230	11.22510	36.33970	18.15620	1.50690	9.02710	-0.01520	0.07500	17.83910	0.02810	94.36960	NaN
Biotite15	0.32470	10.89720	35.93930	18.53240	1.43930	8.80950	-0.00860	0.01460	17.79980	0.04130	93.79810	NaN
Biotite16	0.25710	10.69840	35.85950	18.67590	1.55330	8.78080	0.04230	0.09470	17.73390	0.04730	93.74320	NaN
Biotite17	0.25950	11.07950	35.62040	18.67970	1.38260	8.80550	0.02110	0.05820	18.16090	0.01420	94.08170	NaN
Biotite18	0.22660	11.30590	36.34010	18.56850	1.48140	8.69880	-0.00590	0.08730	17.74360	0.00450	94.45690	NaN
Biotite19	0.26490	11.20800	35.99530	18.44560	1.53510	8.83080	0.03500	0.05920	17.93610	0.02160	94.33140	NaN
Biotite20	0.24360	11.25540	36.40600	18.05220	1.44850	8.88760	0.02570	0.04150	17.92350	0.04220	94.32630	NaN
Biotite21	0.22970	10.95320	35.64000	18.45840	1.44260	8.75890	0.02440	0.08600	18.31190	0.02690	93.93200	NaN
Biotite22	0.20180	11.18310	35.94960	18.23620	1.52940	8.91100	0.01580	0.03840	18.26760	0.03740	94.37030	NaN
Biotite23	0.18750	10.71640	35.81980	18.42970	1.55700	9.03050	0.01910	0.10450	18.58990	0.03140	94.48580	NaN
Biotite24	0.18410	10.97170	36.08070	18.38310	1.51220	8.64280	-0.01650	0.06010	17.78690	0.01470	93.63630	NaN

Continued on next page

Table C.7 – continued from previous page

Phase	Na2O	MgO	SiO2	Al2O3	TiO2	K2O	CaO	MnO	FeO	Cr2O3	Total	Distance μm
Biotite25	0.21260	11.06570	36.01020	18.44060	1.49330	8.96610	0.01380	0.07360	18.43570	0.01840	94.73000	NaN
Biotite26	0.34750	11.27080	35.89450	18.11950	1.36920	8.60660	0.06900	0.08480	18.26370	0.01120	94.03670	NaN
Biotite27	0.12100	10.87560	35.77940	18.12810	1.57150	8.79970	-0.02170	0.06090	18.37840	0.02050	93.73490	NaN
Biotite28	0.24760	10.83910	35.91540	18.39070	1.54370	8.92950	0.07500	0.07250	17.88140	0.03240	93.92740	NaN
Biotite29/1	2.50720	7.99270	40.87840	20.28420	1.03420	6.35160	2.52340	0.05230	12.68540	0.01480	94.32410	0.00000
Biotite29/2	0.19890	10.98030	36.12140	18.59150	1.53590	9.06080	0.03290	0.09180	18.18440	0.04890	94.84670	50.26000
Biotite29/3	0.20310	10.93860	35.82570	18.14040	1.49210	8.72730	0.02820	0.05380	18.04840	0.01870	93.47640	100.21000
Biotite29/4	0.20550	10.85820	36.06940	18.44550	1.50120	8.95190	0.01410	0.07380	18.34780	0.02450	94.49180	150.11000
Biotite29/5	0.22690	11.09630	36.24150	18.24170	1.51280	8.97060	0.00130	0.08010	18.31780	0.01460	94.70370	199.92000
Biotite29/6	0.20040	10.81910	35.94640	18.78710	1.47990	8.40230	0.03620	0.06960	17.82150	0.03150	93.59400	249.76000
Biotite29/7	0.23750	11.03250	36.19840	18.41830	1.53090	8.68790	0.00600	0.08430	18.29970	0.02510	94.52060	299.46000
Biotite29/8	0.21780	11.05910	36.14430	18.45430	1.50050	8.73430	0.00400	0.06220	18.02020	0.02330	94.22000	349.33000
Biotite29/9	-0.01120	0.00250	99.88850	0.02310	0.01140	0.02850	0.00560	0.01650	0.36050	0.01010	100.34660	399.23000
Biotite29/10	0.19440	11.00440	36.33140	18.35280	1.45430	8.87240	-0.01270	0.10530	18.32130	0.02970	94.66600	449.14000
Biotite29/11	0.16430	11.01350	35.79120	18.43230	1.39410	8.73900	0.00400	0.07790	18.45220	0.03580	94.10430	499.04000
Biotite29/12	0.20020	11.11790	36.36520	18.62260	1.42620	9.06340	0.00800	0.07800	18.01570	0.03210	94.92940	548.94000
Biotite29/13	0.21760	11.24430	36.32960	18.50320	1.41390	8.85140	-0.01200	0.08840	18.33890	0.02870	95.01590	598.85000
Biotite29/14	0.21960	11.02050	36.34270	18.27180	1.48630	8.94040	-0.00600	0.09170	17.91010	0.02890	94.31200	648.75000
Biotite29/15	0.00190	0.00190	99.12100	0.03480	-0.01620	0.01630	-0.01110	0.02530	0.21060	-0.00050	99.41180	698.65000
Biotite29/16	0.15730	11.20730	36.01640	18.45600	1.46070	9.00860	0.00800	0.05680	18.28340	0.01170	94.66620	748.56000
Biotite29/17	0.25620	11.09290	36.20360	18.52090	1.48050	8.97490	0.01540	0.05780	18.27590	0.00950	94.88770	798.46000
Biotite29/18	0.22220	11.02370	35.83770	18.29480	1.54920	8.86520	0.00270	0.02100	18.28230	0.04070	94.13940	848.36000
Biotite29/19	0.17220	11.14520	35.99350	18.19700	1.57000	8.90080	0.00870	0.05050	18.04530	0.01950	94.10270	898.27000
Biotite29/20	0.04850	0.01960	99.48260	0.05620	0.00650	0.01730	0.01660	0.01870	0.13930	-0.00820	99.80520	948.17000
Biotite29/21	0.00750	-0.00040	99.04040	0.14400	0.01220	0.00410	0.01250	0.00220	0.06200	0.00350	99.28840	998.08000

Continued on next page

Table C.7 – continued from previous page

Phase	Na2O	MgO	SiO2	Al2O3	TiO2	K2O	CaO	MnO	FeO	Cr2O3	Total	Distance μm
Biotite29/22	-0.02990	-0.00240	99.20470	0.01060	0.00200	0.02030	0.00970	0.00330	0.29270	0.00070	99.54410	1047.98000
Biotite29/23	0.13350	11.25610	36.02340	18.38880	1.44020	8.88070	0.03740	0.02630	18.38910	0.00910	94.58460	1097.88000
Biotite29/24	0.16570	11.10880	35.86930	18.17510	1.38790	9.08260	0.00730	0.10390	18.20080	0.03110	94.13250	1147.79000
Biotite29/25	0.18260	11.10290	36.01620	18.68400	1.38100	8.99940	-0.02000	0.07870	18.23360	0.01610	94.69450	1197.69000
Biotite29/26	0.20830	11.07740	35.87180	18.72880	1.33400	9.16190	-0.01400	0.08290	18.27210	0.00020	94.73720	1247.59000
Biotite29/27	0.24570	11.23120	35.46380	18.07530	1.33620	8.40750	0.10940	0.07340	18.40880	-0.01660	93.35130	1297.50000
Biotite29/28	0.20410	11.14370	36.12470	18.38170	1.44160	9.03810	0.02470	0.05670	18.16730	0.02610	94.60870	1347.40000
Biotite29/29	0.20570	11.56860	35.75150	18.05870	2.07240	7.23780	0.25480	0.06000	16.14500	-0.00430	91.35440	1397.31000
Biotite29/30	0.19780	10.94120	36.06220	18.23140	1.49430	9.02870	-0.01670	0.07130	18.28310	0.00660	94.31640	1447.21000
Biotite29/31	0.24140	11.05060	35.96460	18.64560	1.52370	9.09530	0.01200	0.10520	18.31480	0.03070	94.98400	1497.11000
Biotite29/32	0.20050	11.00370	35.89350	18.49850	1.56010	8.94490	0.02070	0.08930	18.35160	0.01710	94.57980	1547.02000
Biotite29/33	0.15310	11.05990	36.04040	18.20220	1.49440	8.85940	-0.00600	0.09450	18.35440	0.03200	94.29030	1596.92000
Biotite29/34	0.20670	11.06670	36.01470	18.18270	1.58780	9.05830	-0.01530	0.06290	18.37430	0.03030	94.58440	1646.82000
Biotite29/35	0.18090	11.08880	35.88580	18.48850	1.55200	8.96210	0.01140	0.05990	18.33750	0.02610	94.59290	1696.73000
Biotite29/36	0.20710	11.08940	36.05970	18.45520	1.54160	8.73190	-0.01070	0.08500	18.63100	0.03200	94.83290	1746.63000
Biotite29/37	0.23700	11.07560	36.18410	18.23710	1.53020	8.70470	0.02000	0.06720	18.45300	0.01610	94.52490	1796.53000
Biotite29/38	0.25400	10.98650	35.94280	18.19290	1.50280	8.97680	0.00070	0.09540	18.34550	0.03190	94.32930	1846.44000
Biotite29/39	0.21480	11.10680	35.87620	18.24340	1.48200	8.69880	0.05530	0.09220	18.26720	0.02090	94.05770	1896.34000
Biotite29/40	0.21880	11.21820	36.06980	18.15850	1.50780	8.75130	0.04530	0.02720	18.20180	0.02300	94.22170	1946.25000
Biotite29/41	0.24650	11.13970	36.17180	18.20290	1.50400	8.96660	0.00470	0.09950	18.08960	0.02480	94.45010	1996.15000
Biotite29/42	0.24630	11.31880	36.25590	18.30930	1.50460	9.14850	-0.00670	0.08060	18.21850	0.04040	95.12290	2046.05000
Biotite29/43	0.19250	11.10160	36.20830	18.18600	1.48390	8.88800	-0.01930	0.02410	18.04360	0.02360	94.15160	2095.96000
Biotite29/44	0.21410	11.19410	36.47240	18.21200	1.48730	9.01410	-0.01600	0.05540	18.19330	0.04100	94.88380	2145.86000
Biotite29/45	0.19660	11.12110	36.37150	18.17380	1.45550	8.92780	-0.00800	0.03970	17.98210	0.02430	94.29250	2195.76000
Biotite29/46	0.25470	11.26050	35.88040	18.47070	1.49220	9.03700	-0.00860	0.08160	18.17530	0.04200	94.69430	2245.67000

Continued on next page

Table C.7 – continued from previous page

Phase	Na2O	MgO	SiO2	Al2O3	TiO2	K2O	CaO	MnO	FeO	Cr2O3	Total	Distance μm
Biotite29/47	0.20350	11.05560	35.82650	18.39820	1.47460	9.08900	0.00130	0.09710	18.33990	0.02090	94.50660	2295.57000
Biotite29/48	0.13070	11.15230	36.03690	18.08890	1.41520	8.84670	0.02720	0.08240	18.39840	0.02960	94.20830	2345.48000
Biotite29/49	0.05530	4.14640	77.84940	6.79450	0.57850	3.01350	0.05420	0.02250	8.16850	-0.00950	100.68290	2395.38000
Biotite29/50	0.20380	10.97250	35.82940	18.06860	1.51070	8.84340	0.01390	0.11780	18.49530	0.02760	94.08300	2445.28000
Biotite30/1	0.20670	10.95370	36.31550	18.37500	1.39530	8.82340	0.02040	0.05280	17.53010	0.01190	93.68490	0.00000
Biotite30/2	0.26350	11.13500	35.93580	18.25480	1.42100	8.73360	0.03560	0.07460	17.38160	0.03950	93.27500	92.45000
Biotite30/3	0.16250	10.41980	35.89600	18.08180	1.36870	8.59920	-0.01720	0.00930	17.05100	0.02910	91.61730	184.90000
Biotite30/4	0.24710	11.21230	35.89280	18.27130	1.36960	8.57070	0.02040	0.06110	17.62200	0.03130	93.29860	277.35000
Biotite30/5	0.20880	10.82560	35.64620	18.46660	1.36840	8.76170	0.02440	0.07470	17.19720	0.02610	92.59960	369.79000
Biotite30/6	0.19410	11.10430	35.92490	18.39100	1.39190	8.71010	-0.00330	0.06420	17.54980	0.01070	93.34110	462.24000
Biotite30/7	0.19500	10.25410	39.34480	16.87470	1.30370	8.24690	0.04620	0.07370	16.54820	0.02010	92.90750	554.69000
Biotite30/8	0.23000	11.24100	35.67410	18.16990	1.36830	8.71050	-0.02240	0.06840	17.49280	0.01520	92.97030	647.14000
Biotite30/9	0.22130	11.54170	35.42480	18.07450	1.39490	8.74230	0.01120	0.05280	17.48810	0.01150	92.96310	739.59000
Biotite30/10	0.26220	11.43040	35.77760	17.79120	1.36500	8.56350	0.05530	0.03630	17.77870	0.03310	93.09330	832.04000
Biotite30/11	0.22540	11.11490	36.22230	18.28590	1.40130	8.77620	0.00070	0.05390	17.42500	0.02490	93.53040	924.49000
Biotite30/12	0.19650	11.18280	35.53850	18.25230	1.39040	8.73250	0.03690	0.09940	17.64760	0.02420	93.10090	1016.93000
Biotite30/13	0.23860	11.11650	35.65570	18.29740	1.38480	8.78430	0.01780	0.07970	17.59880	0.02990	93.20350	1109.38000
Biotite30/14	0.24680	11.06070	35.64190	18.44120	1.37980	8.89080	0.05850	0.06930	17.66310	0.03070	93.48280	1201.83000
Biotite30/15	0.21100	10.95950	35.46520	18.18100	1.38250	8.61920	-0.01580	0.08180	17.37990	0.02520	92.30540	1294.28000
Biotite30/16	0.24070	11.13240	35.93560	18.46680	1.42230	8.86900	0.02240	0.07870	17.65030	0.02740	93.84550	1386.72000
Biotite30/17	0.26780	10.98140	35.61870	18.27970	1.41510	8.83410	0.02240	0.03520	17.43320	0.01770	92.90520	1479.17000
Biotite30/18	0.24210	11.18150	35.93480	18.32850	1.41200	8.78720	0.02040	0.05900	17.40760	0.02640	93.39950	1571.62000
Biotite30/19	0.21750	11.05790	36.34690	18.07860	1.43940	8.86460	-0.01120	0.06420	17.76640	0.04710	93.88250	1664.07000
Biotite30/20	0.24650	11.12120	36.01230	18.38830	1.43120	8.69910	-0.00660	0.08900	17.47930	0.03590	93.50290	1756.52000
Biotite30/21	0.23890	11.04690	35.41610	18.20510	1.41290	8.75680	0.02040	0.08590	17.71050	0.01850	92.91200	1848.96000

Continued on next page

Table C.7 – continued from previous page

Phase	Na2O	MgO	SiO2	Al2O3	TiO2	K2O	CaO	MnO	FeO	Cr2O3	Total	Distance μm
Biotite30/22	0.14750	10.01790	37.61240	19.36570	1.42350	8.66140	-0.01320	0.04770	17.52210	0.03610	94.83420	1941.41000
Biotite30/23	0.00180	0.01040	99.15790	0.04460	-0.00630	0.05400	0.01090	0.02920	0.42400	0.00830	99.74100	2033.87000
Biotite30/24	0.21900	10.85010	35.87140	18.10100	1.43280	8.98910	0.00400	0.05490	17.22080	0.03640	92.77940	2126.31000
Biotite30/25	0.21330	10.90800	35.80920	18.19190	1.43820	8.72360	0.00990	0.07140	17.54370	0.02960	92.93870	2218.76000
Biotite30/26	0.28020	11.04260	35.76810	18.08840	1.46600	8.99490	-0.00530	0.06520	17.38600	0.02920	93.12060	2311.20000
Biotite30/27	0.16650	10.73480	36.13580	18.24930	1.48130	8.87540	0.01510	0.05070	17.35030	0.03020	93.08950	2403.65000
Biotite30/28	0.22870	11.18840	35.82500	18.17170	1.46470	8.67350	0.01250	0.07560	17.98070	0.03720	93.65790	2496.10000
Biotite30/29	0.25510	10.11730	37.14320	18.97290	1.48400	8.99980	0.00860	0.09630	17.52540	0.04160	94.64430	2588.55000
Biotite30/30	0.27480	10.85270	35.37210	18.25840	1.50770	8.82480	0.00790	0.03000	17.70620	0.03400	92.86870	2680.99000
Muscovite1	0.80780	0.92610	44.98170	34.30210	0.41420	9.68470	0.02780	0.00440	1.07800	0.03620	92.26290	NaN
Muscovite2	0.89360	0.88840	45.57150	35.20060	0.41620	9.68370	0.07080	-0.02400	1.03850	0.04310	93.80610	NaN
Muscovite3	0.69880	1.08160	46.04240	34.37760	0.37000	10.21920	0.00000	-0.01400	1.17820	0.04070	94.00850	NaN
Muscovite4	4.88410	-0.00300	53.78080	29.28800	-0.01590	0.04750	11.39320	0.00540	0.01690	0.00340	99.41930	NaN
Muscovite5	0.00740	-0.01270	99.51850	0.00740	0.01350	-0.00600	0.00000	-0.00330	0.11270	0.00710	99.66650	NaN
Muscovite6	0.03500	0.00080	99.11160	-0.00840	0.00190	0.01010	0.02130	0.02070	0.02110	-0.00810	99.22240	NaN
Muscovite7	7.71800	0.00480	59.34420	25.27880	0.00030	0.08910	6.64530	0.00220	0.03690	-0.00200	99.11960	NaN
Muscovite8	0.55930	1.95260	47.78820	31.31260	0.44370	10.07290	0.01640	-0.00320	1.67100	0.03950	93.85610	NaN
Muscovite9	6.26610	-0.00720	56.15990	27.62100	-0.00150	0.04180	9.32490	-0.01940	0.06160	0.00090	99.47620	NaN
Muscovite10	5.19870	-0.00510	53.47300	29.41320	0.00080	0.05210	11.74350	-0.02580	0.06650	0.00520	99.95300	NaN
Muscovite11	4.47620	0.00290	51.97460	30.40980	-0.00510	0.05870	12.41970	0.05370	0.06350	-0.00180	99.45910	NaN
Muscovite12	0.80690	0.95100	45.69320	35.04030	0.35550	10.16720	-0.01980	-0.02780	1.02050	0.03020	94.06470	NaN
Muscovite13	0.73590	1.11760	46.02070	34.37090	0.36270	10.18280	0.03060	-0.00750	1.31950	0.06430	94.20510	NaN

Table C.8 Sample Z34 EPMA analysis. Composition given in oxide weight percent.

Phase	**Na2O**	**MgO**	**SiO2**	**Al2O3**	**TiO2**	**K2O**	**CaO**	**MnO**	**FeO**	**Cr2O3**	**Total**	**Distance** μm
Biotite1	0.18030	10.78720	36.01360	18.26120	1.91240	8.83060	0.04330	0.03620	18.13710	0.08790	94.28980	NaN
Biotite2	0.00920	0.04500	98.99290	0.10820	0.01020	0.08870	0.01160	0.00970	0.45470	-0.00410	99.73010	NaN
Biotite3	0.27140	10.87310	35.45680	18.30760	1.68230	8.57820	0.09310	0.01130	18.36430	0.08310	93.72130	NaN
Biotite4	0.32470	10.41420	35.91380	18.59590	1.77880	8.83980	0.05240	0.03510	18.55000	0.07500	94.57960	NaN
Biotite5	0.25600	10.98360	36.24340	18.22310	1.72250	8.66640	0.04000	0.02380	18.13940	0.06030	94.35850	NaN
Biotite6	0.21590	10.65720	35.99370	18.81950	1.77290	9.11590	0.00530	0.05890	18.11100	0.04990	94.80020	NaN
Biotite7	0.20730	10.87730	33.32460	17.88550	4.43980	7.94430	0.03390	0.02780	19.28240	0.06100	94.08390	NaN
Biotite8	0.20140	10.98980	36.14590	18.43710	1.81920	9.11790	0.01920	0.02400	18.39300	0.06050	95.20790	NaN
Biotite9	0.29880	10.95940	36.43100	18.01410	1.91100	8.83600	0.00330	0.01460	18.50050	0.06460	95.03340	NaN
Biotite10	0.20400	10.82800	36.09670	18.13960	1.76250	8.95140	-0.01260	0.03560	18.20850	0.09230	94.31860	NaN
Biotite11	0.24790	10.99440	35.87390	17.99070	1.63130	8.82220	0.01400	0.01470	17.53260	0.08940	93.21110	NaN
Biotite12	0.13360	10.61290	35.80940	18.30130	1.71620	8.67280	0.04000	0.02890	18.25250	0.06820	93.63580	NaN
Biotite13	0.20630	11.10020	35.17620	17.92130	1.77070	9.10250	0.03000	-0.01360	17.78310	0.08910	93.17920	NaN
Biotite14	0.19670	10.57440	35.91340	18.54360	1.75290	9.11390	0.03070	-0.02100	18.70440	0.05310	94.88300	NaN
Biotite15	0.17920	10.56440	36.09150	18.50290	1.71550	8.95410	0.03380	0.00960	18.36870	0.08370	94.50320	NaN
Biotite16	0.25020	10.93510	35.86830	18.35140	1.73370	8.89330	0.00140	0.01380	17.81960	0.06390	93.93060	NaN
Biotite17	0.39920	2.06300	8.46140	4.85970	0.01370	0.37900	34.86560	0.19980	12.67880	0.00190	63.92220	NaN
Biotite18	0.21890	10.54250	36.09530	18.10520	1.81710	8.69460	0.06430	0.05470	18.44860	0.10930	94.15050	NaN
Biotite19	0.16580	11.94120	34.28560	18.67630	1.55800	7.12250	0.05630	0.00520	18.83000	0.06720	92.70800	NaN
Biotite20	0.13340	10.78190	36.27690	18.46640	1.70960	8.80180	0.02690	0.03510	18.19400	0.08780	94.51360	NaN
Biotite21	0.19470	11.08180	35.54090	18.22260	1.61130	8.97150	0.02230	-0.00830	18.14660	0.09070	93.88260	NaN
Biotite22	0.17350	10.85340	36.36100	18.25230	1.88080	9.02650	-0.01310	0.05880	18.17960	0.06990	94.85580	NaN
Biotite23	0.20080	10.90980	35.91810	18.36060	1.94510	9.02860	0.01710	0.00310	17.87470	0.05440	94.31220	NaN
Biotite24	0.26780	10.89630	35.82760	18.12470	1.84800	8.95680	0.02230	0.02790	17.58140	0.06170	93.61450	NaN

Continued on next page

Table C.8 – continued from previous page

Phase	Na2O	MgO	SiO2	Al2O3	TiO2	K2O	CaO	MnO	FeO	Cr2O3	Total	Distance µm
Biotite25	0.22960	10.44530	36.09220	18.33940	1.73440	8.93740	0.05020	0.01370	18.38740	0.08300	94.31260	NaN
Feldspar1	6.65530	-0.00770	56.89920	26.98090	-0.02000	0.03150	8.72890	0.01200	0.08340	0.00240	99.39350	NaN
Feldspar2	9.24110	-0.00880	61.67790	23.62650	-0.00430	0.01590	4.75660	0.01740	0.04030	-0.00400	99.37560	NaN
Feldspar3	9.15840	0.00730	63.01880	23.17180	-0.01410	0.05170	4.33590	-0.00440	0.11180	0.00020	99.85590	NaN
Feldspar4	9.32470	-0.01060	62.73890	23.51790	0.00530	0.05470	4.26090	0.01740	0.11790	0.00380	100.04150	NaN
Feldspar5	9.04700	0.02480	62.22920	22.97930	-0.00380	0.03880	4.12770	0.04570	0.87420	0.01140	99.37810	NaN
Feldspar6	9.23700	0.00980	62.21160	23.38860	-0.00570	0.04190	3.50290	0.00660	0.03840	-0.00820	98.43670	NaN
Feldspar7	8.15510	-0.00230	61.30200	24.63590	-0.00630	0.06060	5.65840	0.00870	0.14640	0.01200	99.97910	NaN
Garnet1/1	0.03340	2.54280	36.90590	21.38430	0.05300	-0.01020	5.68210	0.89710	32.71480	0.01270	100.22610	0.00000
Garnet1/2	0.05740	2.39840	37.28090	21.35650	0.11440	0.02130	5.11080	0.98760	33.23470	0.04270	100.60470	31.48000
Garnet1/3	0.07860	2.36770	36.74950	21.90240	0.23130	0.02860	5.34090	1.07490	32.86160	0.04350	100.67910	62.97000
Garnet1/4	0.00000	2.25920	37.11930	21.30660	0.07860	0.01110	5.37570	1.13390	33.21860	0.03950	100.54240	94.44000
Garnet1/5	0.00480	2.28510	36.79270	21.27030	0.11290	0.01290	5.35650	1.00590	33.49390	0.04390	100.37900	125.92000
Garnet1/6	0.01430	2.13500	36.76660	21.29770	0.08440	0.00000	5.52360	1.11300	32.85100	0.03180	99.81760	157.41000
Garnet1/7	-0.03110	2.20670	36.93680	21.15790	0.07820	0.02590	5.76110	1.10390	32.78680	0.04750	100.10490	188.89000
Garnet1/8	0.08120	2.18990	37.17450	21.05340	0.08410	0.00460	5.93410	1.14120	32.84810	0.05500	100.56610	220.37000
Garnet1/9	0.03100	2.22380	36.76660	21.18380	0.07860	-0.01390	5.87590	1.13830	32.53790	0.04950	99.88540	251.85000
Garnet1/10	0.02150	2.24260	36.49520	21.12990	0.05360	0.01020	5.59250	1.16540	32.78250	-0.00620	99.49350	283.33000
Garnet1/11	0.01920	2.13590	36.98740	21.36180	0.05900	0.00550	5.45410	1.17900	33.03240	0.01650	100.25100	314.81000
Garnet1/12	0.02390	2.11950	37.14060	21.31390	0.19730	0.00460	6.38460	1.10970	32.27420	0.05200	100.62030	346.29000
Garnet1/13	0.00480	2.15710	36.69510	21.40920	0.15090	0.01290	5.43520	1.17870	33.18360	0.00160	100.22910	377.77000
Garnet1/14	0.03920	1.89380	48.51140	18.57010	0.03470	-0.02340	4.66470	1.03030	29.04970	0.00950	103.80330	409.25000
Garnet1/15	0.03180	1.71000	52.62740	18.10140	0.05150	-0.00090	4.79940	0.94500	27.27690	0.01640	105.55980	440.73000
Garnet1/16	0.01430	1.98410	34.62040	19.56990	0.10360	-0.02660	9.19170	1.18790	30.31460	-0.00100	96.98640	472.21000
Garnet1/17	0.01190	2.16820	37.08610	21.57070	0.08940	-0.02030	6.06150	1.21460	32.48320	0.01000	100.69570	503.69000

Continued on next page

Table C.8 – continued from previous page

Phase	Na2O	MgO	SiO2	Al2O3	TiO2	K2O	CaO	MnO	FeO	Cr2O3	Total	Distance μm
Garnet1/18	0.00000	-0.00570	99.51630	0.04920	0.00550	-0.00900	0.02450	0.03350	0.68470	0.02240	100.33610	535.18000
Garnet1/19	0.00960	2.05700	37.05050	21.47570	0.06240	0.00180	5.96500	1.23270	32.71720	0.02840	100.60020	566.66000
Garnet1/20	0.17440	11.77510	1.49850	1.95720	0.00530	0.05530	26.73010	0.71560	13.43360	-0.01190	56.34510	598.14000
Garnet1/21	0.04780	2.05820	37.11090	21.43820	0.05540	-0.00280	5.73480	1.35220	32.82880	0.02030	100.64650	629.62000
Garnet1/22	0.01200	2.03790	36.88260	21.25070	0.06740	-0.00650	5.43470	1.35660	32.71870	0.02560	99.78620	661.10000
Garnet1/23	0.03590	2.13390	36.92920	21.55520	0.04380	0.01940	5.41300	1.31710	33.17990	0.00850	100.63590	692.58000
Garnet1/24	0.04070	2.09240	36.72180	21.26450	0.07220	-0.00650	5.44530	1.24680	33.00730	0.00840	99.89920	724.06000
Garnet1/25	0.06470	2.06620	37.05850	21.48990	0.05670	0.01390	5.30990	1.39910	33.26320	0.02780	100.74980	755.55000
Garnet1/26	0.06760	11.95950	0.44970	0.78850	-0.00660	0.00000	27.62000	0.81080	13.52490	0.00070	55.22170	787.02000
Garnet1/27	-0.00480	1.96720	37.04610	21.70120	0.06740	0.02220	5.95670	1.21960	32.82400	0.00870	100.81300	818.50000
Garnet1/28	0.04540	2.16670	37.09230	21.45240	0.01500	0.01570	5.79420	1.25540	32.99230	0.00050	100.82980	849.98000
Garnet1/29	0.00720	2.16590	36.63930	21.36830	0.08320	0.00090	5.71290	1.28880	32.79140	0.01350	100.07130	881.47000
Garnet1/30	0.05960	1.88490	37.53730	22.20100	0.03980	0.01570	5.33950	1.26900	32.79320	0.01920	101.15910	912.95000
Garnet1/31	0.03590	1.80080	29.49550	16.31880	0.01460	0.01000	14.71400	1.16960	27.10350	0.02380	90.68640	944.44000
Garnet1/32	0.03350	2.03710	37.07920	21.28690	0.06240	0.01200	5.72780	1.21160	32.87820	0.01840	100.34710	975.91000
Garnet1/33	0.01430	2.12470	36.89920	21.29530	0.06440	-0.00090	5.79050	1.25380	32.62050	0.02410	100.08680	1007.39000
Garnet1/34	0.04310	2.18620	36.78560	21.25900	0.07450	-0.00180	5.46720	1.21500	33.24370	0.03000	100.30430	1038.87000
Garnet1/35	-0.00480	2.29940	37.30150	21.38160	0.05310	0.01760	5.44380	1.23730	33.06550	0.03060	100.83030	1070.35000
Garnet1/36	0.03110	2.13370	36.90120	21.36980	0.04590	0.00280	5.68250	1.10360	32.98260	-0.00360	100.25320	1101.84000
Garnet1/37	0.06680	2.25350	37.22830	21.56600	0.05420	-0.00650	5.56280	1.15460	33.15830	0.00330	101.04790	1133.31000
Garnet1/38	0.01670	2.24120	38.68980	21.10160	0.01400	0.01300	4.97160	1.14810	33.23930	0.01000	101.44530	1164.80000
Garnet1/39	0.00000	2.08640	37.23310	21.45720	0.05570	-0.01480	5.64560	1.12920	33.09520	0.02230	100.72460	1196.27000
Garnet1/40	0.02380	2.10130	36.87130	21.39130	0.06990	0.01850	6.47130	1.15660	32.17690	0.03720	100.31800	1227.75000
Garnet1/41	-0.02150	2.18560	37.03970	21.36550	0.07520	-0.00740	5.54620	1.11170	33.23930	0.02610	100.58940	1259.24000
Garnet1/42	0.06190	2.14850	37.17360	21.28230	0.10530	0.01480	6.14070	1.06890	32.59410	0.05390	100.64400	1290.72000

Continued on next page

Table C.8 – continued from previous page

Phase	Na2O	MgO	SiO2	Al2O3	TiO2	K2O	CaO	MnO	FeO	Cr2O3	Total	Distance µm
Garnet1/43	0.01910	2.27700	36.74390	21.33920	0.08240	0.01290	5.59840	1.09260	33.12280	0.06140	100.34980	1322.20000
Garnet1/44	0.01910	2.21220	37.21230	21.59470	0.08610	0.01200	5.31220	1.02510	33.17500	0.02620	100.67490	1353.68000
Garnet1/45	0.25850	2.37960	34.77150	20.40620	0.41050	0.10330	5.09580	0.91540	32.31610	0.03900	96.69570	1385.16000
Garnet1/46	0.03800	2.22080	38.27120	21.67910	0.38890	-0.00830	5.80160	0.99290	32.79400	0.05680	102.24340	1416.64000
Garnet1/47	0.03810	2.43830	37.02160	21.37510	0.22710	0.00180	5.41610	0.94770	33.06400	0.04870	100.57860	1448.12000
Garnet1/48	-0.01190	2.47570	36.84860	21.52950	0.07670	0.00740	5.61850	0.81850	32.81280	0.05590	100.24350	1479.60000
Garnet1/49	0.06430	2.56500	37.11700	21.55820	0.05830	0.02500	5.35790	0.80100	33.07010	0.04720	100.66390	1511.08000
Garnet1/50	0.05950	2.68140	37.04280	21.53230	0.04650	0.00550	5.25390	0.84430	33.27280	0.04060	100.77960	1542.57000
Garnet2/1	-0.01430	2.47120	36.82130	21.49280	0.07260	-0.01020	5.20100	0.94920	33.45760	0.02680	100.49250	NaN
Garnet2/2	0.04540	2.18120	36.83280	21.16510	0.06470	0.02030	5.32980	1.10440	33.14270	0.03330	99.91980	NaN
Garnet2/3	0.02870	1.84370	36.65490	21.25490	0.07950	-0.00550	5.77550	1.94700	32.33290	0.03130	99.94830	NaN
Garnet2/4	0.05030	2.04640	36.91090	21.55890	0.08460	-0.00650	5.48860	1.41600	33.50620	0.03140	101.09320	NaN
Garnet2/5	0.01670	2.66990	36.97520	21.56810	0.06320	0.01020	5.20620	0.82980	33.10870	0.00140	100.44920	NaN
Garnet3/1	0.04770	2.65190	36.87650	21.40210	0.07250	0.00550	5.39590	0.81860	33.16660	0.03220	100.46950	0.00000
Garnet3/2	0.27400	3.15170	35.84460	22.85410	0.04620	0.21350	3.98070	0.68050	27.41320	0.04420	94.50250	105.76000
Garnet3/3	0.20630	2.08510	36.64530	21.65000	0.07430	0.06000	6.08960	0.90480	31.91360	0.04190	99.67090	211.52000
Garnet3/4	0.00720	2.17270	36.98250	21.33310	0.07410	0.01850	5.67720	1.06500	33.02070	0.04080	100.39170	317.29000
Garnet3/5	0.07190	0.60270	78.22730	4.99100	-0.01260	0.04100	1.56310	0.35580	9.23100	-0.00520	95.08380	423.05000
Garnet3/6	0.04780	2.13730	36.98640	21.19650	0.04840	0.01840	5.48270	1.18700	33.29320	0.01530	100.41310	528.80000
Garnet3/7	0.06340	1.95040	33.86060	19.56840	4.08910	0.00460	5.01900	1.22480	34.17630	0.01470	99.97110	634.57000
Garnet3/8	0.01670	1.97490	36.86100	21.58030	0.04040	0.01110	5.62140	1.47300	32.66910	0.02800	100.27590	740.32000
Garnet3/9	0.03580	2.05800	36.54810	21.52490	0.06470	-0.01930	5.75320	1.42590	32.79490	0.02600	100.23140	846.08000
Garnet3/10	0.05960	1.96340	36.95210	21.15630	0.07510	0.00000	5.93210	1.46770	32.55880	0.02720	100.19230	951.85000
Garnet3/11	0.04060	1.97840	36.81800	21.15270	0.09810	0.00830	5.73960	1.50790	32.68940	0.02160	100.05450	1057.60000
Garnet3/12	0.21800	1.73020	36.15010	22.70350	0.08180	0.10060	5.53660	1.56830	31.62840	0.02900	99.74650	1163.37000

Continued on next page

Table C.8 – continued from previous page

Phase	Na2O	MgO	SiO2	Al2O3	TiO2	K2O	CaO	MnO	FeO	Cr2O3	Total	Distance μm
Garnet3/13	0.09990	1.97650	36.43600	21.19000	0.06010	0.04600	5.96120	1.61040	31.86240	0.01680	99.25930	1269.13000
Garnet3/14	-0.00240	2.05250	37.13120	21.35960	0.08260	-0.00460	5.96670	1.58630	32.22800	0.01870	100.42550	1374.88000
Garnet3/15	0.05250	2.05100	36.82500	21.40970	0.09440	0.01940	5.71650	1.30290	32.75180	0.02670	100.24970	1480.65000
Garnet3/16	-0.00480	2.19200	37.06320	21.57080	0.06900	0.02770	5.87580	1.21270	32.99490	0.04650	101.05270	1586.41000
Garnet3/17	0.08360	2.08560	33.51570	19.54500	0.45960	0.02290	8.67230	1.06670	30.69380	0.00250	96.14770	1692.16000
Garnet3/18	-0.02150	2.36380	36.85340	21.48250	0.08730	-0.01380	5.22750	0.94290	33.24630	0.02540	100.22920	1797.93000
Garnet3/19	0.01910	2.50670	37.03650	21.49000	0.05680	0.03510	5.48250	0.78670	33.11780	0.01150	100.54270	1903.68000
Garnet3/20	0.07800	2.64990	36.78900	21.67160	0.11080	0.00740	5.62590	0.80000	31.95550	0.02090	99.70910	2009.45000
Garnet4/1	0.00720	2.25370	36.54650	21.37040	0.05690	0.00280	5.55730	1.08000	33.12400	0.01990	100.01880	NaN
Garnet4/2	0.02380	2.33850	37.23590	21.36510	0.06690	-0.01480	5.81260	0.93510	32.74830	0.04530	100.57160	NaN
Garnet5/1	0.04030	2.72070	37.39810	21.42400	0.03240	0.00560	5.78370	0.80760	32.44850	0.04400	100.70490	0.00000
Garnet5/2	0.00560	0.08860	94.47010	0.66830	-0.01130	0.02880	0.23960	0.02800	1.92560	-0.00530	97.45470	70.00000
Garnet5/3	0.04760	2.71710	37.16070	21.44920	0.05970	0.02960	5.08700	0.86530	32.92580	0.02530	100.36740	140.00000
Garnet5/4	0.07890	2.60910	35.33390	20.25160	0.04510	0.01020	4.95130	0.74020	32.03580	0.02510	96.08110	209.99000
Garnet5/5	0.01200	2.53660	36.94790	21.45310	0.04810	0.00370	5.33000	0.90580	33.45210	0.03890	100.72810	279.98000
Garnet5/6	0.06440	2.49160	37.12620	21.54270	0.06420	0.00090	5.44190	0.89030	32.96250	0.04950	100.63430	349.99000
Garnet5/7	0.04790	2.33610	19.70240	10.24090	-0.00910	-0.00180	25.65170	0.62460	20.36150	0.00430	78.96940	419.98000
Garnet5/8	-0.00960	2.41520	36.82480	21.36630	0.12210	0.02870	5.32760	0.94880	33.38510	0.00710	100.42580	489.97000
Garnet5/9	0.04070	2.41320	36.95160	21.37720	0.06860	-0.02130	5.36810	0.99760	33.24010	0.04440	100.50140	559.97000
Garnet5/10	0.00480	2.30810	36.83440	21.26580	0.07410	0.00280	5.17200	1.15660	33.66120	0.03190	100.51170	629.96000
Garnet5/11	0.04800	2.32860	37.05500	21.48750	0.06550	0.00460	5.31600	1.04110	33.54780	0.01650	100.91060	699.96000
Garnet5/12	0.01920	2.21790	36.76630	21.44770	0.07140	0.02320	5.55350	1.08270	33.01440	0.00520	100.20130	769.96000
Garnet5/13	-0.01080	1.05120	64.26530	10.13060	0.00270	-0.01820	2.79360	0.67950	17.74980	0.00400	96.67660	839.95000
Garnet5/14	0.02400	2.32690	36.54620	21.41410	0.07110	0.00190	5.28060	1.00750	33.46230	0.02930	100.16390	909.95000
Garnet5/15	-0.00480	2.44620	37.22580	21.41610	0.07310	-0.00370	5.08140	0.88630	33.43000	0.02710	100.58600	979.94000

Continued on next page

Table C.8 – continued from previous page

Phase	Na2O	MgO	SiO2	Al2O3	TiO2	K2O	CaO	MnO	FeO	Cr2O3	Total	Distance μm
Garnet5/16	0.01110	0.00000	98.71700	0.12090	-0.00720	-0.00600	0.03760	0.02380	0.77190	0.00470	99.68700	1049.94000
Garnet5/17	-0.02390	2.68940	37.19710	21.57970	0.04260	0.00280	5.11740	0.81480	33.30200	-0.00160	100.74570	1119.94000
Garnet5/18	0.01860	2.00450	47.46540	19.37880	0.03130	-0.01780	4.68500	1.28130	29.44970	0.00060	104.31520	1189.93000
Garnet5/19	0.16490	0.27450	5.04960	2.01120	7.21040	0.04220	43.86730	0.06610	5.19850	0.00750	63.89220	1259.94000
Garnet5/20	0.07750	0.14170	96.47190	3.85020	0.01490	0.50130	0.08080	-0.00540	0.46880	-0.00140	101.60710	1329.94000
Garnet5/21	-0.04550	2.60260	37.09630	21.20250	0.05770	-0.00370	5.37410	1.14750	32.26030	0.01660	99.75740	1399.92000
Garnet5/22	0.68560	0.01060	96.03200	3.41550	0.01770	-0.00200	0.96370	-0.01520	0.19590	0.00140	101.32240	1469.92000
Garnet5/23	-0.00240	2.75410	37.60600	21.47740	0.05400	-0.01030	5.46920	0.87280	32.16570	0.04300	100.44220	1539.91000
Garnet5/24	0.05950	2.45940	37.19750	21.33700	0.04490	0.01030	6.34730	1.07080	31.00830	-0.01620	99.53500	1609.91000
Garnet5/25	0.05440	0.10050	96.23280	0.94540	0.00660	-0.02110	0.26420	0.09880	1.73840	-0.00610	99.44110	1679.90000
Garnet5/26	0.02220	2.22500	34.18180	19.33670	5.11710	0.02030	4.74140	0.88570	34.69890	0.03000	101.25900	1749.90000
Garnet5/27	0.04290	2.40750	38.58570	22.46920	0.10540	0.00090	5.70000	0.81230	32.34250	0.02820	102.49460	1819.89000
Garnet5/28	0.05750	2.57270	37.25530	21.53230	0.12120	-0.01210	5.61530	0.92880	32.26620	0.03510	100.38430	1889.89000
Garnet5/29	0.00000	2.64340	37.12200	21.45000	0.05160	-0.01210	5.74710	0.76140	32.69740	0.05840	100.53130	1959.89000
Garnet5/30	0.03600	2.63780	36.96030	21.62350	0.04510	-0.00090	5.79320	0.79670	32.67830	0.04760	100.61850	2029.88000
Garnet6/1	0.04350	2.00220	36.92740	21.44950	0.07670	-0.00840	6.14460	1.24000	32.56890	0.05510	100.50780	NaN
Garnet6/2	0.04110	2.02340	36.94140	21.39010	0.08800	0.02060	6.84280	1.23270	32.13630	0.04550	100.76180	NaN
Garnet6/3	0.05550	2.16180	36.76450	21.25050	0.06880	-0.00280	6.36700	1.10440	32.11080	0.03880	99.92210	NaN
Garnet7/1	0.04370	2.78160	37.14880	21.58540	0.07080	-0.02450	5.00040	0.92740	33.14640	0.00190	100.70640	0.00000
Garnet7/2	0.02430	2.56400	37.01680	21.22380	0.06810	0.01790	5.30200	0.88710	32.75460	0.01700	99.87570	57.33000
Garnet7/3	0.03170	2.38080	37.12460	21.30430	0.04360	0.01130	5.46000	1.06120	32.78490	0.00920	100.21150	114.66000
Garnet7/4	0.05590	2.26320	37.08280	21.54780	0.05790	-0.01130	5.91170	1.09210	32.44720	0.02590	100.48440	171.98000
Garnet7/5	0.04390	2.31220	36.84170	21.50620	0.06770	-0.03120	5.66740	1.06890	32.87880	0.03930	100.42620	229.31000
Garnet7/6	0.01950	2.14690	36.86280	21.22560	0.04470	-0.02830	5.84870	1.11360	32.52430	0.05380	99.83990	286.63000
Garnet7/7	0.02850	0.04170	97.96200	0.92780	0.01220	0.01830	0.22640	0.03960	1.56490	0.01830	100.83980	343.96000

Continued on next page

Table C.8 – continued from previous page

Phase	Na2O	MgO	SiO2	Al2O3	TiO2	K2O	CaO	MnO	FeO	Cr2O3	Total	Distance μm
Garnet7/8	0.04880	2.10880	36.80610	21.34680	0.07730	-0.01410	6.00090	1.21740	32.60440	0.02270	100.23310	401.28000
Garnet7/9	0.03410	2.09160	36.98530	21.14800	0.06600	0.00470	6.24470	1.23610	32.06020	0.01640	99.88710	458.61000
Garnet7/10	0.02910	2.22110	37.01290	21.26200	0.07870	0.00280	6.82250	1.14930	31.40120	0.05400	100.03360	515.94000
Garnet7/11	0.03010	0.00060	99.66780	0.04250	-0.00720	0.02960	-0.00140	0.03870	0.55980	-0.00420	100.36900	573.26000
Garnet7/12	0.02630	0.03220	99.16420	0.21960	-0.00540	-0.00100	0.04600	0.00880	0.17690	0.00110	99.67510	630.59000
Garnet7/13	-0.03570	-0.00040	99.58280	0.00150	-0.00230	-0.00820	0.00420	0.00440	0.18930	0.00260	99.78480	687.92000
Garnet7/14	0.02200	2.14790	36.95120	21.16490	0.06460	0.01230	6.14260	1.27480	32.31270	0.01480	100.10760	745.24000
Garnet7/15	0.13090	1.82750	37.41060	19.85180	0.04820	0.01330	5.36050	1.39340	29.90830	0.02850	95.97300	802.57000
Garnet7/16	1.08160	1.84950	25.05200	19.90610	0.04430	0.20180	4.13140	1.17860	27.82390	0.02720	81.29630	859.89000
Garnet7/17	0.02940	2.00650	36.90380	21.33980	0.08600	0.01140	5.76850	1.57360	32.77970	0.00150	100.50010	917.22000
Garnet7/18	0.08090	1.98670	36.68980	21.36140	0.08280	0.01700	5.59230	1.53660	32.58740	0.04830	99.98320	974.55000
Garnet7/19	0.05860	0.02240	98.39330	0.52680	0.01700	0.03380	0.02230	-0.00440	0.70360	0.00200	99.77990	1031.87000
Garnet7/20	0.00760	-0.01160	99.07770	0.00180	0.00180	-0.01430	0.08670	0.02110	0.50450	-0.00060	99.70110	1089.20000
Garnet7/21	1.88900	1.43830	37.68330	28.23480	0.01480	0.63470	3.55050	0.35050	12.57320	0.01960	86.38880	1146.52000
Garnet7/22	0.09970	0.04190	97.27310	1.52080	0.00300	0.01950	0.06710	0.00220	0.21010	-0.01880	99.23740	1203.85000
Garnet7/23	0.00190	-0.01490	99.60540	-0.00890	-0.00290	0.00820	0.01050	0.04990	0.05440	0.00650	99.73680	1261.18000
Garnet7/24	0.06410	0.03980	98.35700	0.82100	-0.00950	0.03180	0.07070	0.04550	0.16530	-0.00790	99.59520	1318.50000
Garnet7/25	0.05870	0.07500	96.26810	0.48070	-0.00570	-0.00410	0.10420	0.03330	0.62700	-0.01570	97.64700	1375.83000
Garnet7/26	0.00250	2.33630	37.02920	21.24180	0.08920	0.00470	5.29840	1.11770	33.53510	0.03880	100.69360	1433.16000
Garnet7/27	0.02200	2.15510	37.00970	21.33580	0.08940	-0.00090	6.38370	1.02690	32.30310	0.05640	100.38200	1490.48000
Garnet7/28	0.08830	2.37740	37.25470	21.68070	0.07260	0.02380	4.99470	1.04950	33.12170	0.03510	100.69850	1547.81000
Garnet7/29	0.03680	2.55800	36.77670	21.30160	0.06690	0.00290	5.27430	0.98070	33.07090	0.02650	100.09540	1605.14000
Garnet7/30	0.04900	2.81100	36.98620	21.48780	0.06390	-0.00570	5.18690	0.90560	32.93580	0.00850	100.43460	1662.46000
Mica1	1.02840	0.85520	45.75600	35.09910	0.29870	9.58620	0.01150	-0.00210	1.23180	0.08950	93.95650	NaN
Mica2	0.94650	1.21130	45.76430	34.08310	0.39260	9.62980	0.01350	0.01490	1.52090	0.05750	93.63430	NaN

Continued on next page

Table C.8 – continued from previous page

Phase	Na2O	MgO	SiO2	Al2O3	TiO2	K2O	CaO	MnO	FeO	Cr2O3	Total	Distance µm
Mica3	0.98800	0.94600	45.10590	34.53730	0.39600	9.88000	0.01560	-0.00960	1.32810	0.08570	93.28260	NaN
Mica4	4.57290	0.53070	51.70690	29.34060	0.29600	4.53110	2.32230	0.00430	0.93530	0.03700	94.27710	NaN
Mica5	1.01050	1.09540	46.40420	34.35850	0.45050	9.46170	0.07930	-0.00110	1.21770	0.05780	94.13570	NaN
Mica6	0.88070	1.39270	46.53830	33.48270	0.36130	9.94150	0.00070	0.01490	1.44290	0.03920	94.09480	NaN

Table C.9 Sample Z36 EPMA analysis. Composition given in oxide weight percent.

Phase	**Na2O**	**MgO**	**SiO2**	**Al2O3**	**TiO2**	**K2O**	**CaO**	**MnO**	**FeO**	**Cr2O3**	**Total**	**Distance** μm
Garnet1/1	0.03850	2.79860	37.42490	21.45620	0.03210	0.00000	3.01310	0.08280	36.37290	0.01440	101.25030	0.00000
Garnet1/2	0.00120	2.44870	37.41860	21.29140	0.03470	-0.01590	3.96750	0.11570	36.50030	0.03160	101.80960	48.36000
Garnet1/3	0.02500	2.12850	32.06920	19.00240	0.04670	0.00330	3.78510	0.13890	31.68160	0.01660	88.92040	96.66000
Garnet1/4	0.03120	1.93220	37.06820	21.22120	0.06040	0.00830	5.23470	0.23580	35.49130	0.01990	101.30510	144.96000
Garnet1/5	0.03730	11.62720	23.73160	22.13630	0.12420	0.07130	0.04080	0.03210	29.88900	0.01870	87.71140	193.32000
Garnet1/6	0.03170	6.29760	31.69990	22.50540	0.04230	0.00070	3.06110	0.21640	32.68950	0.02150	96.57110	241.61000
Garnet1/7	0.02370	1.33430	36.41680	21.04070	0.04080	-0.00490	5.31100	0.65860	34.48620	0.00430	99.33270	289.92000
Garnet1/8	0.00870	1.30260	37.25460	21.24170	0.04320	-0.00330	5.64460	0.93270	35.23140	-0.02040	101.66770	338.24000
Garnet1/9	0.02620	1.26820	37.10050	21.26250	0.07070	0.00200	5.28990	1.24570	34.89280	0.00970	101.17940	386.56000
Garnet1/10	0.04360	1.24560	37.20260	21.17560	0.07370	0.01250	5.51180	1.52720	34.48310	0.04080	101.31760	434.88000
Garnet1/11	0.03110	1.21910	37.21430	21.20310	0.04260	0.01050	5.42560	1.72180	34.22160	0.01450	101.10420	483.19000
Garnet1/12	0.06480	1.19660	37.11740	21.27870	0.06170	-0.00300	5.53480	1.97470	34.23340	0.02530	101.49290	531.52000
Garnet1/13	0.04240	1.25260	37.34780	21.21680	0.03940	0.01780	5.00740	2.35080	34.26300	-0.01610	101.55800	579.83000
Garnet1/14	0.02620	1.20690	37.22240	21.24320	0.02330	-0.00160	4.80590	2.42900	34.22840	0.01980	101.20510	628.16000
Garnet1/15	0.08880	1.17210	37.16690	21.22540	0.05350	-0.01910	4.32780	2.70440	34.56050	-0.00530	101.29940	676.47000
Garnet1/16	0.28000	1.97570	32.77460	22.19200	6.43810	0.26280	2.54270	1.43690	30.92160	0.01900	98.84890	724.79000
Garnet1/17	0.05760	1.16690	37.07220	21.04540	0.07590	-0.00660	4.24900	2.68890	34.69040	-0.00050	101.05130	773.11000
Garnet1/18	0.08250	1.16170	36.99640	21.06840	0.04780	-0.00560	4.33260	2.70550	34.63470	0.02130	101.05160	821.43000
Garnet1/19	0.03250	1.17440	36.99830	21.29000	0.05880	0.00000	4.23090	2.80090	34.54330	-0.00530	101.14080	869.75000
Garnet1/20	0.02120	1.12340	37.09920	21.12480	0.04850	0.00030	4.70780	2.59010	34.41160	0.02780	101.18140	918.07000
Garnet1/21	0.08970	1.11250	37.22140	21.22790	0.03920	-0.00260	4.86600	2.59210	34.28930	0.02300	101.46100	966.39000
Garnet1/22	0.06360	1.19430	37.04010	21.13620	0.06390	0.00030	4.86360	2.50130	34.33200	0.00590	101.20280	1014.71000
Garnet1/23	0.04730	1.15230	37.05040	21.16460	0.05290	0.00130	5.22360	2.32410	34.35500	0.03850	101.41120	1063.03000
Garnet1/24	0.03300	1.13330	42.66370	20.83980	0.03220	0.00690	5.03940	1.92720	33.33500	-0.00590	105.01400	1111.35000

Continued on next page

Table C.9 – continued from previous page

Phase	Na2O	MgO	SiO2	Al2O3	TiO2	K2O	CaO	MnO	FeO	Cr2O3	Total	Distance μm
Garnet1/25	-0.00280	-0.01040	100.31760	-0.00270	-0.00060	0.01350	0.03030	0.04560	0.70480	0.02680	101.13860	1159.67000
Garnet1/26	0.02110	1.19840	37.25700	21.14360	0.04360	0.01570	5.33790	1.79830	34.42520	0.00110	101.25290	1207.99000
Garnet1/27	0.01120	1.19270	36.92280	21.11840	0.03740	0.00390	5.48680	1.47620	34.51440	0.03800	100.80310	1256.30000
Garnet1/28	0.05710	1.26780	37.09600	21.21740	0.05390	0.00100	5.71640	1.17620	34.76470	0.01870	101.38220	1304.63000
Garnet1/29	0.03480	1.32030	37.19470	21.29460	0.07630	-0.00030	5.41370	0.96860	35.35370	0.01340	101.68460	1352.94000
Garnet1/30	0.03100	1.34330	37.39960	21.32970	0.26650	0.01670	5.38620	0.79460	35.06650	0.01020	101.66170	1401.26000
Garnet1/31	0.14000	9.16930	28.86410	19.90310	0.10170	1.48050	0.86080	0.15850	29.78300	0.00960	90.47050	1449.59000
Garnet1/32	0.08460	5.80320	55.50860	14.63260	0.29140	4.26890	0.26840	0.04670	18.19140	0.03120	99.12710	1497.90000
Garnet1/33	0.06930	1.07110	65.68580	12.85190	0.01930	1.75060	2.02860	0.13480	14.53720	0.00980	98.16680	1546.22000
Garnet1/34	0.03840	1.57050	37.39150	21.18520	0.06200	0.01080	5.62470	0.31500	35.08800	0.03000	101.32640	1594.54000
Garnet1/35	0.03960	1.74970	37.30190	21.35470	0.07240	0.00360	5.41720	0.23010	35.66520	0.03530	101.86970	1642.86000
Garnet1/36	0.04570	1.86180	37.30780	21.30130	0.09240	0.00590	5.31940	0.22500	35.11040	0.01760	101.31080	1691.18000
Garnet1/37	0.00740	2.13760	37.48110	21.21630	0.05690	-0.00720	5.00200	0.16030	35.19420	-0.00050	101.26980	1739.50000
Garnet1/38	0.01850	2.51340	37.37840	21.35070	0.04400	0.00890	4.75640	0.09240	35.37880	0.00750	101.56260	1787.83000
Garnet1/39	0.02610	2.74710	37.14300	21.28330	0.02640	0.00200	2.67450	0.10950	37.04090	0.03120	101.09280	1836.15000
Garnet1/40	1.35620	1.62920	36.25750	21.75750	0.01170	0.06930	1.62200	0.93360	33.39170	0.00690	97.06070	1884.46000
Garnet2/1	-0.00370	2.58690	37.17010	21.32740	0.04270	0.00530	3.89340	0.07660	35.51650	0.01170	100.63040	0.00000
Garnet2/2	0.02470	2.10770	37.26870	21.09520	0.04400	-0.02000	4.63760	0.11910	35.36800	0.03680	100.71480	43.81000
Garnet2/3	0.02850	2.17620	35.68480	20.36030	0.04130	0.00560	5.13950	0.20530	34.89870	0.01600	98.56690	87.61000
Garnet2/4	0.22200	1.22570	39.03480	26.26640	0.06890	0.03010	4.80200	0.22230	31.62470	0.03900	103.55710	131.44000
Garnet2/5	0.03570	2.02900	37.17680	21.26700	0.09160	-0.00560	5.30150	0.29020	34.71800	0.02300	100.93780	175.23000
Garnet2/6	0.06540	2.00880	37.08410	21.23580	0.19400	0.00260	4.96380	0.35190	35.15730	-0.00910	101.06370	219.03000
Garnet2/7	0.04070	1.95890	37.14620	21.18230	0.04570	0.00560	5.16830	0.48760	34.84760	0.02880	100.91960	262.85000
Garnet2/8	0.00490	2.10130	37.11190	21.33990	0.04100	0.00820	4.07460	0.61030	35.61040	0.00160	100.93570	306.65000
Garnet2/9	0.01480	1.87320	37.26640	21.20620	0.06210	0.00330	5.06750	0.88030	34.75600	-0.00160	101.12980	350.46000

Continued on next page

Table C.9 – continued from previous page

Phase	Na2O	MgO	SiO2	Al2O3	TiO2	K2O	CaO	MnO	FeO	Cr2O3	Total	Distance μm
Garnet2/10	0.02100	1.80290	37.09910	21.14380	0.05790	-0.00330	4.76320	1.08900	34.90260	0.03090	100.91530	394.27000
Garnet2/11	-0.00240	9.79720	23.98150	22.16690	0.04390	0.12510	0.05470	0.06470	31.69630	0.01780	87.95620	438.07000
Garnet2/12	0.03220	1.34310	37.00340	21.22550	0.12330	0.00230	5.23200	1.75490	34.33540	0.00530	101.05740	481.88000
Garnet2/13	0.04950	1.20620	37.22550	21.25740	0.05360	-0.00650	5.17100	2.11010	34.17780	0.01010	101.26900	525.69000
Garnet2/14	0.02600	1.19260	37.24150	21.31370	0.03420	-0.00330	4.98090	2.29510	34.12110	0.00370	101.23450	569.49000
Garnet2/15	0.04580	1.14580	37.27210	21.19740	0.04900	-0.00230	4.99510	2.44130	34.14930	0.02610	101.33800	613.30000
Garnet2/16	0.05720	1.19160	37.07940	21.21810	0.05220	0.02120	4.31230	2.63690	34.71130	0.02280	101.31980	657.11000
Garnet2/17	0.06460	1.21670	37.02620	21.07600	0.08120	0.00910	4.15050	2.52820	34.51410	0.01010	100.67660	700.92000
Garnet2/18	0.10040	1.15280	36.94190	21.06250	0.05630	0.00390	4.47110	2.65370	34.05100	0.03240	100.52680	744.72000
Garnet2/19	0.12390	1.16710	36.99770	21.06480	0.04250	0.00390	4.21630	2.76080	34.02220	0.04090	100.46620	788.53000
Garnet2/20	0.14760	1.19380	37.07770	21.22500	0.03270	-0.00390	3.89600	2.78420	34.36350	0.01220	100.74830	832.34000
Garnet2/21	0.12790	1.18120	36.82570	21.25570	0.07580	-0.00650	3.81370	2.86810	34.41040	0.00580	100.57650	876.14000
Garnet2/22	0.10660	1.18400	36.86170	21.13450	0.03240	-0.01270	3.83000	2.79470	34.36050	0.02120	100.35150	919.95000
Garnet2/23	0.09290	1.19350	37.02000	21.08650	0.03920	0.00070	4.00990	2.80520	34.12330	0.01750	100.39430	963.76000
Garnet2/24	0.09810	1.15860	36.95340	21.00650	0.04180	-0.00100	4.16380	2.82200	34.43430	0.01480	100.72220	1007.57000
Garnet2/25	0.08690	1.18220	36.98980	21.07220	0.05430	0.00980	4.34830	2.70410	34.26140	-0.00210	100.71060	1051.37000
Garnet2/26	0.05080	1.16660	37.07430	21.11230	0.05610	0.01500	4.93110	2.54640	33.97180	0.03090	100.95530	1095.18000
Garnet2/27	0.05440	1.12810	36.88570	21.04100	0.02800	-0.00100	5.21010	2.39000	33.88950	0.03140	100.66190	1138.99000
Garnet2/28	0.01110	1.20540	37.16270	21.02900	0.07350	-0.00650	5.11740	2.34430	34.00420	0.03410	100.98750	1182.80000
Garnet2/29	0.02960	1.19980	37.09170	21.07610	0.05670	0.01080	5.43270	2.09800	34.02140	0.03090	101.05550	1226.61000
Garnet2/30	0.00740	1.20020	37.23800	21.19200	0.06230	0.01040	5.12210	1.92140	34.37220	0.00850	101.14000	1270.42000
Garnet2/31	0.01860	1.25730	37.00450	21.02220	0.06980	-0.00420	5.31250	1.61440	34.57930	0.01330	100.90110	1314.22000
Garnet2/32	0.04690	1.26160	37.11090	21.08570	0.05950	0.00100	5.14500	1.29120	34.94010	0.03770	100.98630	1358.03000
Garnet2/33	0.04310	1.28680	37.16490	21.23550	0.05940	0.00070	5.53430	1.16450	34.79240	-0.00210	101.28580	1401.83000
Garnet2/34	0.06290	1.35030	37.08150	21.15080	0.06150	0.00000	5.41820	0.85130	35.13880	0.03130	101.15570	1445.64000

Continued on next page

Table C.9 – continued from previous page

Phase	Na2O	MgO	SiO2	Al2O3	TiO2	K2O	CaO	MnO	FeO	Cr2O3	Total	Distance μm
Garnet2/35	0.02590	1.42070	37.17370	21.22430	0.05880	-0.00850	5.37620	0.58770	35.13600	0.00370	101.00700	1489.45000
Garnet2/36	0.00620	1.44520	37.31150	21.28840	0.09330	-0.00160	5.33620	0.43660	35.29500	0.00960	101.24160	1533.26000
Garnet2/37	0.03450	1.51030	37.34440	21.16300	0.08050	0.00520	5.92100	0.30460	34.91580	0.02130	101.30930	1577.06000
Garnet2/38	0.05670	1.65420	37.40400	21.36650	0.06240	-0.01140	5.14170	0.26060	35.44830	0.01170	101.40600	1620.88000
Garnet2/39	0.05680	1.78410	35.55410	20.54840	0.02730	0.01670	4.45720	0.21970	34.59360	-0.00740	97.27470	1664.68000
Garnet2/40	0.01850	2.06910	37.18240	21.29540	0.03060	-0.01280	4.41930	0.11770	36.09770	0.00160	101.23450	1708.48000
Garnet3/1	0.03440	2.58730	37.19350	21.39230	0.01270	0.01300	3.62300	0.11390	36.20810	-0.01530	101.17820	0.00000
Garnet3/2	0.28730	0.03160	99.31750	0.04560	0.00360	0.08430	0.24360	0.01870	0.86260	0.00360	100.90440	45.84000
Garnet3/3	0.12380	2.33080	33.64320	19.23210	0.04210	0.03080	5.04650	0.21520	34.58570	0.01270	95.26330	91.65000
Garnet3/4	0.10290	1.90070	36.04150	20.81680	0.02020	0.03940	4.53720	0.32430	34.16630	0.00260	97.96410	137.48000
Garnet3/5	0.44940	1.72450	36.50310	21.70320	0.03680	0.17180	4.50980	0.39350	32.23680	0.00210	97.74150	183.31000
Garnet3/6	0.73850	1.69080	31.47080	24.56110	0.07540	0.34130	4.99240	0.38240	29.95320	0.01660	94.24870	229.13000
Garnet3/7	0.01470	1.62990	37.77220	21.35710	0.03570	-0.00360	5.35210	0.51510	35.03720	0.01700	101.74230	274.95000
Garnet3/8	0.40530	2.12950	33.61580	17.67360	0.01060	0.27960	2.78240	0.43310	27.12200	-0.00370	84.46260	320.78000
Garnet3/9	0.05390	1.40680	37.25250	21.15410	0.06860	0.00260	5.74010	0.88580	34.30700	-0.00110	100.87680	366.61000
Garnet3/10	0.02780	1.26960	41.13580	18.41940	0.05140	0.00000	5.08660	1.16290	31.27300	0.01020	98.44730	412.43000
Garnet3/11	0.02340	1.28030	36.96040	21.21890	0.06880	0.00620	5.29910	1.43180	34.92090	-0.01110	101.21230	458.26000
Garnet3/12	0.03570	1.21540	36.90600	21.14790	0.09970	0.00750	5.46810	1.65950	34.50230	0.03020	101.07240	504.09000
Garnet3/13	0.01840	1.18620	37.14720	21.16040	0.06900	-0.00680	5.47400	1.83030	33.96940	0.01480	100.88160	549.91000
Garnet3/14	0.06510	1.19990	37.30750	21.15620	0.03680	-0.00060	4.98280	1.92680	34.41200	-0.00210	101.11030	595.73000
Garnet3/15	0.03310	1.16580	37.16110	21.07900	0.06050	-0.00360	5.30060	2.20490	33.67910	0.02540	100.72320	641.56000
Garnet3/16	0.06020	1.20520	34.57530	20.29190	0.03190	0.07330	4.67550	2.20380	32.04620	0.01270	95.17610	687.38000
Garnet3/17	0.29400	1.37170	32.65890	19.92970	0.06360	0.04690	5.07190	2.33010	32.27020	0.01790	94.05490	733.22000
Garnet3/18	0.05050	1.19190	36.89930	21.18480	0.06400	-0.01170	4.41400	2.75170	34.23310	0.01530	100.80460	779.04000
Garnet3/19	0.03450	1.14080	36.94590	21.00190	0.02410	-0.00750	4.60530	2.82270	34.01140	0.03330	100.62260	824.86000

Continued on next page

Table C.9 – continued from previous page

Phase	Na2O	MgO	SiO2	Al2O3	TiO2	K2O	CaO	MnO	FeO	Cr2O3	Total	Distance μm
Garnet3/20	0.03460	1.15750	37.06870	21.27930	0.05230	-0.01400	4.16010	2.72510	34.58850	0.03580	101.10440	870.69000
Garnet3/21	0.06130	0.86870	34.65520	19.50490	0.04750	0.01260	4.16160	2.71460	34.64180	0.00370	96.68910	916.52000
Garnet3/22	0.07650	1.15560	37.00000	21.15760	0.05650	-0.00360	4.53000	2.67710	34.37970	-0.02380	101.05650	962.34000
Garnet3/23	0.02810	0.61760	62.49950	12.26760	0.00490	0.00440	2.79850	1.56400	22.03240	0.00330	101.82500	1008.17000
Garnet3/24	0.04060	1.11140	37.23780	21.21450	0.05290	0.00680	4.98360	2.44800	34.12000	0.01370	101.23300	1053.99000
Garnet3/25	0.11030	1.38500	34.94430	19.85070	0.06880	0.00550	4.88650	2.17290	34.12700	0.00470	97.55880	1099.82000
Garnet3/26	0.01980	0.86650	55.48570	17.86460	0.02120	0.00330	4.14620	1.57000	28.75290	0.01090	108.74710	1145.64000
Garnet3/27	0.01610	1.50990	35.93430	20.48810	0.05060	0.00490	4.77740	1.66610	34.73850	0.00110	99.19340	1191.47000
Garnet3/28	0.05430	1.22750	36.85920	21.01560	0.06180	0.00100	5.21090	1.59480	34.86190	0.03390	100.92920	1237.30000
Garnet3/29	-0.00250	1.28580	36.87560	21.14190	0.06850	0.00060	5.40230	1.34410	34.52250	0.00160	100.64770	1283.12000
Garnet3/30	0.02950	1.22210	37.29730	21.18860	0.06730	-0.00420	5.71970	1.12860	34.56830	0.00370	101.23430	1328.94000
Garnet3/31	0.33320	0.99730	31.41640	26.28430	0.16700	0.05650	4.89610	0.71410	28.96890	0.00480	93.85470	1374.77000
Garnet3/32	0.04050	1.33950	36.92600	21.18280	0.06840	-0.00390	5.75960	0.67450	34.82730	0.04030	100.87590	1420.60000
Garnet3/33	0.01350	1.42990	37.26270	21.28000	0.06100	0.00520	5.49130	0.51080	34.98270	0.01640	101.05340	1466.42000
Garnet3/34	0.03320	1.46270	37.09980	21.29260	0.06330	0.00980	5.43980	0.45510	35.06150	0.00320	100.92140	1512.25000
Garnet3/35	0.16550	1.19500	49.04410	18.51490	0.03820	1.00610	3.97590	0.33590	25.68340	-0.00770	99.96290	1558.08000
Garnet3/36	0.02070	1.65520	37.13260	21.32580	0.06780	0.40110	5.18630	0.26940	33.81790	0.02660	99.90350	1603.90000
Garnet3/37	0.78150	1.22200	44.84880	35.30810	0.08480	9.55500	0.15810	0.02170	3.44380	0.01720	95.44100	1649.72000
Garnet3/38	0.42960	2.64260	43.65800	33.09160	0.08560	8.81590	0.02780	0.04470	6.67910	0.03980	95.52320	1695.55000
Garnet3/39	0.10650	5.29260	31.30060	21.46750	0.05360	0.02740	3.29580	0.08980	32.42620	0.00050	94.06070	1741.38000
Garnet3/40	-0.01840	2.26140	37.23320	21.28700	0.04380	0.04980	4.38450	0.10020	35.68060	-0.00480	101.05960	1787.21000
Garnet4/1	0.03210	2.74760	37.20680	21.41310	0.02060	0.02650	3.14170	0.09460	36.44360	0.01900	101.16400	0.00000
Garnet4/2	-0.00370	2.52680	37.29640	21.44250	0.03670	-0.00330	4.15140	0.11500	35.67730	0.00850	101.28620	49.86000
Garnet4/3	0.00620	2.19390	37.07580	21.30700	0.06270	0.00950	4.67860	0.12960	35.79100	0.00050	101.25630	99.55000
Garnet4/4	0.02830	1.96500	37.20030	21.30520	0.06560	0.00260	5.15450	0.18920	35.42430	0.00900	101.35670	149.31000

Continued on next page

Table C.9 – continued from previous page

Phase	Na2O	MgO	SiO2	Al2O3	TiO2	K2O	CaO	MnO	FeO	Cr2O3	Total	Distance µm
Garnet4/5	0.02840	1.80700	37.12300	21.23900	0.04700	0.00000	4.96160	0.20410	35.60780	0.01060	101.03030	199.09000
Garnet4/6	0.84170	1.01670	32.82500	27.17870	0.04790	0.18600	3.37270	0.14680	23.13770	-0.00930	88.77800	248.86000
Garnet4/7	0.01850	1.69810	37.43930	21.30740	0.06230	-0.02090	5.52320	0.26040	35.69380	0.01650	102.03680	298.63000
Garnet4/8	-0.02220	1.55510	37.18990	21.11880	0.08080	-0.00260	5.53740	0.30390	35.36400	0.02870	101.20000	348.40000
Garnet4/9	0.05170	1.53730	37.18080	21.24860	0.08930	0.00070	5.87000	0.33010	35.14640	0.00000	101.47800	398.17000
Garnet4/10	-0.00740	1.48480	37.16010	21.39440	0.06790	0.00980	5.65850	0.42650	35.35660	0.02450	101.59520	447.94000
Garnet4/11	-0.00740	1.46230	37.33270	21.36140	0.07540	0.00880	5.76300	0.49370	35.10840	0.01650	101.63660	497.72000
Garnet4/12	0.11680	1.46450	35.83710	23.59010	0.05190	0.01080	5.32160	0.58040	33.56700	0.00960	100.54980	547.49000
Garnet4/13	0.01720	1.37570	37.10110	21.13120	0.08110	-0.00230	6.03290	0.76950	34.95530	0.00800	101.49780	597.26000
Garnet4/14	0.00860	1.34130	36.99560	21.17700	0.07360	-0.00130	5.50610	0.86970	35.05840	0.00640	101.05210	647.03000
Garnet4/15	0.06410	1.26190	37.18800	21.19900	0.06740	0.00160	5.64120	0.97570	34.96780	0.00050	101.36990	696.81000
Garnet4/16	0.00120	1.34730	37.23800	21.16180	0.06580	0.00030	5.63280	1.04500	34.78720	0.01280	101.29220	746.57000
Garnet4/17	0.03930	1.48460	36.73760	22.21490	0.05340	0.00490	5.15400	0.86920	34.75270	0.02130	101.33790	796.35000
Garnet4/18	0.00980	2.04990	37.37730	21.32930	0.04830	-0.00160	4.37550	0.66040	35.51680	0.03390	101.40270	846.12000
Garnet4/19	0.00990	1.97240	37.40560	21.35460	0.00280	-0.00230	3.07580	0.54490	37.35350	-0.01210	101.72660	895.89000
Garnet4/20	-0.01730	5.76120	27.67440	20.98110	0.05160	0.04570	1.08340	0.34520	34.33660	-0.01140	90.94590	945.66000
Garnet4/21	0.03080	2.34670	37.21460	21.23840	0.02250	0.01110	3.78490	0.43220	35.81030	-0.01160	100.90120	995.43000
Garnet4/22	0.02210	2.41210	37.41550	21.31530	0.03300	-0.00590	3.61770	0.54500	35.91600	0.01110	101.28770	1045.21000
Garnet4/23	0.00740	0.65280	83.24480	9.40120	-0.00600	0.01840	1.10680	0.30200	16.46490	0.00740	111.21650	1094.98000
Garnet4/24	0.04540	1.60910	37.18460	21.30390	0.06470	-0.00390	5.48510	1.26680	34.37820	0.00000	101.34380	1144.75000
Garnet4/25	0.02710	1.36330	37.16520	21.19060	0.07100	0.00130	5.20080	1.62570	34.52820	0.02390	101.19690	1194.52000
Garnet4/26	0.03940	1.23550	37.08950	21.16320	0.06810	0.01100	5.31690	1.80820	34.65480	-0.01380	101.39120	1244.29000
Garnet4/27	0.05790	1.25230	37.32960	21.18960	0.07370	-0.00060	5.21610	2.01300	34.57520	0.02700	101.74010	1294.06000
Garnet4/28	0.03570	1.17910	36.12890	20.87680	0.13210	0.00260	5.05810	1.95480	33.66870	0.00050	99.04870	1343.83000
Garnet4/29	0.17000	1.43850	34.20930	19.49000	0.05650	0.00290	5.32800	1.95250	33.58450	0.03330	96.26940	1393.60000

Continued on next page

Table C.9 – continued from previous page

Phase	Na2O	MgO	SiO2	Al2O3	TiO2	K2O	CaO	MnO	FeO	Cr2O3	Total	Distance μm
Garnet4/30	0.18930	1.23220	35.96530	21.97090	0.05670	0.06500	5.44890	1.80150	32.80680	-0.00050	99.54300	1443.37000
Garnet4/31	0.38810	2.74740	34.05700	25.48590	0.06730	0.18330	4.26140	1.07390	29.98370	0.01610	98.27330	1493.15000
Garnet4/32	-0.01350	1.26140	37.08710	21.04900	0.06690	0.00450	5.37080	1.44900	34.62850	0.00530	100.95020	1542.92000
Garnet4/33	0.00980	1.29090	37.00440	21.15100	0.06920	0.01620	5.29840	1.36000	34.80170	-0.00740	101.00820	1592.69000
Garnet4/34	0.02330	1.28330	37.33550	21.24920	0.08030	0.00810	5.68660	1.09040	34.67870	0.04140	101.50360	1642.46000
Garnet4/35	0.10400	1.38290	37.73320	21.78660	0.06220	0.01980	5.47950	0.92290	34.71050	-0.00900	102.20420	1692.23000
Garnet4/36	0.01960	1.46710	37.36770	21.23060	0.06120	0.00580	5.68350	0.60340	34.95950	0.02010	101.42530	1742.01000
Garnet4/37	0.40280	1.17570	37.79010	25.41710	0.07420	0.12540	5.38590	0.32480	31.15910	0.02420	101.89680	1791.78000
Garnet4/38	0.01100	1.62700	37.14230	21.26650	0.06020	0.00260	5.39480	0.29690	35.31840	0.03070	101.17160	1841.55000
Garnet4/39	0.02330	1.84350	37.13740	21.36260	0.07900	0.00290	5.31740	0.22580	35.37300	0.03500	101.42030	1891.32000
Garnet4/40	0.03190	2.41480	37.42740	21.38230	0.04140	-0.00100	4.22240	0.11810	35.83890	0.03120	101.51020	1941.09000
Biotite1	0.11060	8.24410	35.42830	17.17940	1.41020	8.93440	0.00610	0.00790	23.38660	0.01870	94.73210	NaN
Biotite2	0.09360	8.31580	35.41090	17.34200	1.43590	8.96140	-0.01880	0.01720	23.39130	0.05460	95.02270	NaN
Biotite3	0.04770	14.53160	24.50200	22.30520	0.07910	0.01990	0.04160	0.01760	25.36100	0.07170	86.97810	NaN
Biotite4	0.13600	8.74490	35.59730	17.51980	1.28790	8.93280	0.00410	0.04200	22.08630	0.05250	94.40360	NaN
Biotite5	0.25900	8.48160	36.09550	17.95110	1.28920	8.86160	0.03630	0.04250	22.35930	0.03270	95.40880	NaN
Biotite6	0.05400	8.48540	35.44780	17.45460	1.31950	8.76070	0.00820	-0.00980	22.89730	0.05920	94.48680	NaN
Biotite7	0.07830	8.41380	35.42800	17.13500	1.55860	8.74630	-0.00100	0.01360	22.79240	0.06410	94.23010	NaN
Chlorite1	0.04790	13.25280	24.81940	22.23320	0.10980	0.01100	0.00410	0.02140	27.58590	0.04990	88.13520	NaN
Chlorite2	0.01690	15.67920	25.07080	23.17250	0.05690	-0.00440	0.00410	0.00370	23.89740	0.02180	87.92330	NaN
Chlorite3	0.05170	14.30770	24.90040	22.62010	0.06620	0.03170	0.03720	0.04100	25.83890	0.04910	87.95070	NaN
Chlorite4	0.01730	14.04490	24.91270	22.64960	0.10960	0.01270	0.01320	0.03260	26.05660	0.03390	87.88310	NaN
Muscovite1	1.50070	0.61780	46.55320	36.74450	0.26440	9.01610	0.00320	-0.00290	0.95760	0.03670	95.69400	NaN
Muscovite2	1.83400	0.75910	46.15930	35.96000	0.36290	8.48810	0.02430	-0.00290	1.01410	0.05650	94.65810	NaN
Muscovite3	1.13150	0.02270	95.61750	2.09150	0.00080	0.05130	0.10130	0.01880	0.06910	0.01830	99.13530	NaN

Continued on next page

Table C.9 – continued from previous page

Phase	Na2O	MgO	SiO2	Al2O3	TiO2	K2O	CaO	MnO	FeO	Cr2O3	Total	Distance µm
Muscovite4	1.80920	0.54140	46.14850	36.82390	0.27940	8.66770	0.00180	0.00150	0.99520	0.04870	95.31750	NaN
Muscovite5	0.00280	-0.00790	100.65610	-0.02420	-0.00250	0.00960	0.00250	-0.00100	0.06030	0.00120	100.73240	NaN

C.5 Garnet profiles

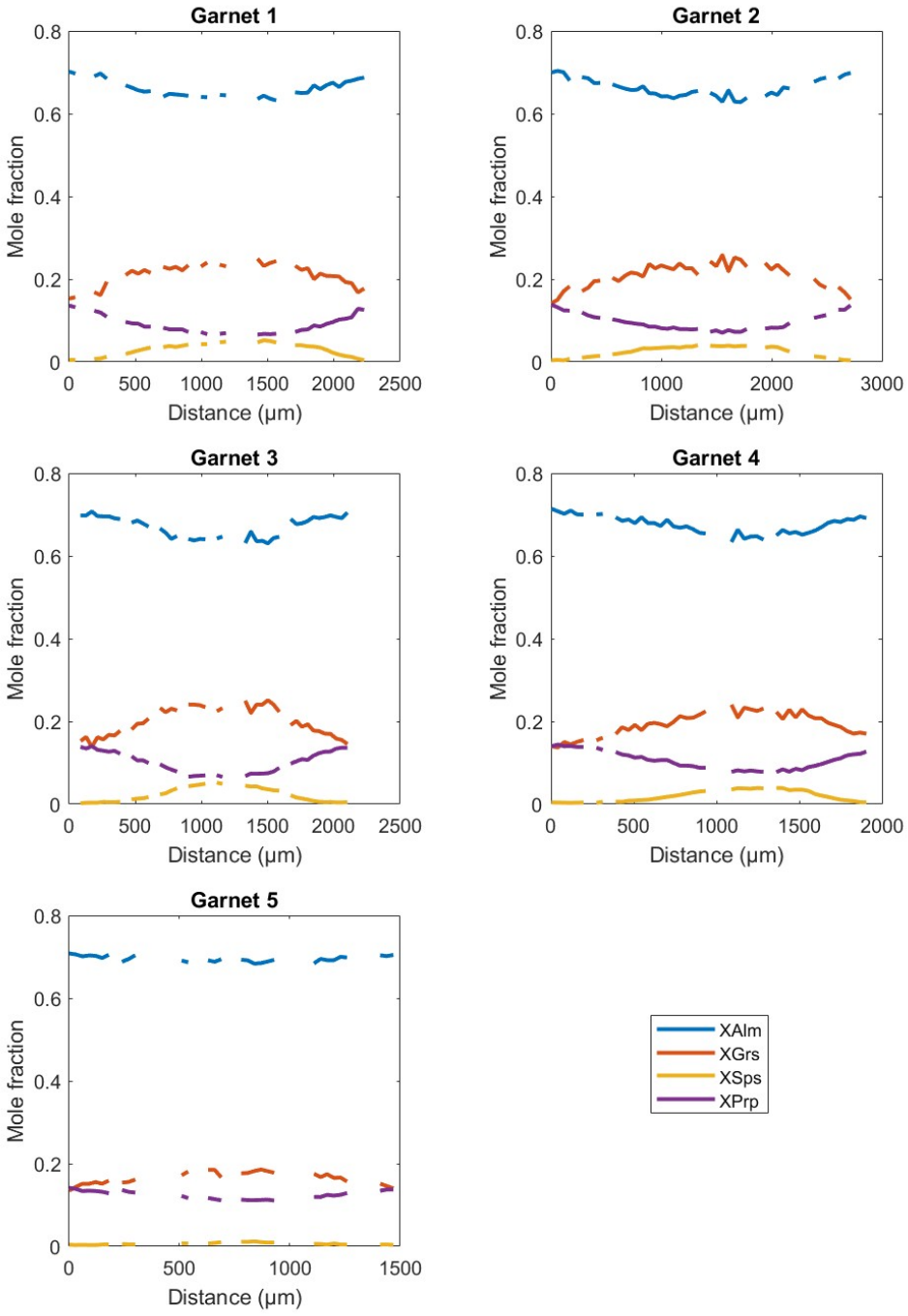

Fig. C.1 Garnet profiles for sample Z03b.

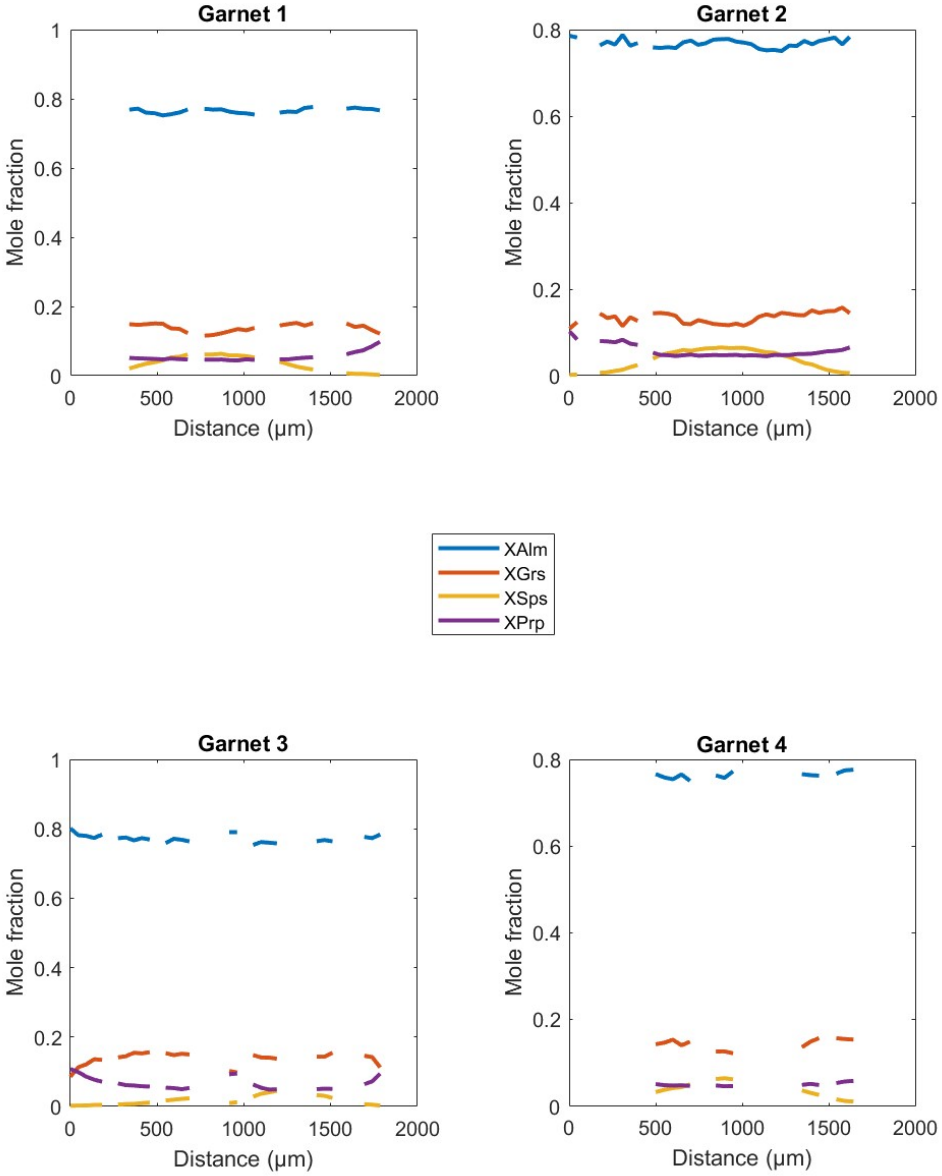

Fig. C.2 Garnet profiles for sample Z36.

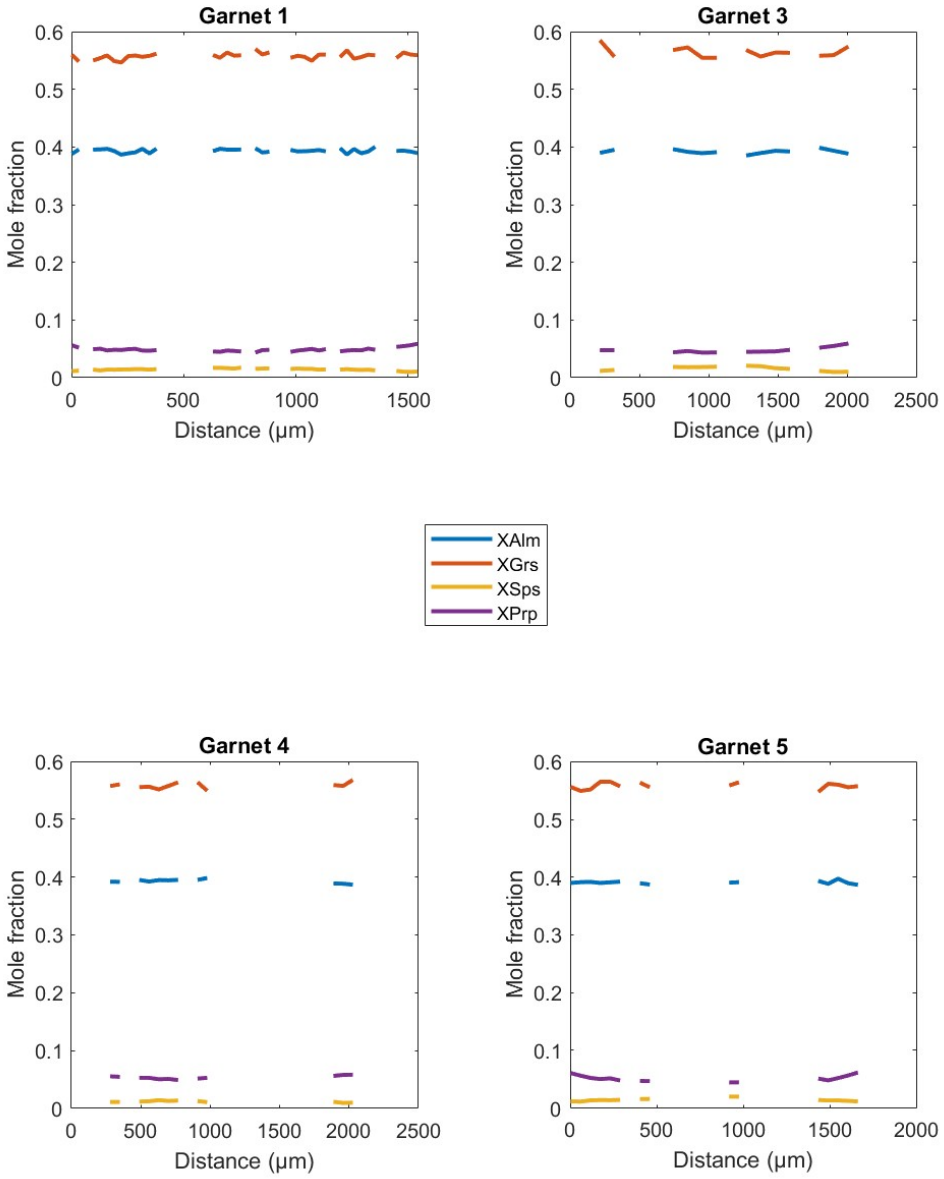

Fig. C.3 Garnet profiles for sample Z34.

Appendix D

The Use of MEMS Accelerometers and Ambient Noise Tomography for Regional Mineral Exploration.

Table D.1 Solwezi Seismograph Network Details

Network	Station	Instrument	Latitude	Longitude	Elevation	StartMonth	EndMonth
SOLWEZI	S2101	WiNG node	-11.98834	26.49255	1441.0	Oct-21	May-22
SOLWEZI	S2102	WiNG node	-12.552	26.47688	1434.0	Oct-21	May-22
SOLWEZI	S2103	WiNG node	-12.02662	26.47947	1444.0	Oct-21	May-22
SOLWEZI	S2104	WiNG node	-12.03742	26.46362	1410.0	Oct-21	May-22
SOLWEZI	S2105	WiNG node	-12.06187	26.45232	1406.0	Oct-21	May-22
SOLWEZI	S2106	WiNG node	-12.06931	26.44954	1412.0	Oct-21	May-22
SOLWEZI	S2107	WiNG node	-12.08141	26.45404	1396.0	Oct-21	May-22
SOLWEZI	S2108	WiNG node	-12.09226	26.45411	1396.0	Oct-21	May-22
SOLWEZI	S2109	WiNG node	-12.130	26.45446	1395.0	Oct-21	May-22
SOLWEZI	S2110	WiNG node	-12.10858	26.43922	1411.0	Oct-21	May-22
SOLWEZI	S2111	WiNG node	-12.11822	26.45813	1403.0	Oct-21	May-22
SOLWEZI	S2112	WiNG node	-12.12442	26.45169	1376.0	Oct-21	May-22
SOLWEZI	S2113	WiNG node	-12.13636	26.44808	1357.0	Oct-21	May-22
SOLWEZI	S2114	WiNG node	-12.14740	26.44312	1374.0	Oct-21	May-22
SOLWEZI	S2115	WiNG node	-12.16107	26.44315	1344.0	Oct-21	May-22
SOLWEZI	S2116	WiNG node	-12.16735	26.43480	1363.0	Oct-21	May-22
SOLWEZI	S2117	WiNG node	-12.17475	26.43325	1376.0	Oct-21	May-22
SOLWEZI	S2118	WiNG node	-12.18158	26.42382	1356.0	Oct-21	May-22
SOLWEZI	S2119	WiNG node	-12.19082	26.41637	1316.0	Oct-21	May-22
SOLWEZI	S2120	WiNG node	-12.20480	26.41713	13.0	Oct-21	May-22
SOLWEZI	S2121	WiNG node	-12.22253	26.41137	1346.0	Oct-21	May-22
SOLWEZI	S2122	WiNG node	-12.23732	26.41353	1295.0	Oct-21	May-22
SOLWEZI	S2123	WiNG node	-12.25816	26.40148	1285.0	Oct-21	May-22
SOLWEZI	S2124	WiNG node	-12.27269	26.39537	1303.0	Oct-21	May-22

Continued on next page

Table D.1 – continued from previous page

Network	Station	Instrument	Latitude	Longitude	Elevation	Start Month	End Month
SOLWEZI	S2125	WiNG node	-12.29438	26.38707	1297.0	Oct-21	May-22
SOLWEZI	S2126	WiNG node	-12.31522	26.37755	1332.0	Oct-21	May-22
SOLWEZI	S2127	WiNG node	-12.32579	26.35791	1330.0	Oct-21	May-22
SOLWEZI	S2128	WiNG node	-12.34981	26.35825	1334.0	Oct-21	May-22
SOLWEZI	S2129	WiNG node	-12.36797	26.33632	1314.0	Oct-21	May-22
SOLWEZI	S2130	WiNG node	-12.37890	26.31699	1312.0	Oct-21	May-22

D.1 Error analysis

Following *Forsyth and Li* (2005), the variance of the inversion solution is found using linear error propagation (Equation D.1).

$$\sigma_m^2 = \frac{qC_{MM}q^T}{\sum q} \tag{D.1}$$

$$C_{MM} = (G^T C_d^{-1} G + C_m^{-1})^{-1} \tag{D.2}$$

Where C_{MM} is the complete, *a posteriori*, model covariance matrix and q are the weights used in the Gaussian model smoothing. The phase velocity residuals (ϵ) are calculated following Equation D.3.

$$\epsilon = \frac{s}{p\phi_T} - \frac{s}{(2\pi\frac{s}{p\bar{c}} + G(m - m_0))p} \tag{D.3}$$

D.2 Resolution estimates

We follow the method outlined in *Barmin et al.* (2001) for quantifying the spatial resolution and amplitude bias of the tomography. The resolution matrix is defined in Equation D.4.

$$R = (G^T C_d^{-1} G + C_m^{-1})^{-1} G^T C_d^{-1} G \tag{D.4}$$

Where each row of R is equivalent to a map defining the resolution for a particular node in the model. For each row, we fit a cone to the map. The width of the cone halfway to the bottom is taken as the spatial resolution (*Ritzwoller et al.*, 2002). The amplitude resolution is estimated using Equation D.5.

$$\hat{m} = Rm \tag{D.5}$$

For each node in the velocity model, we apply the appropriate row of the resolution matrix to a test model (m) consisting of a cylinder of unit height with a diameter equal to twice the spatial resolution ($2\sigma_R$) at the node point. The estimated amplitude of the fit surface ($\hat{m}$) is the average amplitude within σ_R of the centre of the cylinder. The amplitude bias estimate is the relative difference between the input amplitude and the estimated amplitude.

D.3 Phase velocity tomography trade-off

The trade-off analyses plot the sum of the absolute residuals against the model length.

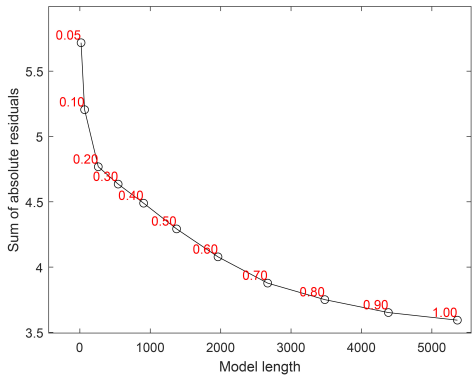

Fig. D.1 Model damping trade-off for phase velocity tomography

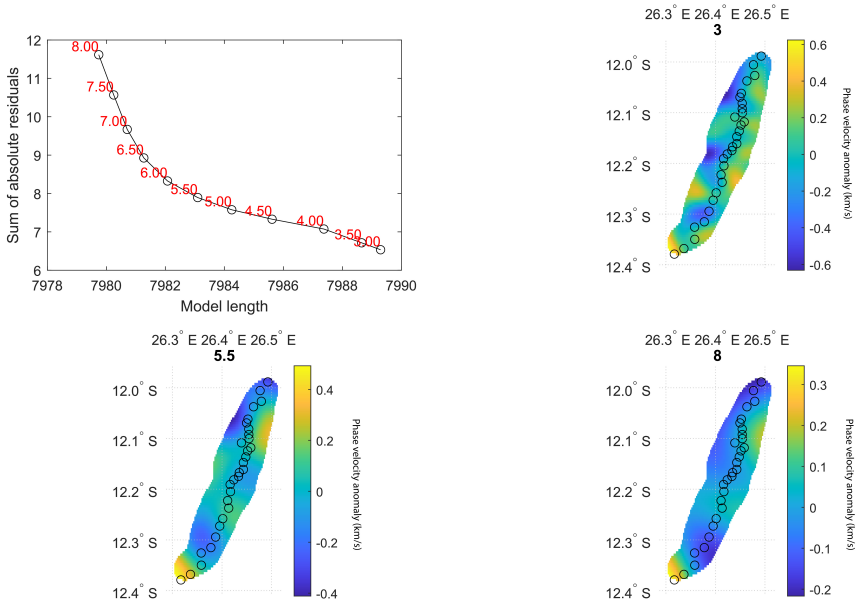

Fig. D.2 Characteristic length trade-off for phase velocity tomography

D.4 Phase velocity maps with accompanying resolution and error estimates

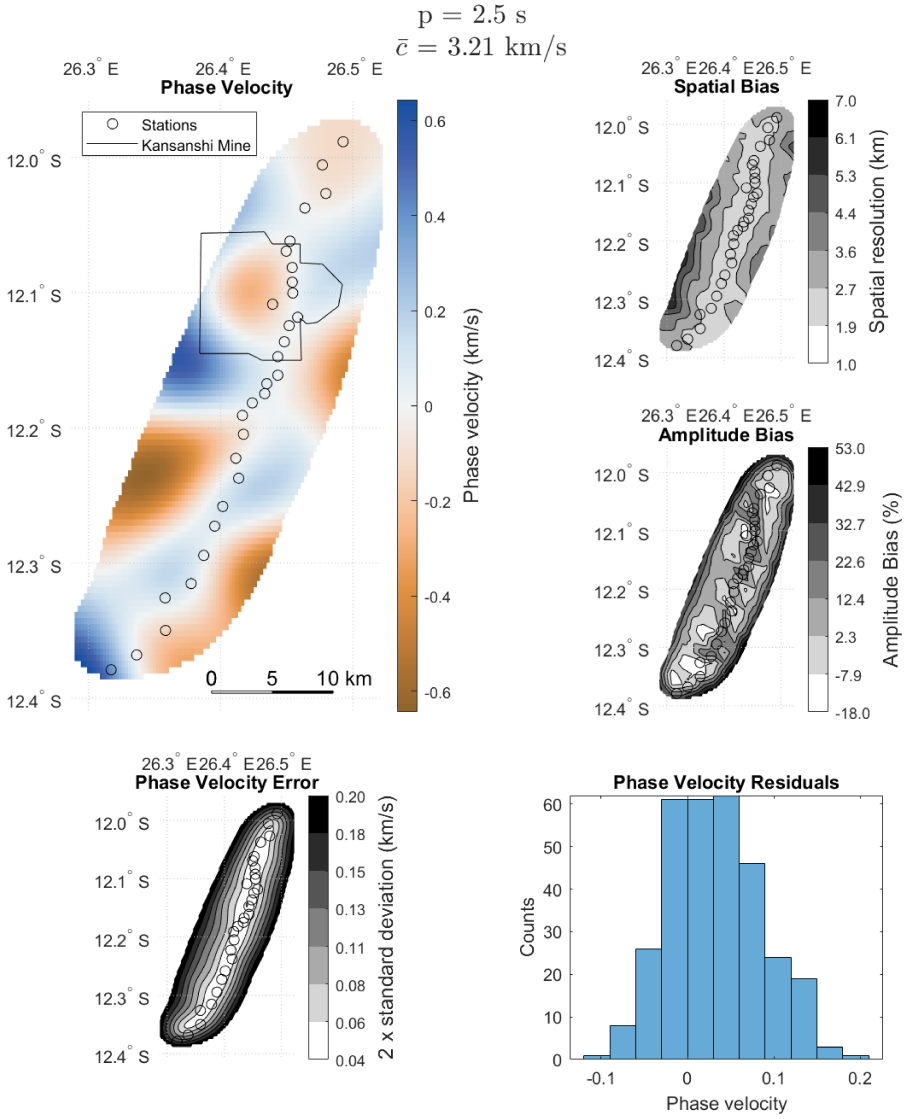

Fig. D.3 Phase velocity tomography outputs for 2.5s Rayleigh wave.

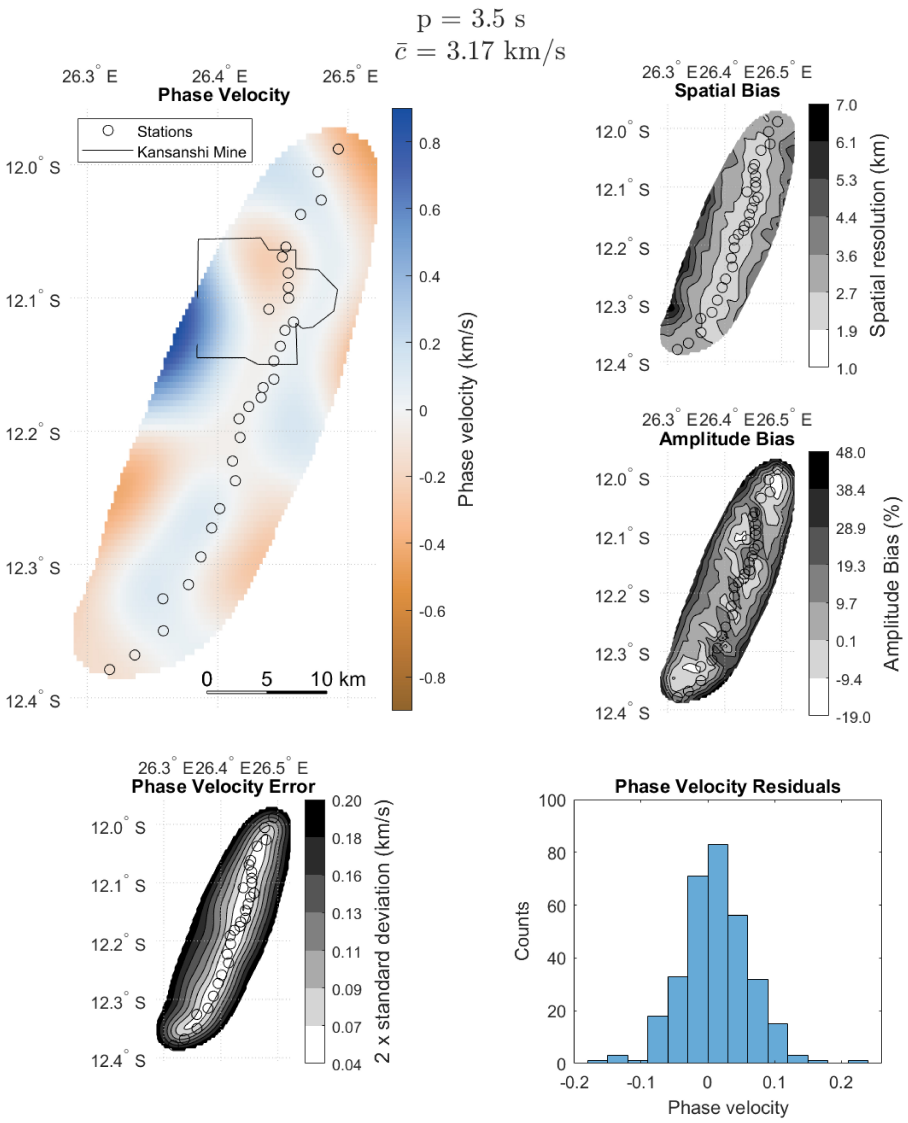

Fig. D.4 Phase velocity tomography outputs for 3.5s Rayleigh wave.

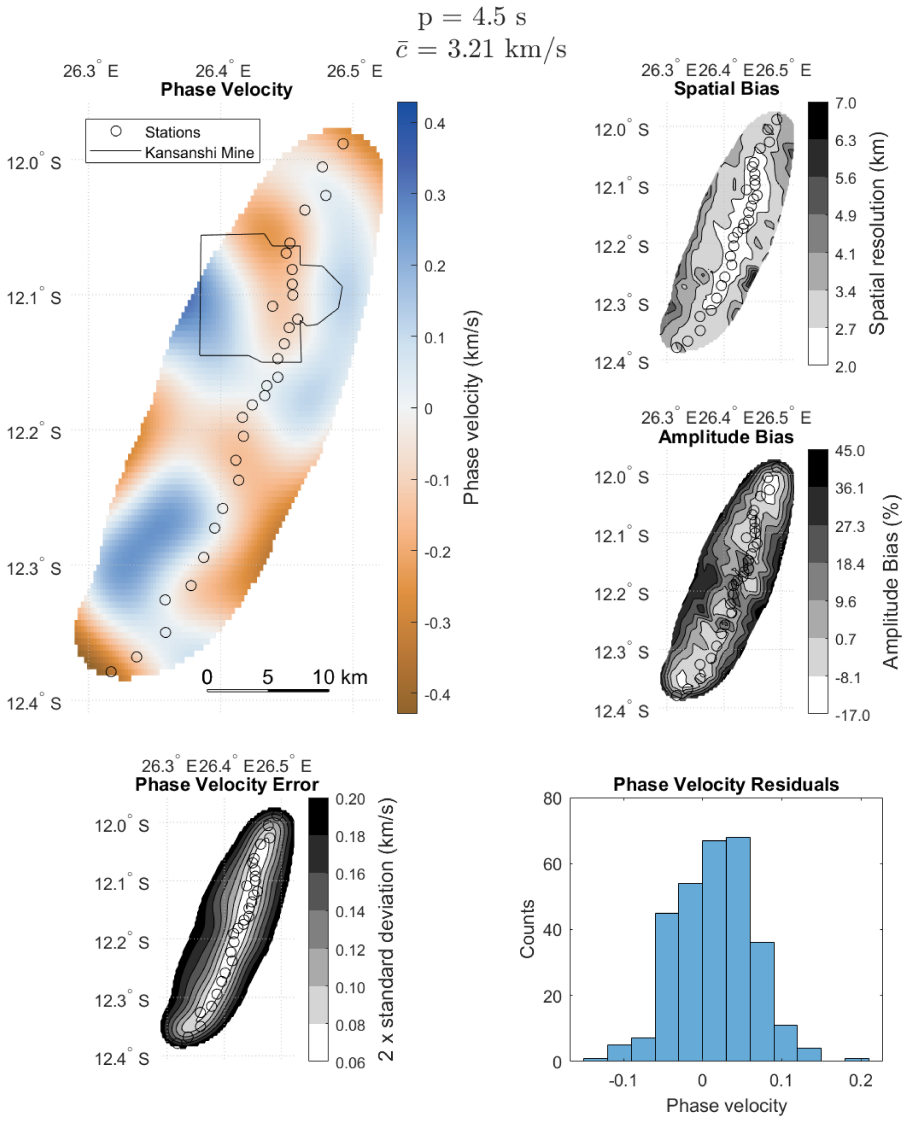

Fig. D.5 Phase velocity tomography outputs for 4.5s Rayleigh wave.

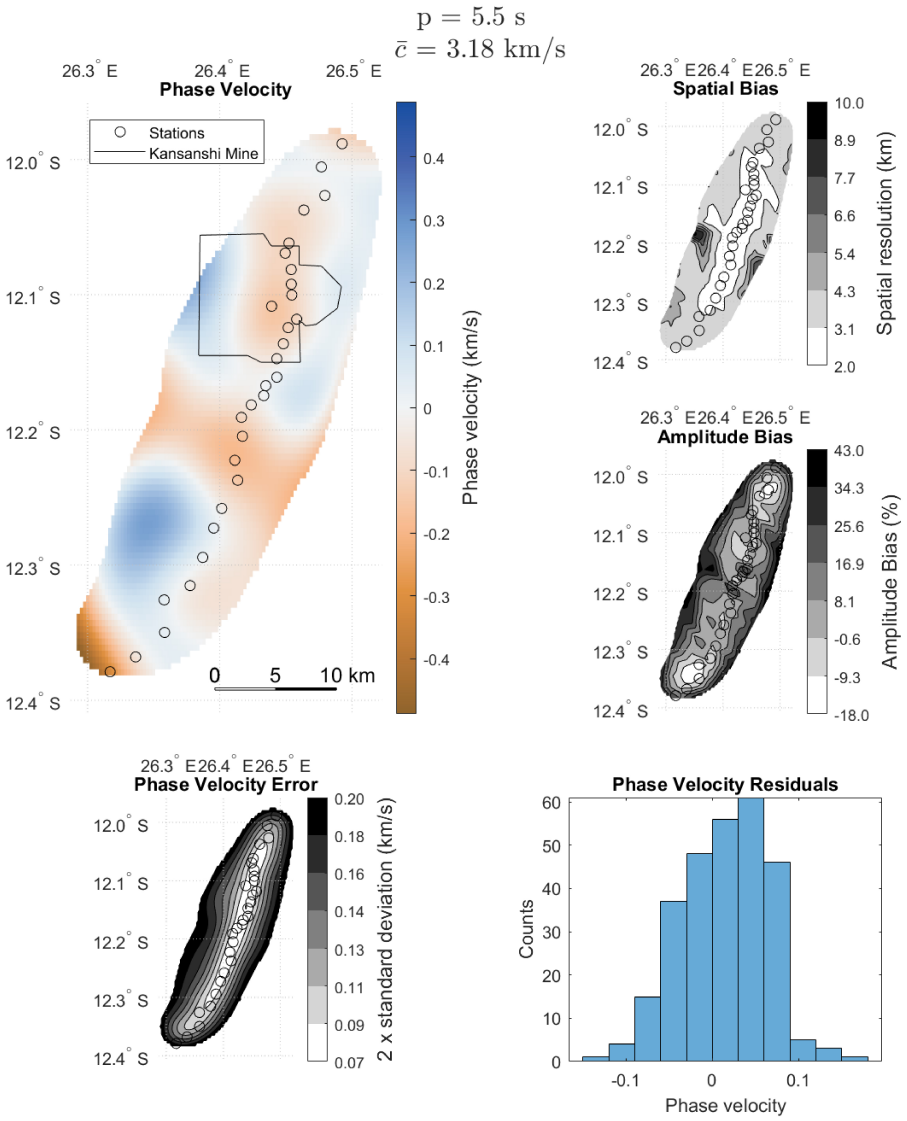

Fig. D.6 Phase velocity tomography outputs for 5.5s Rayleigh wave.

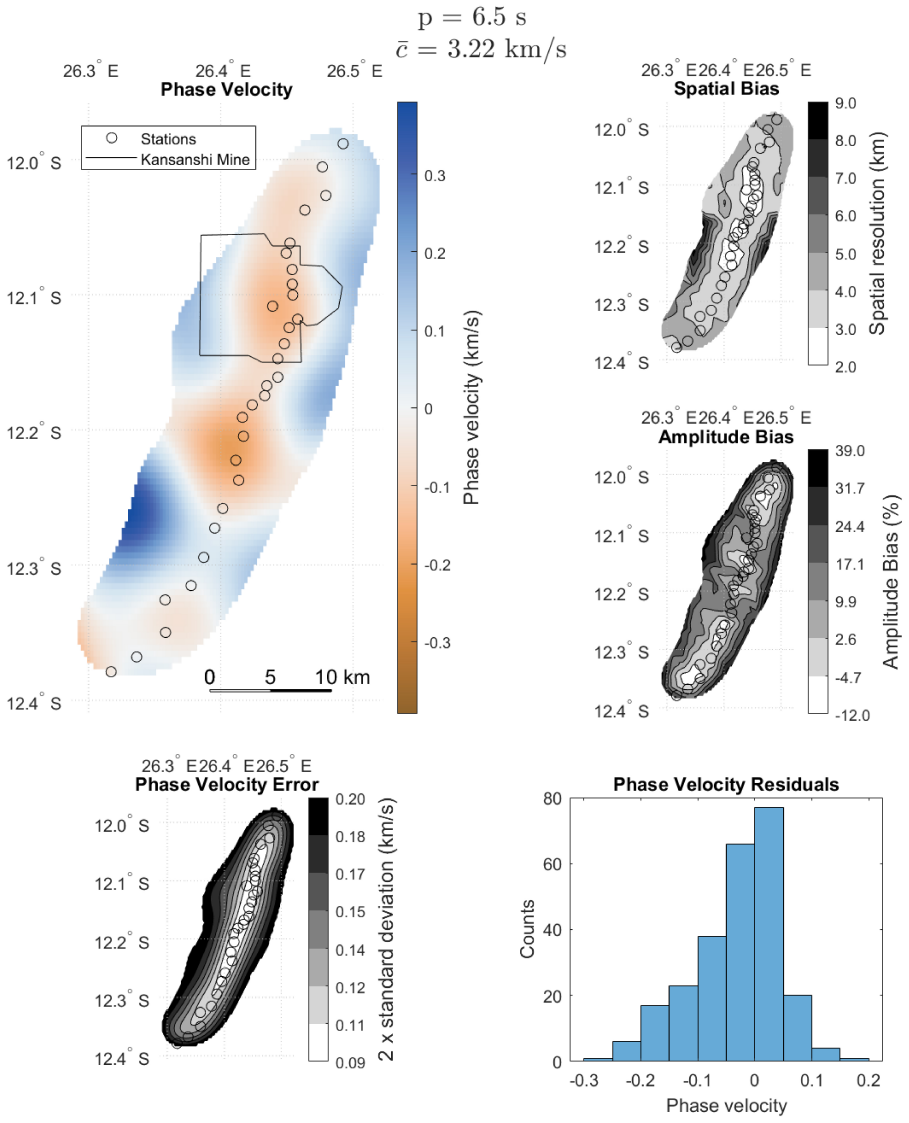

Fig. D.7 Phase velocity tomography outputs for 6.5s Rayleigh wave.

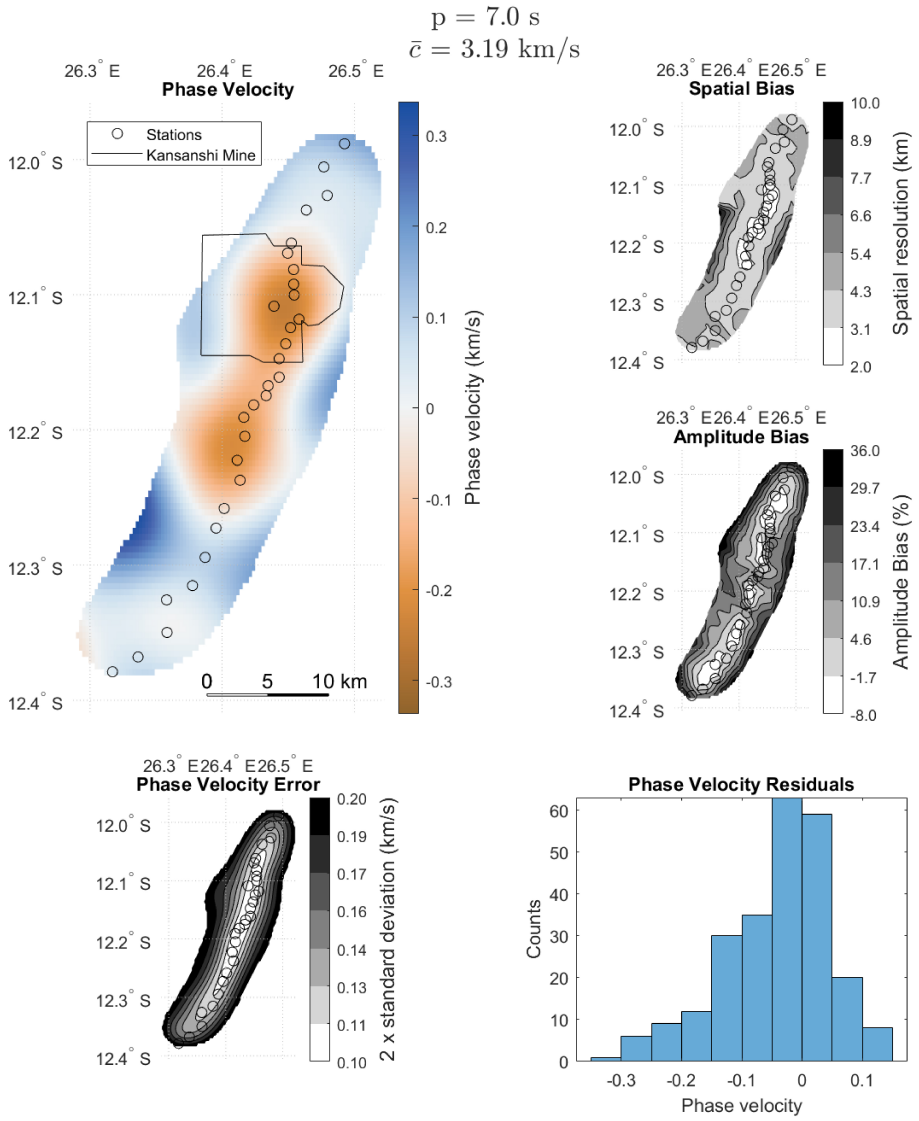

Fig. D.8 Phase velocity tomography outputs for 7.0s Rayleigh wave.

D.5 S-wave inversion trade-off

A damping parameter was selected which minimized the length of the solution (L) while still fitting the data.

$$L = (m - \bar{m})^T (m - \bar{m}) \tag{D.6}$$

Where m is the model vector and $\bar{m}$ is the mean of the model vector. A value of 0.1 was chosen for the damping parameter as it represents the knee of the trade-off curve

between the spread of the resolution matrix and the solution length. A chi-value of less than 1 indicates that the model fits the observed data.

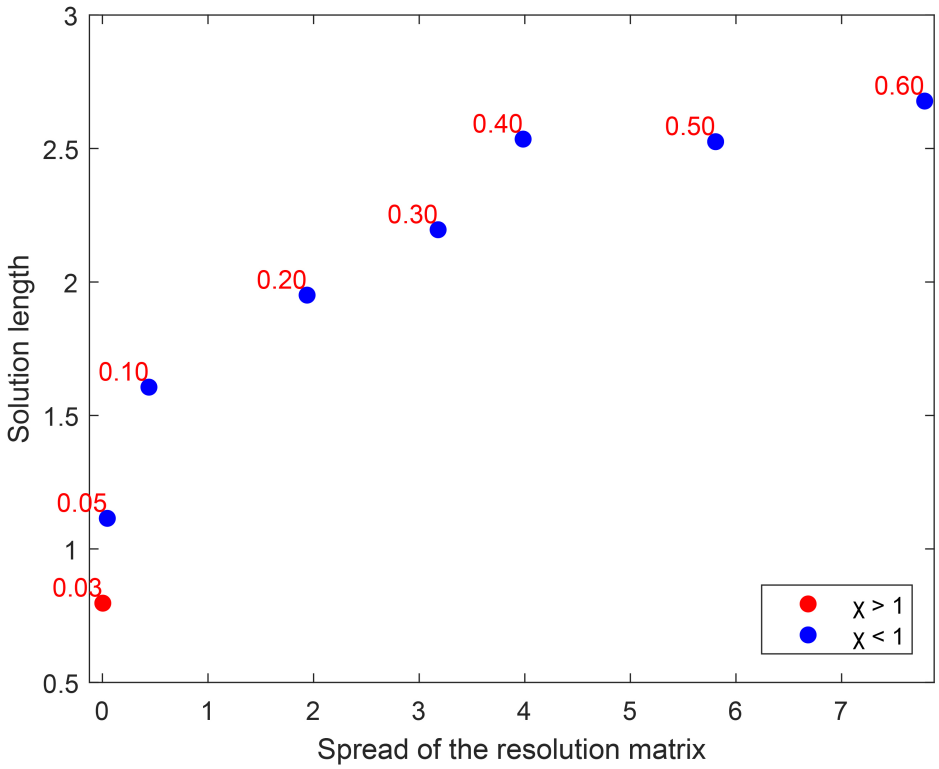

Fig. D.9 S-wave damping trade-off.